Table of Contents

ensn

UMR6637

1.0 INTRODUCTION

The capability of radar to detect point targets beneath vegetation canopies is limited by (1) the extinction due to both absorption and scattering losses from two-way transmission through the canopy and (2) the net backscatter from the canopy itself which affects the target-to-background ratio. Both of the limiting factors are functionally dependent upon the radar wave parameters of wavelength, polarization and angle of incidence. A simplified model of the dominant source terms contributing to the net radar backscatter from a forest canopy σ^o_f is given by

$$\sigma^o_f = \sigma^o_c + (\sigma^o_g + \sigma^o_{gt}) \ /L^2 \qquad (1)$$

where σ^o_c is the backscattering contribution by the foliage and branches in the crown layer and σ^o_g and σ^o_{gt} are respectively the backscatter from the ground and bistatic ground-trunk scatter as reduced by the one-way propagation loss L. Since σ^o_{gt} is produced by a "corner-reflector" mechanism caused by multiple specular reflections from the ground surface and tree trunks, it may be the dominant source of like-polarized backscatter at lower microwave frequencies where L is least.

The radar backscatter from a unobscured point target is given by

$$\sigma^o = \sigma_t/\rho_a\rho_r + \sigma^o_g \qquad (2)$$

where σ_t is the cross-section of the point target and ρ_a and ρ_r are the azimuth and range resoultions respectively. However, when such a target is obscured by a forest canopy, the simplified scattering model (ignoring possible interactions between the target and the canopy) becomes

$$\sigma^o_t = \sigma^o_c + (\sigma_t/\rho_a\rho_r + \sigma^o_g + \sigma^o_{gt})/L^2 \qquad (3)$$

where σ^o_t is the net backscatter from both the target and the forest canopy.

The canopy propagation loss L results from extinction by both the crown layer of foliage and branches as well as the trunk layer and is dependent upon incidence angle and layer thicknesses via

$$L = \exp(\kappa_c h_c \sec\theta) \exp(\kappa_t h_t \sec\theta) \qquad (4)$$

where κ is the one-way extinction coefficient, h is the layer thickness the subscripts c and t refer to the crown and trunk layers respectively, and θ is the angle of incidence with respect to nadir.

It is obvious from (3) that as net canopy propagation loss L increases, the effective radar cross section of the point target is decreased. The magnitude of the canopy extinction is defined by both forest stand conditions and radar wave parameters. It is well known that, in general, canopy extinction increases in proportion to the number density of scattering elements (trunks, branches and leaves) within the canopy. Hence, the propagation loss L can be expected to vary considerably as functions of the height and density of forest stands. In addition, extinction is known to be dependent upon the dielectric properties of a given set of scattering elements. In the case of vegetation, the relative dielectric constant at microwave frequencies is largely controlled by the moisture content and temperature of the canopy elements. Hence, extinction can vary both (1) seasonally in response to phenology (growth) and the freezing and thawing of canopy elements and (2) diurnally in response to evaportransporative control of canopy water status and the orientations of leaves. As a consequence, extinction can be generally expected to be minimized during the frozen conditions of winter and during times of maximum water stress within the growing season (usually mid-afternoon).

With respect to wave parameters of frequency and angle of incidence, canopy extinction is expected to generally increase with frequency since scattering losses increase as the size distributions of the scattering elements (trunks, branches and leaves) approach or exceed wavelength. Consequently, penetration depth is reduced at higher frequencies due to the increased scattering and absorption by the crown layer containing the branches and foliage. Finally, extinction can be expected to increase with angle of incidence via (4) in proportion to the slant path through the canopy.

Besides extinction, a second consideration is the backscatter from the forest canopy itself which both contributes to the net backscatter of the resolution element or elements containing the point target of interest as well as determining the background statistics against which the point target resolution element itself must be compared for purposes of discrimination. The backscatter from a vegetation canopy is determined by the functional relationship between the wave parameters of frequency, polarization and angle of incidence and the canopy parameters of canopy architecture (number density, size, shape and orientation of canopy scattering elements) and the dielectric conditions of the canopy scattering elements and the forest floor (i.e., soil, snow or water).

For a fully foliated tree canopy, antecedent scatterometer investigations (Ulaby and Dobson, 1989) show that radar backscatter can be expected to increase with frequency between L-band and X-band and to generally decrease with $\cos\theta$. In addition, forest canopies are generally found to be highly depolarizing with HH/HV typically <6 dB for frequencies between L- and X-bands due to the complex geometries of the scattering elements. Thus, from the foregoing, it may seem reasonable to presume that a radar operating at low frequency (i.e., L-band or lower) and at incidence angles from 20^{o} to 40^{o} relative to nadir would serve to minimize both the backscatter from the forest canopy and the extinction by the canopy; and hence, optimize point target discrimination. However, when

considering the utility of polarimetric radar, it is important to consider not only the absolute magnitude of the backscatter but also the relative amplitude and phase of the return as a function of polarization state. Of major concern are the relative contributions of a number of distinct, potential source terms to the net canopy backscatter as shown in Figure 1 for various scattering pathways. For a given collection of scattering elements, each pathway presents certain implications with respect to the polarimetric scattering response. For example, scattering term 4 in Figure1 results from multiple forward scattering from the ground surface and the trunks (and the inverse) and yields a "double-bounce" return also characteristic of dihedral corner reflectors. In general, the importance of this ground-trunk interaction term decreases with frequency due both to decreases in forward scattering from the surface and trunks and to increases in crown-layer extinction. Hence, for stands of trees characterized by many or tall vertical trunks with an optically thin crown layer of branches and leaves, a polarimetric radar operating at low frequencies (i.e., $\leq$ L-band) would tend to observe backscatter dominated by this "double-bounce" mechanism and could result in poor polarimetric signal-to-background with respect to dihedral-like point targets of interest.

1.1 Approach

In order to establish a general understanding of the problem with respect to radar backscatter and extinction by forest canopies, two approaches may be taken. The first entails undertaking a expansive series of radar data acquisitions in an effort to empirically determine the statistical properties of forest clutter and extinction for many different forest conditions of interest. Since both the extinction and backscattering coefficients of vegetation canopies are controlled by (1) the number density of scattering elements, (2) the respective size, shape and orientation distributions of these

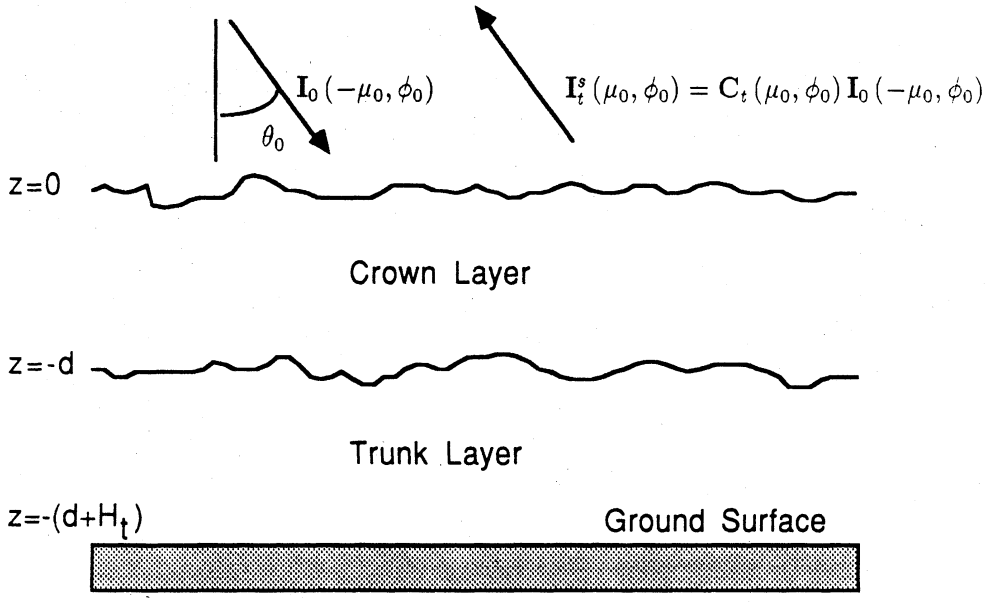

(a) Tree canopy model.

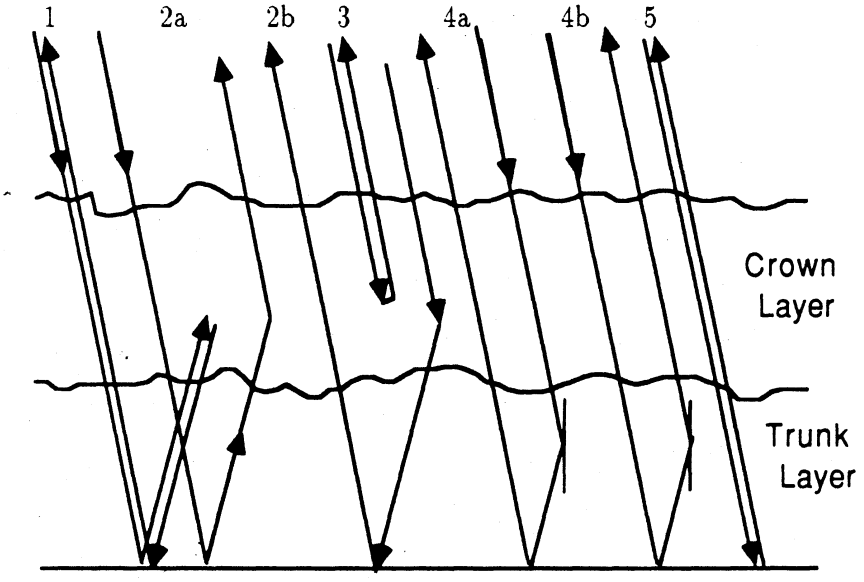

(b) First order contributions to canopy backscatter.

Figure 1: Illustration of (a) the geometry used to model a tree canopy and (b) the scattering contributions obtained by the first-order radiative transfer solution for canopy backscatter.

elements, and (3) their dielectric properties. The number of data acquisitions required by this approach can become quite large. This becomes readily apparent when one considers (1) the nature of spatial variability between forest types with respect to stand architecture, individual tree morphology and tree density and also (2) the known temporal variability related to (a) phenology (or growth and seasonal leaf loss) and (b) dielectric variations induced by temperature changes (i.e., freezing vs. thawed temperature conditions) and daily changes in canopy water status (i.e., those related to evapotranspirative water losses). This approach is also constrained by the ability to adequately calibrate the radar(s) for comparison of data obtained at different times, different places, or by different systems.

The second approach seeks to take advantage of deterministic, theoretical scattering models to predict the quantities of interest, extinction and backscatter, as functions of the pertinent canopy variates. For this approach to succeed, the models must be physically-based and be dependent upon measureable physical quantities whose natural ranges of distribution can be reasonably approximated without undertaking elaborate field studies. Once the scattering and extinction model has been validated using selected test measurements, it can then be used to simulate the quantities of interest in the point target detection problem as functions of the wave parameters of frequency, polarization and angle of incidence over the desired range of canopy conditions. This second approach promises to be the quickest and least expensive; and is the approach taken in this study. In addition, it provides a fundamental understanding of the various scattering mechanisms involved; and hence, can support the development of other applications.

1.2 Objectives

Given the approach outlined in the previous section, the objectives of this study are (1) to validate a physically - based model for radar backscatter and extinction by forest canopies using existent and available data sets and (2) use this model to simulate the expected ranges of canopy extinction and backscatter over a selected range of forest canopy conditions. The model chosen for this study is the Michigan Microwave Canopy Scattering (MIMICS) model which is a first-order radiative transfer approach briefly described in Section 2. This model is validated in comparison to truck-mounted scatterometer data and airborne SAR data obtained by experiments described in Section 3. The model validations and consequent simulations for canopy extinction are presented in Section 4, and the model validations and consequent simulations for backscatter are given in Section 5.

2.0 RADAR SCATTERING MODEL FOR FOREST CANOPIES

A forest canopy is a inhomogeneous medium consisting of scattering elements with many different sizes, shapes and orientations. Radar backscattering from this canopy may include contributions from (1) volume scattering within the crown layer of foliage and branches, (2) surface scattering by the underlying ground surface as well as (3) multiple interactions involving both the canopy and the ground surface. Because the vegetation elements tend to be somewhat random in terms of their spatial locations and orientations, scattering models are usually formulated in terms of statistical distributions characterizing these and other properties of the canopy scatterers. In addition to considering the statistics associated with an individual tree, we have to consider the spatial distribution and number density of trees in the stand, the distribution for the overall shape and dimensions of the trees, and the statistics associated with canopy closure.

There are two approaches commonly used to model a layer containing a random distribution of scattering elements. Models based upon the field approach (Fung and Ulaby, 1978; Tsang and Long, 1981) account for the inhomogeneity of the medium through the correlation function characterizing the fluctuating component of the dielectric constant of the medium. Models based upon the radiative transfer intensity approach (Eom and Fung, 1984; Ulaby et al., 1986; and Tsang et al., 1985) account for the inhomogeneity by averaging the Stokes matrix over the statistical distributions characterizing the sizes, shapes and orientations of the canopy elements. In general, the field approach is appropriate for weakly scattering media in which the ratio of the fluctuating component of the dielectric to the mean value for the medium is small (Lee and Kong, 1985). For a vegetation medium in which the scatterers have discrete configurations and have dielectric constants that are much larger than that of the background (air), the radiative transfer approach is more appropriate.

A first-order radiative transfer model of microwave backscatter from tree canopies has been developed at the University of Michigan (Ulaby et al., 1988 and 1990). This model, known as the Michigan Microwave Canopy Scattering (MIMICS) model, is fully polarimetric and is designed to function over a wide range of incidence angles for frequencies between 0.5 GHz and 10 GHz. The version of MIMICS employed in this study is the first generation research model (MIMICS I) that has been developed for application to tree canopies with continuous crown layers. In modeling canopy backscatter, MIMICS accounts for scattering contributions directly from the trees themselves, direct backscatter from the underlying ground surface, and contributions resulting from multiple interactions between the trees and the ground surface.

MIMICS models the forest canopy as two distinct horizontal vegetation layers superimposed over a dielectric ground surface as illustrated in Figure 1. The top layer contains a laterally continuous layer of tree crowns of vertical

extent d, and consists of the statistical distributions of leaves and branches. The bottom layer contains trunks which are treated as smooth dielectric cylinders with a statistical distribution of height H_t and diameter. The ground layer is treated as a rough dielectric slab which may be layered to account for the presence of other media over the mineral soil (i.e., snow). MIMICS relates the incident Stokes intensity I_0 to the scattered intensity I^s through a transformation matrix C_t as

$$I^s = C_t(\mu_o, \phi_o)\, I_o \qquad (5)$$

where

$$C_t(\mu_o,\phi_o) = \frac{1}{\mu_o} e^{-\kappa_c^+ d/\mu_o} R'(\mu_o,\phi_o + \pi) Q_c(-\mu_o,\phi_o + \pi) A_1 Q_c^{-1}(\mu_o,\phi_o) R'(\mu_o,\phi_o) e^{-\kappa_c^- d/\mu_o}$$

$$+ \frac{1}{\mu_o} e^{-\kappa_c^+ d/\mu_o} R'(\mu_o,\phi_o + \pi) Q_c(-\mu_o,\phi_o + \pi) A_2 Q_c^{-1}(\mu_o,\phi_o) R'(\mu_o,\phi_o) e^{-\kappa_c^- d/\mu_o}$$

$$+ \frac{1}{\mu_o} Q_c(\mu_o,\phi_o + \pi)\, A_3 Q_c^{-1}(-\mu_o,\phi_o)$$

$$+ \frac{1}{\mu_o} Q_c(\mu_o,\phi_o + \pi)\, A_4 Q_c^{-1}(-\mu_o,\phi_o)$$

$$+ \frac{1}{\mu_o} e^{-\kappa_c^+ d/\mu_o} e^{-\kappa_t^+ H_t/\mu_o} R(\mu_o) Q_t(-\mu_o,\phi_o + \pi) A_5 Q_t^{-1}(-\mu_o,\phi_o) e^{-\kappa_c^- d/\mu_o}$$

$$+ \frac{1}{\mu_o} e^{-\kappa_c^+ d/\mu_o} Q_t(\mu_o,\phi_o + \pi) A_6 Q_t^{-1}(\mu_o,\phi_o) R(\mu_o) e^{-\kappa_t^- H_t/\mu_o} e^{-\kappa_c^- d/\mu_o}$$

$$e^{-\kappa_c^+ d/\mu_o} e^{-\kappa_t^+ H_t/\mu_o} G(\theta_o) e^{-\kappa_t^- H_t/\mu_o} e^{-\kappa_c^- d/\mu_o} \qquad (6)$$

Where κ_t^+ and κ_t^- are the extinction matrices of the trunk layer for the positive and negative propagating waves, respectively, κ_c^+ and κ_c^- are the extinction matrices of the crown layers, $\mu_o = \cos\theta_o$ where θ_o is the pointing angle of the radar, $R(\mu_o)$ is the reflectivity matrix of the ground surface in the specular

direction, $G(\theta_o)$ is the backscattering matrix for the ground surface and

$$R'(\mu_o,\phi_o) = e^{-\kappa_t H/\mu_o} \cdot R(\mu_o) \cdot e^{-\kappa_t H/\mu_o} \qquad (7)$$

The Q_c, Q_t and A_n terms are matrices derived using first-order radiative transfer theory and correspond to the different scattering processes being considered. Expressions for these matrices can be found in Ulaby, et al. (1988 and 1990). The values of these matrices depend on the average scattering matrices and the phase matrices of each layer. The various terms in (6) correspond to specific scattering pathways 1-5 as shown in Figure 1.

A vegetation layer may be divided into K groups, each of which represents a class of vegetation constituents, such as leaves, branches, or stems. If a vegetation layer is divided into K such classes, then the phase matrix for the layer is specified by

$$P(\theta_s,\phi_s;\theta_i,\phi_i) = \sum_{k=1}^{K} N_k \int\int\int\int f_k(a, b; \theta, \phi) L_k(\theta_s,\phi_s;\theta_i,\phi_i;\theta, \phi)\, da\, db\, d\theta\, d\phi \qquad (8)$$

where the summation over k represents an addition over the constituent classes within the layer, N_k is the number density per unit volume of each constituent class and L_k is the Stokes matrix of constituent k. The phase matrix is a function that describes the scattering by a volume of vegetation for radiation incident from the direction (θ_i, ϕ_i) and scattered into the direction (θ_s, ϕ_s).

The probability density function (PDF) $f_k(a,b;\theta,\phi)$ specifies the distribution in the size parameters (a,b) and in the orientation parameters (θ,ϕ) for constituents in class k. Figure 2 shows how the orientation parameters are used to specify the orientation of branches and leaves. For a branch, shown here as a dielectric cylinder, θ specifies the angle from zenith of the vector parallel to the cylinder axis. For a leaf, shown here as a

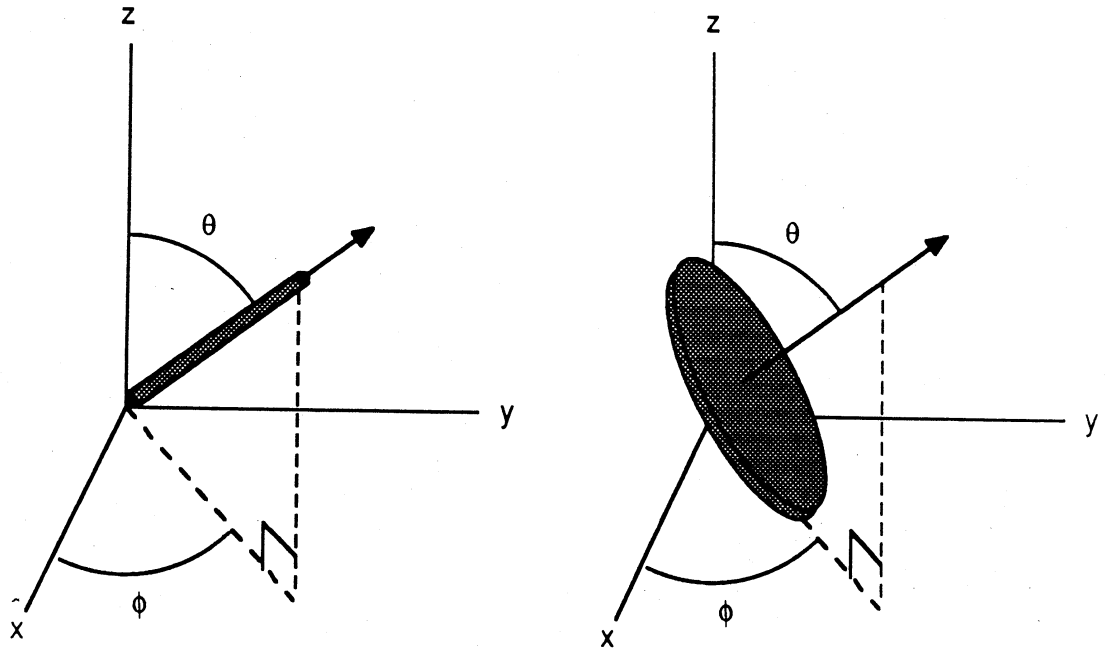

Figure 2: Branch and leaf orientation geometries.

flat disk, θ specifies the angle from zenith of the vector normal to the leaf surface. In both cases ϕ specifies the azimuth direction of the appropriate vector. All constiuents considered here will be assumed to have distributions uniform in ϕ.

The extinction matrix of the layer is defined as

$$\kappa = \begin{bmatrix} -2\mathrm{Re}(M_{vv}) & 0 & -\mathrm{Re}(M_{vh}) & -\mathrm{Im}(M_{vh}) \\ 0 & -2\mathrm{Re}(M_{hh}) & -\mathrm{Re}(M_{hv}) & \mathrm{Im}(M_{hv}) \\ -2\mathrm{Re}(M_{hv}) & -2\mathrm{Re}(M_{vh}) & -[\mathrm{Re}(M_{vv}) + \mathrm{Re}(M_{hh})] & [\mathrm{Im}(M_{vv}) - \mathrm{Im}(M_{hh})] \\ 2\mathrm{Im}(M_{hv}) & -2\mathrm{Im}(M_{vh}) & -[\mathrm{Im}(M_{vv}) - \mathrm{Im}(M_{hh})] & -[\mathrm{Re}(M_{vv}) + \mathrm{Re}(M_{hh})] \end{bmatrix} \quad (9)$$

where

$$M_{mn} = \sum_{k=1}^{K} \frac{i2\pi N_k}{k_o} \langle S_{mnk}(\theta_i,\phi_i;\theta_i,\phi_i) \rangle \quad m,n = v,h \quad (10)$$

where k_o is the free space wave number, S_{mnk} is the component of the scattering matrix corresponding to polarization mn for constituent k and the symbol $\langle \cdots \rangle$ represents statistical averaging over the size and orientation distribution of the constituent class.

The scattering and Stokes matrix elements used in (8) and (10) have been derived for various classes of particles. Two cylinder scattering models are used to model the branches and stems in the canopy. The larger size classes of branches are modeled using a scattering model based on the exact solution for an infinitely long homogeneous dielectric cylinder as discussed by Ruck et al., (1970). A stationary phase approximation is applied to the infinite cylinder solution to determine the solution for the finite cylinder case. The smaller size classes of branches are modeled using a solution for small prolate sphereoids as discussed in Tsang, et al. (1985). Similarly, the scattering and stokes matrix elements for leaves are modeled using a solution for small oblate sphereoids.

The transformation matrix $C_t(\mu_o,\phi_o)$ represents a fully polarimetric solution for canopy backscatter. That is, the backscattering coefficient for any transmit- and receive-polarization combination may be determined by applying wave synthesis techniques to $C_t(\mu_o,\phi_o)$. The present study focuses on the linerarly polarized backscattering coefficients

$$\sigma^o_{vv} = 4\Pi \cos\theta_o[C_t(\mu_o)]_{11} \quad (11)$$

$$\sigma^o_{HH} = 4\Pi \cos\theta_o[C_t(\mu_o)]_{22} \quad (12)$$

$$\sigma^o_{HV} = 4\Pi \cos\theta_o[C_t(\mu_o)]_{21} \quad (13)$$

$$\sigma^o_{VH} = 4\Pi \cos\theta_o[C_t(\mu_o)]_{12} \quad (14)$$

In order to model the microwave extinction and backscatter from a forest stand using MIMICS, the stand must be well characterized with respect to the sizes, shapes and orientations of canopy elements and their respective dielectric properties. In addition, validation of the modeling products requires associated measurements of one- or two-way transmission loss through the canopy and net canopy backscatter. Two recent experimental investigations meet these criteria in terms of both the requisite ancillary measurements of canopy properties and measurements of the backscattering coefficient σ^o and/or extinction κ. The first is a field experiment conducted at the Kearney Agricultural Center near Fresno, California during the summer of 1987 as part of the NASA funded Eos Synergism Study. This test site consisted of orchard stands of six-year old black walnut trees which were observed by tower-mounted L-, C- and X-band scatterometers on a nearly continuous basis over a two week period in late August. The second is an airborne SAR experiment conducted at the Bonanza Creek Experimental Forest near Fairbanks, Alaska in March of 1988 with initial data acquisition supported by NASA as part of an ERS-1 preparatory study for applications to forest ecology. This test site consisted of mature stands of white spruce, black spruce, balsam poplar, and alder trees located

along the floodplain of the Tanana River. Selected stands contained arrays of trihedral corner reflectors for determination of two-way transmission loss through the canopy. The test site was observed over a two week period by repeated overflights of the NASA/JPL P-, L- and C-band SAR aboard a NASA/Ames DC-8 aircraft and also the ERIM/NADC L-, C- and X-band SAR aboard a NADC P-3 aircraft.

3.0 FOREST CANOPY DATA SETS

This section provides a brief description of each of the two experimental data sets including the conditions under which the data were acquired, the systems or techniques used to obtain the data, tabulations of the data itself, and the models and assumptions used to generate higher-order statistical descriptions of the forest canopies as required as input into MIMICS. In so doing, each experiment is seperately treated. The data derived from the tower-mounted scatterometer studies of the walnut orchard near Fresno, California in the summer of 1987 are used in Section 5 to validate MIMICS with respect to L-band backscatter as a function of polarization and angle of incidence and also as functions of time-variant properties of the orchard canopy and the underlying soil. The data derived from the Alaskan SAR experiment near Fairbanks, Alaska in March of 1988 is used (1) in Section 4 to validate MIMICS with respect to one-way canopy extinction for selected test stands and (2) in Section 5 to validate MIMICS with respect to backscatter as observed by the two SAR systems at L-, C- and X-bands.

3.1 Walnut Orchard Data

The walnut orchard at the Kearney Agricultural Center was established to investigate the effects of water availability and salinity on productivity. The orchard had been subdivided into treatment plots, of 24 trees each, receiving specified water

applications by sprinkler irrigation relative to estimates of their potential evapotranspirative demand. The treatment levels were 33%, 66%, and 100% of evaportranspirative demand. While all three treatment levels were observed by the scatterometers, the bulk of the measurements were made for two adjacent 100% of ET treatment plots.

The average spacing between orchard rows was 6.7 m with an average distance of 3.3 m between trees along a row. A hedgerow pruning technique had been used on these trees for several years, and there was not crown closure between rows. The scatterometer systems at L-, C- and X-bands were mounted atop a mobile tower at a height of 12.2m. The product beamwidths of the dish antennas were about 3^{o} at C- and X-bands and 6^{o} at L-band. The resultant viewing geometry imposed by the inter-row gaps in the crown and beamwidth is not consistent with the continuous crown assumption required by MIMICS at C- and X-bands. However, this assumption is fairly well approximated for the larger beamwidth L-band measurements. Hence, only the L-band data will be described in detail for use in MIMICS validation.

3.1.1 Site Description and Ancillary Data

A very extensive set of ancillary data was collected to characterize the walnut orchard in terms of canopy architecture (Martens et al., 1990) and dielectric properties (Cimino et al., 1988; and Dobson, 1988).

Tree Architecture.

Tree architecture data was obtained by measurement of the length, diameter at mid-length, and the zenith and azimuth orientation angles for all branches with diameters greater than 2 cm for eight trees. The number and size classes of all lateral branches were also recorded. All branch segments were numbered so that the tree skeletons could be reconstructed

from these observations. In addition, the smaller branches with diameters less 4 cm were statistically sub-sampled by class size. Four sample classes were considered: 0-1, 1-2, 2-3, and 3-4 cm diameters.

The measured tree and branch geometry data were adapted for input into MIMICS by dividing the canopy into distinct crown and trunk layers with heights of 2.5 m and 1.7 m, respectively. The branches are then divided into the four size classes specified in Table 1. Figure 3 is a sketch of the geometry of an individual tree showing the trunk, the four branch classes, and the leaves. Since the larger branches tend to be in the lower portion of the canopy, they are considered to be part of the trunk layer which includes the vertical trunks and all branches greater than 4 cm in diameter. The remaining three smaller branch classes are considered to be randomly distributed throughout the crown layer along with the leaves. Table 1 summarizes the size and orientation parameters of all four branch classes as well as their respective densities (number of branches per unit volume).

With respect to orientation, the larger branches generally tend to have mostly vertical orientations whereas the measured data shows the smaller branches to exhibit no preferred orientation. The large branches in the trunk layer are assigned a $\cos^6\theta$ distribution so that mean $\theta = 0^o$. The primary branches are assigned a distribution of $\sin^4 2\theta$ so that mean $\theta = 45^o$. The secondary branches and stems are assigned spherical distribution functions ($\sin\theta$); and hence show no preferred pointing direction which implies that the branch axial directions are uniformly distributed on a spherical surface. These functions are converted into probability distributions for use in MIMICS by dividing each by a normalizing factor given by $\int_0^\pi f(\theta)\, d\theta$. The PDFs for these branch orientations are shown in Figure 4.

Table 1. Canopy Branch Classes.

	Branch Size Class			
Constituent Class	Trunk	Crown Branches		
Characteristic	Branches	primary	secondary	stems
Max. Diam. (cm)	-	4.0	0.9	0.4
Min. Diam. (cm)	4.0	0.9	0.4	-
Ave. Diam. (cm)	7.3	1.9	0.6	0.1
Ave. Length (cm)	92.8	35.8	10.9	5.0
Density (#/m^3)	0.13	1.55	1.41	900
Orientation f (θ)	$\cos^6\theta$	$\sin^42\theta$	$\sin\theta$	$\sin\theta$

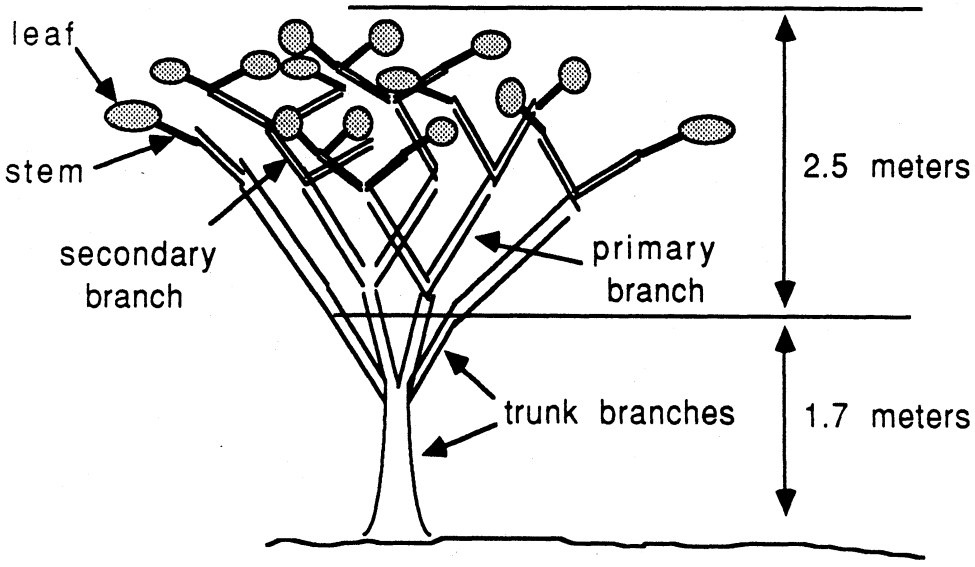

Figure 3: Illustration of a walnut tree showing the four branch classes and the leaves.

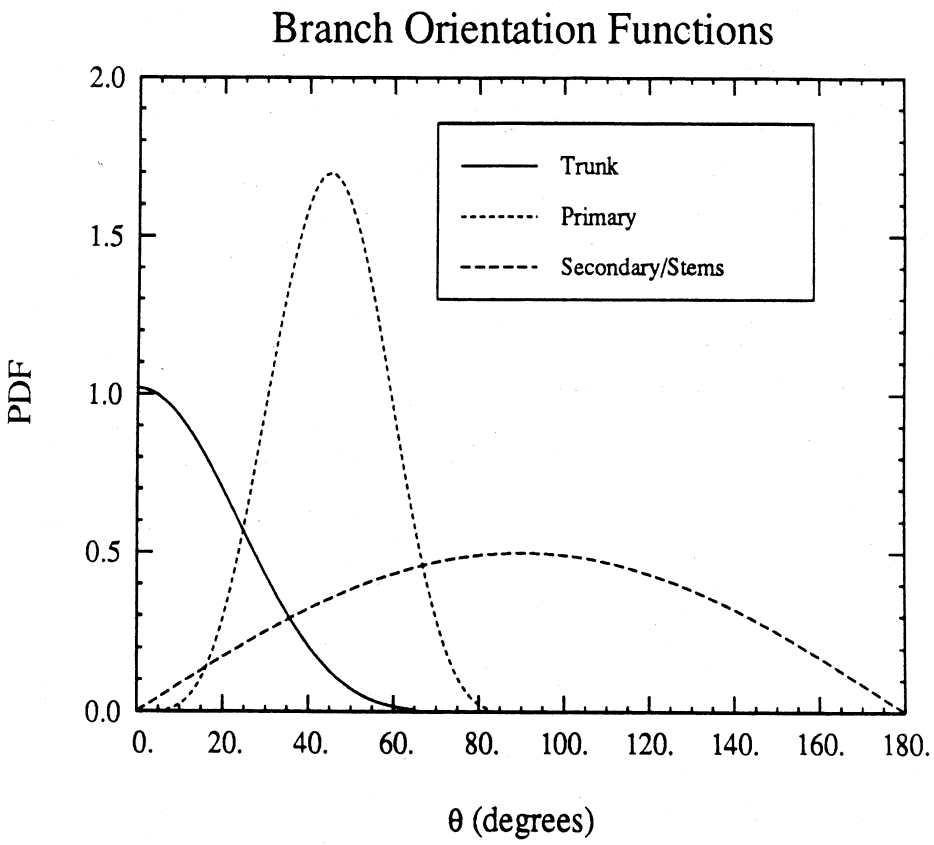

Figure 4: Branch orientation probability distribution functions (PDFs).

Dielectric Properties

Observations of the relative dielectric constant of the mineral soil and vegetation were made in situ at 1.2 GHz using a portable dielectric probe which measures the reflection coefficient from a coaxial probe tip terminated by the medium of interest. This instrument was used with certain modifications to monitor both the surface layer of the soil and also the woody and fruit components of the walnut trees. This technique was not well-suited to measurement of the relative dielectric constant of leaves due to their small thickness. However, the average measured gravimetric leaf moisture of O.8 (wet weight basis) is converted to a relative dielectric constant of $\varepsilon_l = 36.5\text{-}j11.3$ at L-band using a dielectric model for foliage (Ulaby and El-Rayes, 1987).

In order to measure the relative dielectric constant of the tree trunks, an array of specially designed coaxial probe tips were inserted to various depths into one of the boles in the 100% treatment plots observed by the scatterometers. The RF probe could then be attached to any of these probe tips for observation of the dielectric constant. Since the sensing probe tips were 0.141" in diameter, the effective sensing volume for a dry medium extended to a maximum of 0.18 cm from the tip. Interrogation of the probe tip array allowed the construction of a dielectric profile for the tree bole which is not a homogeneous dielectric cylinder.

The dielectric properties of the tree trunks were found to vary dramatically with time and exhibit a distinct diurnal pattern which depended upon the insertion depth of the probe tip into the tree trunk (Dobson, 1988). Figure 5a shows a piecewise fit to the average diurnal response for the real part of the dielectric constant at 1.2 GHz. Data are shown for two insertion depths during a three day period coinciding with acquisition of diurnal scatterometer observations of the walnut plot. The numbers on the X-axis correspond to midnight on the indicated day in August. The dielectric constant is seen to reach

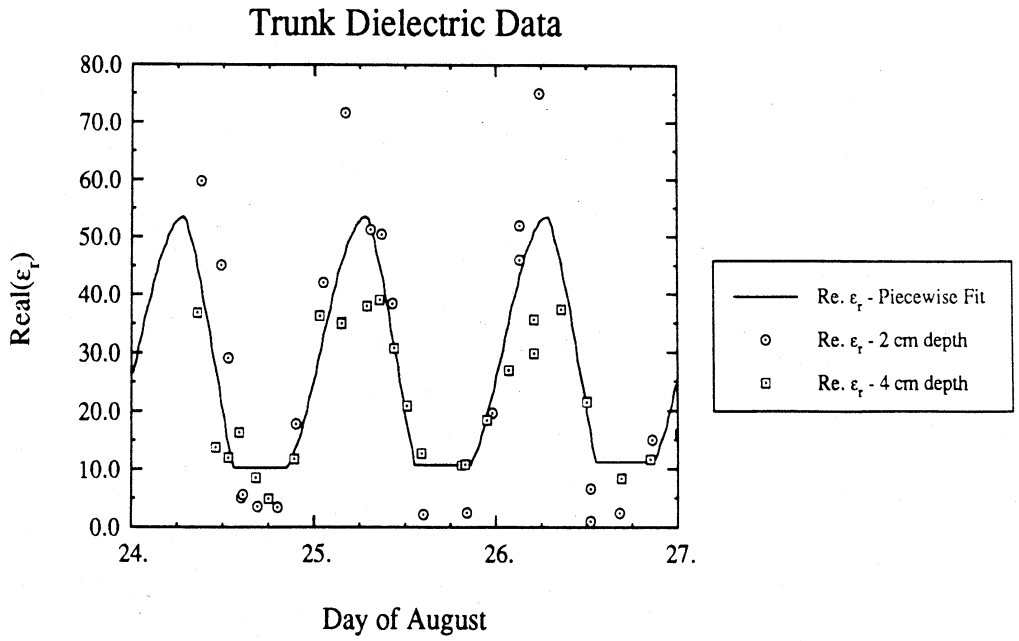

(a) Comparison with two insertion depths.

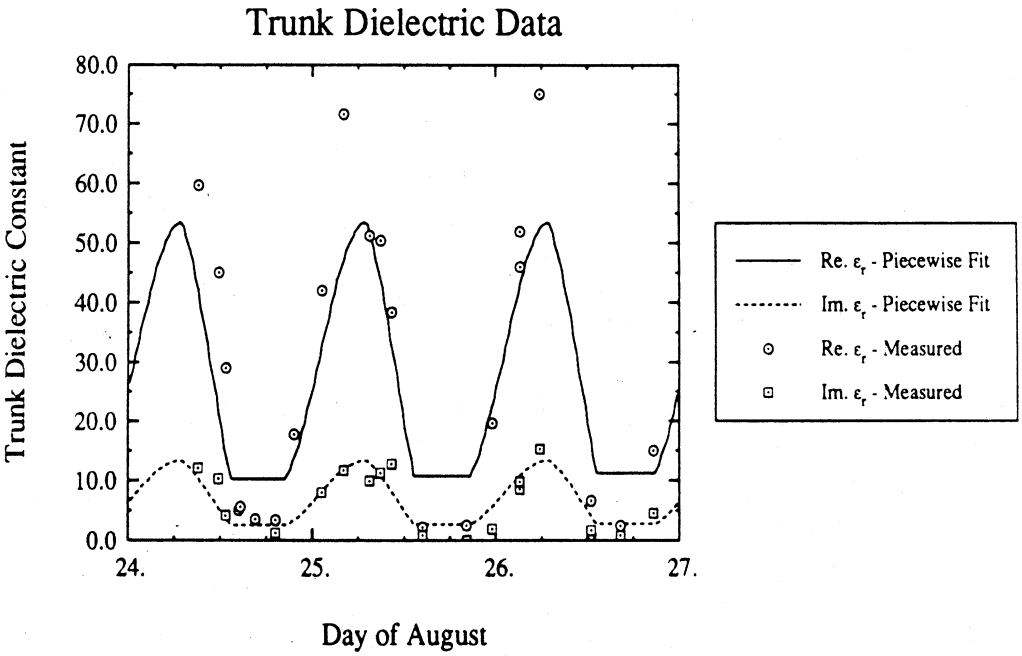

(b) Comparison with real and imaginary parts.

Figure 5: Comparison of a periodic piecewise fit to measured trunk dielectric constant data for (a) two insertion depths and (b) real and imaginary parts.

a peak near daybreak at about 6:00 a.m. Shortly thereafter, the values decrease rapidly until a minimum is reached in the early afternoon corresponding to maximum insolation of the canopy. In the evening, as the sun sets, the dielectric constant increases until the maximum is again reached. These trends were observed consistently over the two week course of the experiment. Figure 5a shows the diurnal variation in the relative dielectric constant recorded at two insertion depths, 2 cm and 4 cm. The piecewise fit represents the effective dielectric average which is used by MIMICS for the trunks. This fit is also shown in Figure 5b along with a loss tangent $\varepsilon'/\varepsilon'' = 0.25$ as compared to the observed values for ε at a 2 cm insertion depth.

While very few dielectric measurements were obtained for the branch and stem classes specified in Table 1, these also show a duirnal variation but not as pronounced as that noted for the trunks. A substantial number of measurements were made of the leaf water potential which is a complex characteristic of all plant tissue that defines the thermodynamic state of water in the plant. Measurement of water potential provides a sensitive means of assessing plant water status. Water potential reaches a minimum when the plant reaches the period of highest water demand or when it is water stressed. Figure 6 shows the measured values of leaf water potential over the three day period of scatterometer observations. More negative values of water potential indicate a stronger draw of water by the leaf from the plant. Since water movement throughout the plant is controlled by the pressure gradient extending from the leaves through the branches, trunk, and roots to the soil, this phenomenon should have some effect on the branch dielectric constants. Specifically, the branch dielectric constant should decrease as leaf water potential becomes more negative; and conversely, as water potential becomes less negative and the leaves draw less water from the branches, the branch dielectric should increase. Consequently, the branch dielectrics are modeled as exhibiting diurnal

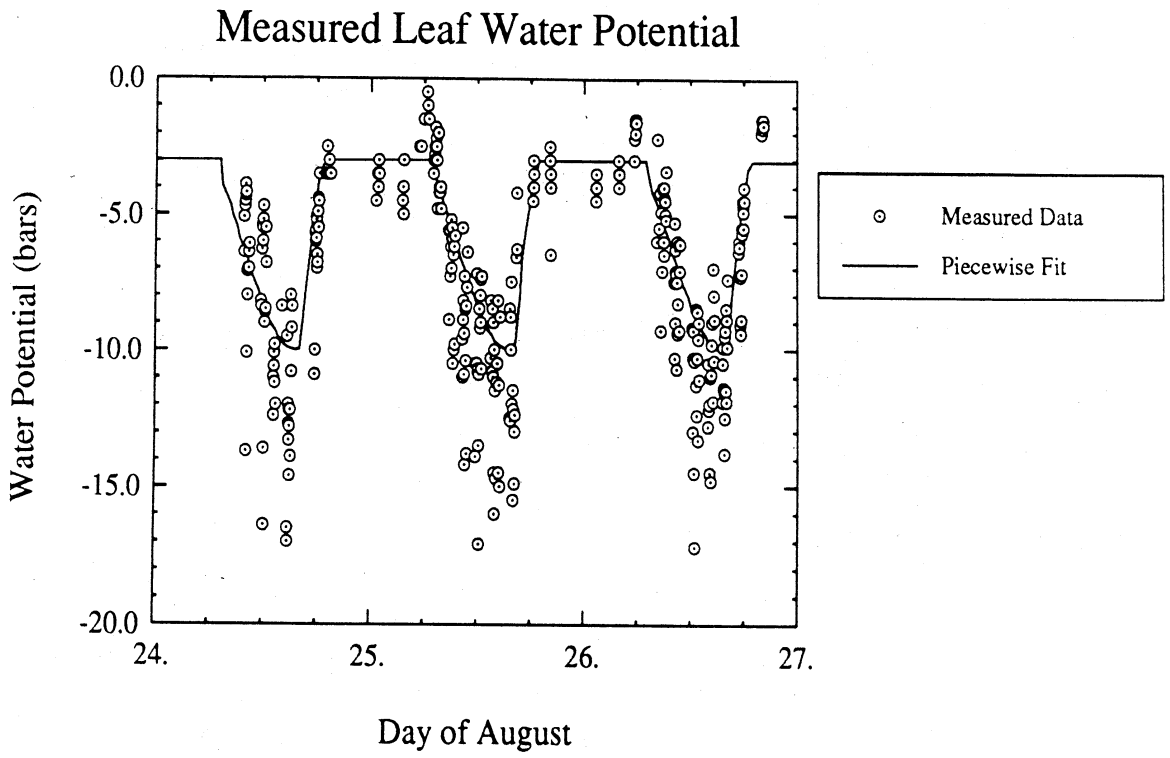

Figure 6: Measured leaf water potential.

behavior intermediate to leaf water potential (at one end of the gradient) and trunks (at the other end). Figure 7 shows the modeled dielectric behavior of the branch constituents with the loss tangent $\varepsilon''/\varepsilon' = 0.25$.

The soil dielectric properties were observed on an hourly basis using a transect sampling strategy wherein measurements were made at 30 cm intervals across the orchard row structure. The effective sampling depth for the dielectric probe was less than or equal to 0.4 cm. Since there was considerable spatial variation in the irrigation and consequently in the moisture patterns within the orchard and since each hourly transect was not made at the same spatial position, the average dielectric properties of the soil are determined by linear regression of the measured values versus time. The regression result shown in Figure 8 for the three-day period of scatterometer observations. The drop in dielectric values corresponds to a marked decrease in near-surface soil moisture.

3.1.2 Scatterometer Observations

Several sets of scatterometer data were recorded during the experiment (Cimino, et al., 1988). The first set is comprised of multiangle data in which the same set of trees in the 100% treatment plots were observed at incidence angles from 40° to 55°. These measurements were obtained over a two hour time period during mid-afternoon. The second data set to be discussed herein consists of a three-day measurement series during which the same set of trees (also in the 100% treatment plot) were observed continuously over a three day time period at a 55° angle of incidence.

The L-band data were recorded using the University of Michigan POLARSCAT which was boom-mounted on a mobile platform. POLARSCAT is an externally calibrated polarimetric radar system which measures the amplitude and phase of the backscattered signal for the four linear polarizations (HH, VV, HV, VH). The center frequency of the system is at 1.6 GHz with

Table 2. Leaf Characteristics.

Leaf density = 652 leaves per cubic meter
Leaf Dielectric Constant = 36.5 - j11.3
Average leaf diameter = 5.0 cm
Average leaf thickness = 0.02 cm
Leaf area index = 3.2
Leaf Orientation PDF = spherical

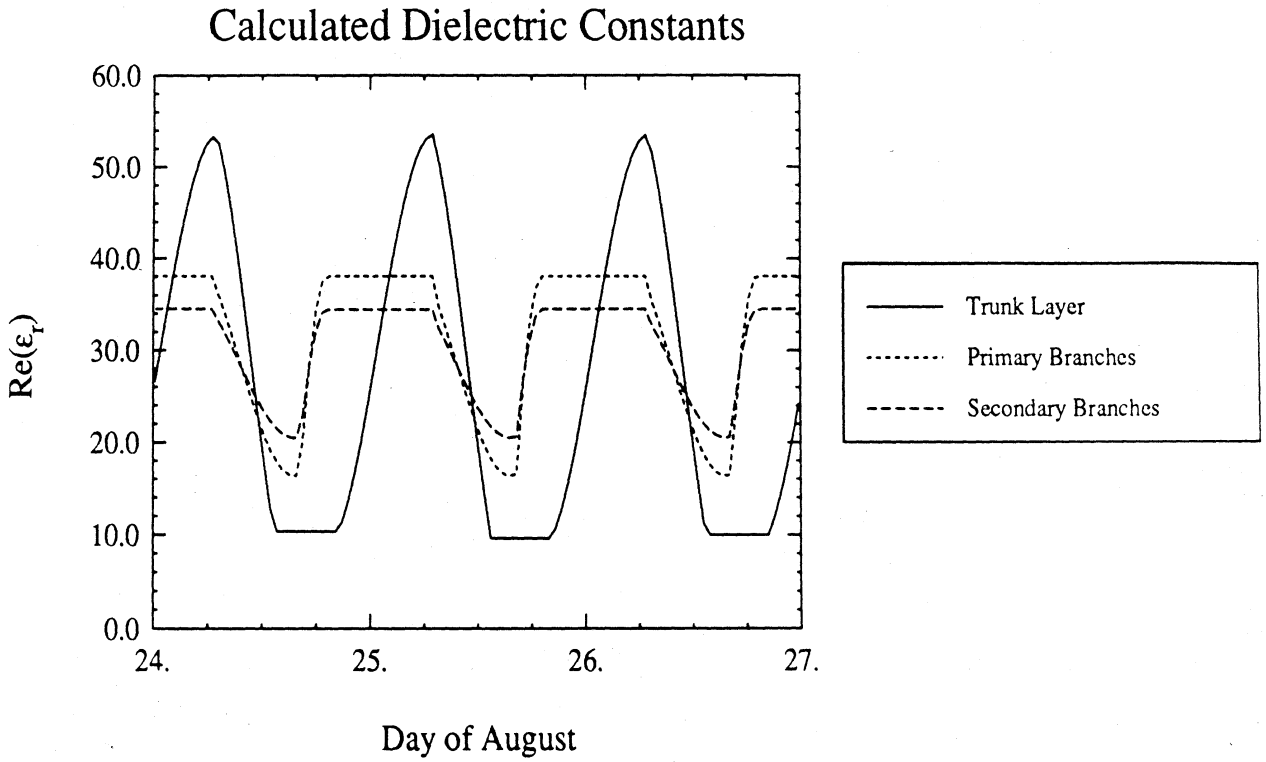

Figure 7: Piecewise fit of dielectric constants for the trunks and branches.

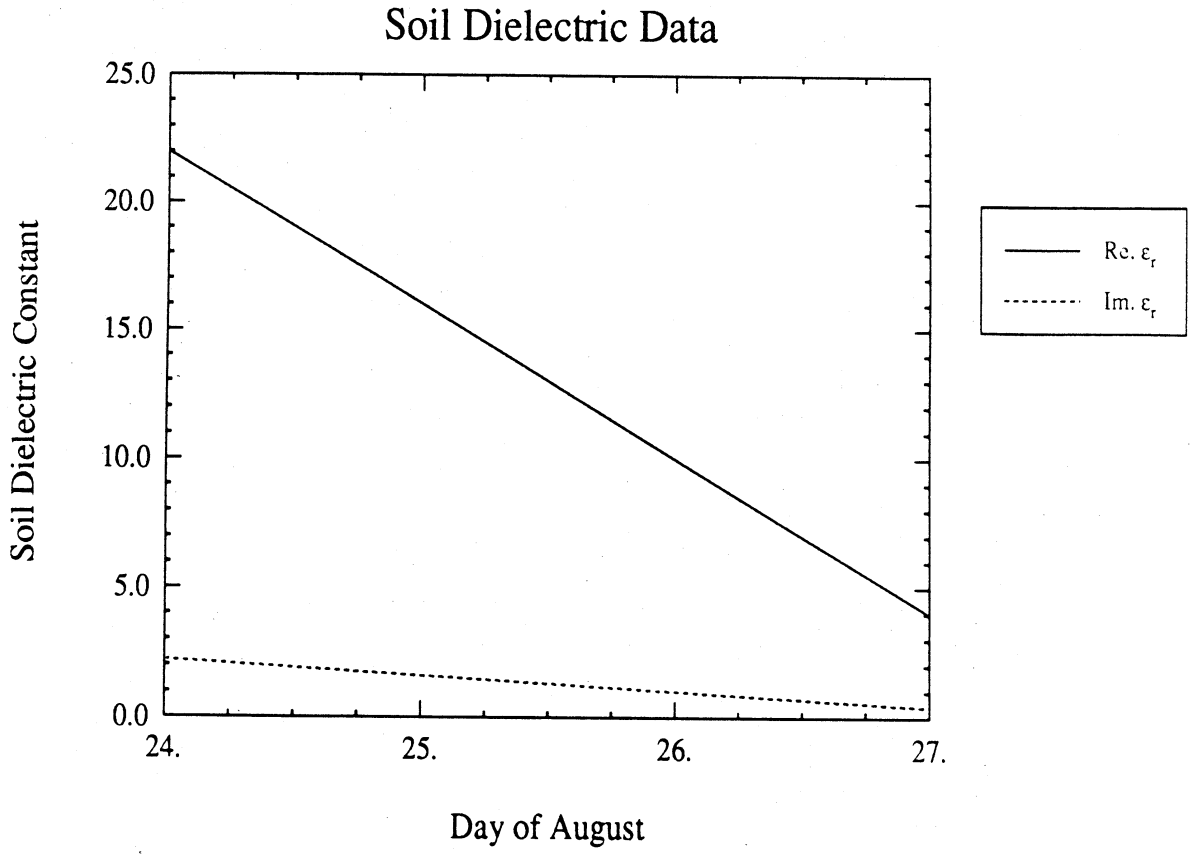

Figure 3: Behavior of soil dielectric constant.

a 200 MHz bandwidth. The noise equivalent σ^o is -40 dB. An HP 8753 network analyzer provides the source and primary signal processing. The antennas were mounted on an elevation positioner atop an azimuth rotatable boom. The system was parked adjacent to the orchard and the boom elevated to an antenna height of 12.2 m.

Each canopy measurement was recorded for a fixed incidence angle and polarization configuration by rotating the antennas in azimuth and recording 30 independent spatial samples over the azimuth extent of the orchard. These 30 samples were then averaged together to yield a mean backscatter value as a function of range into the canopy. Summation of the average backscattered power over the range extent of the target yields an average backscattering coefficient σ^o with a sample size sufficient to reduce the uncertainty due to signal fading to $\pm$ 0.5 dB. The scatterometer was externally calibrated at periodic intervals with reference to a polarimetric target comprised of an array of parallel wires oriented at 45^o with respect to the antenna polarization vectors and also a Luneberg lens. These calibrations were used to remove system temperature dependencies from the reported measurements (Cimino, et al., 1988; and McDonald, et al., 1989).

The L-band multiangle data is shown in Figure 9 for linear polarized backscatter. Figure 10 shows the variation in measured backscatter over the three-day period at $\theta = 55^o$; each sample is approximately one-half hour apart.

3.2 Alaskan Boreal Forest Data

Two airborne SARs were deployed to Fairbanks, Alaska in March of 1988 with the prime objective of imaging sea ice in the Arctic Ocean and the Bearing Sea. The Jet Propulsion Laboratory's P-, L-, and C-band quad-polarized SAR, mounted aboard a NASA/Ames Research Center DC-8, operated at center frequencies of 450 MHz, 1.26 GHz and 5.3 GHz, respectively. The Naval Air Development Center/Environmental Research

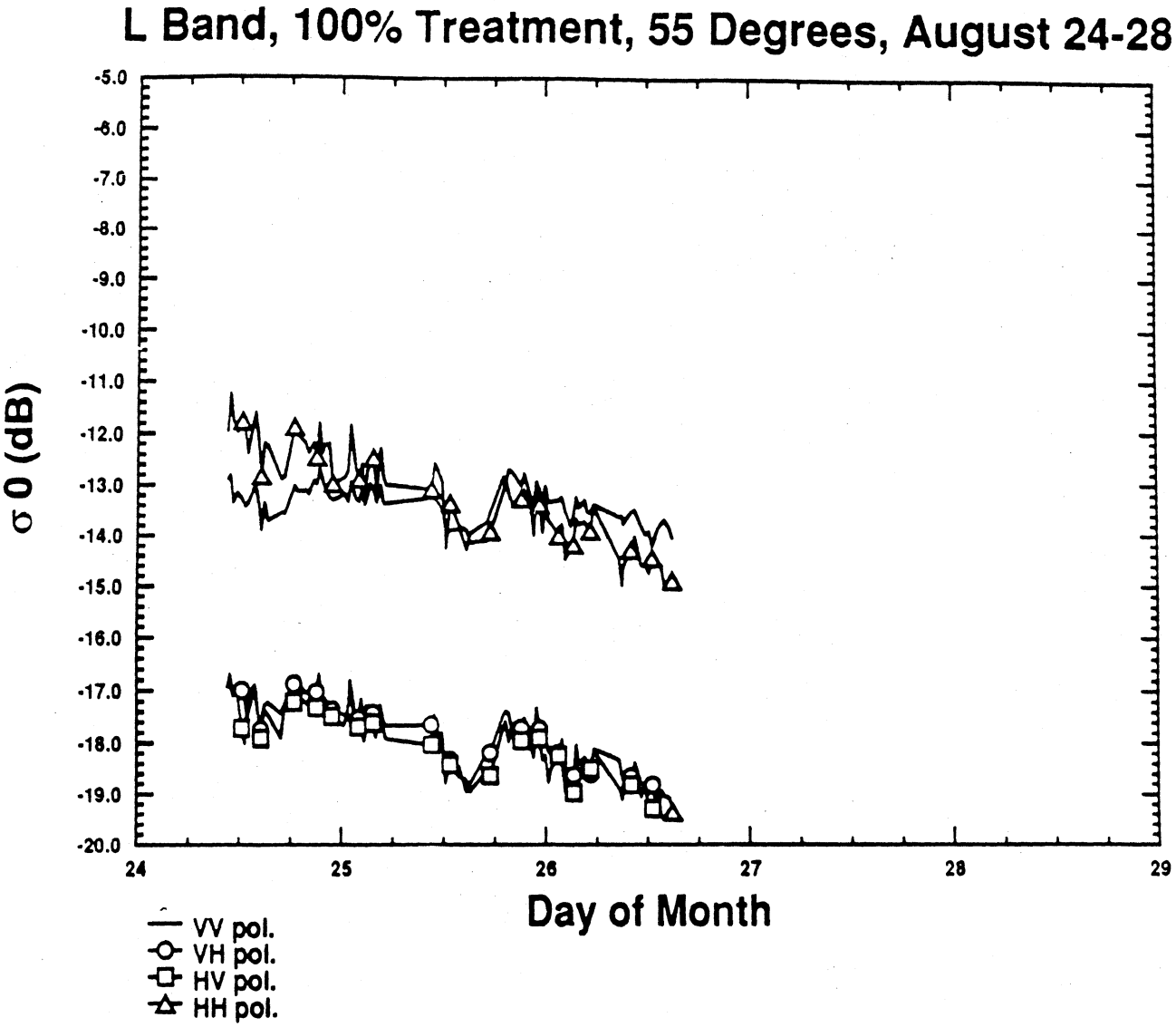

Figure 9: Backscatter observed by POLARSCAT at L-band for a Walnut Orchard.

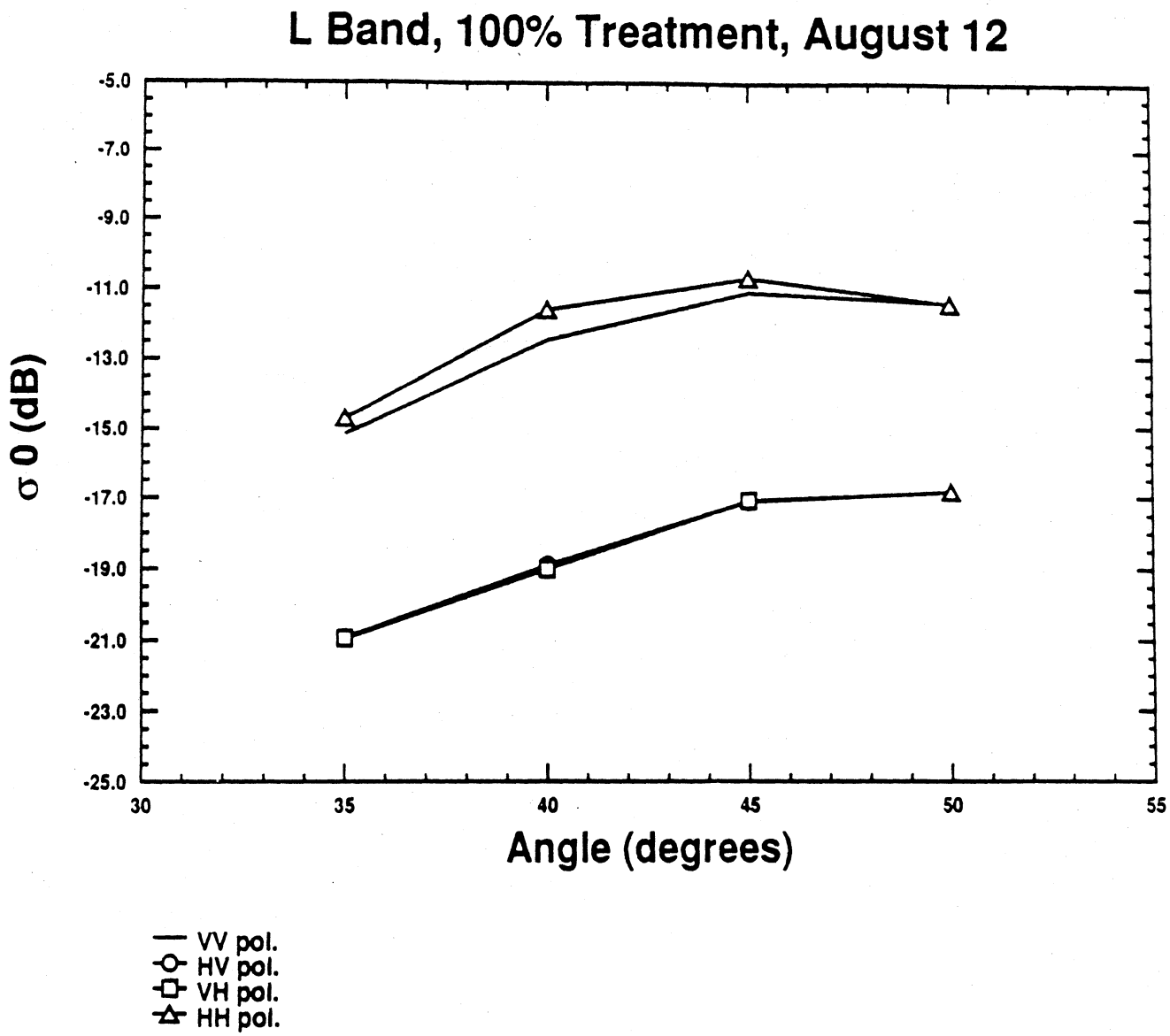

Figure 10: Angular Variation in L-band Backscatter observed by POLARSCAT for a Walnut Orchard.

Institute of Michigan's L-, C-, and X-band quad-polarized SAR, mounted on a Navy P-3, operated at center frequencies of 1.25 GHz, 5.26 GHz and 9.38 GHz, respectively. In order to provide a means for external calibration of these SARS, an array of passive reflectors and active transponders was established in the vicinity of the Fairbanks International Airport for imaging on the return leg to the airport. The Bonanza Creek Experimental Forest, located along the Tanana river about 20 km from the airport, was also imaged during five of the seven deployments of the NASA DC-8 and on two of the P-3 deployments. This coverage is summarized in Table 3.

Since only a limited portion of the data listed in Table 3 has been processed to date, this study will focus upon the data obtained by the JPL SAR on March 13 at 15:03 and March 19 at 23:17 and by the ERIM/NADC SAR on March 22. All of these passes have a common northwesterly look direction. These dates were selected to encompass the range of local environmental conditions over the experimental period; that is a warm period of thawed conditions extending through the evening of March 13 and followed by more normal subfreezing temperatures for the remainder of the period. The major effect of the changing temperature conditions is to modulate the dielectric properties of the canopy elements and the surface layer of a 20 cm to 30 cm snow substrate as liquid water is frozen, and thereby modify the scattering and absorption properties of the various media which collectively constitute the scene.

3.2.1 Test Site Description and Ancillary Data

The Bonanza Creek Experimental Forest is 30,000 hectares in size and is contained within the Tanana Valley State Forest west of Fairbanks, Alaska. This boreal forest site lies within a zone of discontinuous permafrost along the Tanana River and adjacent hillslopes to the north. The high frequency of forest fires in the upland areas and the active erosion of the Tanana

Table 3 Summary of Alaskan SAR Data in March, 1988.

Date	Local Time	Channels	Incidence Angle	Look Direction	Aircraft
3/11/88	14:02	P, L, C	9°	NW	DC-8
3/13/88	14:34	P, L. C	14°	NW	DC-8
	14:51	P, L, C	37°	SE	DC-8
	15:03	P, L, C	41°	NW	DC-8
3/17/88	14:22	P(HH), L, C	30°	NW	DC-8
	14:39	P(HH), L, C	36°	SE	DC-8
	14:54	P(HH), L, C	40°	NW	DC-8
3/19/88	23:04	P(HH), L, C	43°	SE	DC-8
	23:17	P(HH), L, C	39°	NW	DC-8
3/21/88	23:38	P(HH), L, C	48°	NW	DC-8
3/22/88	0:36	X	29°	NW	P-3
	0:50	X	55°	NW	P-3
	19:22	C(HH, VV), X(HH, VV)	35°	NW	P-3
	19:38	C(HH, VV), X(HH, VV)	49°	NW	P-3
	19:58	X	56°	NW	P-3
	20:10	C	56°	NW	P-3

NOTES: (1) channels are quad-pol unless otherwise noted
(2) incidence angle is determined at center of Seven Mile Island in Bonanza Creek Experimental Forest

River result in a wide diversity of forest successional stages within the Bonanza Creek Experimental Forest. Upland forest types include: aspen (Populus tremuloides), birch (Betula papyrifera), and white spruce (Picea glauca) on the warmer, south-facing slopes and black spruce (Picea mariana) stands on the colder, north-facing slopes. The primary succession on the floodplain starts with the growth of dense stands of willows and alders which are replaced with balsam poplars (Populus balsamifera) and white spruce. Prolonged shading of the forest floor under these stands contributes to the development of a permafrost layer on the older terraces and the consequent replacement of the balsam poplars and white spruce by bogs and black spruce (Van Cleve and Viereck, 1981).

A sketch of a representative image swath for the SARs over the test site is shown in Figure 11. The aircraft headings are 54° (T) for the DC-8 and either 54° or 234° (T) for the P-3. Although the south-facing hill slopes located north of the Tanana River were imaged by the SARs, the forest stands selected for investigation by this study are concentrated on the relatively flat islands scattered along the Tanana River. This choice minimizes the effects of variations in the slope of the terrain upon the backscatter from various species and stands of trees.

A series of forest stands were selected on the basis of forest cover conditions and accessibility for use in canopy extinction studies utilizing point targets. Arrays of passive corner reflectors, dihedral and trihedral, were positioned both on an unforested sandbar and within forested stands adjacent to the sandbar (Kasischke, et al., 1989). Only the trihedral reflectors proved to be useful in this study due to the small size of the dihedral corner reflectors and due to problems in positioning them properly. The relative locations of 25 trihedral reflectors positioned on the snow-covered sandbar and within stands of alder, poplar and white spruce are shown in Figure 12. The sizes of these reflectors range from 60 cm to 122 cm and yield corresponding radar cross sections from 21

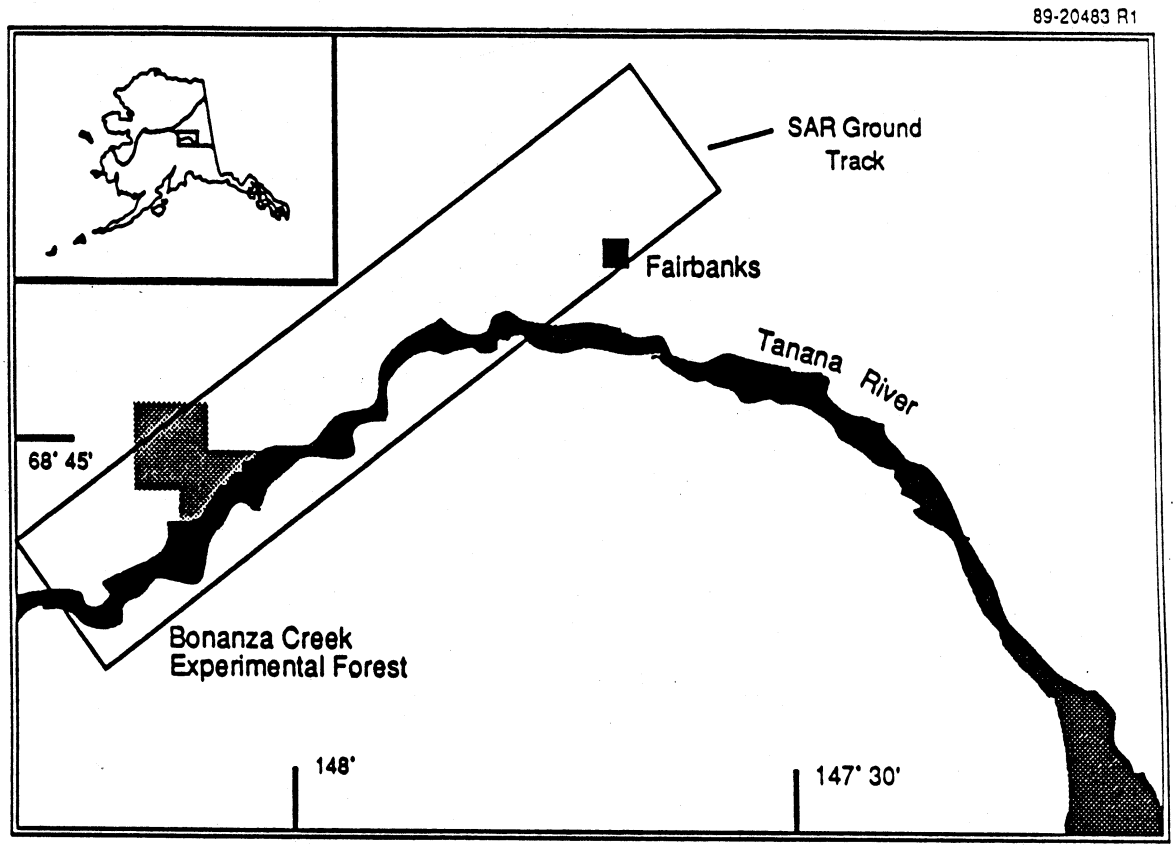

Figure 11: Location of Alaska P-3/SAR Flights Near Fairbanks, AK in March of 1988.

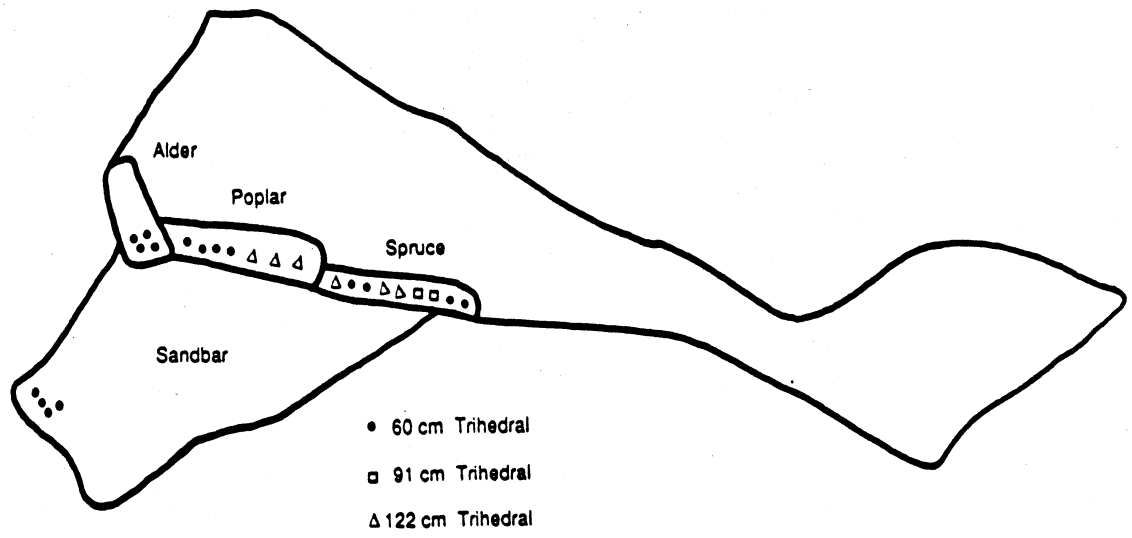

Figure 12: Locations and Sizes of Targets Placed in Three Forest Stands.

dBm^2 to 35.2 dBm^2 at C-band and 25.9 dBm^2 to 40.4 dBm^2 at X-band as listed in Table 4. These reflectors were boresighted with an azimuth heading of 144° (T) for expected illumination by the P-3 SAR with a look direction of 324° (T) and oriented with an elevation angle of 45°. It should be noted that only the alder stand is mono-specie; the stands of poplar and spruce are mixed specie stands.

In addition to the arrays of passive reflectors deployed for measurment of two-way canopy extinction at C- and X-bands using the P-3 SAR, five L-band active radar calibrators were deployed within mature white spruce stands on a different island and adjacent to an unforested, but snow-covered, sandbar with three additional active radar calibrators. The active radar calibrator is a transponder with large cross-section (Brunfeldt and Ulaby, 1984). Several of these calibrators incorporated a recirculating feature through a delay line which functions to yield multiple images of the calibrator with each image offset in range and decremented by a known loss. The use of these active targets for determination of two-way transmission loss through the canopy presumes that the radar cross sections of the targets are accurately known. However, unlike the passive reflectors, the cross-section of the active targets is dependent upon ambient temperature due primarily to variations in amplifier gain. Day-to-day changes in the measured air temperature on the Tanana River floodplain at the times of the overflights were on the order of 25°C. Although there are two possible approaches to correct for these temperature effects via use of amplifier gain versus temperature curves or via inference of this from observations of the decrement in calibrator recirculations, these approaches have not been implemented to date and are being deferred pending the resoultion of more general L-band SAR calibration issues. Hence, the ancillary data characterizing the stands surrounding the L-band active radar calibrators will not be discussed herein.

Table 4 Trihedral Reflector Sizes and Placement

Site	Specie Composition	Reflector Size	Number	Radar Cross Section ($dB\ m^2$) C-Band	X-Band
Sandbar	No trees	60cm	4	21.0	25.9
Alder	Alder	60cm	4	21.0	25.9
Poplar	Alder and Balsam	60cm	4	21.0	25.9
	Poplar	122cm	3	35.2	40.4
Spruce	Alder, Balsam	60cm	4	21.0	25.9
	Poplar, and White	91cm	2	29.6	34.5
	Spruce	122cm	3	35.2	40.4

In addition to those stands selected for canopy extinction measurements, 43 other stands were selected as a sample population for extraction of average backscattering coefficients from the SAR data. Each stand is of uniform age with a single-specie composition and encompasses at least 4 hectares in area. Of this population of 19 white spruce, 12 balsam poplar, and 11 black spruce stands, ancillary stand data has been obtained and summarized for seven stands (Jaeger, 1988). The location of these stands are shown in Figure 13. The measured and derived stand characterizations for these seven stands and the stands surrounding the reflectors provide the foundation for the MIMICS simulations of canopy extinction and backscatter.

Temperature Conditions

An unseasonably warm spell in February and early March, 1988 induced thawing conditions in the tree canopies and formation of a melt zone in the surface layer of the snow during the SAR overflights by the DC-8 on the afternoons of March 11 and 13. Recorded air temperatures during the SAR overpasses ranged between 7.5°C to 9.5°C on March 11 and between 2.0°C to 9.5°C on March 13. More seasonal subfreezing temperatures returned on March 14 for the remainder of the experimental period as shown in Figure 14. The recorded air temperatures at the times of the SAR overpasses varied across the Tanana River floodplain, but ranged between -11.5°C to -13.0°C on March 17, -14°C to -14.5°C on March 19, and were less than -20°C on both March 21 and 22.

Surface Conditions

The ground surface was covered with a snow layer typically ranging from 20cm to 30cm in depth. Beneath the snow, the upper 20cm of the mineral soil was frozen throughout the entire experimental period with temperatures $< -2^{o}C$. Typical snow profiles for white and black spruce are shown in

Figure 13: Locations of some Forest Stands in the Bonanza Creek Experimental Forest.

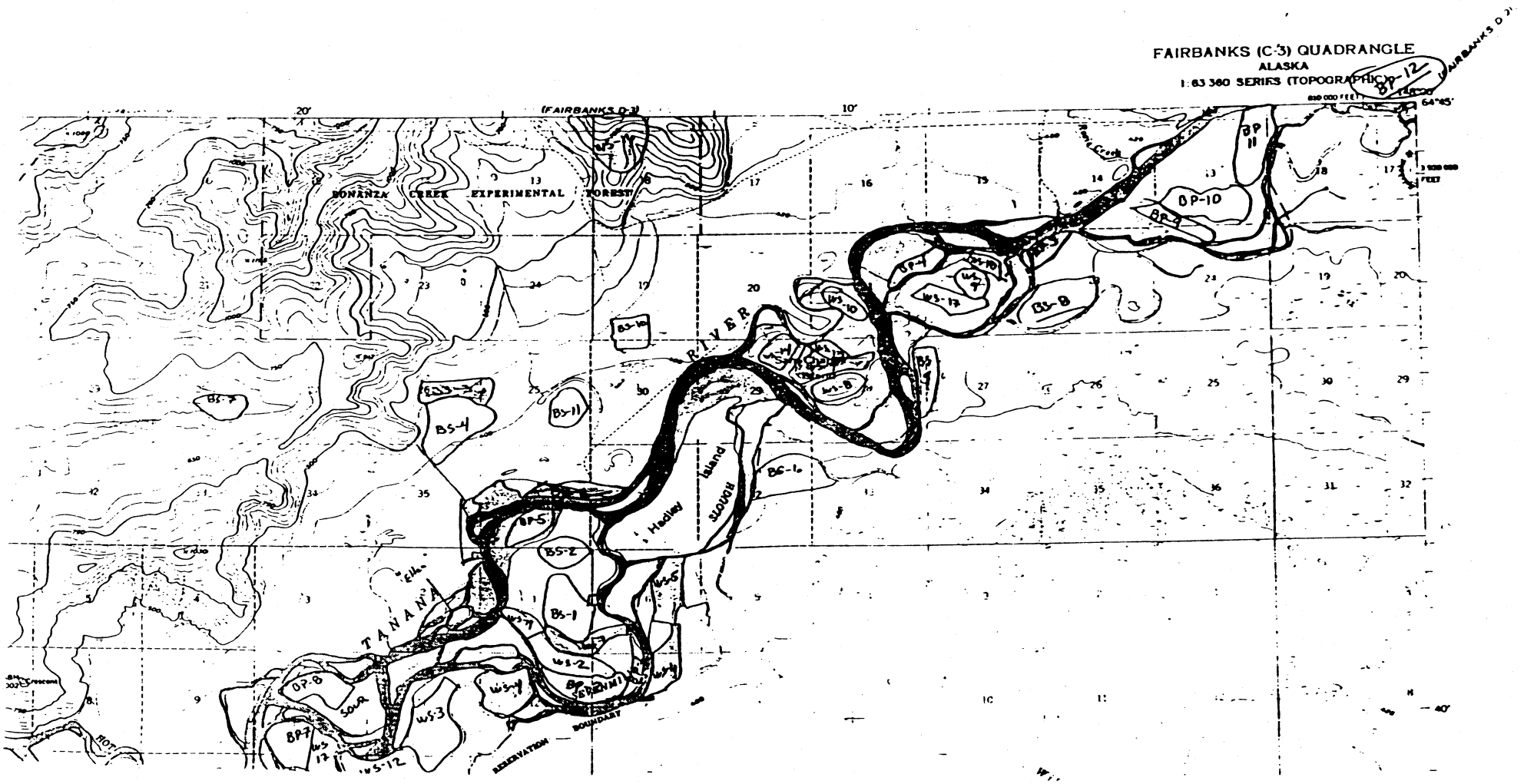

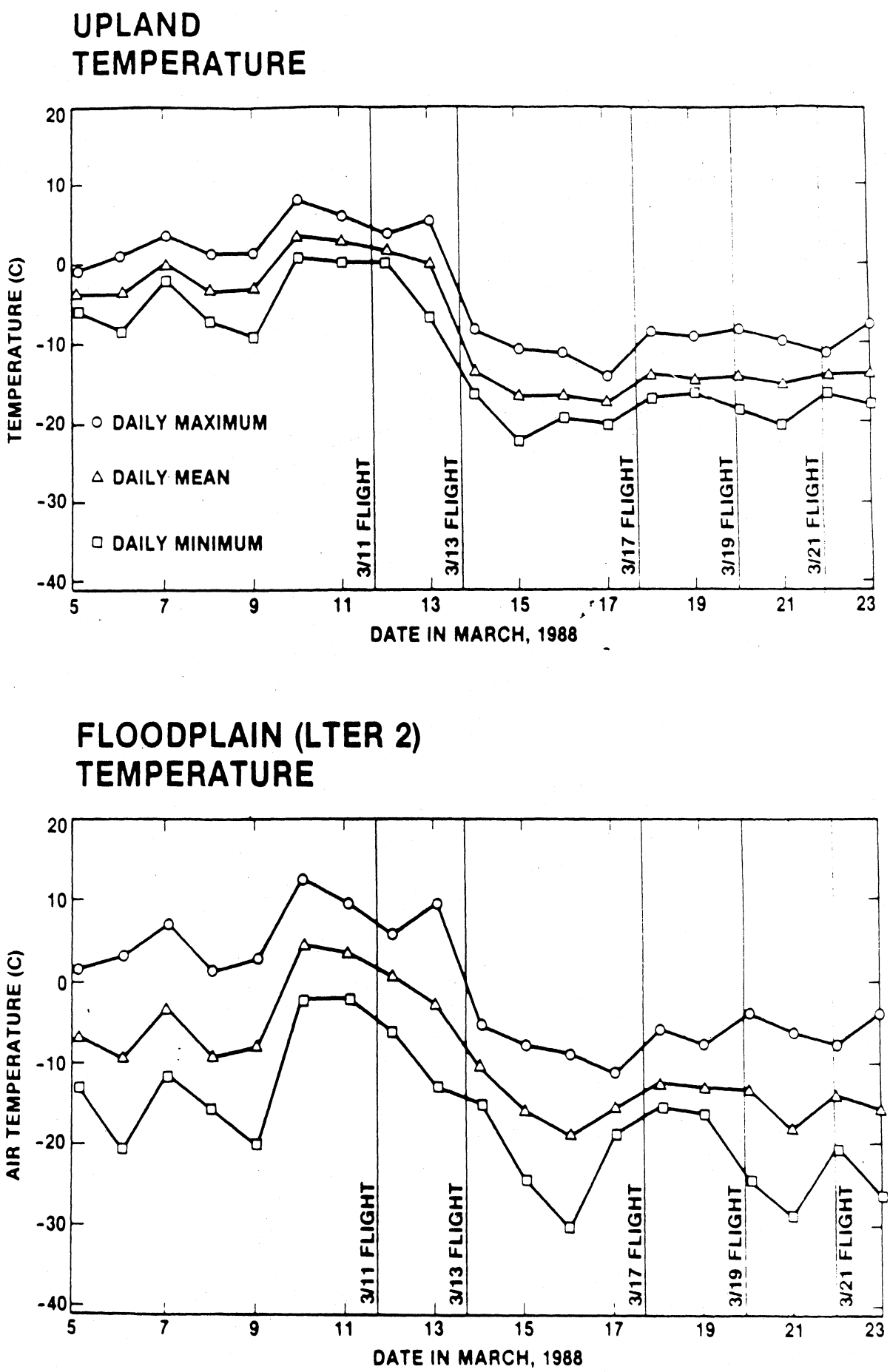

Figure 14: Air Temperature at the Bonanza Creek Experimental Forest.

Figure 15. Detailed measurements of the snow pack were made for one stand each of white spruce (WS-2) and black spruce (BS-1) at the times of the aircraft overflights. These measurements included air and snow temperature profiles, snow depth, snow density profile, and snow wetness. Snow wetness measurements included a hydrochloric acid detection technique (Davis, et al., 1985) and in situ dielectric measurements at L- and C-bands.

The early March thaw caused the melting of snow in the canopy crown layer. This wet snow fell from the crowns of the white sprcue stands as spheroidal nodules with diameters of 3cm to 5cm and embedded themselves in the upper 5cm of the snowpack. On the relatively warm days of March 11 and 13, these fresh nodules of wet snow were estimated to have volumetric moisture contents of 30-40% on the basis of in situ dielectric measurements. The remainder of the upper 3cm to 7cm layer of snow were found to have volumetric moisture contents ranging from 2% to 7% on the warm days. For overflights after March 13, the surface snow layer was frozen and the wet snow nodules formed ice balls; the measured snow wetness for all layers was found to be 0% by volume. The average dry density of the snow pack was found to be approximately 0.2 g/cm^3 throughout the experiment.

Although measurements of snow wetness varied considerably with spatial location, depth, and time on March 11 and 13, they yielded an average maximum of 10% by weight for the times of the SAR overpasses. Hence, the average volumetric moisture of the snow was considered to be 2%. The dielectric properties of the snow pack as a function of frequency were calculated using the Debye-like model of Hallikainen, et al. (1986) where the relative dielectric constant of snow $\varepsilon_s^* = \varepsilon'_s - j\varepsilon''_s$ is given by

$$\varepsilon'_s = A + \frac{B m_v^x}{1 + (f/f_o)^2} \qquad (15)$$

Figure 15. Detailed measurements of the snow pack were made for one stand each of white spruce (WS-2) and black spruce (BS-1) at the times of the aircraft overflights. These measurements included air and snow temperature profiles, snow depth, snow density profile, and snow wetness. Snow wetness measurements included a hydrochloric acid detection technique (Davis, et al., 1985) and in situ dielectric measurements at L- and C-bands.

The early March thaw caused the melting of snow in the canopy crown layer. This wet snow fell from the crowns of the white sprcue stands as spheroidal nodules with diameters of 3cm to 5cm and embedded themselves in the upper 5cm of the snowpack. On the relatively warm days of March 11 and 13, these fresh nodules of wet snow were estimated to have volumetric moisture contents of 30-40% on the basis of in situ dielectric measurements. The remainder of the upper 3cm to 7cm layer of snow were found to have volumetric moisture contents ranging from 2% to 7% on the warm days. For overflights after March 13, the surface snow layer was frozen and the wet snow nodules formed ice balls; the measured snow wetness for all layers was found to be 0% by volume. The average dry density of the snow pack was found to be approximately 0.2 g/cm^3 throughout the experiment.

Although measurements of snow wetness varied considerably with spatial location, depth, and time on March 11 and 13, they yielded an average maximum of 10% by weight for the times of the SAR overpasses. Hence, the average volumetric moisture of the snow was considered to be 2%. The dielectric properties of the snow pack as a function of frequency were calculated using the Debye-like model of Hallikainen, et al. (1986) where the relative dielectric constant of snow $\varepsilon_s^* = \varepsilon'_s - j\varepsilon''_s$ is given by

$$\varepsilon_s = A + \frac{Bm_v^x}{1 + (f/f_o)^2} \qquad (15)$$

$$\varepsilon_s'' = \frac{C + (f/f_o)m_v^x}{1 + (f/f_o)^2} \qquad (16)$$

where m_v is the snow wetness (volume %), f is the frequency (GHz), f_o is the resonant frequency of liquid water at 0°C (GHz), and the coefficients A,B,C and X are empirically derived for f≤ 15 GHz as

$$A = 1.0 + 1.83\ \rho_{ds} + 0.02\ m_v^{1.015} \qquad (17)$$

$$B = C = 0.073$$

$$X = 1.31$$

where ρ_{ds} is the dry snow density (g/cm^3). Solving (17) at $m_v = 0$ and 2% yields A = 1.366 for frozen snow and A = 1.4064 for the wet snow on March 11 and 13. Solving (15) and (16) at L-, C-, and X-band center frequencies yields the snow dielectric values given in Table 5 for both frozen and thawed conditions.

The surface roughness of the air/snow interface was not measured, but is assumed to be smooth with a root mean square deviation of 1.2 cm and a surface correlation length of 24 cm.

A trench cut into the permafrost was used to measure the relative dielectric constant of the frozen mineral soil using the portable dielectric probes. Average ε* soil was found to be 7.96-j0.96 at L-band. The roughness of the snow/soil interface could not be determined. As a consequence, the MIMICS simulations, described in this report, model the surface as a half-space of snow (either wet or dry).

Stand Characteristics

In order to model the extinction and backscatter from a given forest stand using MIMICS, the stand must be characterized with respect to the sizes, shapes and orientations

Table 5 Modeled Relative Dielectric Constants of Snow for the Frozen and Thawed Conditions.

Frequency (GHz)	Thawed Period (March 11 and 13)		Frozen Period (after March 13)	
	ε'_s	ε''_s	ε'_s	ε''_s
1.25	1.58	0.024	1.37	0.0
5.3	1.54	0.079	1.37	0.0
9.6	1.49	0.09	1.37	0.0

of the various canopy elements and their respective dielectric properties. This characterization proceeds at three levels: (1) stand characterization, (2) tree geometry, and (3) dielectric properties of canopy elements. Stand characterization entails determination of total stand biomass and its apportionment into constituent canopy components such as trunks, branch classes, and leaves. This is usually accomplished via some field observations of stand density, tree diameter and tree height in combination with empirically determined allometric relationships to calculate and apportion biomass. The geometry describes the pdfs for each canopy component in terms of size, shape and orientations, and is usually ascertained by destructive sampling methods. The dielectric properties can be measured in situ and/or modeled as functions of frequency on the basis of the dry density and moisture content of the various canopy components.

For each forest stand, a ground survey was conducted to record the number of trees per unit area by species and also record their respective diameters as measured at breast height dbh (1.3m). Stand enumerations were conducted in March of 1988 and again during July to September of 1988 for seven stands at the Bonanza Creek Experimental Forest (Jaeger, 1988). The enumeration methodology utilized a line trasect along the longest axis of a stand. Ten sample plots were established at random locations along the transect, where each sample plot was circular with a measured radius sufficient to include 20 to 30 trees. Within each plot, the dbh (cm) and species of all stems (trunks) greater than 1 cm dia and taller than 30 cm (i.e., sufficient to have stood above the snow layer in March) were recorded. Each tree was noted as to its status: alive and undamaged, broken, or dead. Height was also measured for at least four live trees per plot (i.e., $\geq$ 40 trees per stand) for determination of allometric relationships relating height to dbh. A sample of the enumerated data is shown in Table 6 for sample plot 1 of white spruce stand WS-1. Histograms of dbh for four white spruce stands (WS-1, WS-2, WS-5, and WS-7), a

Table 6. Sample of Stand Characterization Data for Plot 1 of White Spruce Stand WS-1.

Date	Stand code	Plot No.	Plot size (m^2)	Specie code	dbh (cm)	height (m)	height (m) broken trees	status live, dead broken	lean direction (ϕ)	lean orientation (θ)
9 22	20	1	200	4	6.9	.	1.5	3	.	.
9 22	20	1	200	4	3.4	.	.	1	190	75
9 22	20	1	200	4	11.8	.	.	1	.	.
9 22	20	1	200	4	9.8	.	.	1	.	.
9 22	20	1	200	4	7.5	.	.	1	78	65
9 22	20	1	200	4	6.6	.	3.0	3	.	.
9 22	20	1	200	4	6.2	.	.	1	145	70
9 22	20	1	200	4	10.5	9.0	.	1	.	.
9 22	20	1	200	4	6.3	.	3.0	3	.	.
9 22	20	1	200	4	11.8	.	.	1	32	10
9 22	20	1	200	4	8.4	.	.	1	.	.
9 22	20	1	200	4	5.8	.	.	1	106	90
9 22	20	1	200	4	5.0	.	3.5	3	.	.
9 22	20	1	200	4	9.0	.	.	1	.	.
9 22	20	1	200	4	9.2	6.5	.	1	.	.
9 22	20	1	200	4	9.2	.	.	1	.	.
9 22	20	1	200	4	7.7	.	.	1	190	90
9 22	20	1	200	4	10.7	.	.	1	196	15
9 22	20	1	200	4	5.3	.	.	1	.	.
9 22	20	1	200	4	9.9	.	.	1	.	.
9 22	20	1	200	4	7.6	7.5	.	1	.	.
9 22	20	1	200	4	8.0	.	.	1	.	.
9 22	20	1	200	4	6.1	.	.	1	115	85
9 22	20	1	200	4	8.8	.	2.0	3	.	.
9 22	20	1	200	4	6.6	.	.	1	210	45
9 22	20	1	200	4	8.6	.	.	1	.	.
9 22	20	1	200	4	8.3	.	3.0	3	.	.
9 22	20	1	200	4	7.7	.	4.0	2	212	20
9 22	20	1	200	4	6.8	.	.	1	222	45
9 22	20	1	200	4	9.5	.	.	1	.	.
9 22	20	1	200	4	9.7	.	.	1	.	.
9 22	20	1	200	4	3.8	.	.	1	314	25
9 22	20	1	200	4	9.9	.	.	1	.	.
9 22	20	1	200	4	8.7	.	.	0	230	55
9 22	20	1	200	4	10.1	8.0	.	1	.	.
9 22	20	1	200	4	11.2	8.0	.	1	.	.
9 22	20	1	200	4	5.4	.	3.5	3	.	.
9 22	20	1	200	4	10.2	.	.	1	.	.
9 22	20	1	200	4	8.1	.	.	1	.	.
9 22	20	1	200	4	5.8	.	.	1	308	15
9 22	20	1	200	3	13.4	.	.	1	.	.
9 22	20	1	200	4	11.1	.	.	1	.	.
9 22	20	1	200	4	6.5	6.0	.	1	.	.
9 22	20	1	200	4	3.8	.	.	1	165	60

black spruce stand (BS-1), and a balsam poplar stand (BP-2) are given in Figures 16-21, respectively.

In order to estimate total aboveground biomass for each stand, the enumerated stand data is used in concert with allometric expressions. The enumerated stand data for height and dbh have been used to establish empirical allometric relationships for both the live and broken stems of each specie in each stand. These relationships take the forms

$$H = a + b\,(dbh) + c\,(dbh)^2 \qquad (18)$$

$$H = a + b\,(dbh) \qquad (19)$$

where H is the height in meters and dbh is in cm.

The measured dbh, heights from (18) or (19), and the status of each tree (i.e., live, dead, and/or broken) are also used to estimate quantities including basal area, biomass volume, and biomass (with and without summer foliage) on the basis of allometric expressions drawn from the literature for each specie (Kirby, 1960; Manning, et al., 1984; Singh, 1984; and Yarie and Van Cleve, 1983). These expressions have been derived for stands in Alaska and in the Yukon and Northwest Territories of Canada. The specific equations utilized are listed in Jaeger (1988). When applied to each individual tree in the enumerated sample plots, these expressions produce biomass estimates as shown in Table 7. These estimates were then summed over all trees in a stand to yield and total biomass estimates given in Table 8 as averaged over the net areas of all sample plots in a given stand.

The average densities of the white spruce stands are shown in Table 8 to vary by a factor of 2 from 1,123 to 2,073 trees per hectare with a mean of 1,482. However, the average basal areas of the white spruce stands are nearly equivalent wih a mean of 44 m^2/ha; and the estimated average dry biomass of these stands varies by only $\pm$ 9% about a mean of 19.5 kg/m^2. The balsam poplar stand BP-2 is shown to be comparable to the mean white spruce conditions in terms of

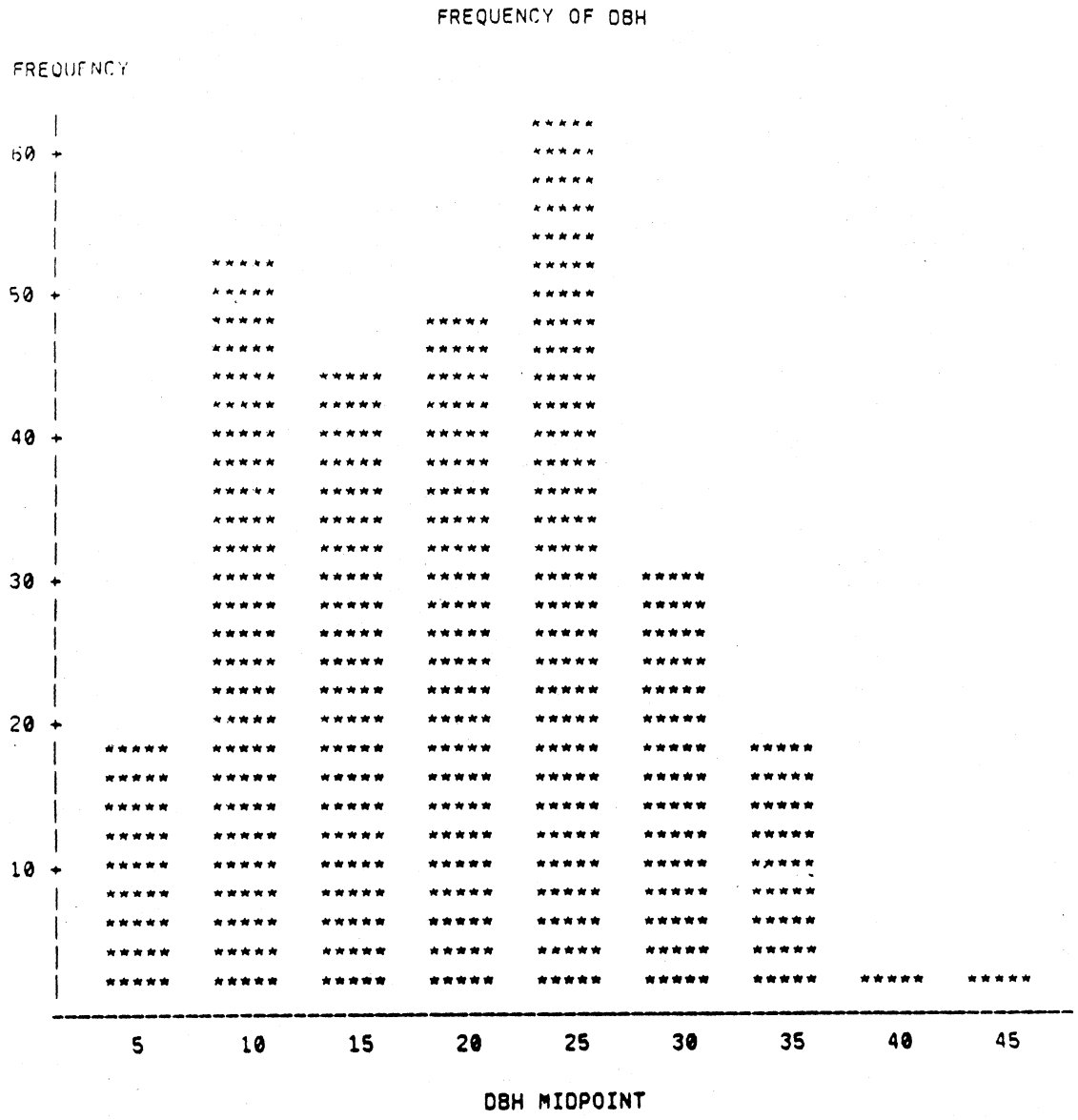

Figure 16: Histogram of DBH Distribution for White Spruce Stand WS-1.

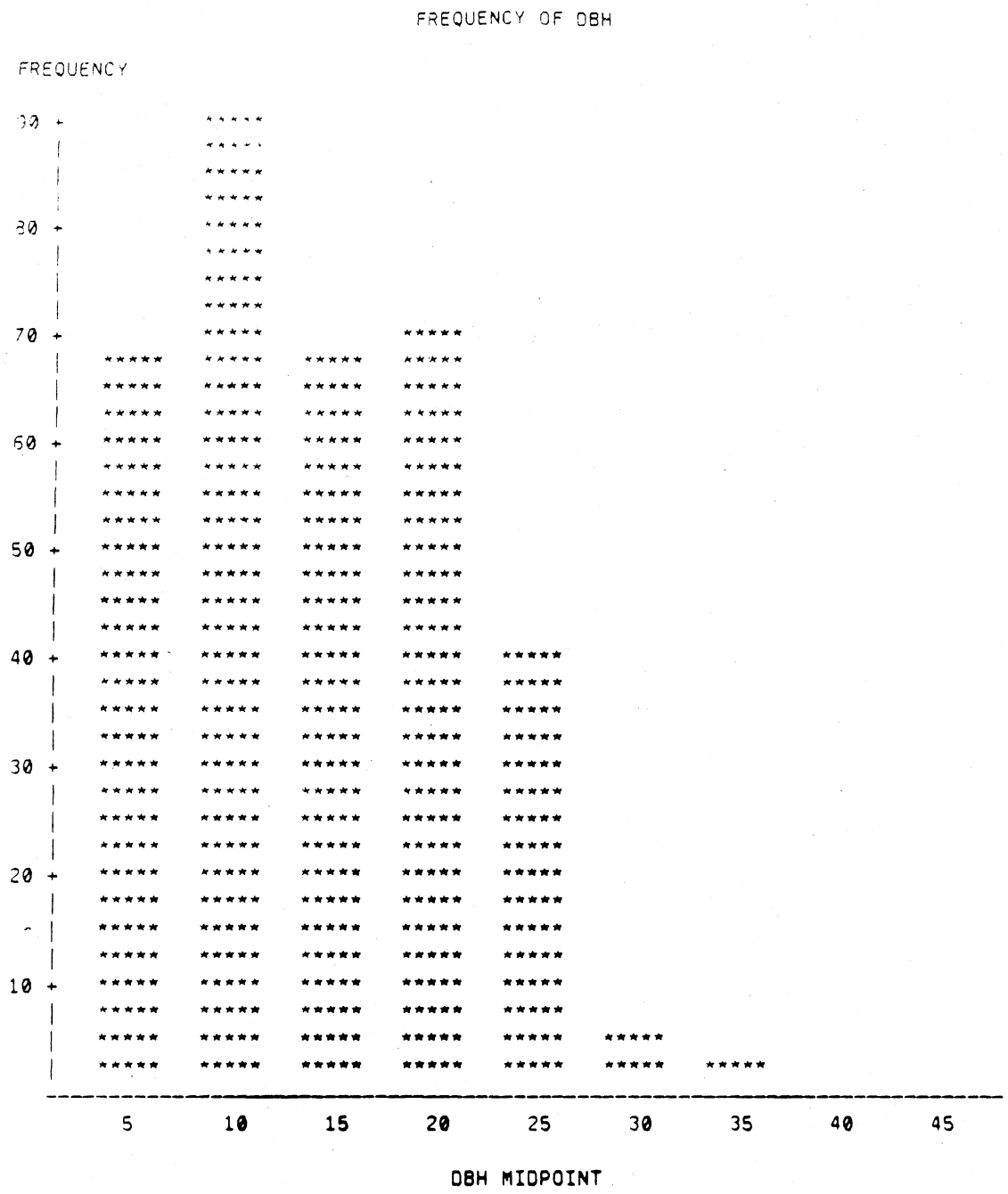

Figure 17: Histogram of DBH Distribution for White Spruce Stand WS-2.

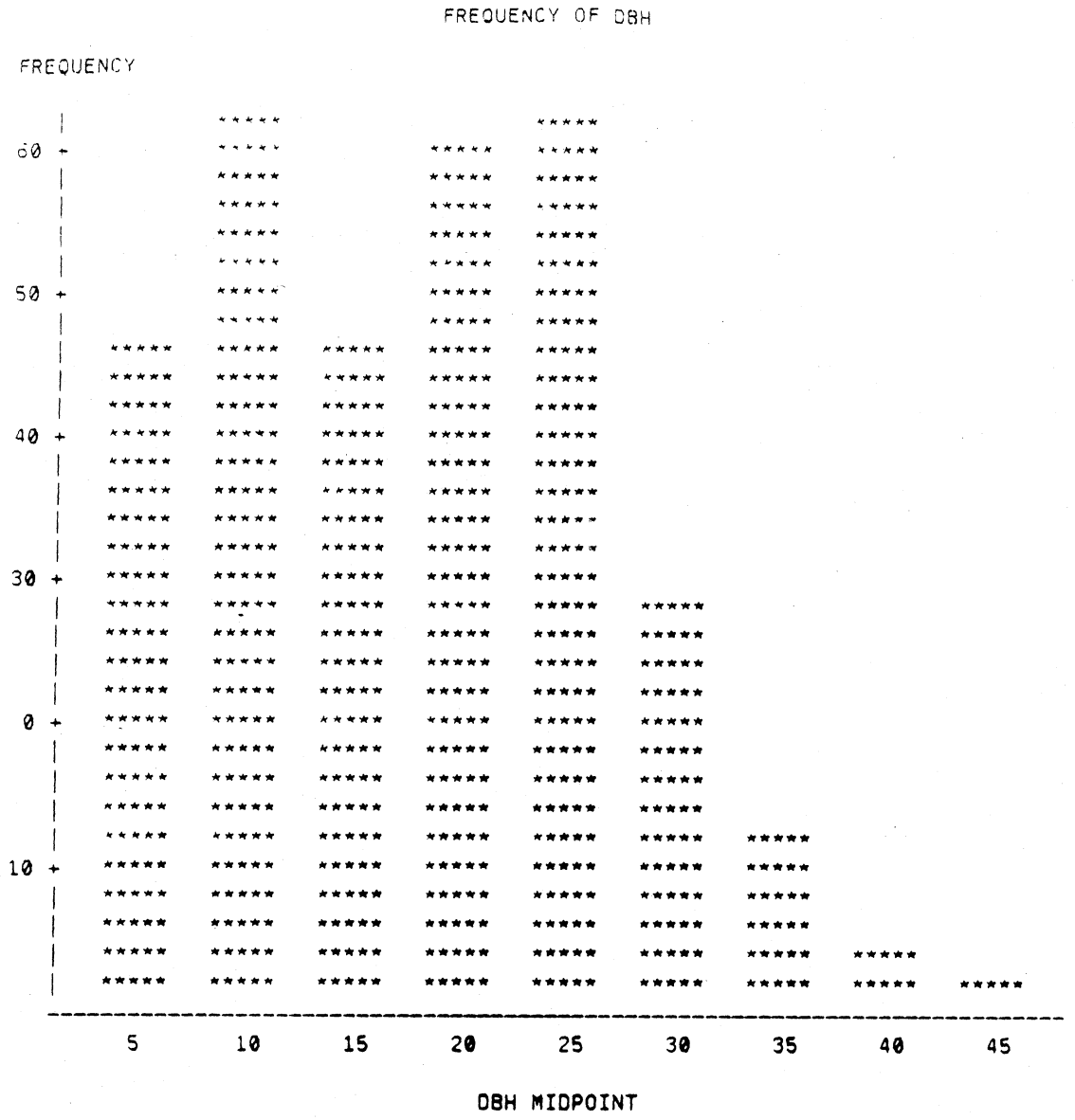

Figure 18: Histogram of DBH Distribution for White Spruce Stand WS-5.

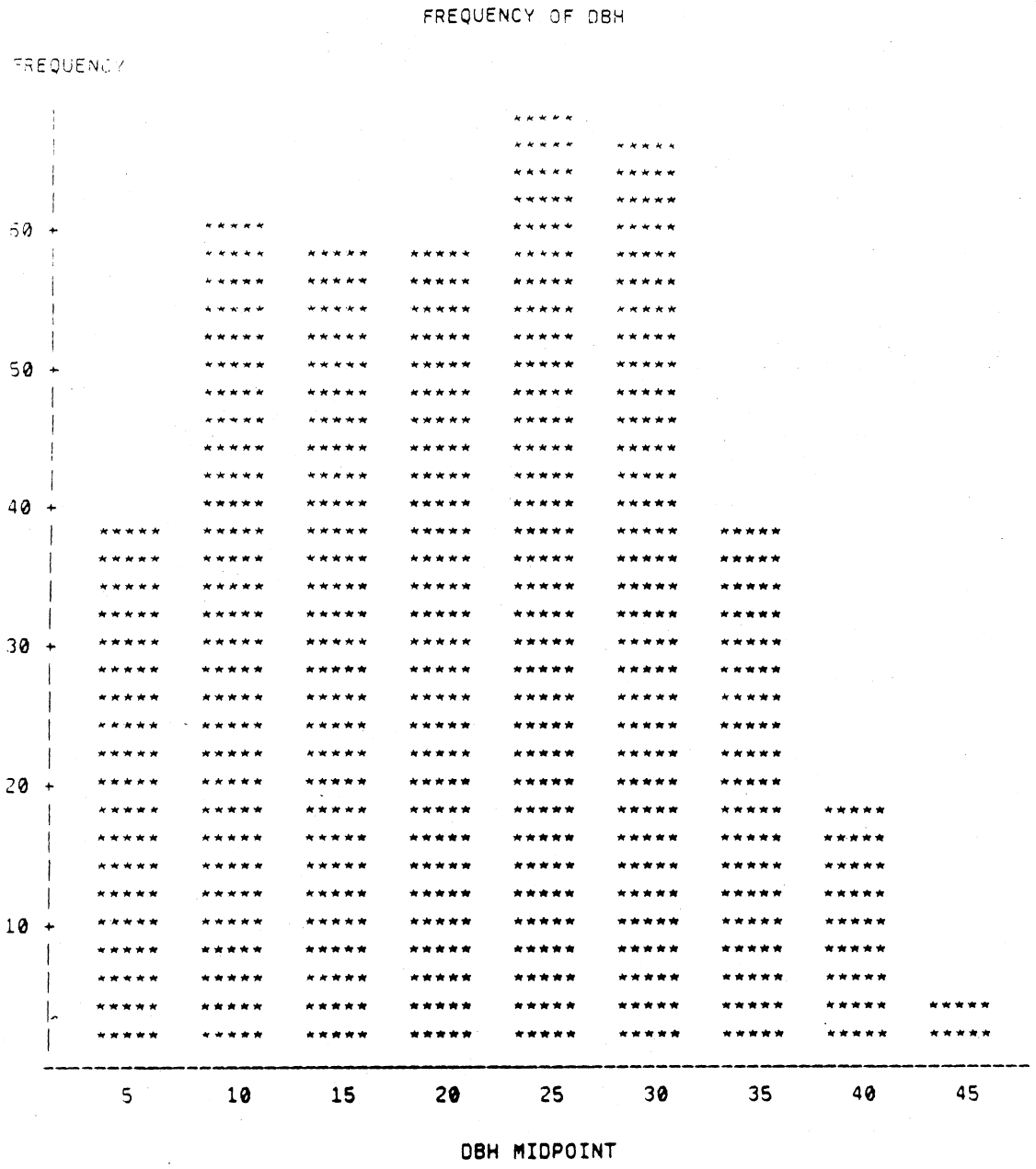

Figure 19: Histogram of DBH Distribution for White Spruce St and WS-7.

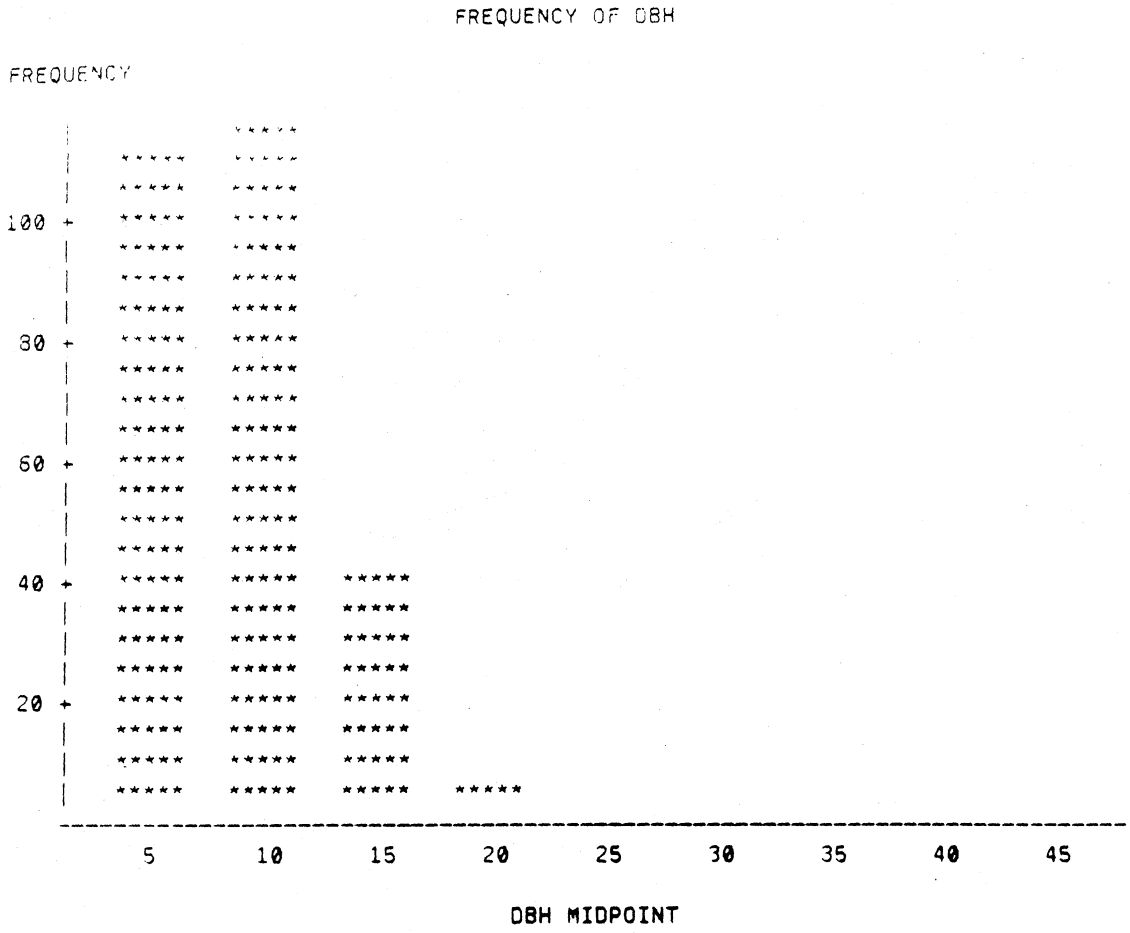

Figure 20: Histogram of DBH Distribution for Black Spruce Stand BS-1.

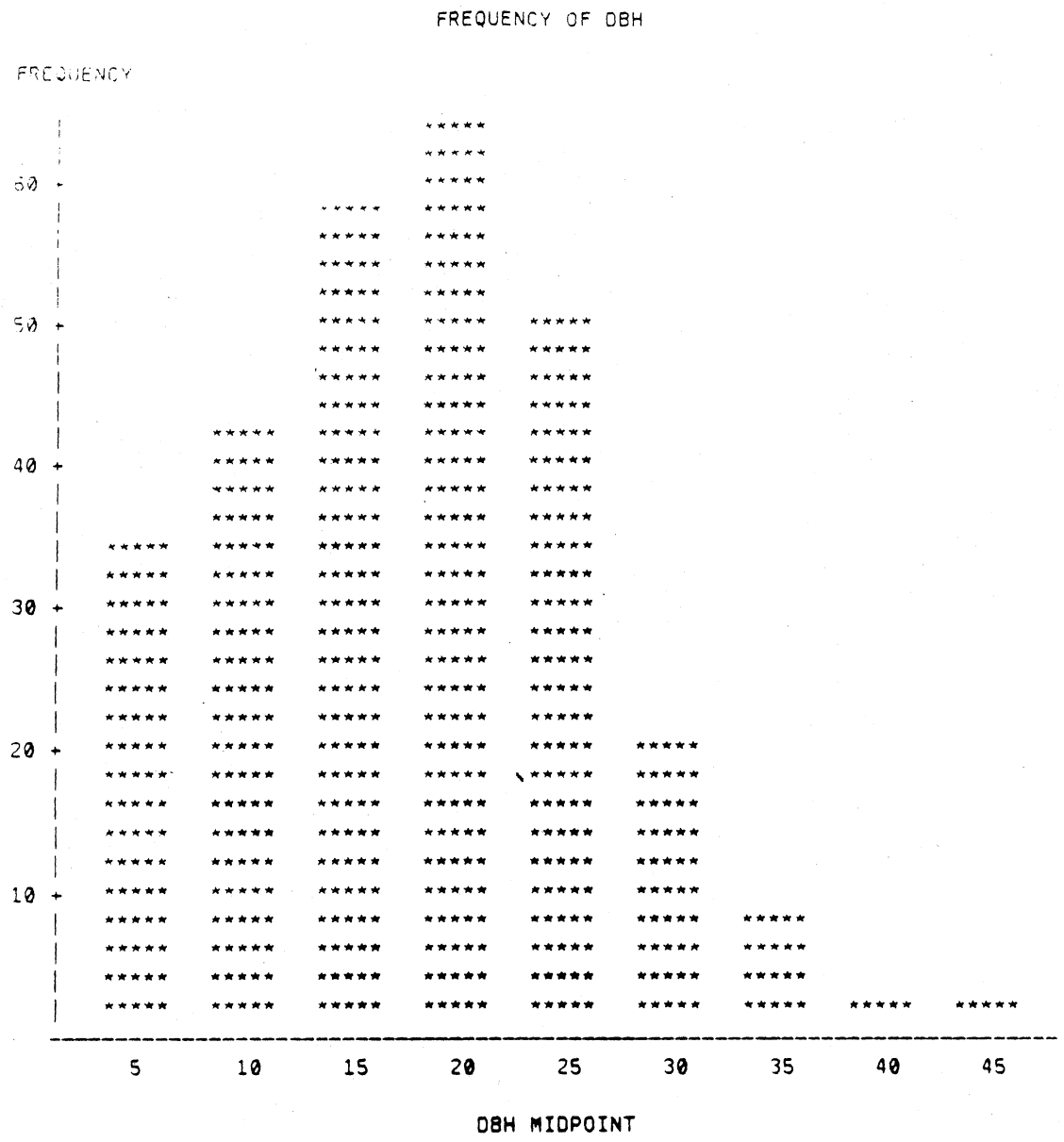

Figure 21: Histogram of DBH Distribution for Balsam Poplar Stand BP-2.

Table 7. Sample of Tree Biomass Calculations for Plot 1 of White Spruce Stand WS-1.

Stand ID	Plot No.	Specie code	dhd (cm) dbh	Regression height (m)	volume m^3/ha	basal area (m^2/ha)	basal area (m^2)	Biomass with leaves (Kg)	Biomass with leaves (Kg/ha)
4 20	1	4	6.9	6.8	1.3	.0037	0.19	354	7.1
4 20	1	4	3.4	3.6	0.1	.0009	0.05	134	2.7
4 20	1	4	11.8	10.0	2.4	.0109	0.55	1827	36.5
4 20	1	4	9.8	8.5	1.4	.0075	0.38	1101	22.0
4 20	1	4	7.5	6.7	0.7	.0044	0.22	554	11.1
4 20	1	4	6.6	6.8	1.2	.0034	0.17	338	6.8
4 20	1	4	6.2	5.7	0.4	.0030	0.15	357	7.1
4 20	1	4	10.5	9.0	1.7	.0087	0.43	1326	26.5
4 20	1	4	6.3	6.8	1.1	.0031	0.16	323	6.5
4 20	1	4	11.8	10.0	2.4	.0109	0.55	1827	36.5
4 20	1	4	8.4	7.4	0.9	.0055	0.28	736	14.7
4 20	1	4	5.8	5.4	0.3	.0026	0.13	310	6.2
4 20	1	4	5.0	6.8	0.7	.0020	0.10	259	5.2
4 20	1	4	9.0	7.8	1.1	.0064	0.32	879	17.6
4 20	1	4	9.2	8.0	1.2	.0066	0.33	931	18.6
4 20	1	4	9.2	8.0	1.2	.0066	0.33	931	18.6
4 20	1	4	7.7	6.8	0.7	.0047	0.23	591	11.8
4 20	1	4	10.7	9.1	1.8	.0090	0.45	1395	27.9
4 20	1	4	5.3	5.0	0.3	.0022	0.11	259	5.2
4 20	1	4	9.9	8.5	1.5	.0077	0.38	1131	22.6
4 20	1	4	7.6	6.8	0 7	.0045	0.23	573	11.5
4 20	1	4	8.0	7.1	0.8	.0050	0.25	650	13.0
4 20	1	4	6.1	5.6	0.4	.0029	0.15	345	6.9
4 20	1	4	8.8	6.8	2.1	.0061	0.30	453	9.1
4 20	1	4	6.6	6.0	0.5	.0034	0.17	410	8.2
4 20	1	4	8.6	7.5	1.0	.0058	0.29	781	15.6
4 20	1	4	8.3	6.8	1.8	.0054	0.27	426	8.5
4 20	1	4	7.7	5.1	1.2	.0047	0.23	341	6.8
4 20	1	4	6.8	6.2	0.5	.0036	0.18	439	8.8
4 20	1	4	9.5	8.2	1.3	.0071	0.35	1013	20.3
4 20	1	4	9.7	8.4	1.4	.0074	0.37	1071	21.4
4 20	1	4	3.8	3.9	0.1	.0011	0.06	152	3.0
4 20	1	4	9.9	8.5	1.5	.0077	0.38	1131	22.6
4 20	1	4	8.7	7.6	1.0	.0059	0.30	553	11.1
4 20	1	4	10.1	8.7	1.6	.0080	0.40	1194	23.9
4 20	1	4	11.2	9.5	2.1	.0099	0.49	1581	31.6
4 20	1	4	5.4	6.8	0.8	.0023	0.11	278	5.6
4 20	1	4	10.2	8.8	1.6	.0082	0.41	1226	24.5
4 20	1	4	8.1	7.2	0.8	.0052	0.26	671	13.4
4 20	1	4	5.8	5.4	0.3	.0026	0.13	310	6.2
4 20	1	3	13.4	11.2	3.5	.0141	0.71	2313	46.3
4 20	1	4	11.1	9.4	2.0	.0097	0.48	1543	30.9
4 20	1	4	6.5	5.9	0.5	.0033	0.17	396	7.9
4 20	1	4	3.8	3.9	0.1	.0011	0.06	152	3.0

Table 8. Summary Table of Stand Density, Basal Area, Volume, and Biomass on a per Hectare Basis.

	Stand					
	WS-1	WS-2	WS-5	WS-7	BS-1	BP-2
Density (Stems/ha)						
Mean	1,248	2,073	1,484	1,123	1,975	1,615
Stand. Dev.	342	576	618	654	1,483	407
Basal Area (m^2/ha)						
Mean	46	41	44	46	12	50
Stand. Dev.	16.6	7.0	8.5	12.4	3.3	25.8
Volume (m^3/ha)						
Mean	442	332	392	442	51	344
Stand. Dev.	169	60	100	115	12	190
Dry Biomass-Summer (kg/m^2)						
Mean	21.7	16.7	18.1	21.5	3.7	18.2
Stand. Dev.	8.8	3.6	4.8	6.1	0.8	10.9
Dry Biomass - Winter (kg/m^2)						
Mean	21.7	16.7	18.1	21.5	3.7	17.9
Stand. Dev.	8.8	3.6	4.8	6.1	0.8	10.7

Standard deviations are based upon between plot variance within a stand.

density, basal area, volume, and biomass. In contrast, the black spruce stand BS-1 has a large number of small diameter trunks, and hence, basal area is about 25% that of the other stands. In addition, the short height of the black spruce contributes to an average biomass roughly 20% that found for the mean white spruce conditions.

In addition to the six stands listed in Table 8, the tree stands containing the trihedral corner reflectors were also enumerated with respect to density, height and diameter (Kasischke, et al., 1989; and Jaeger, 1988). These stands included a single specie stand of alder and mixed specie stands of alder, balsam poplar, and white spruce. A comparison between stands for mean dbh, height and basal area is given in Table 9. The small diameters of the alders are offset by a large density to yield a basal area of 66.5 m^2/ha which is about 50% greater than that found for the white spruce and balsam poplar stands listed in Table 8. In contrast, the two mixed specie stands containing the trihedral corner reflectors are found to have basal areas about 50% less than the more mature single specie stands of white spruce (WS -1 to 7) or balsam poplar (BP-2).

In order to statistically summarize the trunk layer for use in MIMICS, the dbh histograms shown in Figures 16 to 21 are normalized and used in conjunction with the allometric height equations given in Table 10 to describe the joint pdf of trunk height and diameter within a given forest stand. This pdf is then multiplied by the average stem density of the stand to characterize the trunk fraction on an area basis.

The thickness of the crown layer containing the branches and foliage is determined on the basis of field observations. For both white spruce and black spruce, the tree form is excurrent and conical with the lowest live branches almost at ground level. Hence, crown thickness is taken to be equal to average tree height for spruces. For alders and balsam poplars, which are also excurrent in form but are deciduous trees with no leaves in March, the crown thickness is estimated from the

Table 9. Comparision of Mean DBH, Height, and Basal Area for Various Forest Stands

Stand Name	Specie	Stand Means DBH (cm)	Height (m)	Basal Area (m^2/ha)	
WS-1	white spruce	19.6	22.1	46	
WS-2	white spruce	14.5	20.1	41	
WS-5	white spruce	17.9	21.3	44	
WS-7	white spruce	21.4	24.5	46	
BS-1	black spruce	8.8	7.6	12	
BP-2	balsam poplar	18.0	17.6	50	
Stands with trihedral reflectors					
Alder	alder	6.0	6.3	66.5	
Balsam Poplar	balsam poplar	11.0	12.7	22.9	26.0
	alder	6.0	6.3	3.1	
White spruce	white spruce	7.8	8.6	12.4	
	balsam poplar	9.4	11.6	10.0	27.8
	alder	6.1	6.3	5.4	

Table 10. Tree Height Equations Used to Establish Trunk PDFs

White spruce (Picea glauca)

$$H = -1.7096 + 1.4224 (dbh) - 0.016 (dbh)^2$$

Black spruce (Picea mariana)

$$H = 0.9494 + 0.7657 (dbh)$$

Balsam poplar (Populus balsamifera)

$$H = 1.0526 + 1.143 (dbh) - 0.0145 (dbh)^2$$

Mountain alder (Alnus tenuifolia)

$$H = 2.871 + 0.5666 (dbh)$$

H = height in meters
dbh = diameter in cm as measured at breast height

height of the lowest branches and is assumed to be 25% of average height.

Total stand biomass in Table 8 was estimated using allometric equations. However, MIMICS requires that this total biomass be apportioned amongst the various constituent components of the trunk and crown layers. This is done on a stand basis using allometric equations derived from destructive sampling as reported in the literature. These biomass equations are generally based upon both height and diameter and commonly take the form

$$B_c = a + b\,(dbh)^2 H \qquad (20)$$

where B_c is the dry biomass of some component c. Seperate equations are often given for the dry biomass of the whole tree, the bark of the trunk, the wood of the trunk, the branches, and the twigs plus foliage. An example of these equations is given in Table 11 for white spruce (Manning, et al., 1984; Yarie and Van Cleve, 1983). Equations for both white spruce and black spruce are given by Singh, (1983). Biomass equations for alder are given in terms of basal diameter d as measured at the base of the trunk (Van Cleve and Viereck, 1972).

$$B_{trunk} = \text{alog}\,(2.57 \log d - 1.65)$$
$$B_{branches} = \text{alog}\,(2.79 \log d - 2.38)$$

and hence this quantity was also enumerated for alder trees.

Since most of these equations were empirically derived for stands outside of the Bonanza Creek Experimental Forest, perhaps with differing local site conditions, they may produce errors in characterizing the biomass apportionment of the Bonanza Creek stands. However, they are the best available sources of information.

In addtion to the possible statistical errors associated with transporting the allometric equations to the Bonanza Creek stands, these equations do not adequately subdivide the crown

Table 11. White Spruce Dry Biomass Equations

A. For white spruce <6 cm dbh (Manning, et al., 1984)

$$B_{trunk} = B_{bark} + B_{wood}$$
$$B_{bark} = 0.1506 + 0.00193\ (dbh)^2H$$
$$B_{wood} = 0.277 + 0.0124\ (dbh)^2H$$

$$B_{branches} = 0.2519 + 0.001191\ (dbh)2_H$$
$$B_{twigs\ +\ foliage} = 0.9265 + 0.00241\ (dbh)^2H$$
$$B_{tree} = 1.6914 + 0.01891\ (dbh)^2H$$
$$H = -1.7096 + 1.4224\ (dbh) - 0.016\ (dbh)^2$$

B. For white spruce $\geq$ 6 cm dbh (Yarie and Van Cleve, 1983)

$$B_{trunk} = B_{bark} + B_{wood}$$
$$B_{bark} = -0.072 + 0.037\ (dbh)^2$$
$$B_{wood} = -4.829 + 1.062\ H + 0.01\ (dbh)^2H$$
$$B_{branches} = -1.093 + 0.049\ (dbh)^2$$
$$B_{twigs\ +\ foliage} = 0.007 + 0.036\ (dbh)^2$$
$$B_{tree} = -1.283 + 0.184\ (dbh)^2 + 0.009\ (dbh)^2H$$

B = dry biomass in kg
dbh = diameter at breast height in cm
H = tree height in m
The branch fraction includes branches greater than 1/2 cm diameter

layer of branches and foliage into the component parts required by MIMICS (i.e., primary branches, secondary branches, and foliage). For example, the allometric equations listed in Table 11 for the dry biomass of branches only includes branches with diameters greater than 0.5 cm while the remaining branch and twig mass is combined together with the foliage into another allometric relationship. Hence, further apportionment of biomass into discrete branch size classes and into the foliar component is accomplished for the Alaskan data on the basis of destructive sampling undertaken at the time of the overflights in March, 1988. Destructive sampling in white spruce stand WS-1 and black spruce stand BS-1 included: trunk height and diameter, number of branches, branch lengths and diameters, orientation angles of branches, needle density and size, and wet and dry mass determinations for subsamples of each component.

Using white spruce as an example, the destructive sampling data is used to augment the allometric relationships in apportionment of biomass for use by MIMICS. The biomass apportionment equations of Singh (1983) are solved for the sampled tree height and yield:

Component	% of total dry biomass
stump	3.33
bole $\geq$ 10 cm dia	79.35
2 cm $\leq$ bole < 10 cm	3.11
Total trunk	85.79
branches $\geq$ 2 cm dia	6.13
branches < 2 cm plus foliage	8.08
Total	100

From destructive sampling of three white spruce trees with a total of 177 branches, it was found that 12.4% of the branches were $\geq$ 2 cm diameter (mean length = 113 cm and mean

diameter = 2.24 cm) and the remaining 87.6% of the branches were < 2 cm diameter (mean length = 57.2 cm and mean diameter = 1.04 cm). Assuming the branches to be cylindrical with a constant dry density for all size classes, the dry biomass (or volume) ratio of small to large branches (i.e., branches < 2 cm dia. to branches ≥ 2 cm dia.) = 0.7703. Since branches ≥ 2 cm dia comprise 6.13% of total biomass according to Singh (1983), then the total dry biomass fraction for branches < 2 cm dia. becomes 0.7703 x 6.13 = 4.72%. Consequently, the total dry biomass fraction of needles plus twigs becomes 8.08 - 4.72 = 3.36%.

In order to seperate the foliage biomass from that of the twigs, we again use the destructive sampling data. On average, it was determind that there are 14.42 needles/cm of twig with a dry mass ratio of 3.36 g needle /g twig. Hence, the needle (foliage) biomass fraction becomes 0.77 x 3.36 = 2.6%; and the twig biomass fraction becomes 0.23 x 3.36 = 0.76%.

Assuming the primary branch class for white spruce includes those branches ≥ 2 cm diameter and the secondary branch class includes branches < 2 cm diameter plus the twig component, the biomass apportionment to be used by MIMICS is

trunk	85.79%
primary branches	6.13%
secondary branches	5.48%
foliage	2.60%

The biomass apportionment for black spruce is conducted in a similar fashion using detructive sampling data to augment the allometric equations given by Singh (1983). These results, as well as the biomass apportionments for balsam poplar and alder are given in Table 12. However, since destructive sampling of balsam poplar and alder trees was not conducted at the Bonanza Creek Experimental Forest, the apportionment of biomass into primary and secondary branch classes assumes that these species fit the biomass models determined for

Table 12. Dry Biomass Fractions of Various Canopy Components for Use by MIMICS as % of Total.

	White Spruce	Black Spruce	Balsam Poplar	Alder
Trunk	85.79	86.45	90.0	90.0
Primary Branches	6.13	4.94	4.9	4.9
Secondary Branches	5.48	5.06	5.1	5.1
Foliage	2.60	3.55	NA	NA
Total	100	100	100	100

trembling aspens (Manning, 1984; Nelson, et al., 1981) as adjusted for the absence of foliage in March.

The number densities of a given canopy element (in number per unit volume) can be readily determined as

$$N = \frac{\text{net stand biomass x biomass apportionment fraction}}{\text{biomass of a single element x crown layer thickness x stand area}}$$

where the biomass of a single element is calculated from the average length, diameter and dry density of that element as determined by destructive sampling.

Tree Geometry

Tree geometry is required by MIMICS to describe the pdfs of each canopy component in terms of size, shape and orientation. For the trunk layer of all stands, this is done using the measured dbh histograms and associated allometric equations for height. Although the distribution of orientation angles (relative to vertical) was enumerated for each stand the number of leaning trunks (i.e., non-vertical) was very small and ranged over small angles. Model runs of MIMICS showed negligible sensitivity to the actual orientations of the trunks when compared to assuming all trunks to be vertical. Hence, the orientations of all trunks is assumed to be vertical in the MIMICS simulations.

The size, shape and orientations of components of the crown layer are those derived from field observations (including destructive sampling) as augmented by the literature for balsam poplar and alder by assuming the applicability of a trembling aspen tree morphology. For white spruce, the destructive sampling measurements of primary branches, those $\geq$ 2 cm diameter, yield an average length of 113 cm and diameter of 2.24 cm. The secondary branches, those < 2 cm diameter, were found to have an average length of 57.2 cm and diameter of 1.04 cm. The needles of the white spruce were

found to average 1.6 cm in length and have an effective diameter of 0.1 cm.

Destructive sampling of black spruce trees ascertained the average primary branch length to be 81.3 cm with a diameter of 2.37 cm. The secondary branches, with diameters < 2 cm, were found to average 51.2 cm length and 1.06 cm diameter. The needles were estimated to have an average effective diameter of 0.1 cm with an average length of 0.8 cm.

The branch class sizes for balsam poplar and alder are assumed to be similar to those of trembling aspen. The observations of Nelson, et al. (1981) of young aspen clones are used to subdivide the measured branch population into approximately equal portions on a mass or cylindrical volume basis. This yields a primary branch class with a length of 200 cm and a diameter of 1.5 cm and a secondary branch class with a length of 100 cm and a diameter of .75 cm.

The average sizes of each component and their respective orientation functions are given in Table 13. The orientation functions are expressed in terms of θ where 0^o connotes a vertically oriented axis of symetry for a cylindrical element. The orientations of all elements are assumed to be uniformly distributed in azimuth. The functions for inclination angle θ are approximate and based upon visual estimates and not a rigorous series of observations. The functions given in Table 13 are also plotted in Figure 22. The needles are shown to have a spherical distribution. The primary and secondary branches of the spruce trees are assumed to have higher order sin functions which approximate the observed tree profiles. The angular orientation functions for balsam poplar and alder are modeled as those for trembling aspen clones, and approximate the observations of initial and terminal branch angles by Nelson, et al. (1981).

Table 13. Geometry of Crown Layer Components

Specie	Canopy Component	Average Length (cm)	Average Diameter (cm)	Orientation Function
White Spruce	primary branches	113	2.24	$Sin^4\theta$
	secondary branches	57.16	1.04	$Sin^9\theta$
	needles	1.6	0.1	$Sin\theta$
Black Spruce	primary branches	81.3	2.37	$Sin^9(\theta-30)$
	secondary branches	51.17	1.06	$Sin^9\theta$
	needles	0.8	0.1	$Sin\theta$
Balsam Poplar	primary branches	200	1.5	$Sin^9(\theta+60)$
	secondary branches	100	0.75	$Sin^9(\theta+60)$
Alder	primary branches	200	1.5	$Sin^9(\theta+60)$
	secondary branches	100	0.75	$Sin^9(\theta+60)$

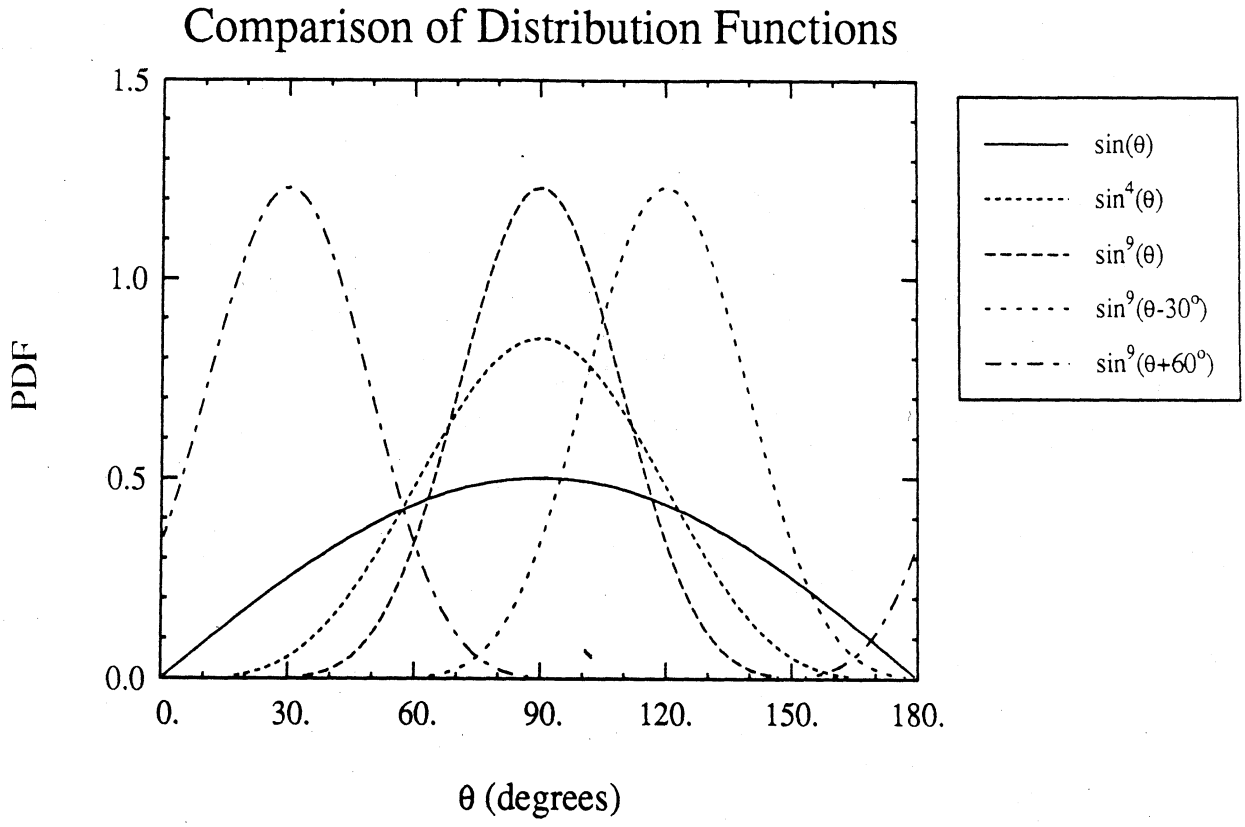

Figure 22: Orientation Distribution Functions for Canopy Elements.

Tree Dielectric Properties

The dielectric properties of canopy elements vary as functions of frequency and canopy component properties such as the dry density of the media and the volume fraction and chemistry of liquids. In additon, environmental conditions exert control over the relative dielectric constant as the relaxation frequency of the liquid fraction is dependent upon temperature; and freezing temperatures may convert the liquid fraction to ice. The dielectric properties of the forest stands at the Bonanza Creek Experimental Forest were determined using a combination of in situ measurements with portable dielectric probes operating at L- and C-bands and dielectric models. The models are based upon destructive sampling determinations of wet and dry biomass, dry density, and temperature.

For white spruce, black spruce and balsam poplar, dielectric measurements were made using the portable dielectric probes fitted with the 0.141 inch diameter coaxial probe tip. These measurements were made at L- and C-bands during both the warm period prior to March 14 and the ensuing period of sub-freezing temperatures. Measurements were made on standing trees by incrementally boring into the trunk and obtaining samples of the relative permittivity at each sample depth.

Examples of the depth profile of L-band permittivity and loss tangent are shown in Figure 23 for white spruce and balsam poplar during both thermal conditions (i.e., thawed and frozen). Depth into the trunk is given on the basis of using the bark surface as a reference. During the thawed conditions, both white spruce and balsam poplar are characterized by a permittivity on the order of 3 for the bark layer. Immediately beneath the bark, the permittivity and the loss tangent are found to increase dramatically to 30 to 40 and 0.35 to 0.4, respectively within the zone containing the phloem and cambium. With increasing depth into the sapwood, the permittivity decreases to an intermediate value of about 10 for

Figure 23. Effect of Temeperature Change Over a 3-day Period on the L-band Dielectric Constant of Tree Trunks

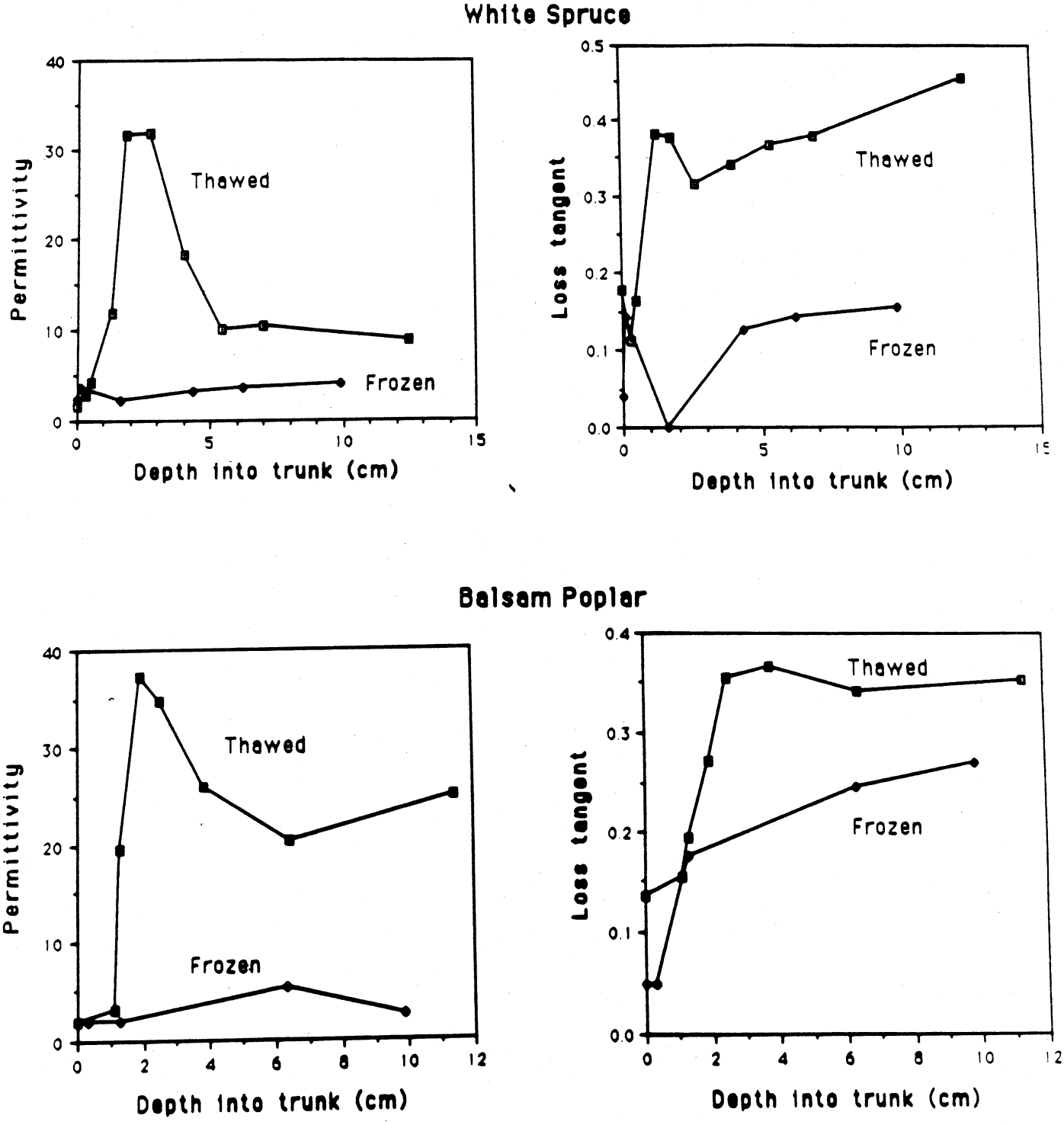

the white sprcue and about 25 for the balsam poplar, and reflects differences in the density and moisture content of the thawed sapwood. The loss tangent of this layer remains nearly constant at 0.35 to 0.45. In contrast, the relative permittivity of the trunks are nearly constant with depth during freezing conditions with air and trunk tempeatures of approximately -15°C. In addition, the loss tangent is found to be much lower for the frozen conditions; indicating that most, but not all, of the liquid fraction is frozen. A similar relationship was observed at C-band.

A somewhat different behavior was observed for the dielectric properties of black spruce trunks which tend to contain much smaller volume fractions of liquids. Figure 24 shows measured values of the C-band relative dielectric constant as a function of depth increment into the bole (trunk) for both frozen and thawed conditions. The depth profile for the thawed conditions is found to be much lower than that observed for the more moist white spruce and balsam poplar trees. With the exception of the bark layer, the effect of freezing is to reduce ε^* by a factor of 2 to 4 depending upon depth.

The depth profile of ε^* at L-band for an aspen tree is shown in Figure 25 for a thawed condition. It is somewhat similar in form to that observed for the balsam poplar in Figure 23 but with a much lower peak value just beneath the bark. The increase in ε' from about 7 at a 5 cm depth to $\varepsilon' > 20$ at greater depths corresponds to a wet, rotted zone in the tree. Liquid exudate from this zone was found to yield $\varepsilon = 58.6 - j12.8$.

In summary, for the thawed conditions prevalent March 11 and 13, all of the tree species are shown to have depth dependent dielectric profiles which are somewhat unique for each specie. In contrast, the dielectric profiles are relatively constant with depth for the frozen conditions existant during SAR overpasses after March 14. Since the current version of MIMICS assumes the trunks to be uniform dielectric cylinders,

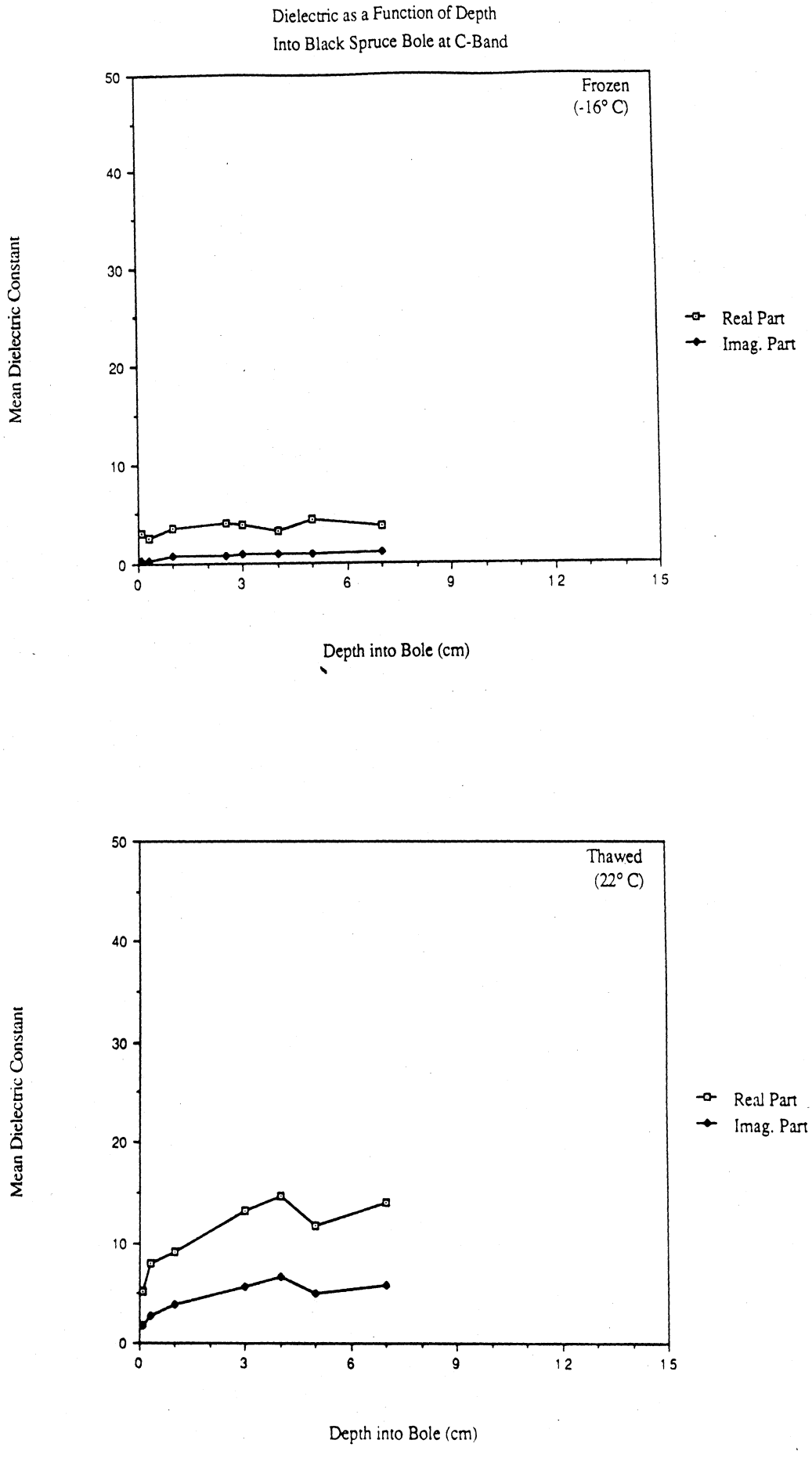

Figure 24: C-band Dielectric Profiles for Black Spruce Trunks with Frozen and Thawed Conditions.

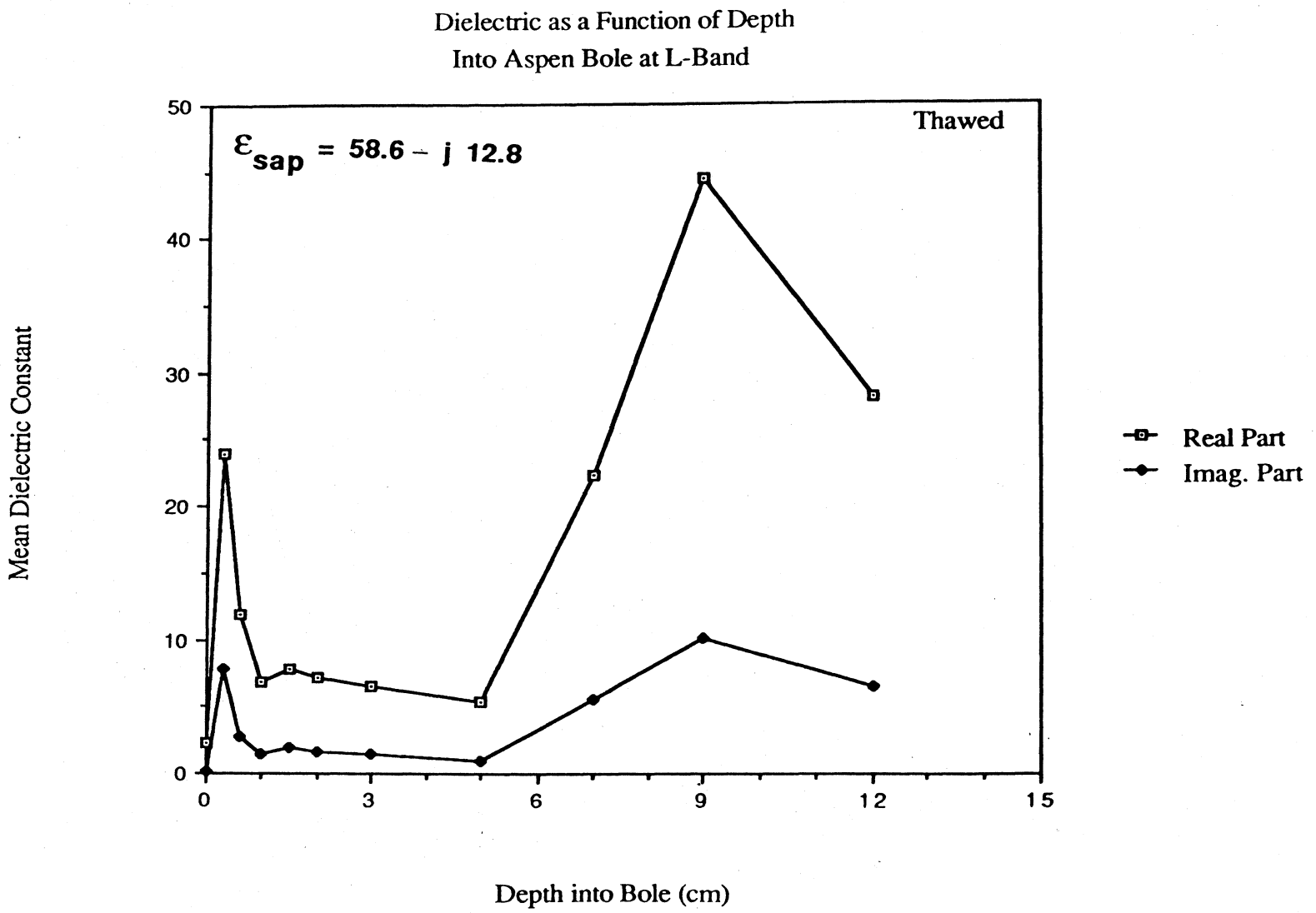

Figure 25: Typical L-band Dielectric Profile for an Aspen Trunk at above Freezing Temperatures.

it is necessary to calculate effective trunk dielectrics. It can be shown that for a medium comprised of dielectric layers which are thin relative to wavelength in the medium, it is appropriate to calculate an effective average value of the relative dielectric constant (Sarabandi, 1989). For the Alaskan stands, it is assumed that this layer is the outer 5 cm of the trunks or branches.

The above assumption is required to extend the measured values of ε^* at L- and C-bands for the tree trunks (1) to other frequencies such as X-band and (2) to the branches which were not well characterized by field observations. This extension is accomplished via use of field observations of wet and dry biomass for the branches and needles coupled with a dielectric model which is verified against the ε^* measurements for the trunks at L- and C-bands. The dielectric model is that developed by El-Rayes (1986) for use with vegetation as modified to account for the effects of freezing temperatures on the liquid fraction in the plant material. The model treats the net relative dielectric constant of the vegetation ε_v as the linear sum of three components, two of which are dispersive

$$\varepsilon_v = \varepsilon_r + V_f\varepsilon_f + V_b\varepsilon_b \qquad (21)$$

where ε_r is a residual non-dispersive component primarily dependent upon the nature and density of the plant's solid material, V_f is the volume fraction of free water in the plant, V_b is the volume fraction of bound water, ε_f is the complex dielectric constant of free water, and ε_b is the complex dielectric contant of bound water. ε_r is independent of frequency f and temperature T, whereas ε_f and ε_b are both dependent upon f and T.

El-Rayes and Ulaby (1987) suggest that ε_r can be approximately related to moisture and density of the plant material by the empirically generated relationship

$$\varepsilon_r = 1.7 + 3.2M_v + 6.5\ M_v^2 \qquad (22)$$

where M_v is the water volume fraction determined from low temperature drying of the plant material at 70°C. Furthermore, V_f and V_b can also be found from empirical relationships with M_v as

$$V_f = M_v (0.82 M_v + 0.166) \quad (23)$$

$$V_b = 31.4 M_v^2 / (1 + 59.5 M_v^2) \quad (24)$$

The dielectric constant of free water ε_f is taken to be $\varepsilon_f = 3.15$ for $T \leq 0^oC$ as this water becomes ice; and for $T > 0^o$, ε_f is determined by a Debye equation.

$$\varepsilon_f = \varepsilon_{f\infty} + \frac{\varepsilon_{fo} - \varepsilon_{f\infty}}{1 + j2\pi f \tau_f} + \frac{\sigma}{j2\pi\varepsilon_o f} \quad (25)$$

where $\varepsilon_o = 8.854 \times 10^{-12}$; $\varepsilon_{f\infty} = 4.9$ and is independent of temperature and salinity; and ε_{fo}, τ_f and σ are functions of both temperature $T(^oC)$ and salinity $S(^o/_{oo})$ of the free water.

$$\varepsilon_{fo} = \varepsilon_{fo}(T, 0)\, a(T,S) \quad (26)$$

$$\varepsilon_{fo}(T,0) = 87.134 - 1.949\times10^{-1}T - 1.276\times10^{-2}T^2 + 2.491\times10^{-4}T^3 \quad (27)$$

$$a(T,S) = 1.0 + 1.613\times10^{-5}TS - 3.656\times10^{-3}S + 3.21\times10^{-5}S^2 - 4.232\times10^{-7}S^3 \quad (28)$$

$$\tau_f(T,S) = \tau_f(T, 0)\, b(T, S) \quad (29)$$

$$2\pi\tau_f(T, 0) = 1.1109\times10^{-10} - 3.824\times10^{-12}T + 6.938\times10^{-14}T^2 - 5.096\times10^{-16}T^3 \quad (30)$$

$$b(T,S) = 1.0 + 2.282\times10^{-5}TS - 7.638\times10^{-4}S - 7.76\times10^{-6}S^2 + 1.105\times10^{-8}S^3 \quad (31)$$

$$\sigma(T,S) = \sigma(25, S)e^{-\Phi} \quad \text{for } 0 \leq S \leq 40\ ^o/_{oo} \quad (32)$$

$$\sigma(25, S) = S\,[0.18252 - 1.4619\times10^{-3}S + 2.093\times10^{-5}S^2 - 1.282\times10^{-7}S^3] \quad (33)$$

$$\phi = (25-T)\,[2.033\times10^{-2}+1.266\times10^{-4}(25-T) + 2.464\times10^{-6}(25-T)^2 - S[1.849\times10^{-5} - 2.551\times10^{-7}\,(25-T) + 2.551\times10^{-8}(25-T)^2]] \quad (34)$$

Solving (26) to (34) for the thawed conditions (T = 5°C) assuming S = 8.5% as found by Ulaby and El-Rayes (1987) for various plant material yields: ε_{fo} = 83.439, the relaxation frequency $f_o = 1/2\pi\tau_f$ = 10.744×10^9, and the conductivity σ = 0.9086. Substituting these values into (25) and solving at the SAR center frequencies of 1.25, 5.3, and 9.6 GHz yields the following values of ε_f at 5°C: 82.39-j22.08 (1.25 GHz), 68.07-j34.24 (5.3 GHz), and 48.57-j40.72 (9.6 GHz).

In a similar fashion, the dielectric constant ε_b of the bound water fraction is given by a Debye-like dispersion

$$\varepsilon_b = \varepsilon_{b\infty} + \frac{\varepsilon_{bo} - \varepsilon_{b\infty}}{1 + (j2\pi f \tau_b)^{1-\alpha_b}} \quad (35)$$

where the temperature dependence of dielectric constant of the bound water fraction is empirically determined by El-Rayes (1986) as

$$\varepsilon_{bo} = 35.461 + 0.262\,T \quad (36)$$

$$\varepsilon_{b\infty} = 6.457 - 0.146\,T \quad (37)$$

$$\alpha_b = 0.207 + 0.007\,T \quad (38)$$

$$f_{ob} = \frac{1}{2\pi\tau_b} = 1.296\,(273+T)\exp\left(\frac{-1882.238}{273+T}\right) \quad (39)$$

Solving (36) to (39) at the Alaskan SAR ambient temperatures of +5°C (thawed) and -10°C (frozen) yields the values in Table 14.

The relaxation frequency of the free water at 5°C was found to be 10.74 GHz whereas that of the bound water is only 415 MHz at 5°C and decreases to 267 MHz at -10°C. Substitution of these values into (35) and solving at L-, C- and X-bands shows that (1)

Table 14 Effects of Temperature on the Dielectric Properties Calculated for Bound Water

$$\epsilon_b = \epsilon_{b\infty} + \frac{\epsilon_{bo} - \epsilon_{b\infty}}{1 + (j2\pi f \tau_b)^{1-\alpha_b}}$$

	Temperature	
	+5°C	-10°C
ϵ_{bo}	36.771	32.841
$\epsilon_{b\infty}$	5.727	7.917
α_b	.242	.137
$\frac{1}{2}\ \pi\ \tau_b$	.415	.267
ϵ_b at 1.25 GHz	14.3 - j 9.0	11.35 - j 6.29
ϵ_b at 5.3 GHz	7.79 - j 3.7	8.44 - j 1.78
ϵ_b at 10.6 GHz	6.87 - j 2.31	7.93 - j 0.63

for the thawed conditions (T=5°C) ε_b decreases from 14.3 - j9.0 at L-band to 6.9 - j2.3 at X-band and (2) for the frozen conditons (T=-10°C) ε_b is reduced to 11.35-j6.3 at L-band and 7.93 - j0.6 at X-band.

The volume fractions V_f and V_b and the non-dispersive component of (21) are determined from the densities and moisture contents of the canopy components as determined via destructive sampling. These values are given in Table 15 for the various tree species and canopy component elements. For trunks, these values are based upon the outer 5 cm of the bole and include the bark.

For the thawed conditions, the values of ε_v predicted by the dual-dispersion model (21) compare very favorably to the measured values of ε using the dielectric probes at L- and C-bands on the trunk layer. These estimates are listed in Table 16. However, at $T \leq$ -10°C, this model predicts values of ε_v which are considerably greater than those observed for the boles of frozen trees with temperatures ranging from -10°C to -20°C. The dielectric model of El-Rayes (1986) is based upon the temperature dependence of corn leaves which are modelled to have a bound water fraction consisting of a sucrose solution. Hence, the temperature dependence of ε_b is primarily that of a sucrose solution. This model may not be entirely appropriate for winter-hardened trees in the boreal forest. During the winter period, photosynthesis is low and the production of photosynthate and subsequent conversion to sucrose for transport throughout the tree is at a minimum. The relative volume fractions of wood solids, bound water, and free water are shown in Figure 26 for a spruce tree (Zimmerman and Brown, 1971). The bound water fraction V_b is shown to be on the order of 12%. This value of V_b is much lower than that estimated by the model although the two are not directly comparable since the value estimated by (24) is based upon an assumed sucrose concentration with the ratio of six water molecules being bound by each sucrose molecule.

Table 15 Average Values of Density and Moisture Determined from Destructive Sampling and Estimates of ϵ_r and the Volume Fractions V_f and V_b Used to Calculate Dielectric Properties of the Canopy.

Specie	Canopy Component	Density $\left(g / cm^3\right)$	M_v (cm^3/cm^3)	ϵ_r	V_f	V_b 5°C	V_b -15°C
White Spruce	Trunk	.37	.508	5.003	.296	.495	.247
	Primary Branches	.37	.49	4.829	.278	.493	.246
	Secondary Branches	.40	.29	3.175	.117	.440	.220
	Needles	.30	.335	3.50	.148	.459	.229
Black Spruce	Trunk	.363	.186	2.520	.059	.355	.177
	Primary Branches	.359	.215	2.688	.074	.387	.193
	Secondary Branches	.356	.238	2.838	.086	.407	.203
	Needles	.30	.280	3.106	.111	.435	.217
Balsam Poplar	Trunk	.347	.444	4.402	.235	.486	.243
	Primary Branches	.365	.444	4.402	.235	.486	.243
	Secondary Branches	.365	.444	4.4-2	.235	.486	.243

NOTE: For frozen conditions ($T \leq -15°$) $V_b(-15°C) = V_b(+5°C)/2$

Table 16. Values of the Relative Dielectric Constant Estimated by the Modified Dual - Dispersion Model for the Outer 5 cm of the Trunk at L- and C- bands.

Specie	Frequency	ε_v	
		+5°C	-15°C
White spruce	1.25	36.47-j10.99	5.19-j1.09
	5.3	29.01-j11.97	4.85-j0.32
Black spruce	1.25	12.46-j4.50	3.72-j0.78
	5.3	9.30-j3.33	3.47-j0.23
Balsam poplar	1.25	30.71-j9.56	4.95-j1.07
	5.3	24.18-j9.85	4.61-j0.32

Note: model for T = -15°C is given by

$\varepsilon_v = \varepsilon_r + V_f\varepsilon_s + V_b(-15°C)\,\varepsilon_b$

where $V_b\,(-15°) = V_b\,(+5°C)/2$

$\varepsilon_r = 1.7$

$e_s = 3.15 - j0$

$\varepsilon_b = 10.32-j4.39$ at 1.25 GHz

$8.94-j1.31$ at 5.3 GHz

$8.78-j.071$ at 9.6 GHz

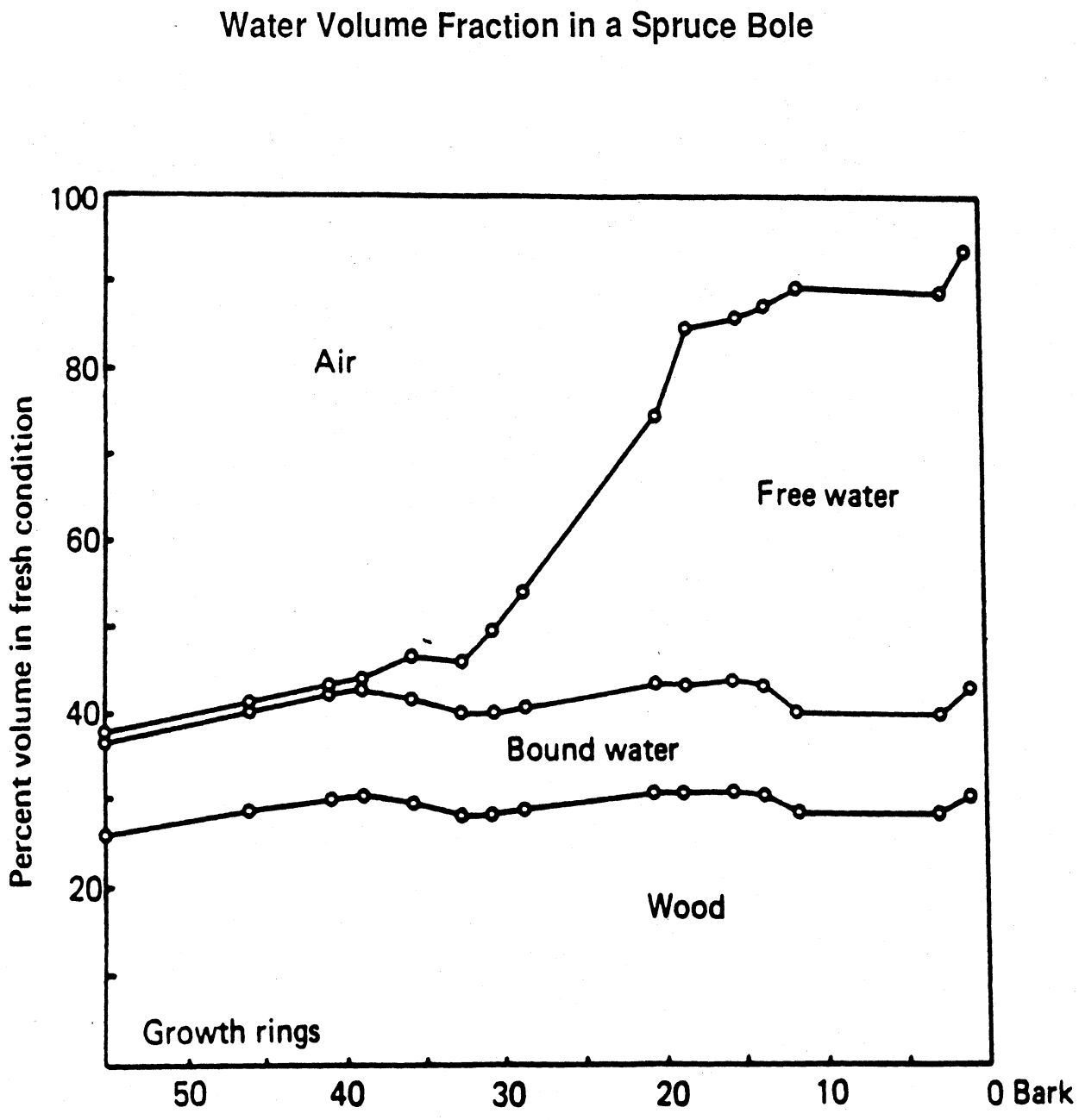

Figure 26. Volume Apportionment of Constituent Parts of a Spruce Trunk (from Zimmerman and Brown, 1971).

Since it is well known that sucrose production is limited by freezing conditions (Zimmerman and Brown, 1971), it is not unreasonable to presume that V_b decreases at temperatures below freezing. If we let

$$V_b(-10^oC) \approx \frac{V_b(+5^oC)}{2} \qquad (40)$$

and set ε_r = 1.7 (since M_v = 0 for frozen conditions) and ε_f = 3.15-j0 for ice, then the estimated values of ε_v using (21) do compare very favorably with those observed for the frozen tunks as shown in Figures 23 and 24. These values of ε_v are given in Table 16 and are those used by MIMICS. The dielectric constant of alder trunks was not measured, nor were alder trees destructively sampled for determination of densities and moisture contents of the canopy components. Therefor, it is assumed that the dielectric values of ε_v determined for balsam poplar can be used to represent conditions in the alder stand.

3.2.2 SAR Observations

The dates and times of the various SAR overpasses of the Bonanza Creek Experimental Forest are listed in Table 3. Of the flights by the NASA/JPL SAR, only the L-band polarimetric data obtained on March 13 and 19 has been processed and calibrated for use by this study. For the ERIM/NADC SAR, two flights occurred on March 22 with a total of six passes. No L-band data were collected by the ERIM/NADC SAR over the forest site due to transmitter problems. Hence, there is no direct comparison between the two SAR data sets. Since the ERIM/NADC SAR uses a four channel recorder, a strategy was persued to obtain polarimetric data with three X-band passes at $\theta = 29^o$, 55^o and 56^o at the center of the site (Seven Mile Island) and one polarimetric pass at C-band with $\theta = 56^o$. The

remaining two passes were used to obtain simultaneous C- and X-band like - polarized data with $\theta = 35^o$ and 49^o. However, the pass at 19:38 with $\theta = 49^o$ was acquired with variable attenuator settings on the SAR, and this data is not useable in the present analysis. Details of the SARs and the data collections are given in Cimino, et al. (1990) and Kasischke, et al. (1989).

Canopy Extinction Data

The primary objectives for the C- and X-band passes by the ERIM/NADC SAR were (1) to obtain estimates of the two-way extinction by the frozen forest canopies using observations of the trihedral corner reflectors and (2) to obtain estimates of the average backscattering coefficient σ^o for the stands containing the reflectors as well as for other large area-extended stands for comparison to MIMICS simulations. The extinction measurements were performed by comparing the point target responses of the SAR for the trihedral reflectors under the forest canopies to those for the reflectors placed in the open on a sandbar. The background clutter was removed for each target response and the image intensity was then normalized to correct for known effects such as range fall-off and antenna variations. It is estimated that the errors associated with this process and with alignment uncertainties for the trihedral reflectors produce a confidence interval of $\pm$ 1 dB associated with each extinction measurment. The canopy extinction coefficients are detailed in Kasischke, et al. (1989) and are summarized in Table 17.

Since each extinction measurement represents a discrete realization of what is arguably a random process, it is beneficial to briefly consider the conditions existent within the test stands. Three stands were selected for deployment of the reflector arrays (1) an alder stand containing even aged alders, (2) a stand of balsam poplars containing a variable density of

Table 17 Measured Values of One-Way Propagation Loss Through the Canopy From ERIM/NADC SAR Observations of Trihedral Corner Reflectors at Incidence Angles of 36° and 56°.

One - Way Propagation Loss (dB)

		C-Band					X-Band			
	Reflector Size (cm)	H		V			H		V	
Stand		36°	56°	36°	56°		36°	56°	36°	56°
Alder	60	2.28	3.87		6.19		4.32	4.15	4.54	7.07
	60	.38	4.92	.06			1.40	3.58	2.31	5.31
	60	.65	6.01	1.88			3.18		4.48	
	60		5.44		4.98					
	Mean	1.10	5.06	.97	5.59		2.96	3.87	3.78	6.19
	Standard Dev.	0.84	.79	.91	.60		1.20	.28	1.04	.88
Balsam Poplar	60	.00	2.96	0.0	3.65		1.77	2.02	3.20	4.42
	60		4.07	2.95	4.11			3.78		5.25
	60	.93		.27	5.23		4.66	4.26	6.78	5.95
	60	.63		.97			1.62	6.04	1.67	6.75
	120	.45	6.31	.13	6.45		3.24	6.04	3.42	6.99
	120	5.21	7.91	5.20	8.68		6.89	5.86	7.24	6.82
	120	.68	6.23	.27	7.79		3.04	5.82	3.40	7.29
	Mean	1.32	5.50	1.40	5.99		3.54	4.83	4.28	6.21
	Standard Dev.	1.76	1.76	1.82	1.84		1.81	1.43	2.02	.97

White Spruce	120	3.71	5.94	3.20	5.35		6.11	6.24	5.61	7.26
	120	1.37	10.05	.23	9.02		3.23	7.21	3.17	8.79
	60			1.89			4.70	5.57	5.74	5.75
	60						3.65		4.20	
	120	1.48	4.08	.79	4.05		1.76	3.32	2.46	3.82
	90	2.97	9.45	2.76	9.12		2.87	9.86	3.61	9.61
	90	1.64	6.46	2.65	7.11		2.34	6.99	3.55	8.25
	60	2.63		2.24	6.22		1.02	6.81	2.93	6.35
	60	0.0		.87	5.79		.48	5.77	1.24	5.52
	Mean	1.97	7.19	1.83	6.67		2.91	6.47	3.61	6.92
	Standard Dev.	1.14	2.24	1.01	1.74		1.67	1.72	1.35	1.80

shorter alder trees and (3) a white spruce stand containing a variable mixture of both alders and balsam poplars. At each reflector site, the stand statistics of tree type, location, diameter and height were tabulated for the area around the reflector as shown in Figure 27 and used to subdivide the stand characteristics into those for the stand as a whole as well as those in the 90° quadrant between the reflector and the SAR as shown in Figure 28. Tabular summaries of these data (Kasischke, et al., 1989) reveal considerable local variance in the stand characteristics, both locally in azimuth around a specific target as well as generally in comparing different targets within each of the three stands. Table 18 illustrates this within stand variance in terms of the relative tree densities, diameters and heights as summarized for each specie.

For the four reflectors placed within the single-specie stand of alders, the average one-way propagation loss through the canopy (from Table 17) at C-band was found to increase from about 1 dB at $\theta = 36^{o}$ to 5 dB at $\theta = 56^{o}$. For X-band, the average one way propagation loss by the alders was found to increase from about 3 dB at $\theta = 36^{o}$ to 4 dB for HH polarization and 6 dB for VV polarization at $\theta = 56^{o}$.

There were seven reflectors placed within the balsam poplar stand. This stand contained both alders and balsam poplars and is characterized by considerable spatial variance in the number densities of the two tree species (see Table 18). This is evident in the larger standard deviations associated with the average extinction values given in Table 17 when compared to those obtained for the more uniform alder stand. Figure 29 shows average canopy extinction of the balsam poplar stands to be greater than that observed for the alder stands. At C-band, a mean value of about 1.4 dB at $\theta = 36^{o}$ increases to >5.5 dB at $\theta = 56^{o}$. At X-band, a mean value of about 4 dB at $\theta = 36^{o}$ increases to >5 dB at $\theta = 56^{o}$ depending upon polarization.

Nine reflectors were emplaced within the white spruce stand. This stand is also a mixed-specie stand (see Table 18)

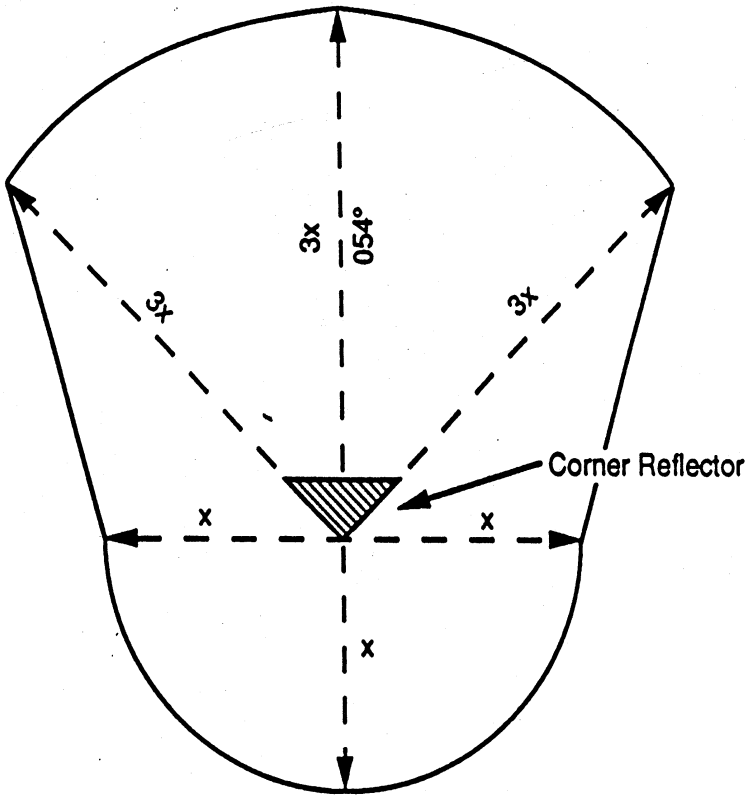

Figure 27: Location of Area Surrounding a Corner Reflector Included in Survey of Trees.

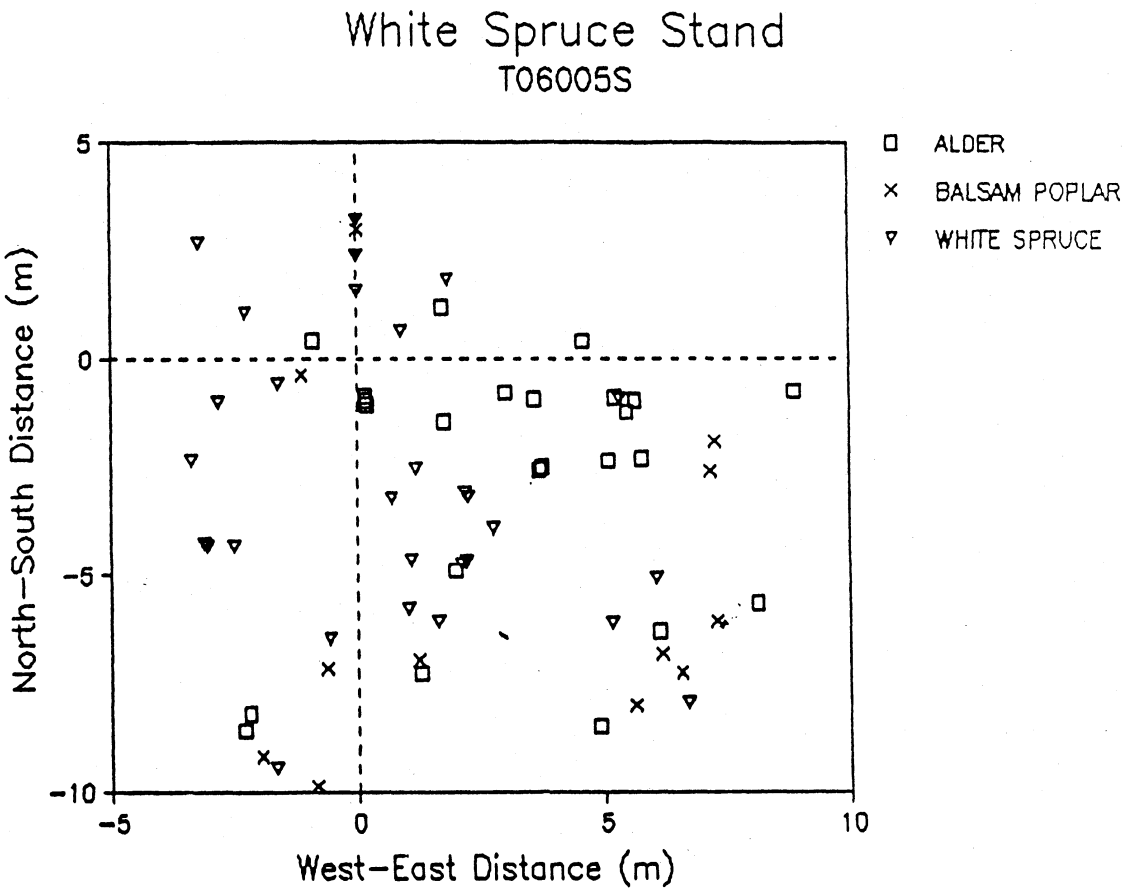

Figure 28: Example of Plot of Locations of Trees Surrounding a Corner Reflector in the White Spruce Stand.

Table 18. Stand Characterizations for Boresight Quadrant of Each Trihedral Corne Reflector.

TARGET	TREE SPECIES	STEMS/HA	AVG DBH	AVG HT	BA/HA
T06017A	ALDER	18333	6.09 (1.46)	6.32 (.83)	56.50
T06020A	ALDER	17778	7.00 (1.89)	6.84 (1.07)	73.99
T06018A	ALDER	30000	5.78 (1.49)	6.15 (.84)	84.03
T06076A	ALDER	40000	5.49 (1.72)	5.98 (.98)	47.69
T06026P	ALDER	1375	8.13 (1.44)	7.47 (.81)	7.36
	BALSAM POPLAR	1250	8.49 (1.60)	11.84 (1.80)	7.33
T06008P	ALDER	1125	5.38 (1.46)	5.92 (.83)	2.74
	BALSAM POPLAR	3125	10.64 (3.33)	12.62 (2.16)	30.51
T06006P	ALDER	476	5.43 (.29)	5.95 (.16)	1.11
	BALSAM POPLAR	2540	8.86 (4.02)	11.00 (2.95)	18.89
T06021P	ALDER	1665	6.59 (2.50)	6.60 (1.41)	6.49
	BALSAM POPLAR	1905	11.50 (5.22)	12.34 (3.60)	23.87
T12201P	ALDER	606	5.63 (2.22)	6.06 (1.26)	1.75
	BALSAM POPLAR	1313	11.85 (4.17)	13.71 (2.18)	16.28

*Numbers in parentheses are standard deviations.

Table 18. (continued)

TARGET	TREE SPECIES	STEMS/HA	AVG DBH	AVG HT	BA/HA
T12202P	ALDER	2063	4.28 (0.95)	5.29 (0.54)	3.11
	BALSAM POPLAR	4286	11.55 (4.34)	12.95 (2.73)	51.26
T12203P	ALDER	273	7.50 (0.73)	7.12 (0.42)	1.22
	BALSAM POPLAR	1091	14.66 (4.91)	14.45 (2.71)	20.48
T12201S	ALDER	0	.00 (0)	.00 (0)	.00
	BALSAM POPLAR	600	11.40 (3.89)	12.80 (2.26)	6.84
	WHITE SPRUCE	2200	10.45 (4.72)	10.86 (3.86)	22.70
T12202S	ALDER	938	6.55 (2.10)	6.58 (1.19)	3.48
	BALSAM POPLAR	1250	11.54 (3.32)	13.35 (2.22)	14.15
	WHITE SPRUCE	469	15.60 (2.86)	15.10 (1.82)	9.26
T06005S	ALDER	2333	5.66 (3.37)	6.08 (1.91)	7.88
	BALSAM POPLAR	778	9.29 (3.74)	11.63 (2.81)	6.12
	WHITE SPRUCE	1556	8.32 (3.99)	9.17 (3.61)	10.40

*Numbers in parentheses are standard deviations.

Table 18. (continued)

TARGET	TREE SPECIES	STEMS/HA	AVG DBH	AVG HT	BA/HA
T06011S	ALDER	947	6.73 (4.77)	6.69 (2.70)	4.81
	BALSAM POPLAR	1900	8.03 (4.04)	10.30 (3.94)	11.42
	WHITE SPRUCE	1700	7.28 (3.80)	8.23 (2.72)	9.01
T12203S	ALDER	1375	5.77 (1.96)	6.14 (1.11)	4.02
	BALSAM POPLAR	750	10.85 (2.82)	12.75 (1.48)	7.40
	WHITE SPRUCE	1500	7.36 (4.49)	8.25 (3.96)	8.75
T09101S	ALDER	1647	6.41 (2.24)	6.50 (1.27)	5.97
	BALSAM POPLAR	2235	8.69 (3.52)	11.26 (2.73)	15.45
	WHITE SPRUCE	4235	5.62 (2.38)	6.72 (2.15)	12.37

*Numbers in parentheses are standard deviations.

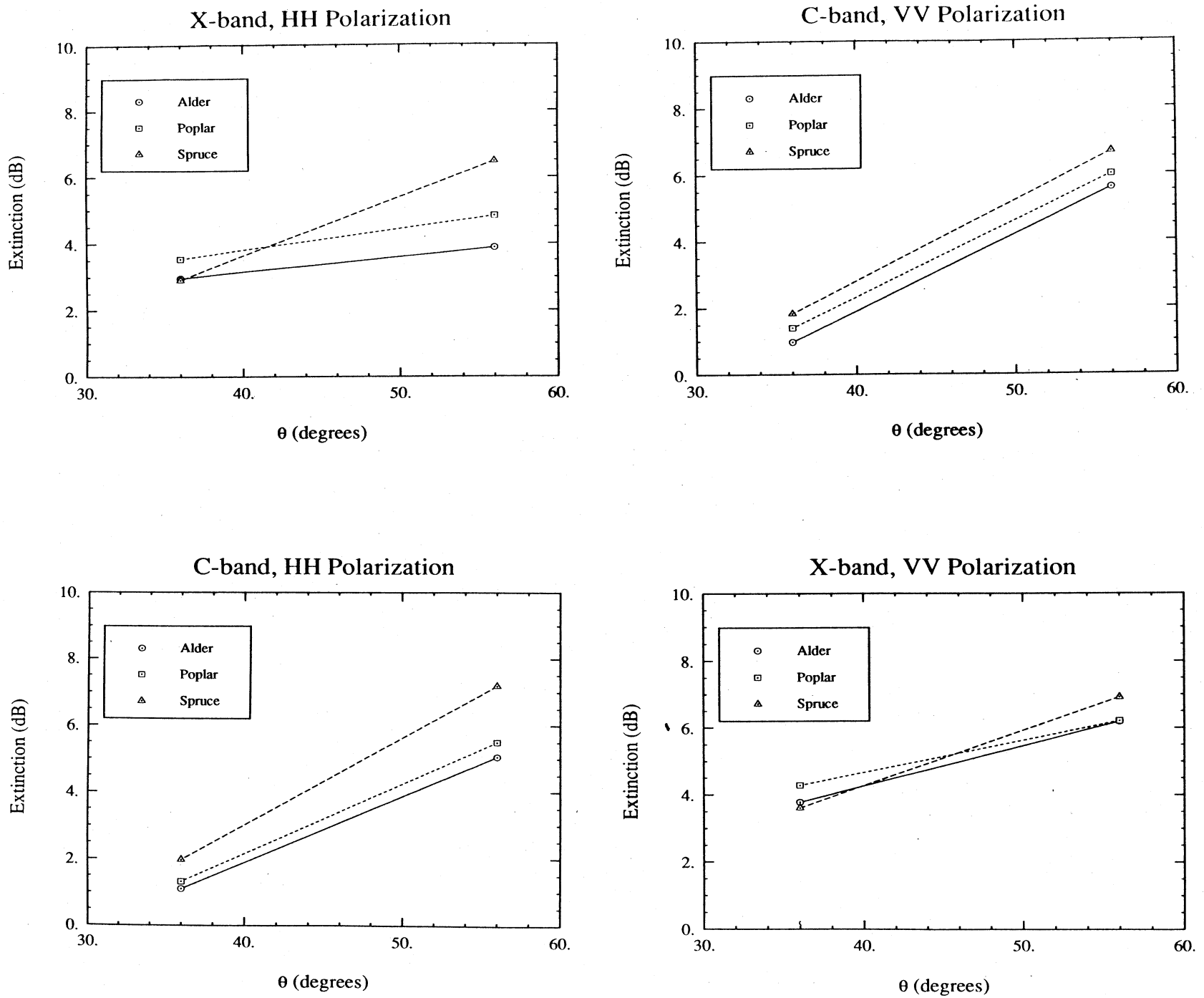

Figure 29. Average Measured One-way Canopy Extinction as a Function of Incidence Angle at C- and X-bands.

containing variable densities of alder, balsam poplar and white spruce. Consequently, there is a considerable amount of variance in the extinction data as seen in Table 17. Figure 29 shows the white spruce to generate the highest extinction of the three stands at C-band with average values increasing from about 2 dB at $\theta = 36^{o}$ to 7 dB at $\theta = 56^{o}$. For X-band, the average extinction is observed to increase from about 3 dB at $\theta = 36^{o}$ to >6.5 dB at $\theta = 56^{o}$.

In considering these data, there are several points worth noting. First, the sample size of the data is small with sample sizes ranging from four to nine reflectors per stand. Second, there is an inherent bias in the experimental procedure toward observation of low (0 dB) extinction due to the logistics of emplacing physically large reflectors within a discontinuous medium of large, discrete objects such as trees. Ideally, one would like to have an infinitely small physical target of large radar cross section which could be placed at a statistically significant number of completely random sample locations within a given stand of trees. Finally, there are errors associated with target positioning and the measurement extraction process estimated to be on the order of $\pm$ 1 dB.

Backscatter Data

In addition to the extinction measurements using the NADC/ERIM SAR, the image data was also segmented for extraction of the average backscattered power from large single-specie forest stands. These values were obtained through spatial averaging of the return from a given stand. Since the antenna gain pattern contains ripples which are not fully characterized, the data cannot be considered fully calibrated in absolute level. This limits valid comparisons of the data to those comparing stands at a common range (θ) within a given pass. Comparisons of a given stand from pass-to-pass (i.e., at different incidence angles) are only approximate as each pass may have different biases. In a similar fashion,

comparisons between frequencies can only be considered relative. Hence, data comparisons to MIMICS predictions are restricted to those comparing relative backscatter between those stands at a common range location on a given SAR pass. The data are listed in Table 19 (Kasischke, 1989).

Since the JPL airborne SAR utilizes a patch antenna design with separate antenna for each frequency, the antenna pattern is relatively smooth; and consequently, it is easier to correct the SAR data for antenna gain variations. The 2 passes of L-band data are calibrated on the basis of SAR point target response to trihedral corner reflectors, 182 cm in size, located at the Fairbanks International Airport. The calibration methodology also uses the assumption that the like-and cross-polarized components of the backscatter from azimuthally symetric distributed targets are uncorrelated (Klein, 1989). The calibration matrix derived for the SAR scene containing the airport is then assumed to be valid for the scene containing the Bonanza Creek Experimental Forest some 20 km away.

The L-band polarimetric SAR data were then segmented and backscatter values extracted for rectangular windows centered over the forest stands of interest at the Bonanza Creek Test Site. The same rectangular windows were used to segment the imagery for both dates (March 13 and March 19). The resultant σ^0 values are given in Table 20 for both the thawed canopy conditions on March 13 and the frozen canopy conditions on March 19.

4.0 Model Validation for Canopy Extinction

The values of canopy propagation loss measured by the ERIM/NADC SAR for frozen tree conditions on March 22, 1988 are listed in Table 17. The averages of these values by stand are plotted versus angle of incidence in Figure 29. In order to validate MIMICS using these observations, the MIMICS model was initialized for the local stand conditions surrounding each of the 20 trihedral corner reflectors distributed within the

Table 19. Relative Backscatter Measured by the ERIM/NADC SAR for Passes on March 22, 1988.

Site	Specie(s)	Band	Incidence Angle	σ^o (dB) HH	σ^o (dB) VV
Corner reflector/ Alder	Alder	C	36°	-18.56	-19.08
			57°	-20.18	-19.28
		X	31°	-11.72	-12.38
			36°	-13.11	-15.54
			57°	-15.33	-15.17
Corner reflector/ Balsam poplar	Balsam poplar and alder	C	36°	-16.77	-11.83
			57°	-17.52	-18.68
		X	31°	-10.99	-11.73
			36°	-13.36	-14.98
			57°	-15.21	-15.5
Corner reflector/ White Spruce	White spruce, balsam poplar and alder	C	36°	-15.24	-14.88
			57°	-17.42	-19.27
		X	31°	-9.47	-13.91
			36°	-13.3	-14.62
			57°	-15.37	-16.34
WS-1	White spruce	C	27°	-14.03	-15.98
			31°	-12.75	-14.79
			53°	-15.78	-22.87
			55°	-17.64	-21.68
		X	27°	-5.88	-17.17
			31°	-9.5	-12.81
			53°	-7.89	-13.83
			55°	-10.19	-14.63
WS-2	White spruce	C	27°	-12.96	-15.36
			31°	13.85	-15.36
			53°	-16.64	-23.27
			55°	-17.59	-21.38
		X	27°	-6.7	-18.6
			31°	-9.15	-15.26
			53°	-8.76	-13.74
			55°	-10.0	-14.55

Table 19. (cont.)

Site	Specie(s)	Band	Incidence Angle	σ^o (dB) HH	VV
WS-5	White spruce	C			
			53°	-16.53	-23.15
			55°	-16.45	-21.06
		X	25°	-7.99	-11.93
			53°	-9.0	-13.37
			55°	-9.29	-14.08
BS-1	Black spruce	C	31°	-15.67	-15.41
			55°	-18.01	-21.16
		X	31°	-9.93	-16.34
			55°	-11.07	-14.96
BP-2	Balsam poplar	C	27°	-12.24	-15.02
			53°	-17.37	-23.67
		X	27°	-7.2	-16.91
			53°	-9.22	-13.43
Alder	Alder	C	31°	-19.02	-18.49
			55°	-19.36	-19.91
		X	25°	-13.51	-15.17
			31°	-13.33	-16.26
			55°	-12.7	-14.01

Table 20. Backscattering Coefficients Extracted from JPL L-band SAR Imagery Obtained on March 13 and 19, 1988.

Stand	Incidence Angle	Backscattering Coefficient σ^o (dB)					
		March 13			March 19		
		HH	VV	HV	HH	VV	HV
White spruce WS-1	43.1	-10.0	-10.4	-15.2	-13.1	-14.9	-21.0
WS-2	42.7	-8.4	-9.9	-14.2	-11.4	-14.5	-20.4
WS-5	43.5	-8.1	-9.1		-11.1	-14.8	
Black spruce BS-1	44.6	-12.9	-14.4	-20.0	-14.9	-16.4	-23.7
Balsam Poplar BP-2	41.4	-9.2	-10.4		-12.7	-14.8	
Alder	46.0	-8.7	-9.7		-11.3	-14.0	
Clearcut	43.7	-12.6	-13.0		-12.9	-13.7	
Oxbow Lake	50.9	-16.1	-15.7		-15.9	-15.7	
Sandbar A	50	-19.5	-19.3	-30.2	-20.1	-19.8	-32.6
Sandbar B	50	-18.8	-18.5	-28.1	-19.6	-19.5	-31.6

three stands (alder, balsam poplar and white spruce). The enumerated statistics for stand density, dbh and height (from allometric regressions) for the 90° quadrant centered on the SAR viewing direction are used by MIMICS to characterize the average stand conditions for each target. However, the measured extinction values for the SAR represent discrete realizations over only the several degrees required to construct the synthetic aperture over the targets.

For the pure stands of alder which contained four reflectors, MIMICS simulations evaluated only the extinction caused by the trunk layer. The crown layer was ignored since (1) it is estimated to comprise only 10% of the total biomass and (2) the apportionment of the crown biomass into branch size classes using an aspen model may not be a very good approximation.

For the mixed specie stands of balsam poplar (containing seven reflectors) and white spruce (containing nine reflectors), the enumerated stand statistics were subdivided into subpopulations for each specie within the quadrant toward the SAR. Extinction values were then computed by MIMICS for each specie seperately and then summed to provide the net extinciton for all species present in the vicinity of a given reflector. In other words, for each of the seven reflectors in the balsam poplar stand, MIMICS calculated the propagation loss for a sub stand of balsam poplar and a sub stand of alder; the net propagation loss is the sum of the two.

When evaluating the extinction for balsam poplars and white spruce, only the extinction due to the frozen trunk layer was computed. The rationale for this is that (1) the average trunk layer statistics were well characterized by enumerated data, (2) the biomass apportionment equations for the crown layer of branches in balsam poplar is only approximate, and (3) the added time costs of computing crown layer extinctions for the large number of reflectors times N species (when given the limits of the biomass apportionment approximations) was not acceptable. As a consequence, the MIMICS runs for the three

stands containing the corner reflectors only calculated extinction by the trunk layer. However, the expected extinction caused by the crown layers of pure stands of both balsam poplar and white spruce is modeled by MIMICS and is discussed later in this section.

For each of the three stands, MIMICS predictions of the maximum and minimum one-way propagation loss through the trunk layer, as calculated for each reflector in the stand, are plotted versus depression angle for H and V polarizations in Figures 30 and 31 for C-band and X-band, respectively. These results are very encouraging. In all cases, trunk layer extinction is found to decrease smoothly as viewing angle approaches nadir. The extinction is proportional to stand density, height and tree diameter. Hence, those stands with the greatest biomass/ha yield the largest propagation loss through the trunk layer. The extinction calculated at X-band is generally greater than that at C-band. The extinction for V polarization is always greater than that calculated for H polarization with the difference in propagation loss V/H being generally less than 1 dB.

Also shown in Figures 30 and 31 are the measured propagation losses derived from the ERIM/NADC SAR data. If all of the canopy extinction were due to the trunk layer for frozen trees, that is to say that crown layer extinction due to branches and foliage is negligible, then the MIMICS derived curves for the maximum and minimum biomass conditions should bound all of the measured values. At C-band, Figure 30 shows this to be approximately true, but with some notable exceptions. For the alder stand, the measured one-way transmission losses are generally 3 dB less than those predicted by MIMICS; although the general form of the model predictions and the relative polarization effects are well described. This overprediction in magnitude may be related to (1) the large local variance in tree density for the 90^{o} arc considered by MIMICS versus the several degree arc for the SAR and (2) the very high density of the alder stand leads to a sample bias in

Figure 30 One-Way Canopy Loss for the Trunk Layer at C-Band

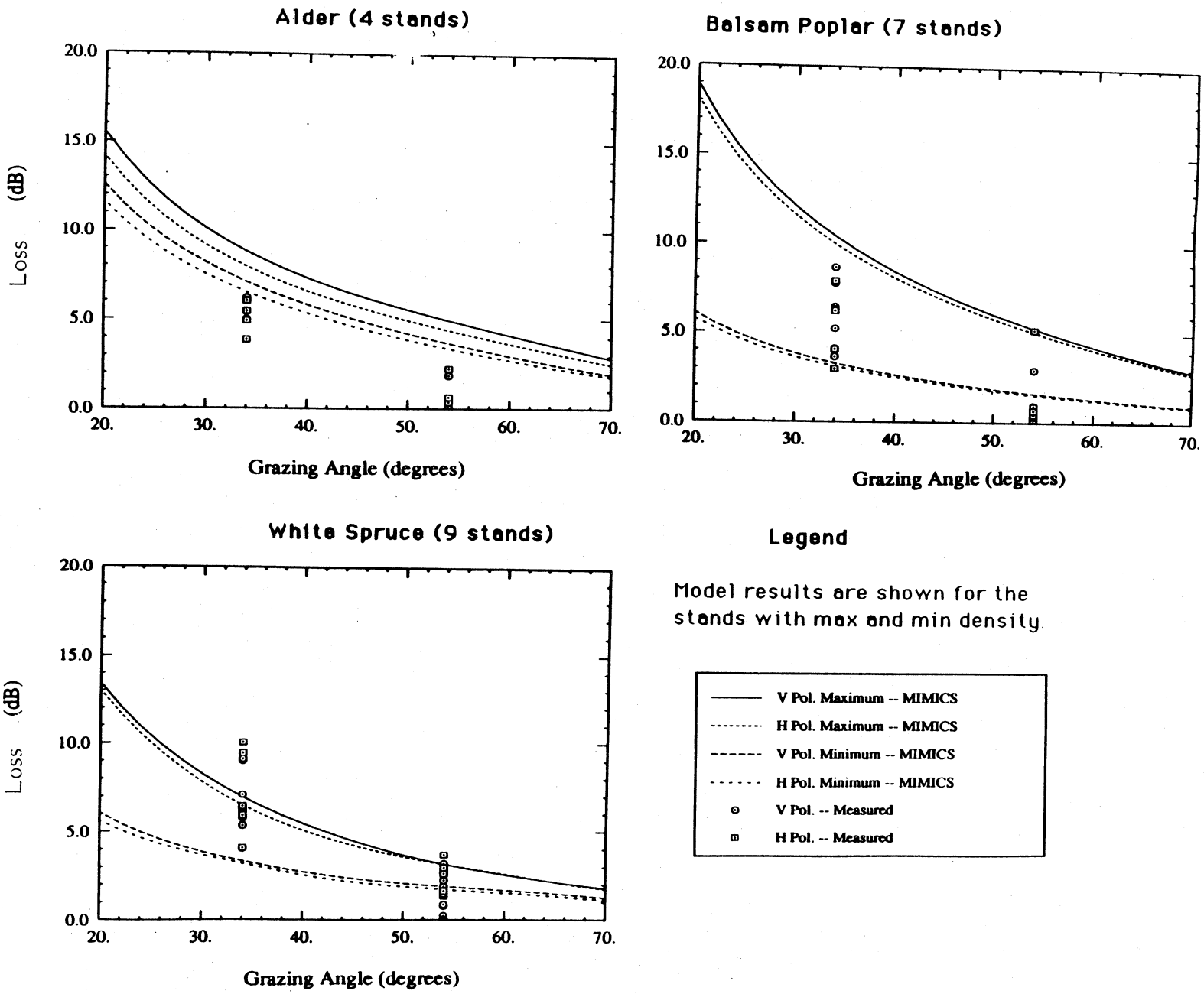

Figure 31: One-Way Canopy Loss for the Trunk Layer at X-band.

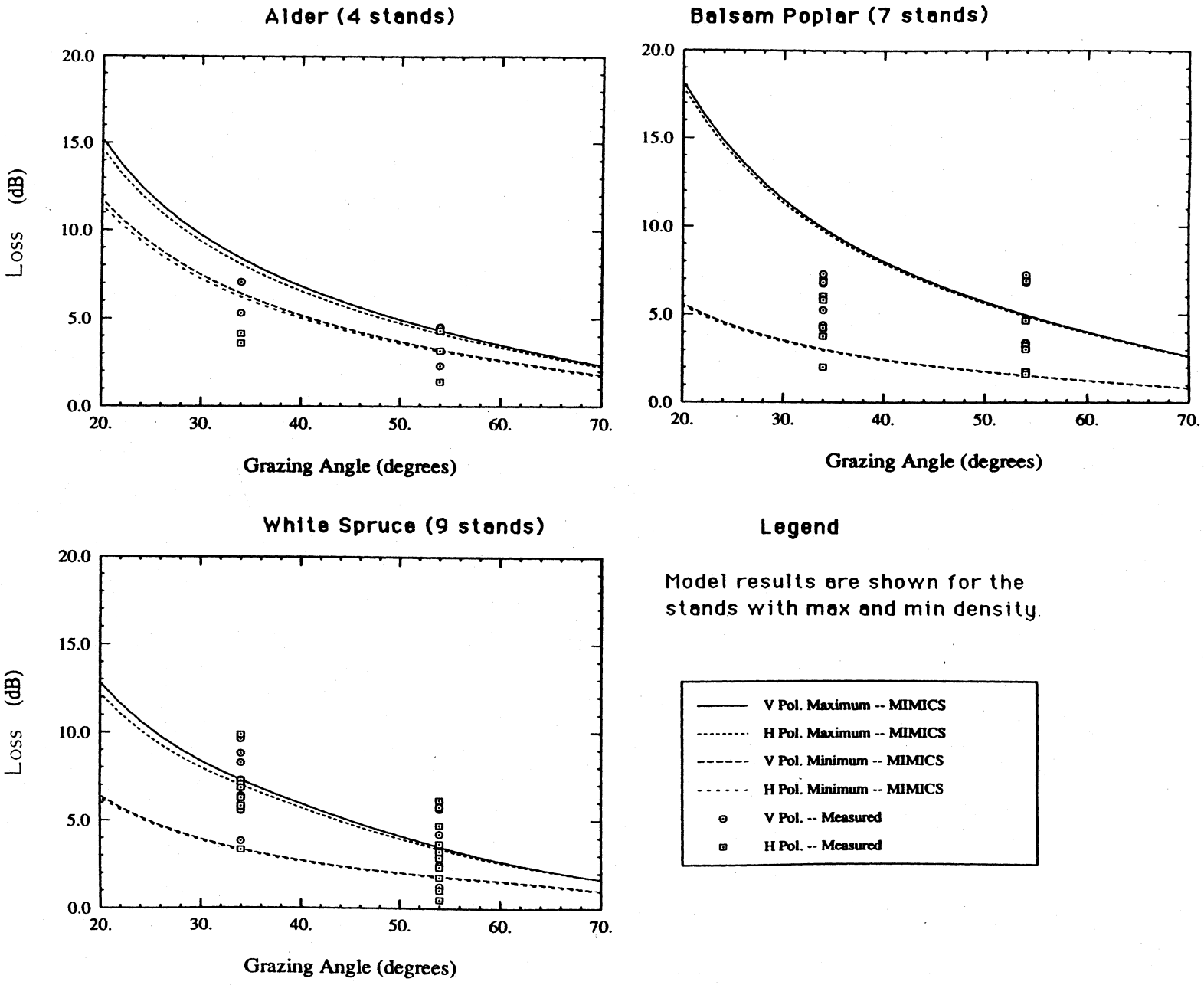

favor of emplacement of targets within a local clearing and this results in a bias in the measured extinction toward smaller values. Similar tendencies are observed at X-band in Figure 31.

For the seven reflectors within the balsam poplar stand also containing alder trees, the measured values are well bounded by the MIMICS predictions for maximum and minimum density conditions at both frequencies. However, the larger diameters of the balsam poplar trees, relative to alder, and their lower densities leads to a greater variance in the measured data because the magnitude of a given measurment is more dependent upon the specific locations of fewer and larger trees in front of the reflectors. This increase in the variance of the measured extinction (see Table 17) is also evident for the white spruce stand at both C- and X-bands.

For the white spruce stand containing nine trihedral corner reflectors, there is a tendency for MIMICS to under predict the observed one-way canopy extinction at shallow depression angles. This is true at both C- and X-bands. This underprediction, which varies in magnitude with depression angle, is attributed to the effects of crown layer extinction which is not included in these MIMICS simulations.

The combined effects of (1) not including crown layer extinction, (2) variance in local stand conditions surrounding each reflector and (3) methodologic biases in reflector emplacement leading toward oversampling of minimum extinction conditions are illustrated by Figure 32. Comparison of measured to modeled propagation loss for each reflector at C-band in Figure 32 shows good correlations of measurements with model predictions with linear correlation coefficients $R \geq 0.75$. However, the MIMICS simulations, which are based upon average stand conditions, will never predict the 0 dB transmission losses observed by placement of reflectors in gaps within the canopy. This suggests that a statistically larger sample population and with a more random positioning of targets within the stands is well worth pursuing in future field

Figure 32: Measured One-Way Propagation Loss Through the Frozen Canopies at C-band Versus MIMICS Predictions of Loss Through the Trunk Layer for each Reflector.

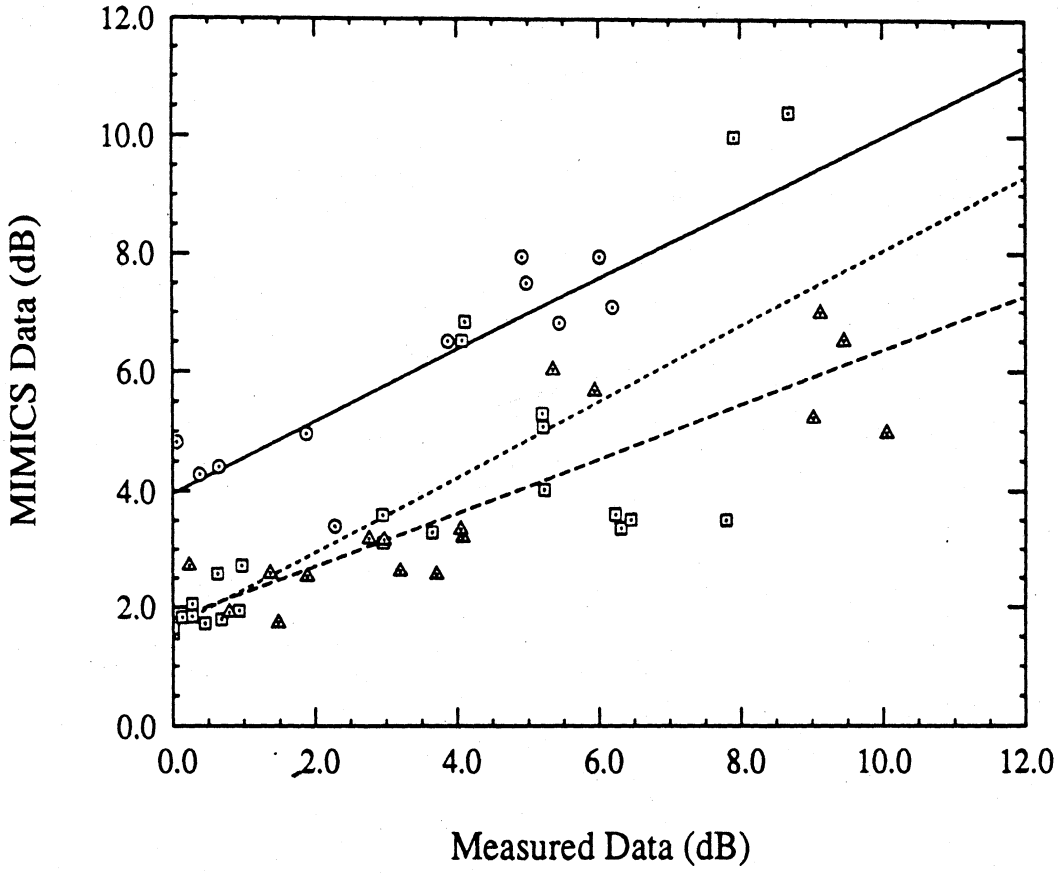

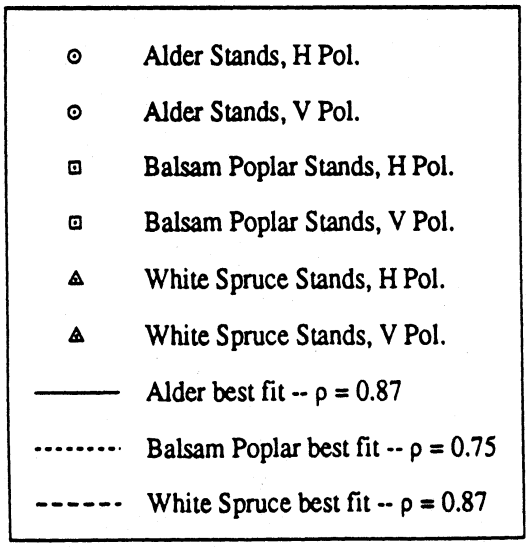

experimentation. In addition, underestimation of the total canopy extinction, particularly at high incidence angle ($\theta = 56^o$) for the white spruce stand, indicates the importance of the crown layer contribution to extinction.

An evaluation of the impact of the crown layer constituents on net canopy extinction was performed via MIMICS simulations of a mature stand of white spruce. Stand WS-2 was selected since it had net biomass most closely approximating those found in the younger mixed-specie stand of white spruce used by the corner reflector measurements. The MIMICS predictions of one-way propagation losses for WS-2 under frozen conditions are plotted in Figure 33 for L-, C- and X-bands. The plots show the total loss, as well as the contributions of trunk and crown layer losses, as functions of incidence angle. The net extinction at all three frequencies is shown to be dominated by that of the crown layer comprised of branches and needles. When extinction by the crown layer is included, the net loss calculated by MIMICS is nearly identical to the average loss measured for the white spruce stand. Table 21 presents a comparison of the average measured values to the MIMICS predictions at an incidence angle of 55^o where the importance of crown layer effects should be maximized. Even at X-band, the predicted values from MIMICS are shown to be within a standard deviation of the mean (of N=9) observations.

In summary, MIMICS accurately predicts the general behavior of canopy extinction for frozen boreal forest conditions in terms of the observed dependence upon the wave parameters of frequency (C- and X-bands), angle of incidence ($\theta = 36^o$ and 56^o), and polarization (H and V). Furthermore, the importance of the crown layer contribution to total canopy extinction is well demonstrated by MIMICS and highlights the importance of proper biophysical characterization of this, somewhat difficult to reach, layer. Finally, point-to-point comparisons of the model to measurements illustrate the statistical nature of the media and emphasize the need for careful experimental procedures and utilization of a statistically

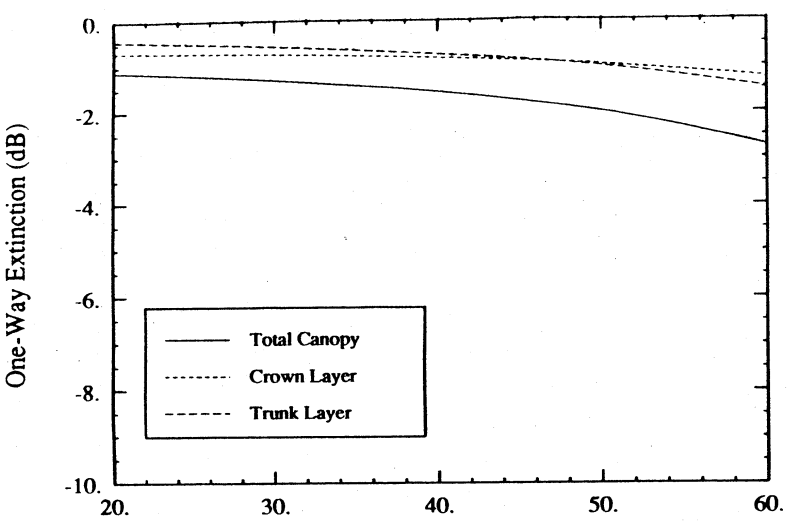

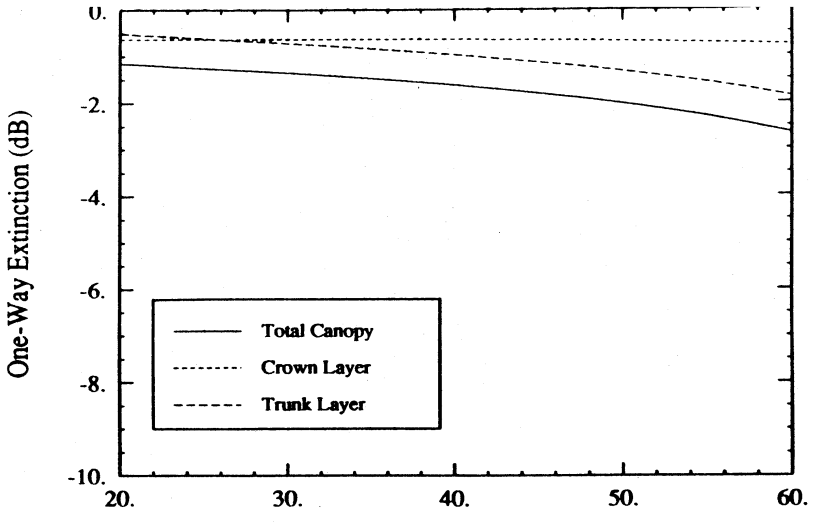

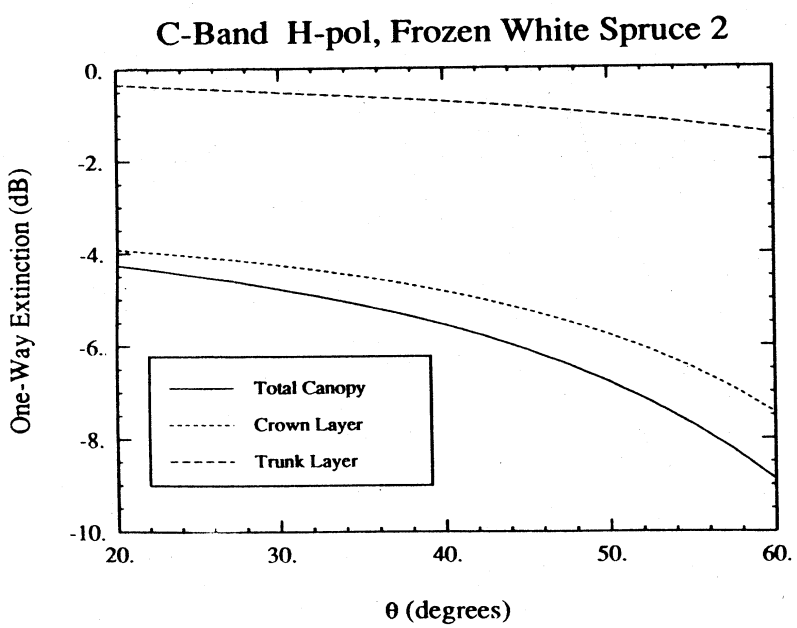

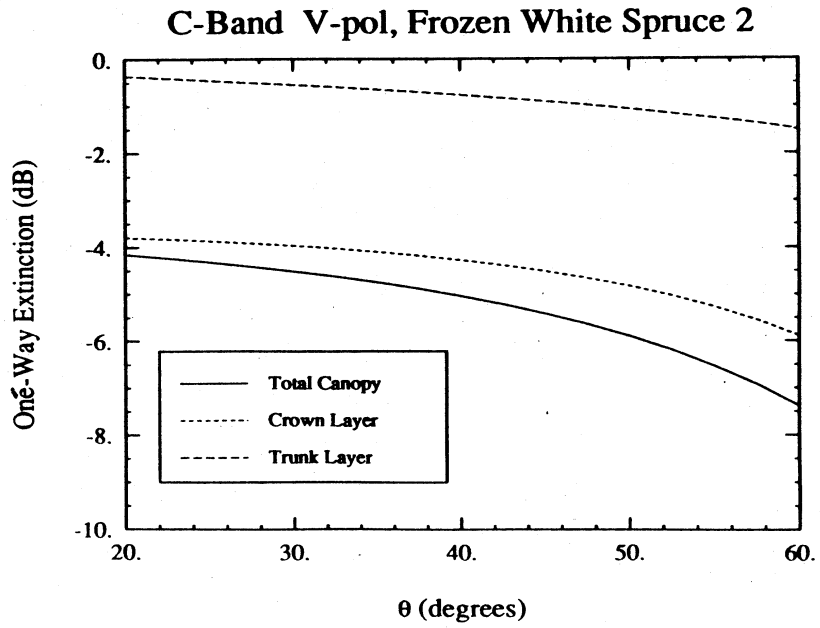

Figure 33. MIMICS Simulations of Canopy Propagation Losses for White Spruce Stand WS-2 with Frozen Conditions.

Table 21. Comparison of One-Way Propagation Losses Modeled by MIMICS for Frozen WS-2 at $\theta = 55^{o}$ to the Average Propagation Loss Measured by the ERIM/NADC SAR.

Band	Polarization	One-way Propagation Loss (dB)				
		MIMICS			Measured	
		Trunk	Crown	Total	Mean	Stand. dev.
C	V	1.3	5.3	6.5	6.7	1.7
	H	1.2	6.5	7.7	7.2	2.2
X	V	1.1	6.6	7.8	6.9	1.8
	H	1.1	7.4	8.5	6.5	1.7

large number of reflectors which are preferrably placed within homogeneous stands.

Accepting MIMICS as providing good first-order estimates of canopy extinction, the model can be used to simulate the propagation losses of other canopy or environmental conditions. Figure 34 shows MIMICS predictions of total canopy loss and the contributions of the crown and turnk layers for thawed conditions using the white spruce stand (plotted in Figure 33 for frozen conditions). Upon thawing extinction is shown to increase at all frequencies, polarizations and angles. A similar result is obtained for balsam poplar as shown in Figures 35 and 36 for frozen and thawed conditions, respectively. This functional dependence of extinction on the dielectric properties of the canopy elements is also demonstrated for stands with a very low tree density such as black spruce as shown in Figure 37 for MIMICS simulations of stand BS-1.

5.0 Model Validation for Canopy Backscatter

The section treats the comparison of MIMICS simulations of radar backscatter to the experimental data presented in Section 3. The MIMICS validation using the walnut orchard data only considers the L-band scatterometer data. The validation using the airborne SAR data from Alaska considers L-, C-. and X-band SAR observations for only those forest stands with adequate characterization of canopy properties.

5.1 MIMICS Predictions for the Walnut Orchard

MIMICS was initialized using the walnut orchard canopy specifications presented in Section 3, and simulations of backscatter at L-band were computed for $40^o \leq \theta \leq 55^o$. The dielectric constants of the various orchard constituents are: (1) ε = 25-j2.5 for the soil layer, (2) ε = 45-j11.2 for the trunks, (3) ε = 34-j8.5 for the primary branches, (4) ε = 30-j7.5 for the secondary branches, and (5) ε=36.5-j11.3 for the twigs and

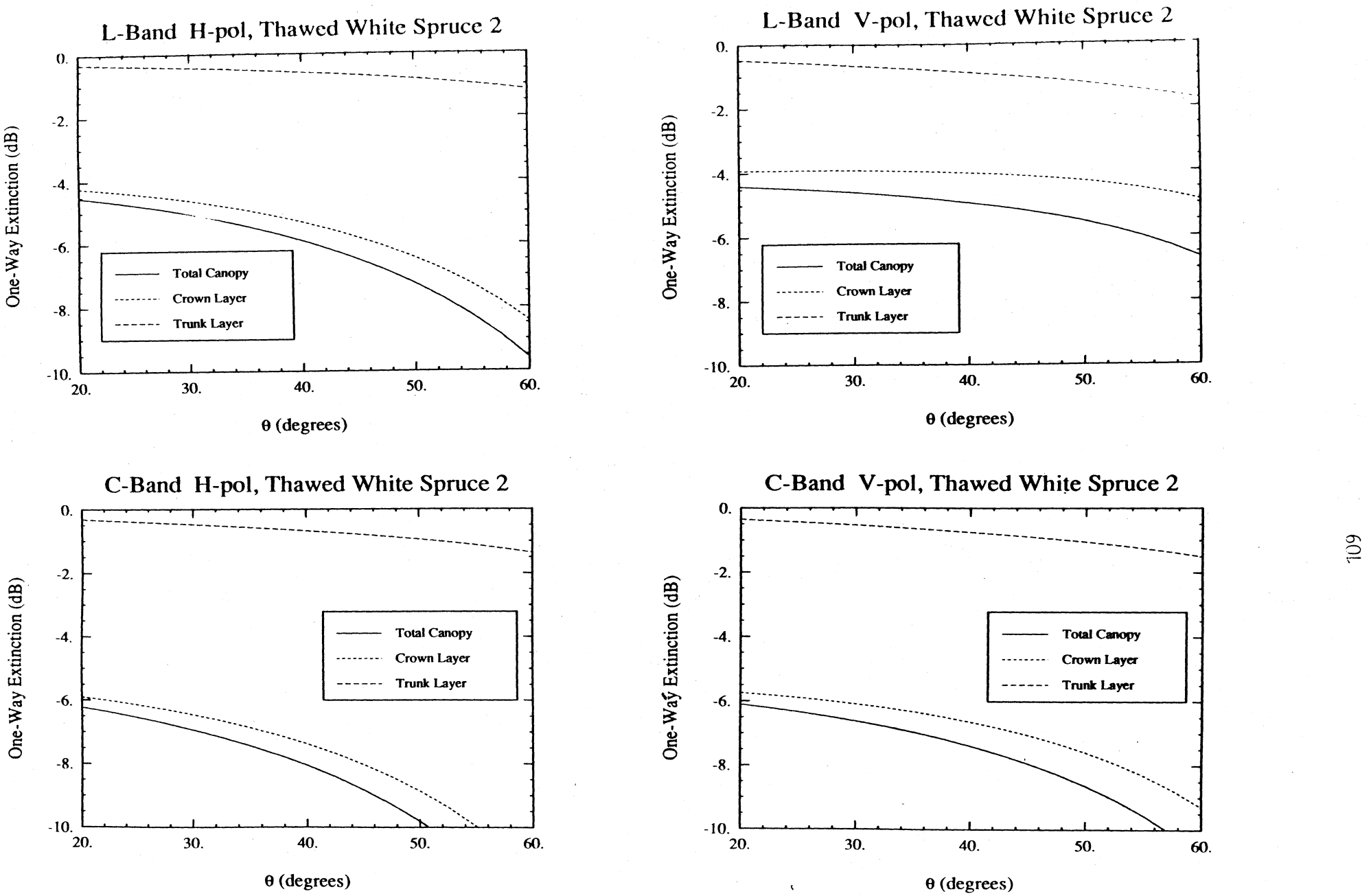

Figure 34. MIMICS Simulations of Canopy Propagation Losses for White Spruce Stand WS-2 with Thawed Conditions.

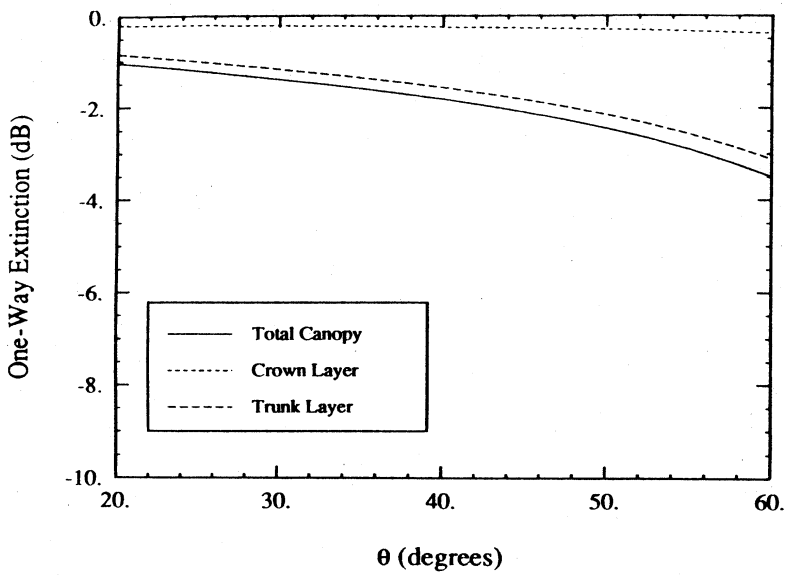

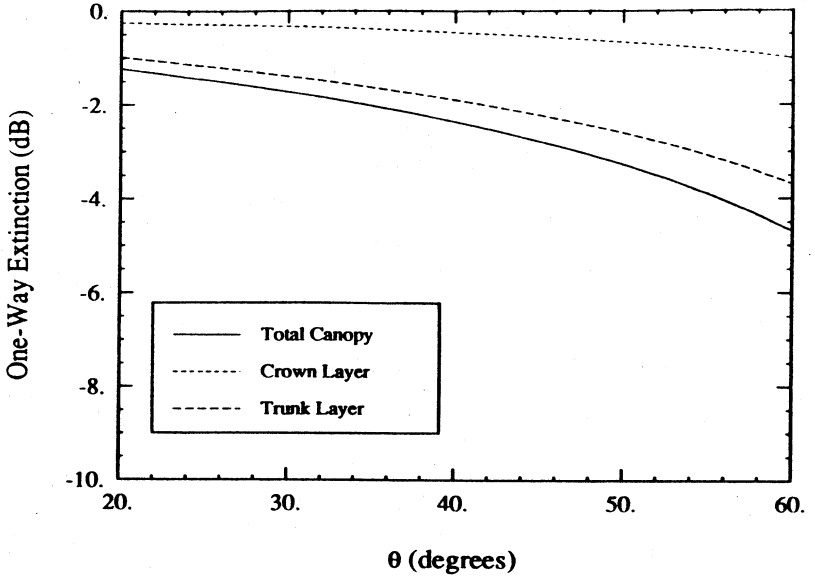

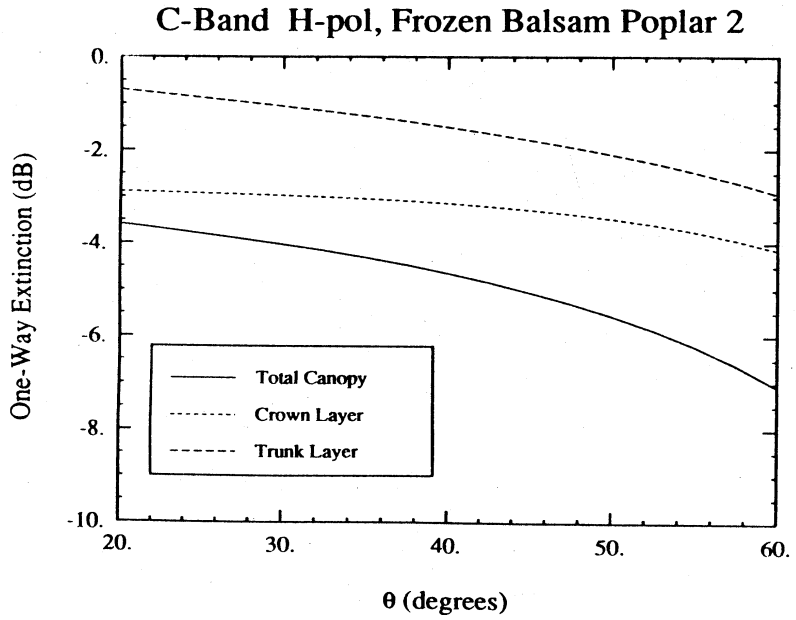

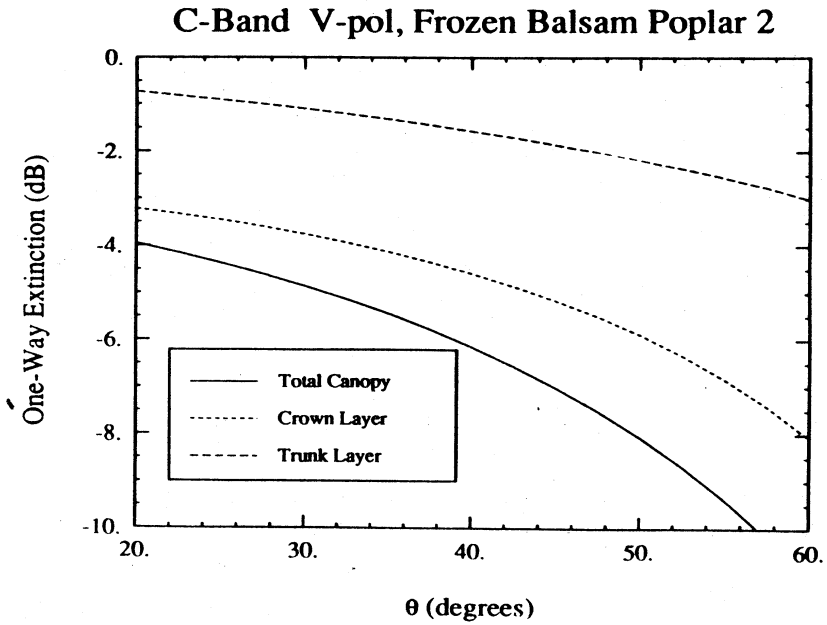

Figure 35. MIMICS Simulations of Canopy Propagation Losses for balsam poplar stand BP-2 with Frozen Conditions.

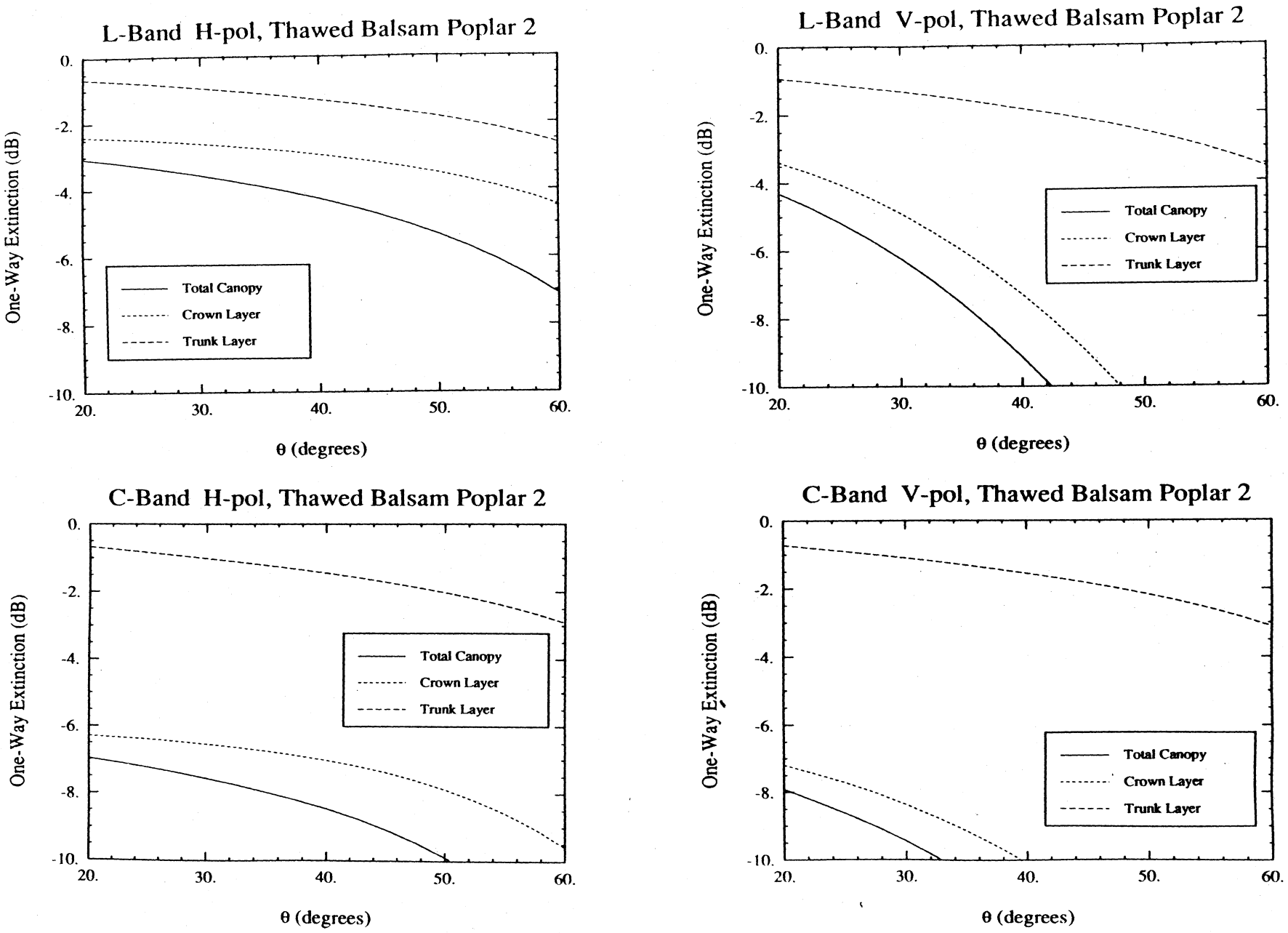

Figure 36. MIMICS Simulations of Canopy Propagation Losses for balsam poplar stand BP-2 with Thawed Conditions.

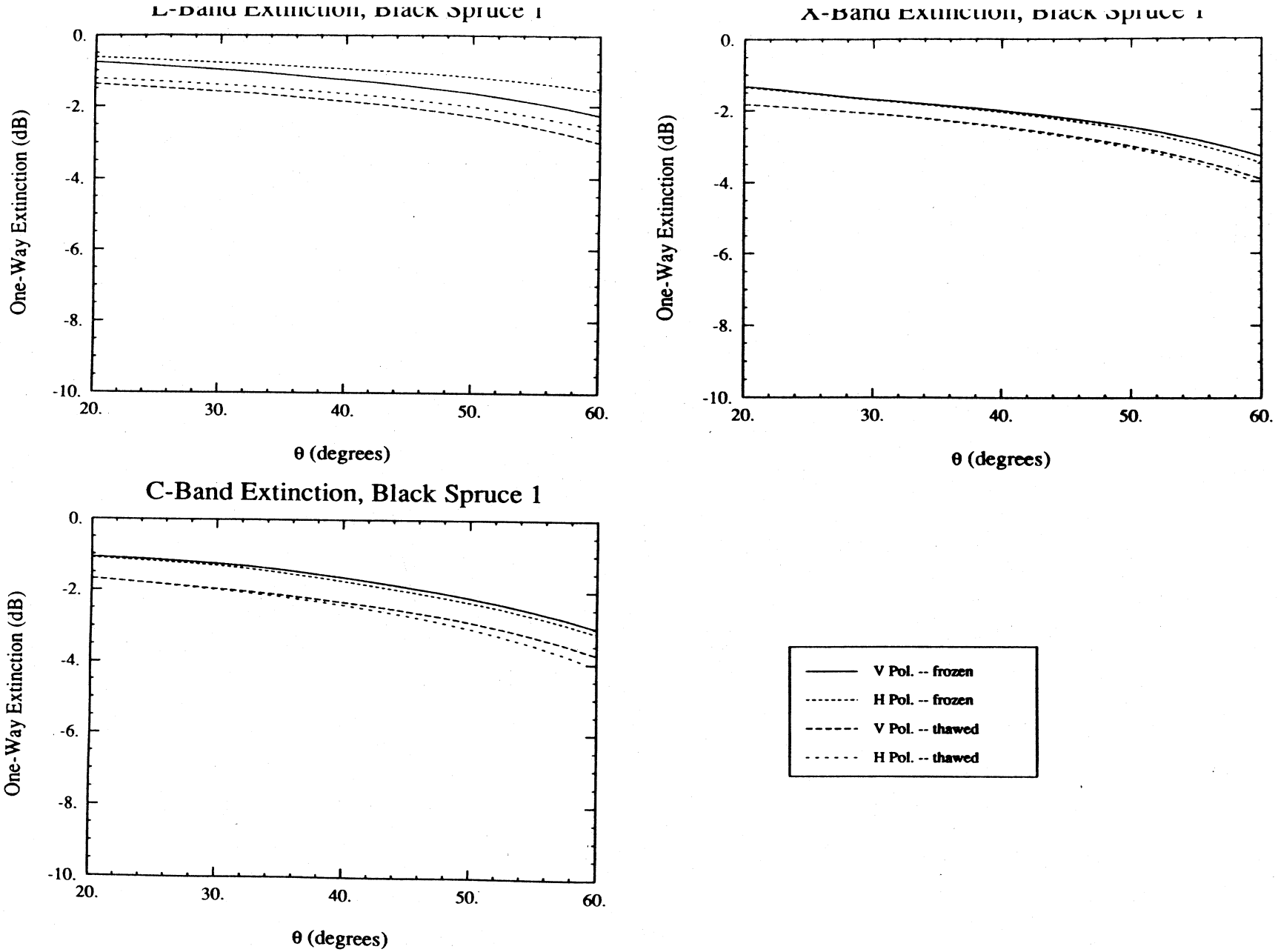

Figure 37. MIMICS Predictions of Total Propagation Loss through the Canopy for a black spruce stand (BS-1) under both frozen and thawed conditions.

leaves. These values correspond to the average condtions during the time period required to obtain the scatterometer data.

The backscatter values predicted by MIMICS are compared to the measured values in Figure 38 for linear polarizations HH, VV and HV. The figure demonstrates excellent agreement between the model and the measurements in terms of both the trends and absolute levels of backscatter. Since the levels of HV and VH return are found to be identical for both the model and the measurements, only the HV return is plotted.

Figures 39 and 40 show the relative contributions of the three most important terms contributing to the total like-polarized backscatter. The crown-ground component corresponds to terms (2a + 2b), the direct crown component to term (3), and the ground-trunk component to terms (4a + 4b) in Figure 1. Backscattering from the crown layer is observed to dominate the VV polarized return, while the HH polarized backscatter is dominated by terms incorporating specular scatter from the soil layer interacting with either the crown layer or the trunk layer. Figure 41 shows the major contributors to the HV polarized backscatter. For HV, those scattering mechanisms involving the crown layer are shown to dominate. This is expected since the branches in the crown layer are oriented such that they depolarize more than the trunk layer constituents.

Having established that MIMICS successfully predicts canopy backscatter as a function of angle for the walnut orchard, the model is run at a constant angle of incidence, $\theta = 55^{o}$, while varying the canopy and soil dielectric properties in order to simulate the variations in σ^{o} seen over the three day diurnal experiment as seen in Figure 10. Figures 42 to 44 present the backscatter simulated by MIMICS along with the measured values for HH, VV and HV polarizations respectively. In each case, MIMICS successfully predicts the approximate level of the measured data as well as the decreasing trend in σ^{o}

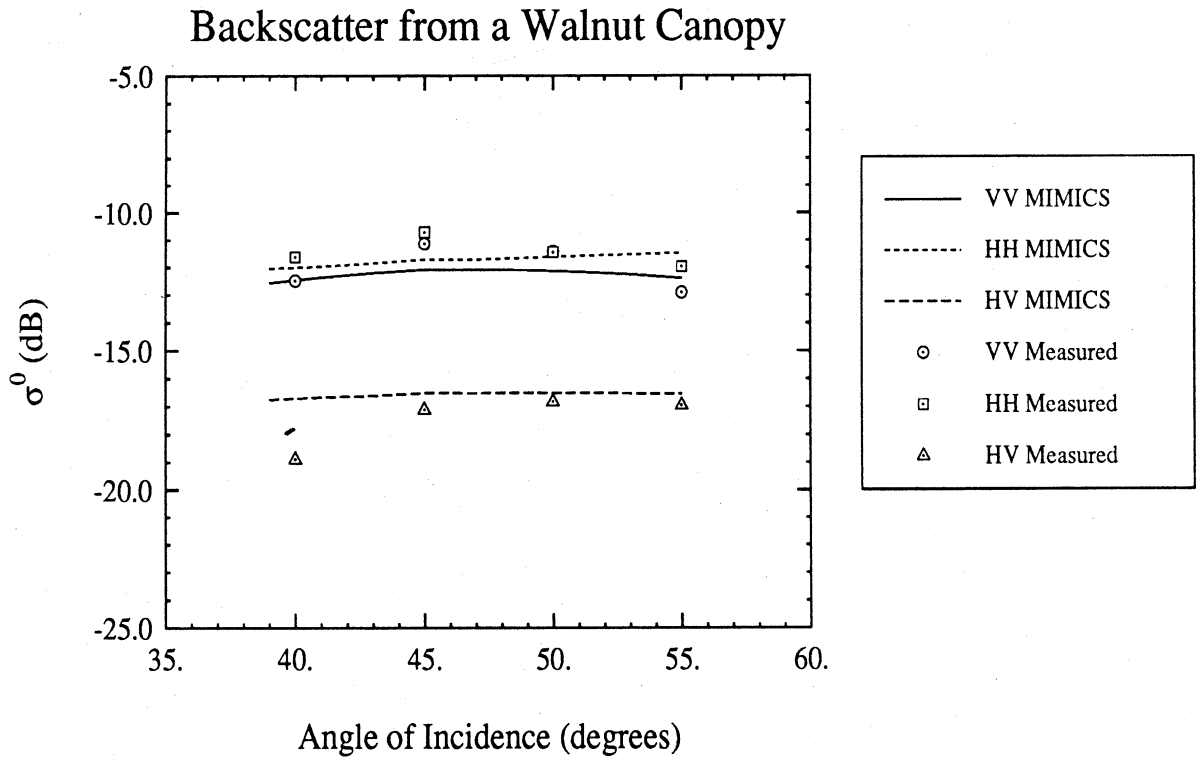

Figure 38: Comparison of MIMICS with recorded data.

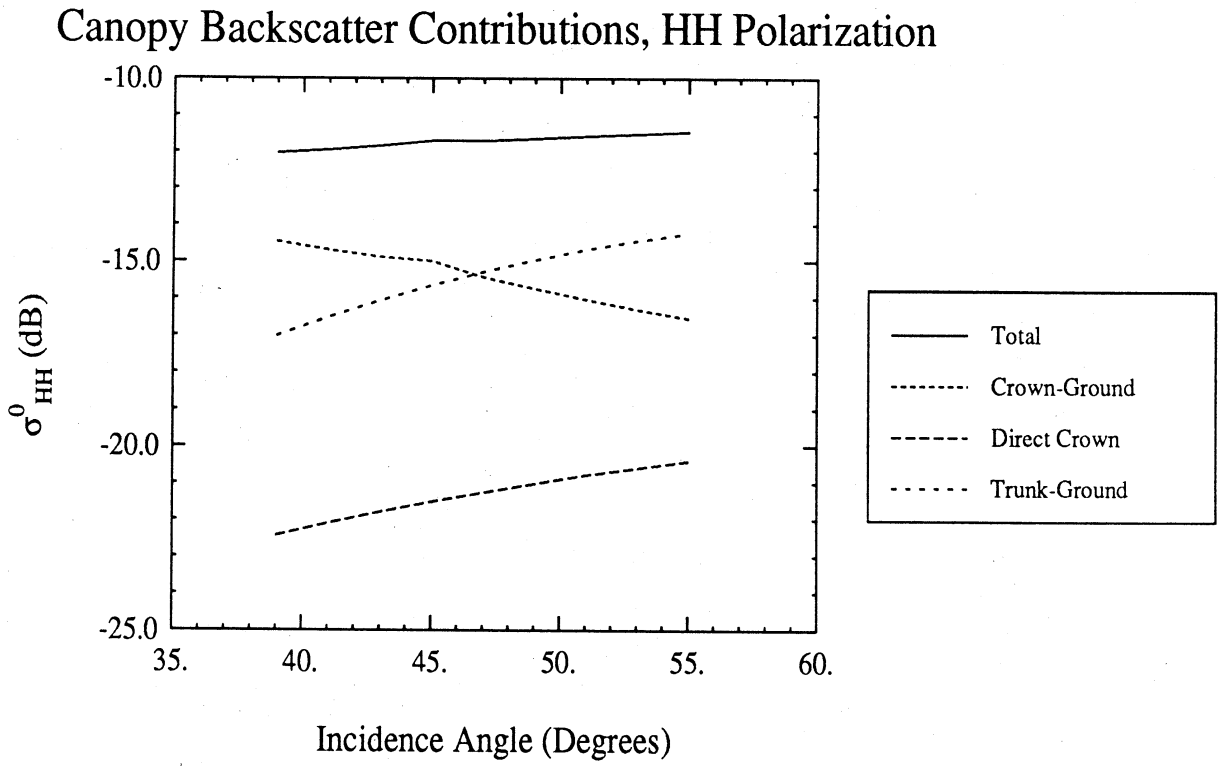

Figure 39. Components of HH polarization backscatter.

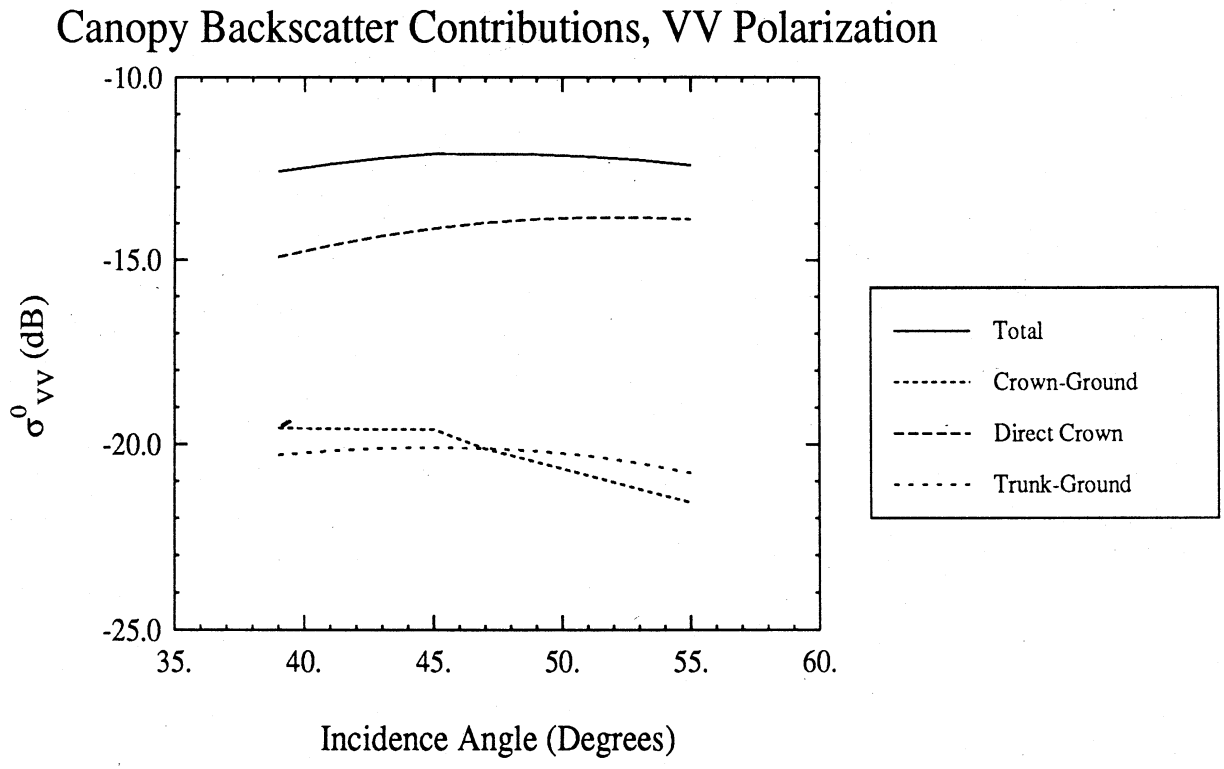

Figure 40. Components of VV polarization backscatter.

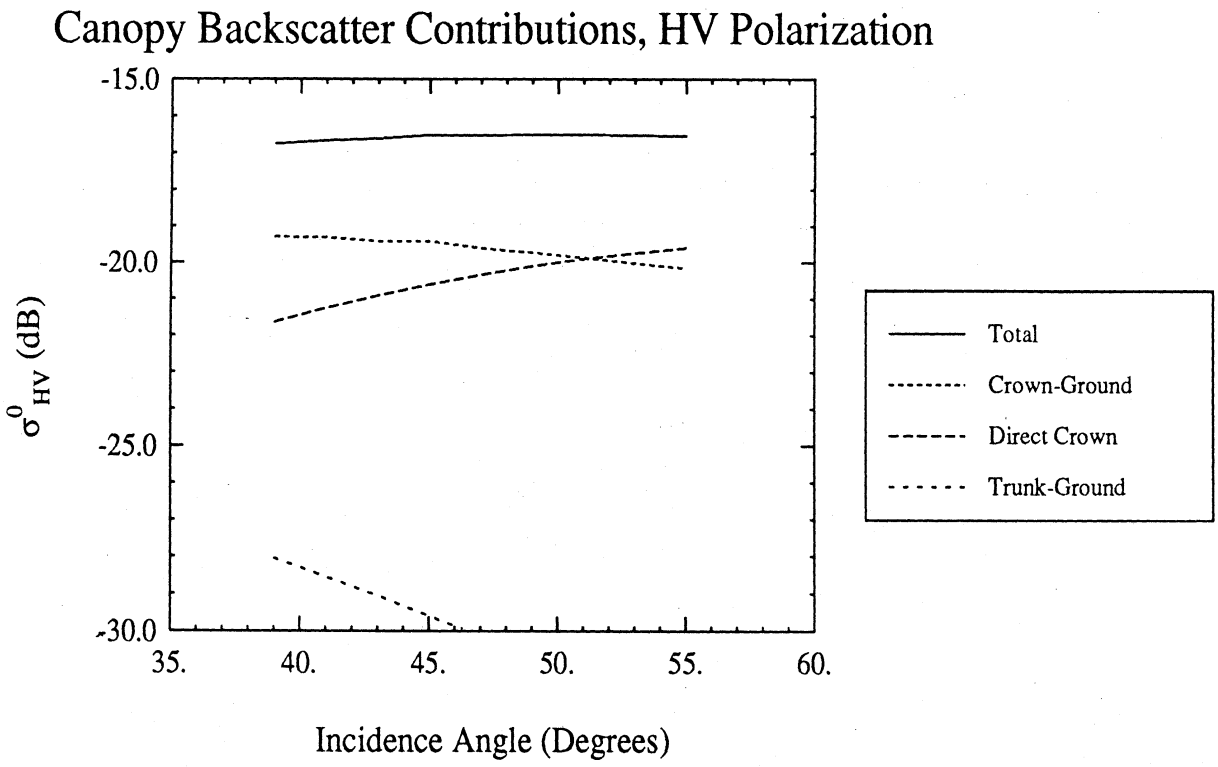

Figure 41. Components of HV polarization backscatter.

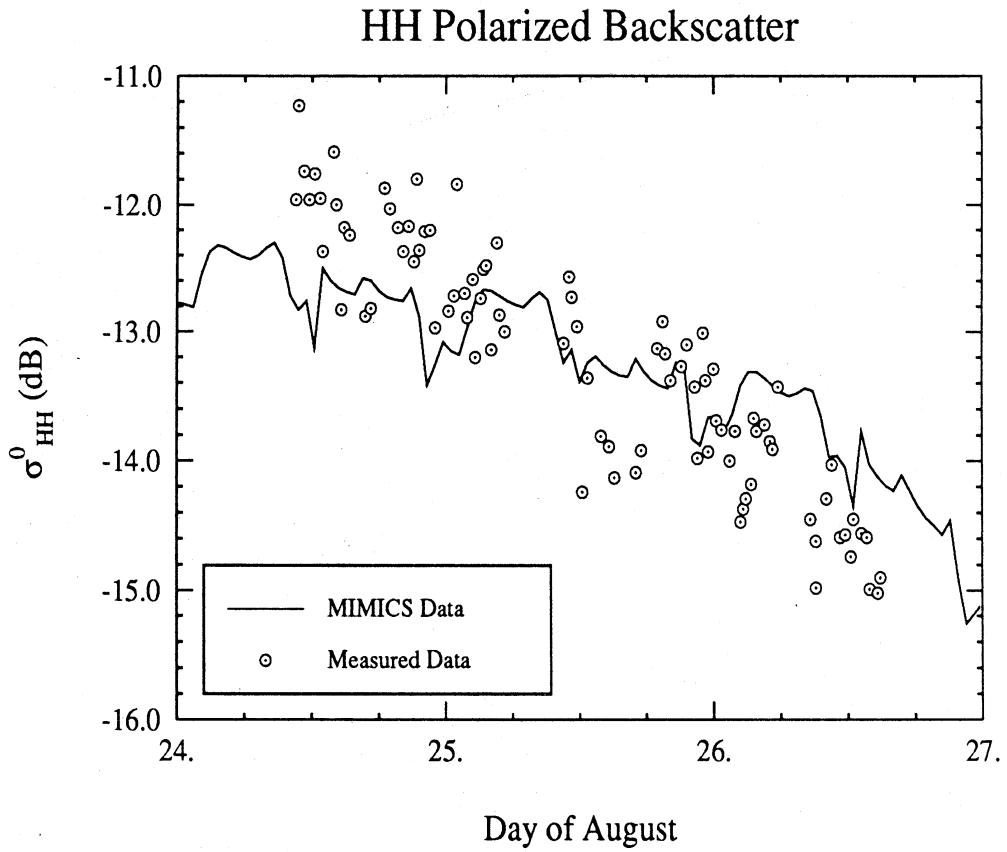

Figure 42. Measured and predicted HH polarized backscatter.

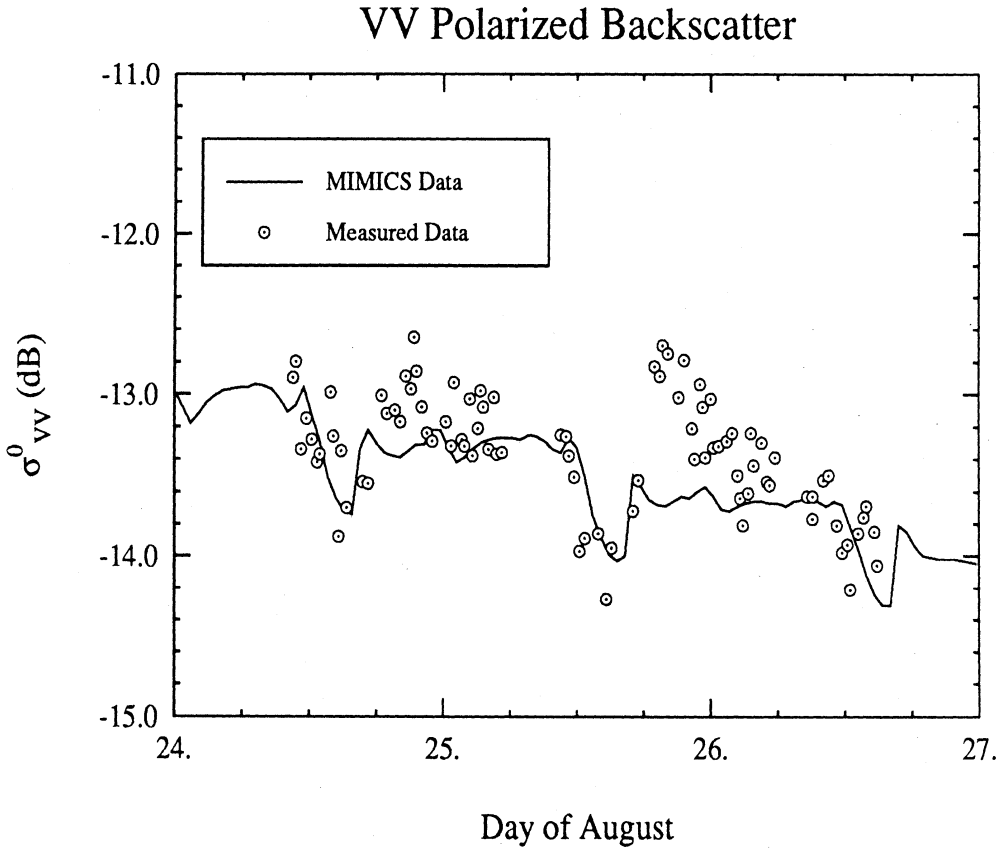

Figure 43. Measured and predicted VV polarized backscatter.

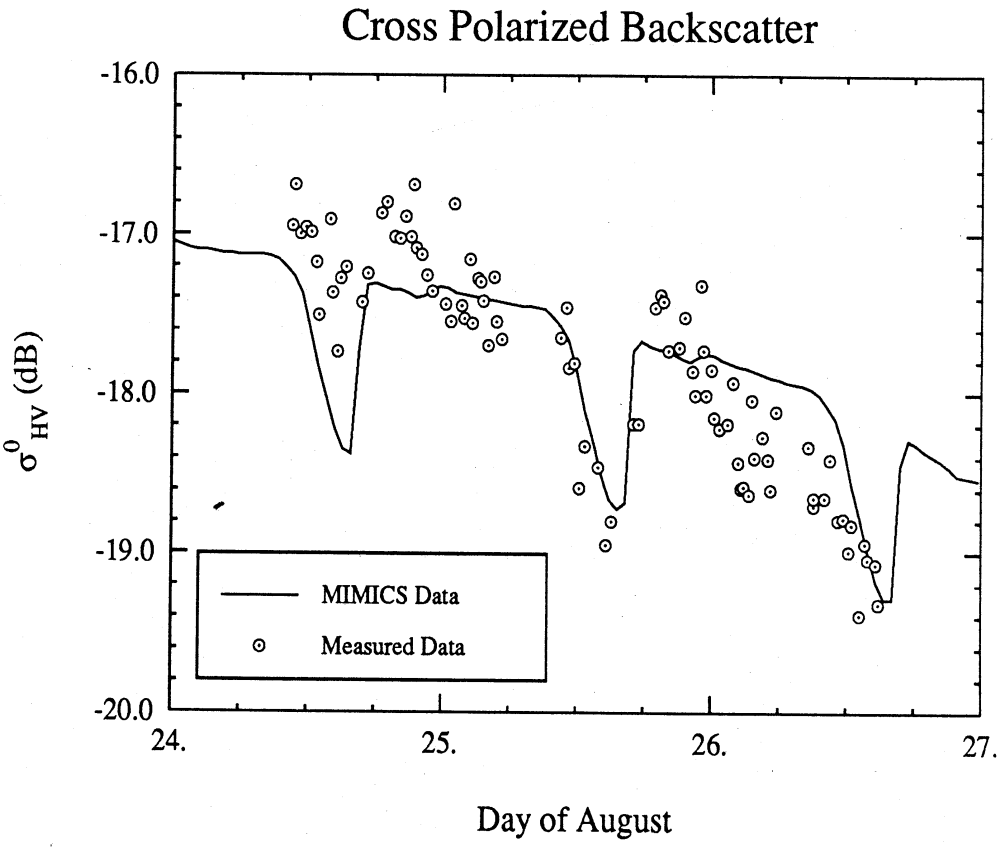

Figure 44. Measured and predicted cross polarized backscatter.

observed over the period. Furthermore, in the case of σ^o_{VV} and σ^o_{HV}, MIMICS predicts the 1 to 2 dB dip in backscatter that occurs in the early afternoon of each day.

In comparing the model predictions to the measured data it must be considered that variation in the measured data comes primarily from three sources. The first is true variation in average properties of the canopy and soil substrate. The second arises from the scatterometer scanning process used to statistically sample an inhomogeneous canopy structure with a discontinuous crown layer and non-random distribtuion of trunks. The third is fading and is a consequence of the coherent nature of the scatterometer. The scanning technique provided 30 spatially discrete samples over a given azimuth sweep. The locations sampled within the canopy by each of these 30 samples do not correspond precisely to those observed during other azimuth sweeps. The measurement error associated with fading is expected to be approximately $\pm$ 0.5 dB. Hence, the modeling results shown in Figures 38 to 44 demonstrate extraordinarily good agreement with the measured backscatter, especially when measurement variability is taken into account.

The comparison of modeled and measured canopy backscatter allows some insight into the sources of backscatter variation that are caused by changes in the physiological state of the vegetation and soil. The trends in σ^o over the three day period are partly explained by Figures 39 to 41. At $\theta = 55^o$, σ^o_{HH} is dominated by the trunk-ground backscatter component which responds directly to changes in both trunk and soil dielectric properties. σ^o_{VV} is dominated by the direct crown component which depends strongly on changes to the dielectrics of the crown layer constituents. While the components of σ^o_{VV} which interact with the ground do have a measureable contribution to the total backscatter, they do not dominate as they do with σ^o_{HH}. Therefor, it is expected that σ^o_{VV} should exhibit some sensitivity to changes in soil and trunk dielectric, but not as much as σ^o_{HH}. The cross polarized backscatter is

dominated by both the crown-ground and direct crown components. Since the trunk-ground component is more than 10 dB below these other two for σ^0_{HV}, it should have almost no effect at $\theta=55^o$. Consequently, σ^0_{HV} should respond mostly to changes in crown-layer and ground dielectric properties.

5.2 MIMICS Predictions for the Alaskan Boreal Forest

In contrast to the thorough characterizations of the canopy structure and dielectric properties obtained for the walnut orchard, the boreal forest stands in Alaska were only partially characterized by on-site sampling. Biomass apportionment, the structure of the crown layer, and dielectric properties of the canopy and snow were estimated using models as described in Section 3. Hence, the errors inherent in these models used to describe the physiology and architecture of the boreal forest canopies will be transported into the MIMICS simulations based upon them.

In addition, attempts to compare MIMICS simulations of σ^o to observations by the airborne SARs are further complicated by the issue of SAR calibration. For the L-band average σ^o data derived from the JPL SAR as given in Table 20, daily calibrations permit one-to-one comparisons with model results for both the thawed conditions on March 13 and the frozen conditions on March 19. However, the C- and X-band data derived from the ERIM/NADC SAR imagery for the frozen conditions on March 22 lacks adequte calibration for one-to-one comparison to the model results on an absolute basis; but valid comparisons can be made on the basis of between stand differences at a common angle of incidence.

MIMICS simulations of backscatter at L-, C- and X-bands use the canopy architecture and dielectric properties presented in Section 3. For both frozen and thawed conditions, the substrate layer is treated as a half-space of snow with the dielectric properties given in Section 3. As will be shown, this is

an oversimplification as it ignores scattering at the interface between the snow layer and the underlying soil. This simplification, while not entirely desireable, is made because the roughness of this interface is not known and can only be estimated through model fitting by leaving roughness descriptors as free parameters in the model. Obviously, the model results would be improved by such a proceedure, but it is our intent herein to examine the model behavior with all inputs constrained and without resorting to parameter fitting.

White Spruce

MIMICS simulations have been performed for four stands of white spruce: WS-1, WS-2, WS-5 and WS-7. Of these discussion will concentrate on the first three since backscatter observations are not currently available for WS-7 from the SAR imagery.

White spruce stand WS-5 has an average biomass of 18.1 kg/m^2 which is intermediate for the white spruce stands modeled. The net backscatter simulated by MIMICS at L-, C-, and X-bands is shown in Figure 45 for the frozen conditions prevalent on March 19 and 22. The model calculations are performed in 1^o increments for $20^o \leq \theta \leq 60^o$. At L-band, σ^o_{HH} is found to be -12 dB and nearly constant with θ, σ^o_{VV} decreases from about -13 dB at $\theta=20^o$ to -17.5 dB at $\theta = 60^o$, and σ^o_{HV} is approximately 9 dB below the average like polarized backscatter. The modeled backscatter at C- and X-bands are very similar to each other and are greater than determined at L-band. σ^o_{VV} is typically on the order of 1 dB below σ^o_{HH}; and σ^o_{HV} is about 10 dB to 12 dB below the like polarized backscatter.

The source components of the net backscatter shown in Figure 45 are presented in Figures 46 to 48 for L-, C-, and X-bands respectively. For frozen conditions in stand WS-5, Figure 46 shows the L-band return to be dominated by scattering in

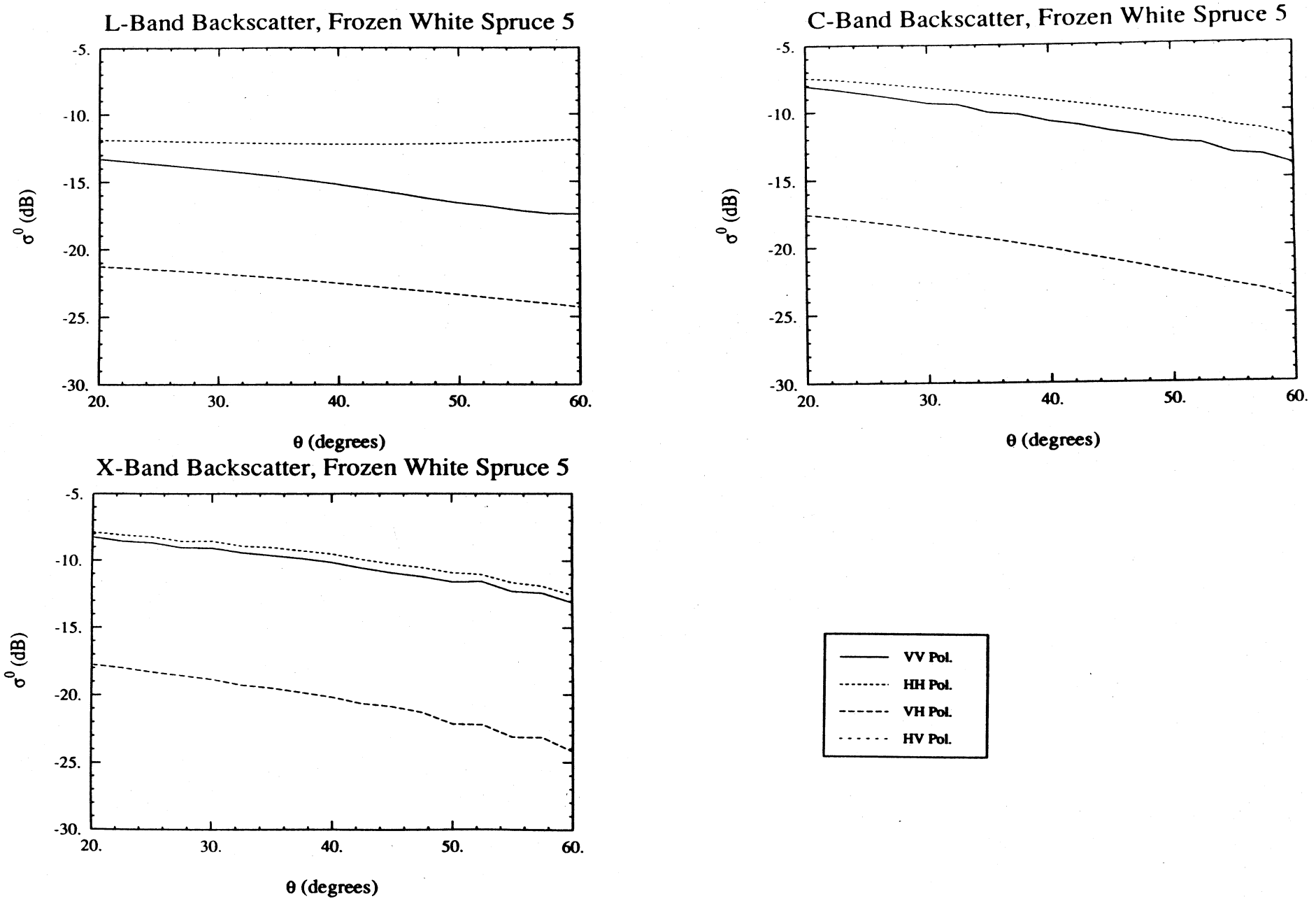

Figure 45. Modelled backscatter for white spruce 5 with frozen conditions.

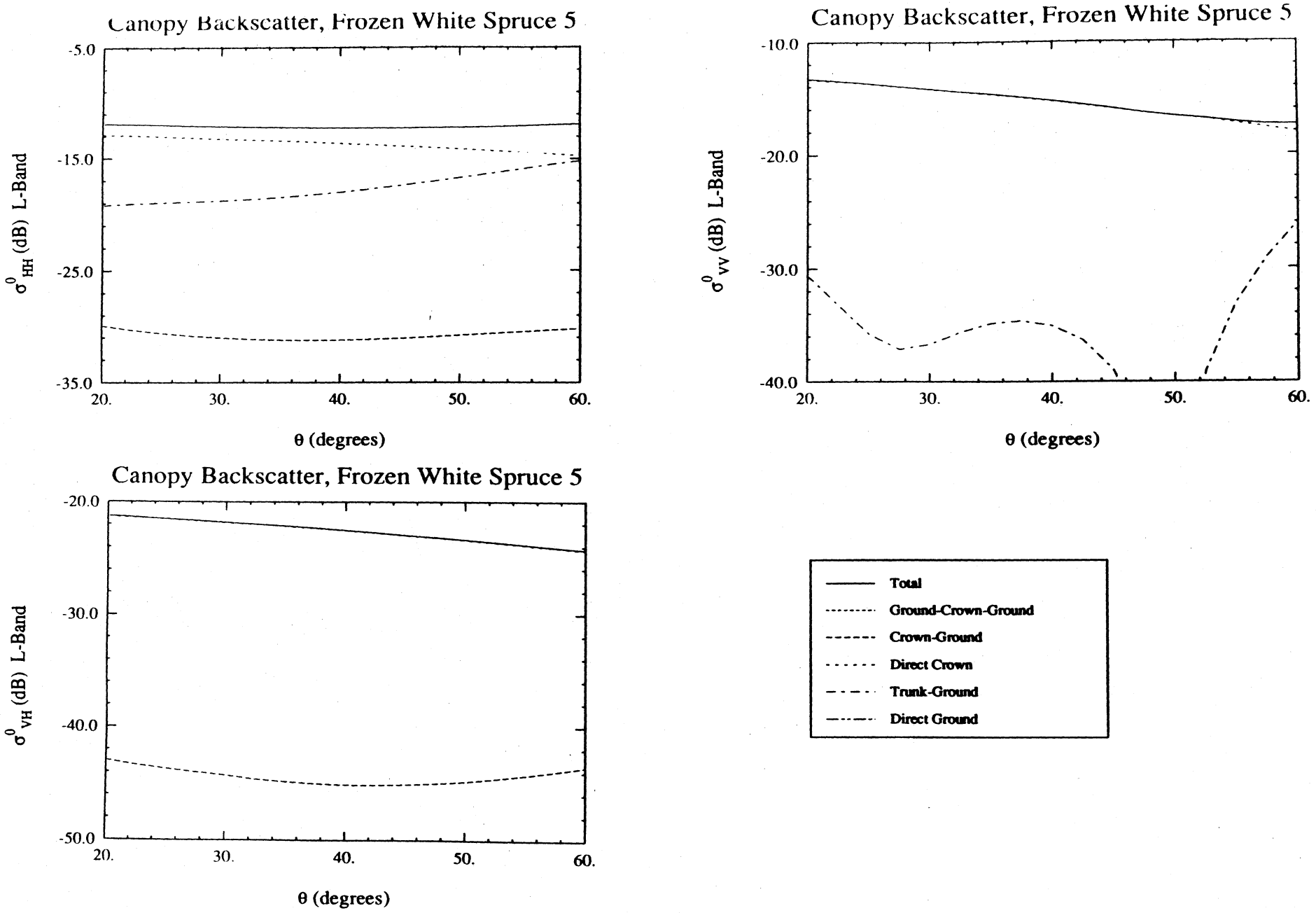

Figure 46. Components of Modeled backscatter at L-band for white spruce 5 with frozen conditions.

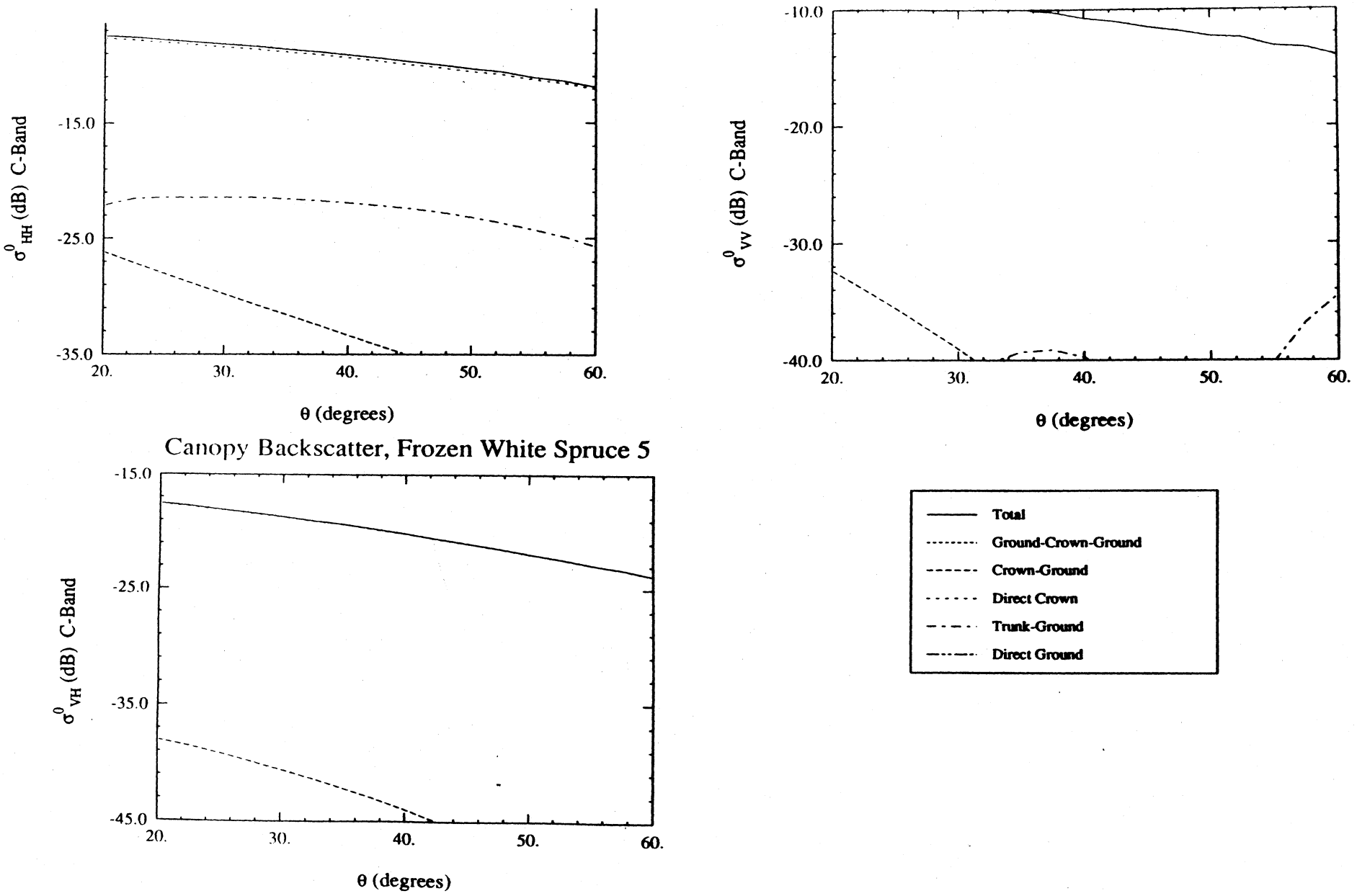

Figure 47. Components of Modeled backscatter at C-band for white spruce 5 with frozen conditions.

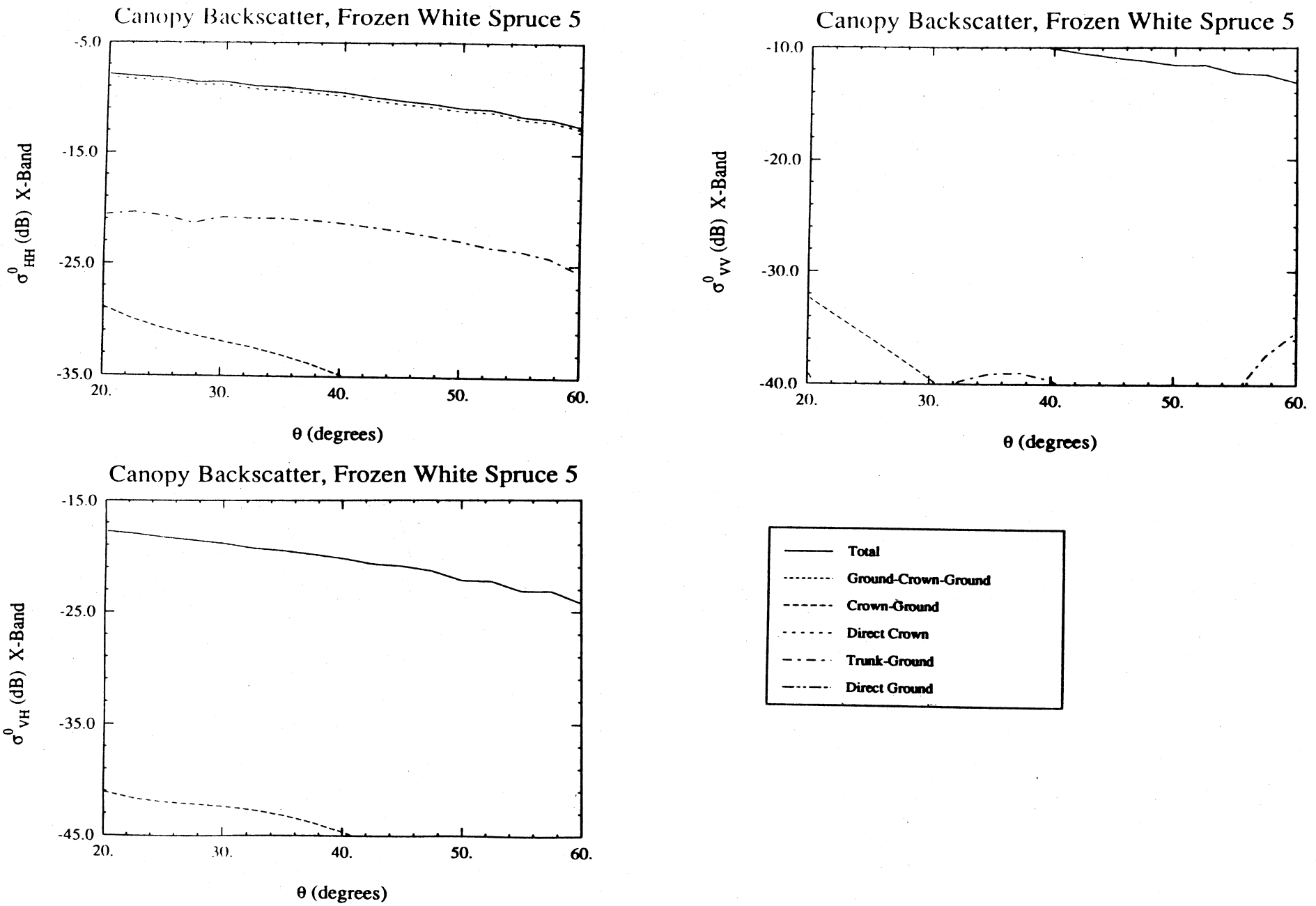

Figure 48. Components of modelled backscatter at X-band for white spruce 5 with frozen conditions.

the crown layer for all three linear polarizations HH, VV and HV. The scattering resulting from interaction with the snow half-space is shown to be of secondary importance and is only significant for σ^o_{HH}. For C-band and X-band backscatter, Figures 47 and 48, respectively, show the direct backscatter from the crown to also dominate the net return at all polarizations. The secondary role of interaction terms involving forward scattering from the snow layer is reduced, when compared to L-band, by the greater extinction of the canopy.

MIMICS predictions of the backscatter from white spruce stand WS-5 for the thawed conditions prevalent on March 13 are shown in Figure 49 for L-, C- and X-bands. When compared to frozen conditions (in Figure 45), thawing of the canopy is estimated to yield increases in σ^o at L-band, and decreases in σ^o at C- and X-bands. At L-band, σ^o_{HH} decreases from -7.5 dB at $\theta=20^o$ to -11 dB at $\theta = 60^o$, σ^o_{VV} varies from 1 dB less than σ^o_{HH} at 20^o to 5 dB less at 60^o, and σ^o_{HV} is only 4 dB below the average like polarized backscatter for the thawed conditions. At C-band, the two like polarized returns are modeled to be nearly identical at $\theta = 20^o$ and with $\sigma^o_{VV} > \sigma^o_{HH}$ by 1 dB at $\theta > 50^o$; σ^o_{HV} is shown to be 5 dB to 7 dB below the like polarized return. At X-band, $\sigma^o_{HH} > \sigma^o_{VV}$ by less than 1 dB and σ^o_{HH} decreases from -10 dB at $\theta = 20^o$ to -15 dB at $\theta = 60^o$ which is about 2 dB less than that predicted for the frozen conditions in Figure 45. The cross polarized return at X-band is shown to be on the order of 15 dB below the like polarized return.

The major source terms contributing to the net backscatter of WS-5 for thawed conditions are plotted in Figures 50 to 52 for L-, C-, and X-bands, respectively. In a fashion similar to that observed for the frozen conditions, σ^o is shown to be dominated by direct backscatter from the branches and foliage in the crown layer. The minor secondary importance of source terms incorporating forward scattering from the snow layer is shown to increase slightly with frequency for σ^o_{HH} and is generally comparable to that observed

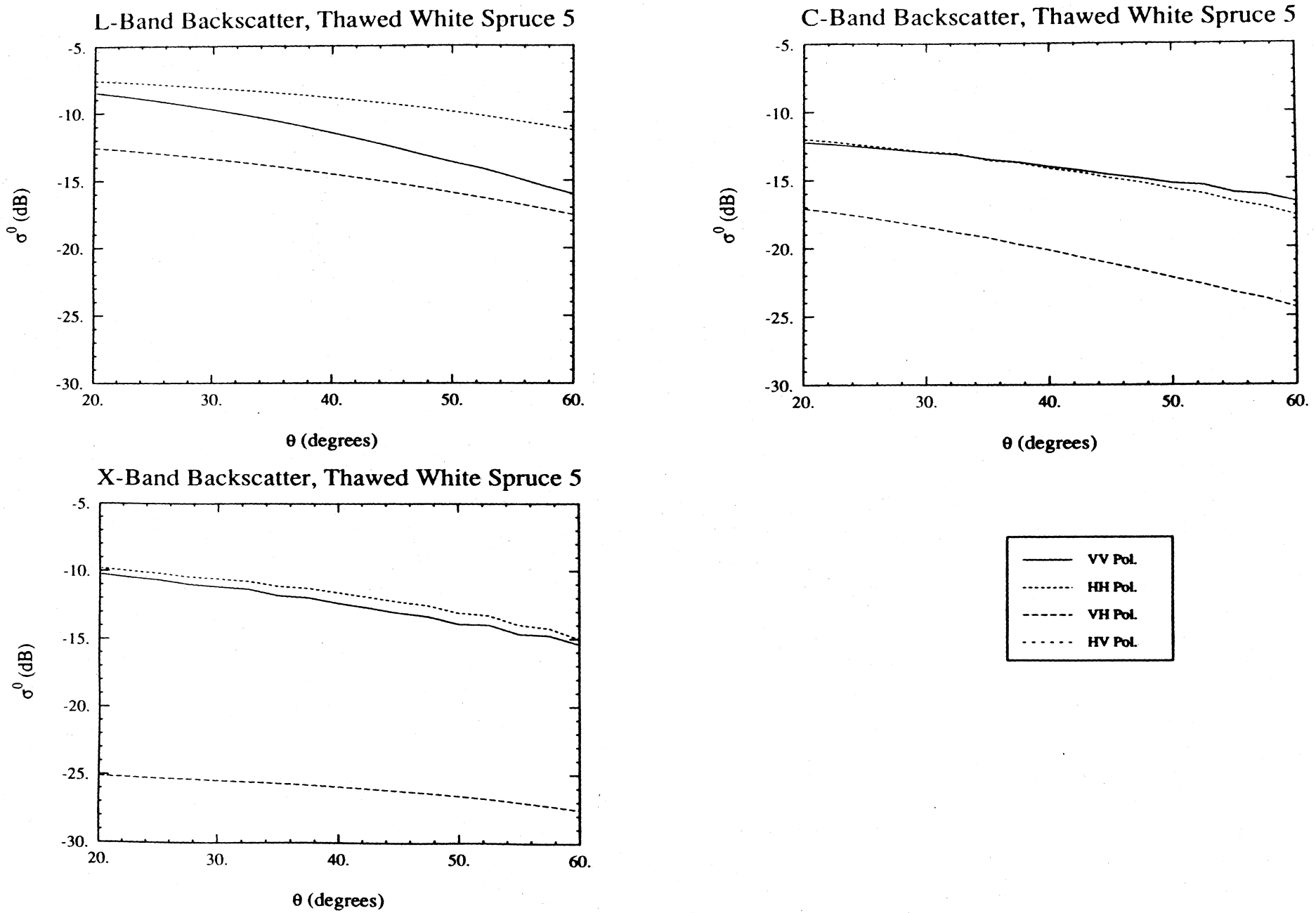

Figure 49. Modelled backscatter for white spruce 5 with thawed conditions.

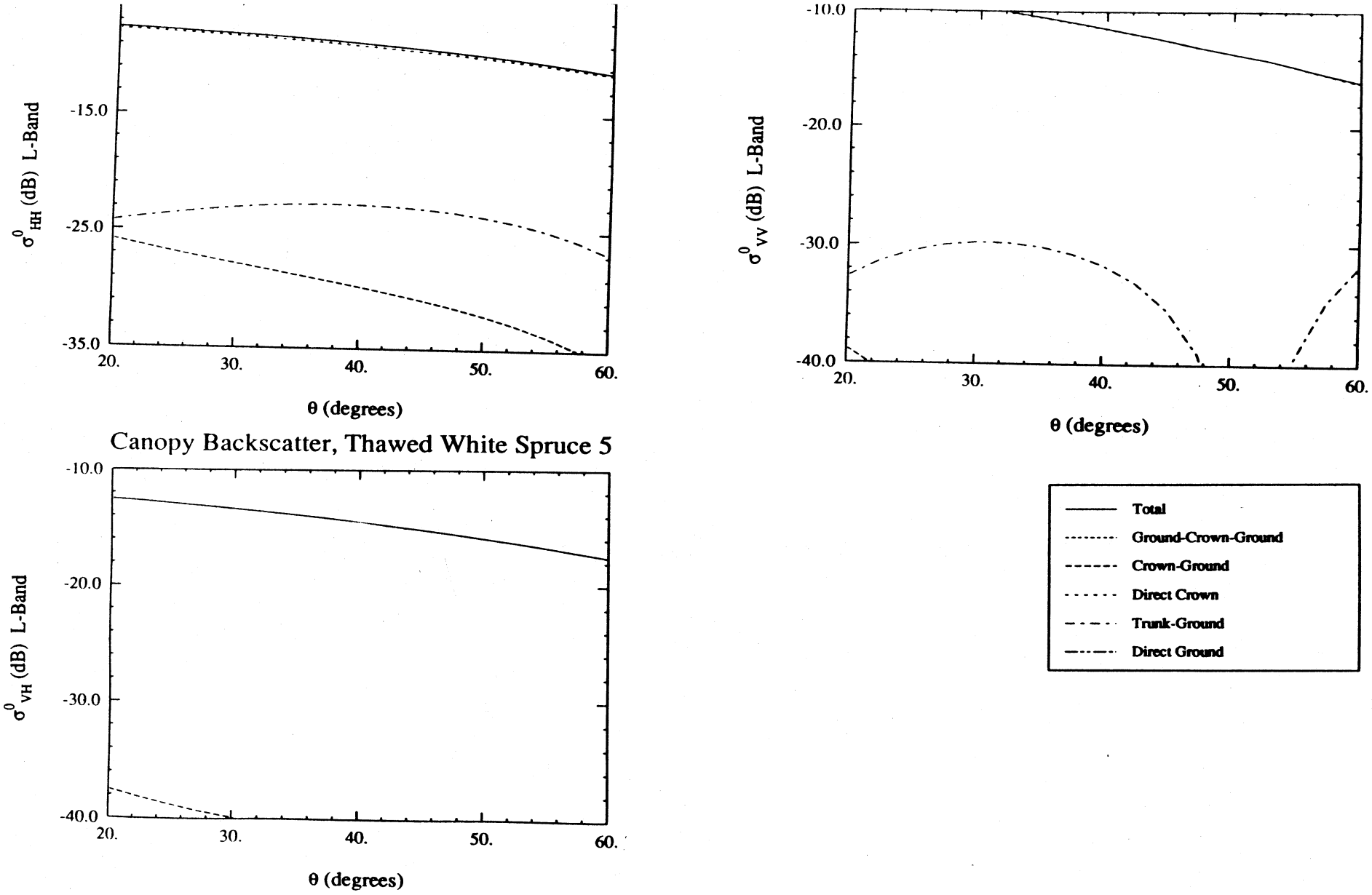

Figure 50. Components of modelled backscatter at L-band for white spruce 5 with thawed conditions.

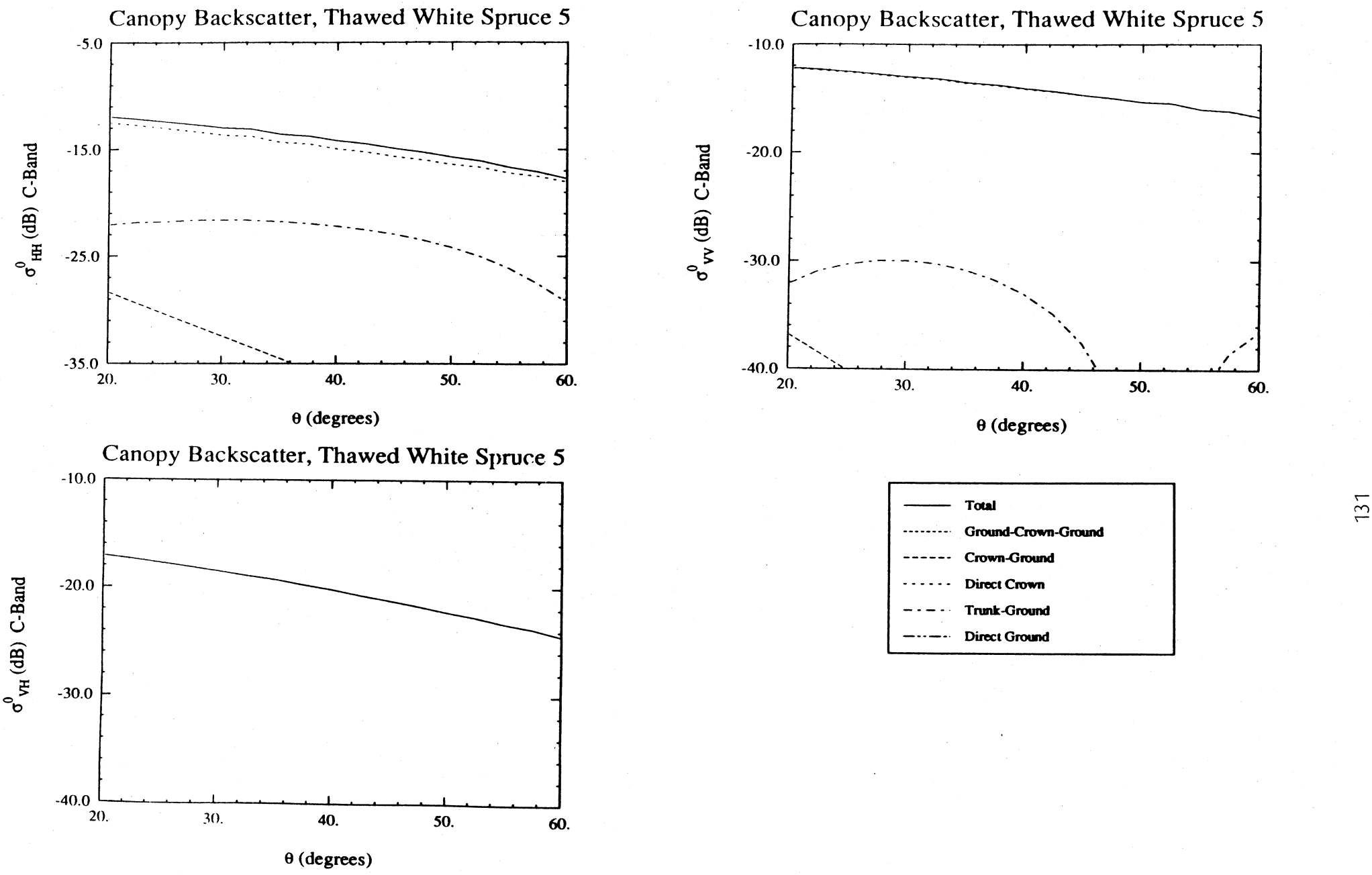

Figure 51. Components of modelled backscatter at C-band for white spruce 5 with thawed conditions.

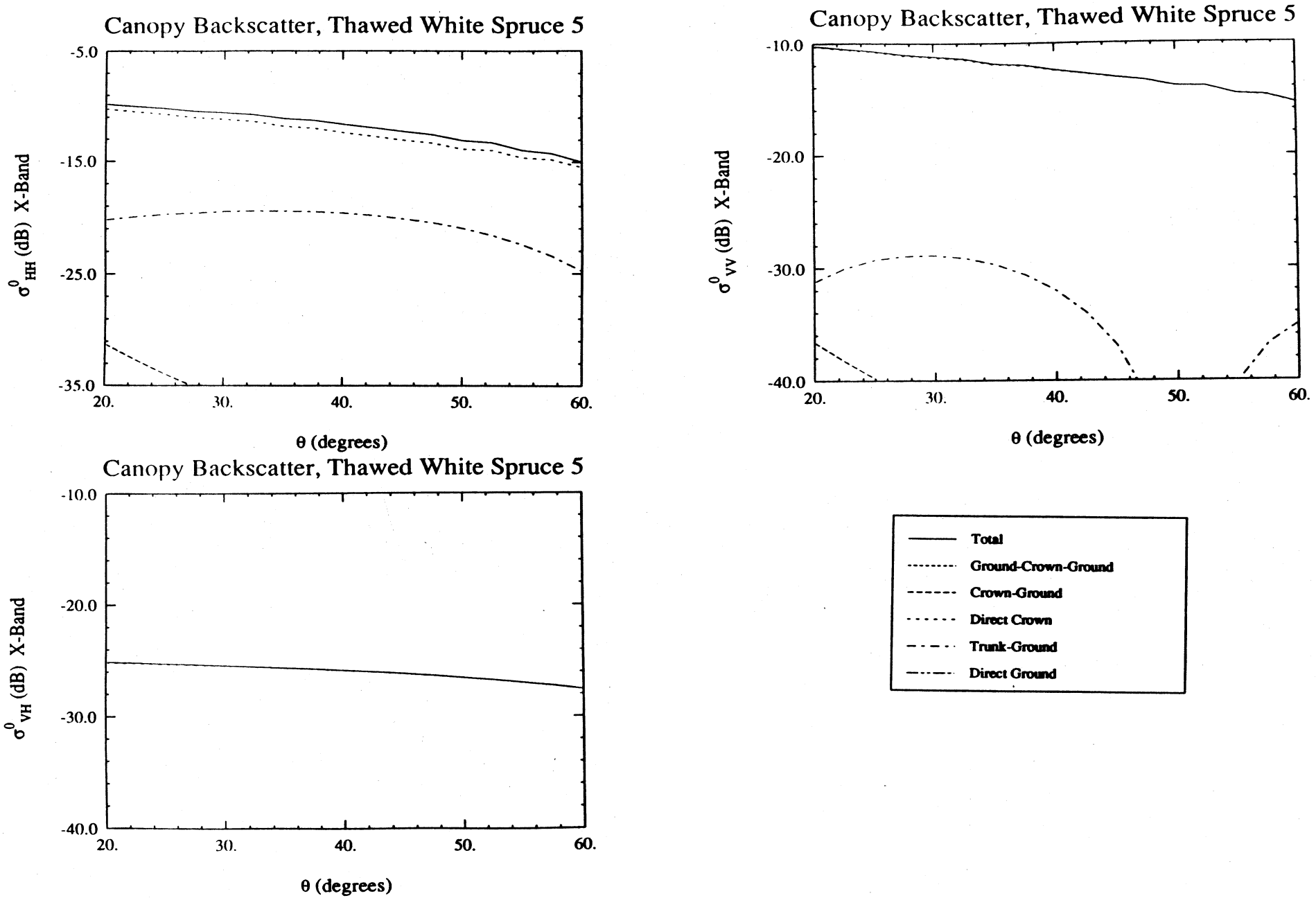

Figure 52. Components of modelled backscatter at X-band for white spruce 5 with thawed conditions.

for the frozen conditions except at L-band where the ground-crown interaction term is enhanced by increased scattering in the thawed crown layer while the trunk-ground interaction term is reduced by the greater extinction during two-way propagation through the thawed crown layer.

Thus, for white spruce stand WS-5, MIMICS predicts that the freezing of a previously thawed stand will result in a decrease in σ^o at L-band for all polarizations. In addition, the relative secondary importance of the multiple interaction terms involving forward scattering from the snow layer is shown to be more significant for the frozen conditions than for the thawed conditions at L-band. Although the higher dielectric constants characterizing the thawed conditions induce greater forward scatter from various canopy components and the snow surface, the extinction of the canopy layer is also greatest for the thawed conditions. This model result is confirmed by the polarimeteric L-band SAR observations which clearly indicate a greater tendency toward dihedral-like "double-bounce" returns in the frozen condition imagery obtained on March 13. Figure 53 illustrates this effect with polarization signatures for white spruce stand WS-4 obtained on the two dates.

MIMICS results for the other white spruce stands with greater and lower biomass are very similar to those presented for WS-5 in Figures 45 to 52. Model predictions of net backscatter from stands WS-2 and WS-1 are shown in Figures 54 to 57 for both frozen and thawed conditions. Average aboveground biomasses are computed to be 21.7, 16.7 and 18.1 kg/m^2 for stands WS-1, WS-2 and WS-5 respectively. Comparison of Figures 54 to 57 to Figures 45 and 49 shows that σ^o is not simply proportional to net biomass for all combinations of wave parameters and scene conditions (i.e., frozen and thawed).

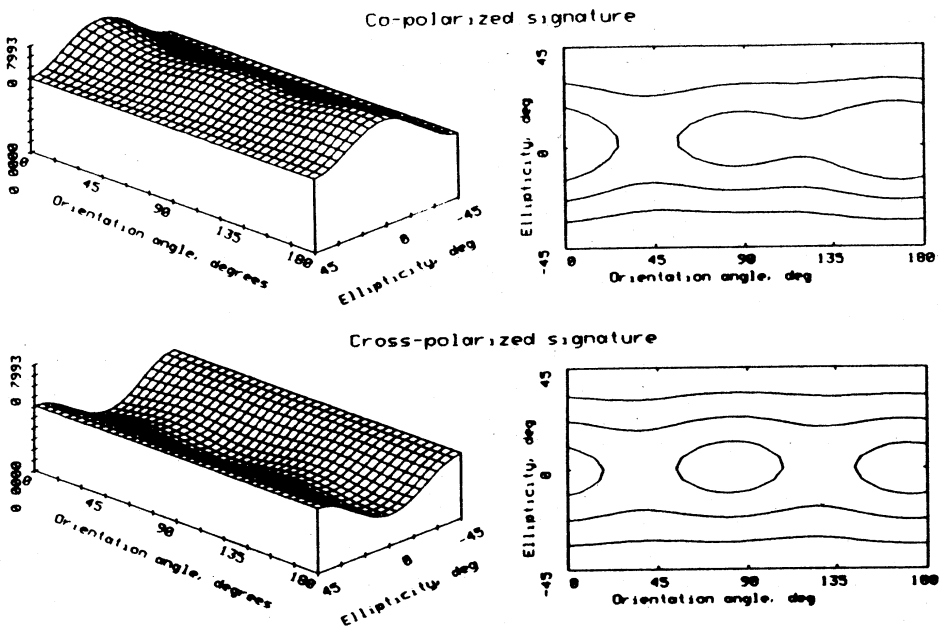

Site number 12
Site location 508 401

Incidence angle 43.671616
Size 23

Stokes matrix

1.000000	0.018502	-0.023713	-0.038406
0.018502	0.536007	-0.036165	0.012919
-0.023713	-0.036165	0.435779	0.004439
-0.038406	0.012919	0.004439	0.028215

Field products

ShhShh* =	0.79	ShhSvv* =	0.20
SvvSvv* =	0.75	ShhShv* =	-0.03 0.01
ShvShv* =	0.23	SvhSvv* =	0.01 0.03

Total power 130.616699
Coefficient of variation 0.28
Fractional polarization 0.56

Linear min, max	0.69	0.80	
Co pol max	0.80	0.00	170.00
Co pol min	0.48	-45.00	180.00
Cross pol max	0.49	45.00	180.00
Cross pol min	0.23	0.00	170.00

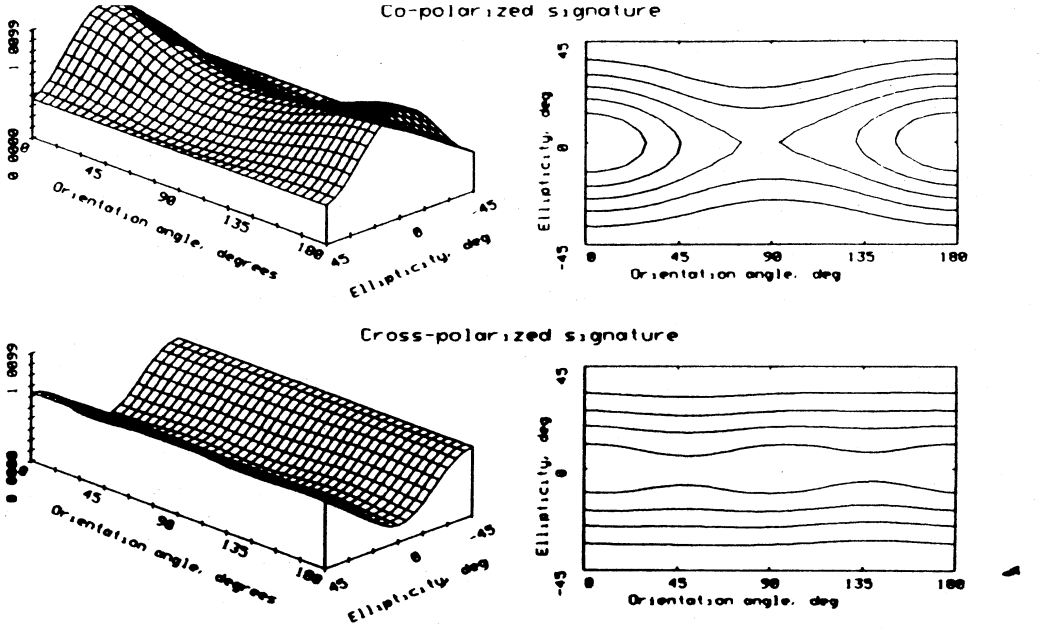

Site number 12
Site location 424 442

Incidence angle 43.140747
Size 23

Stokes matrix

1.000000	0.169844	-0.009993	0.001802
0.169844	0.680193	0.009915	-0.007679
-0.009993	0.009915	0.598790	0.030180
0.001802	-0.007679	0.030180	-0.278982

Field products

ShhShh* =	1.01	ShhSvv* =	0.44
SvvSvv* =	0.67	ShhShv* =	0.00 0.00
ShvShv* =	0.16	SvhSvv* =	-0.01 0.00

Total power 49.472729
Coefficient of variation 0.16
Fractional polarization 0.73

Linear min, max	0.67	1.01	
Co pol max	1.01	0.00	180.00
Co pol min	0.34	40.00	85.00
Cross pol max	0.64	45.00	180.00
Cross pol min	0.16	0.00	5.00

Figure 53. Comparison of L-band polarization signatures for white spruce stand WS-4 with thawed (3/13/88) and frozen (3/19/88) conditions.

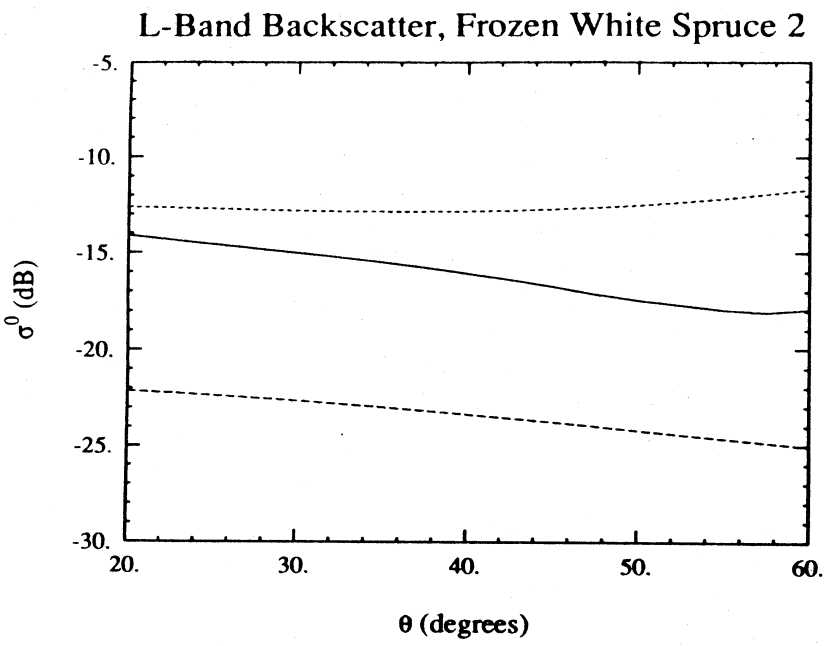

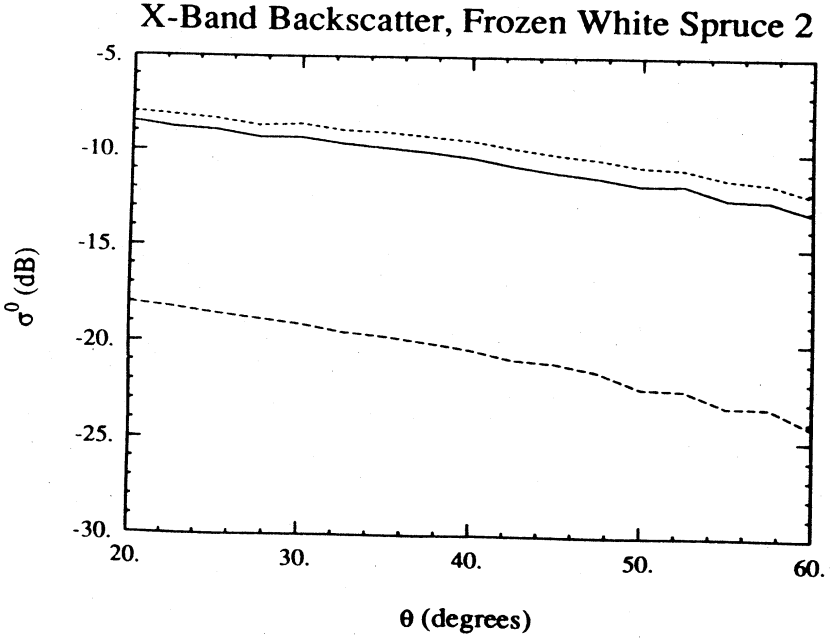

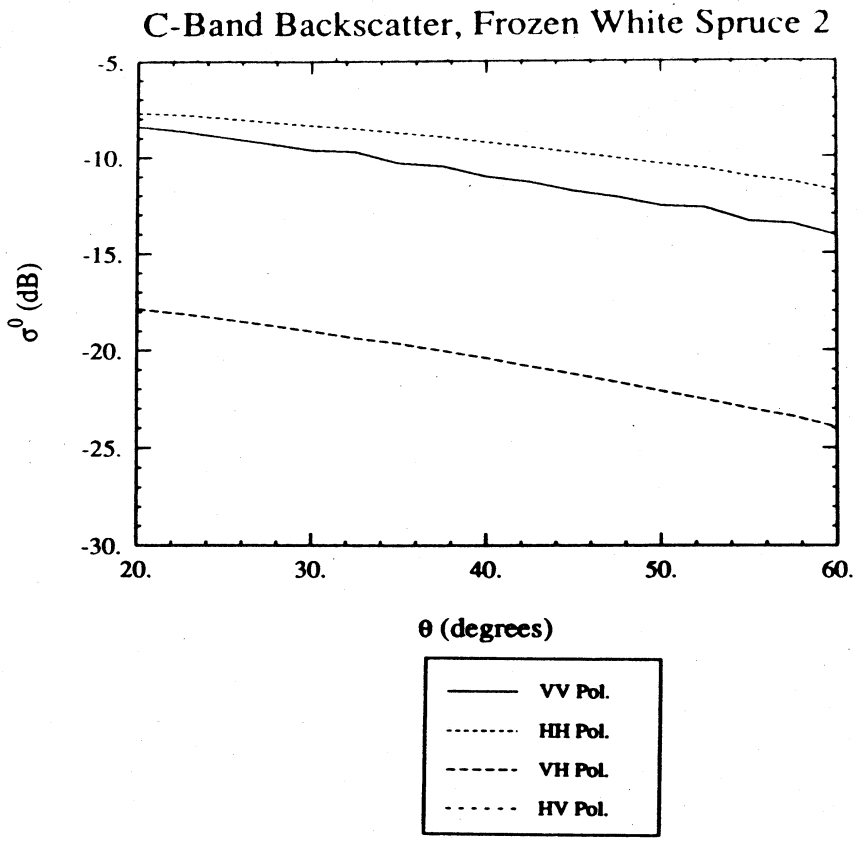

Figure 54. Modelled backscatter for white spruce 2 with frozen conditions.

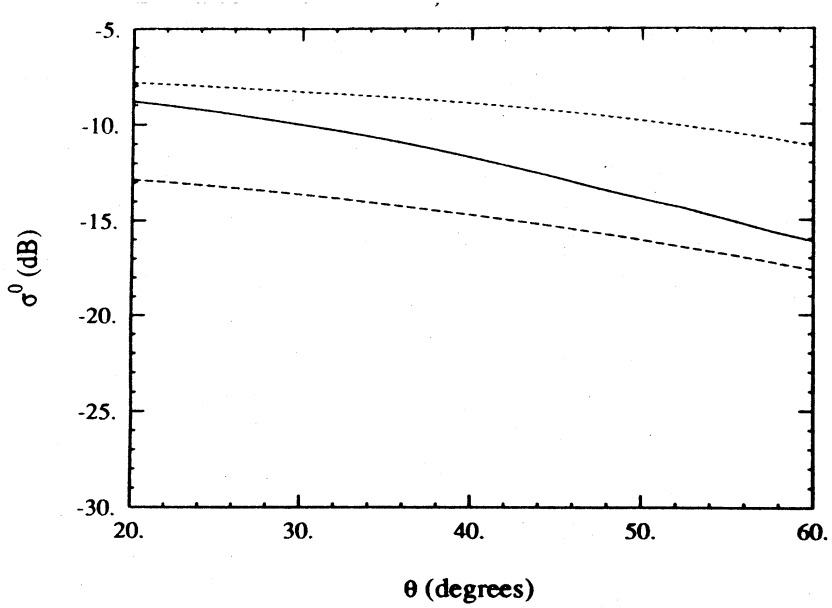

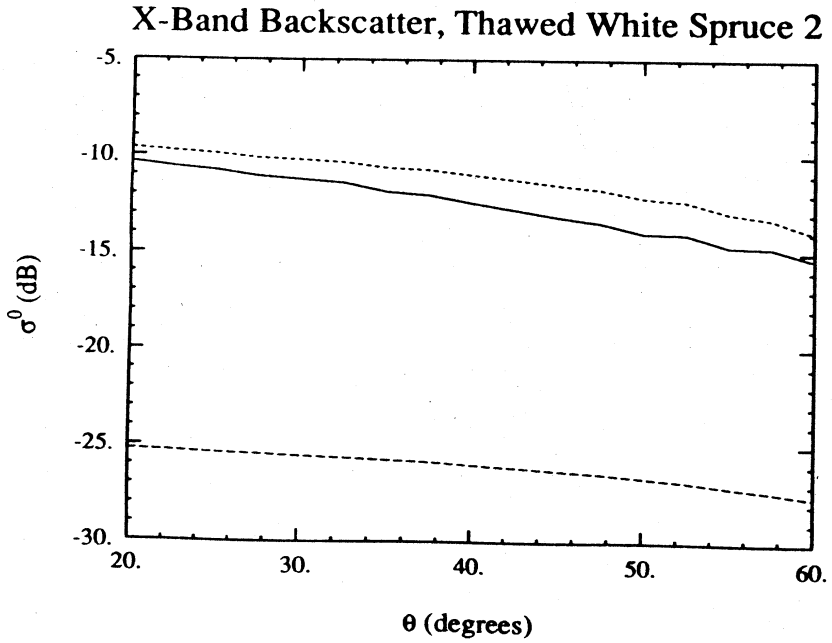

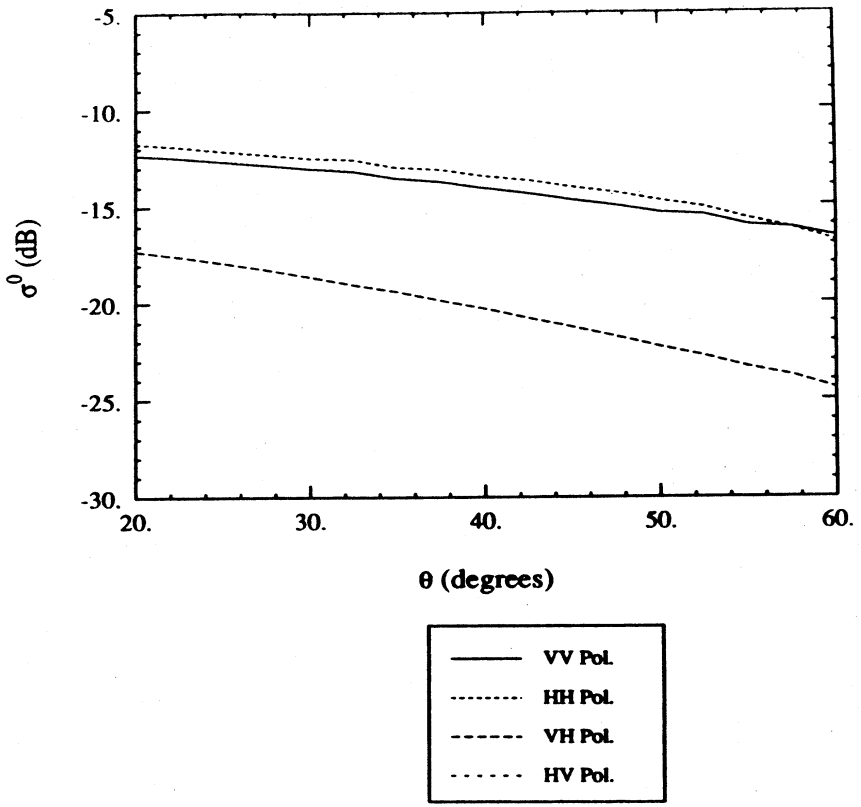

Figure 55. Modelled backscatter for white spruce 2 with thawed conditions.

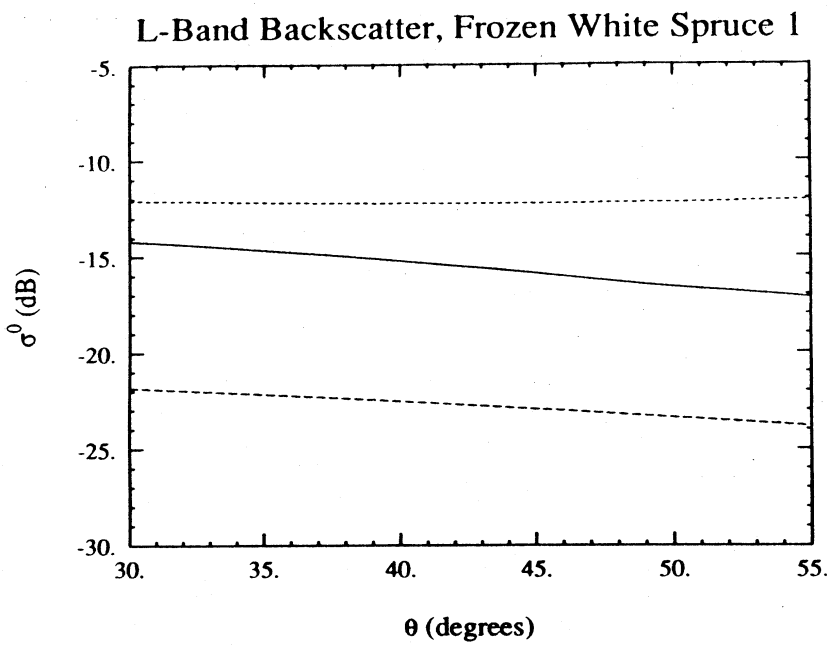

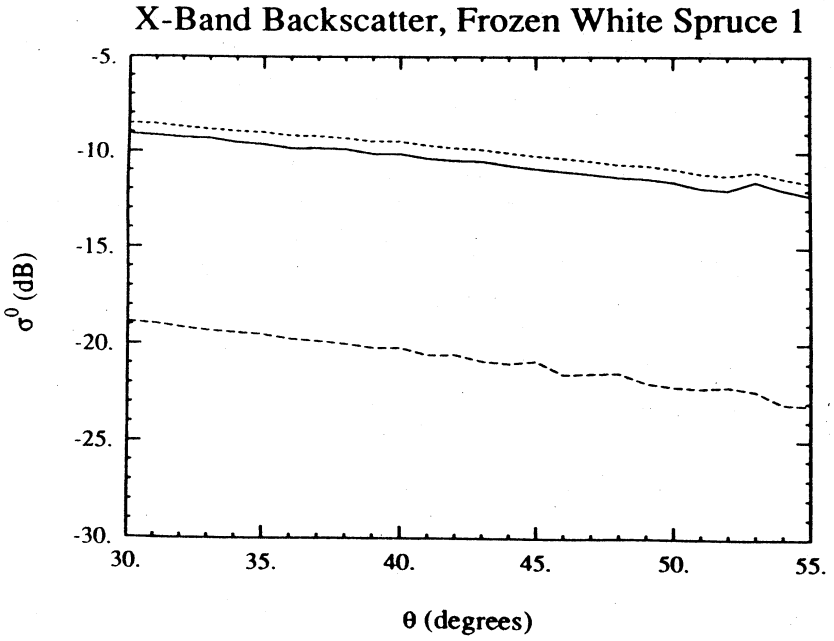

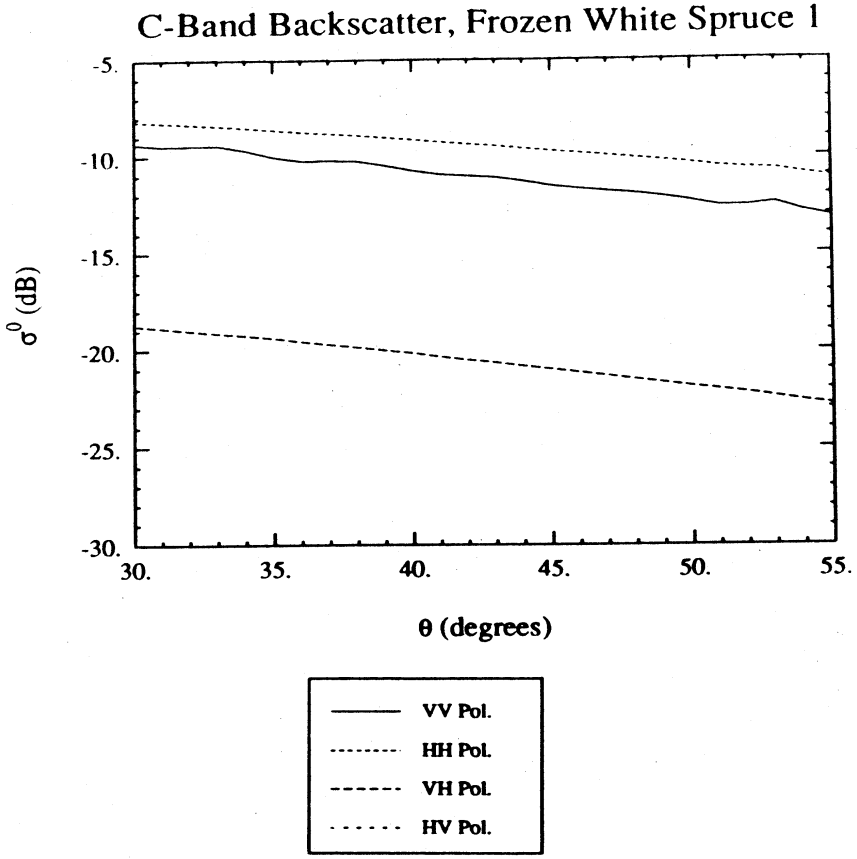

Figure 56. Modelled backscatter for white spruce 1 with frozen conditions.

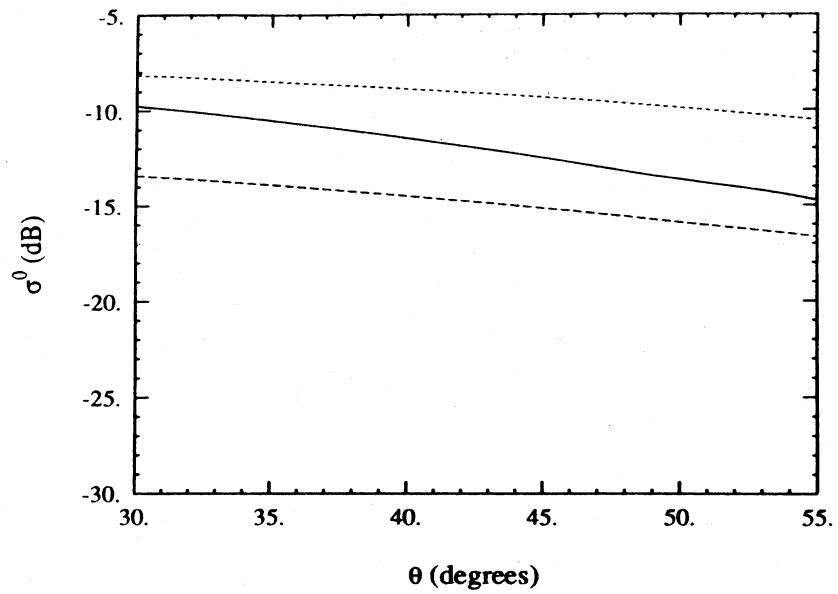

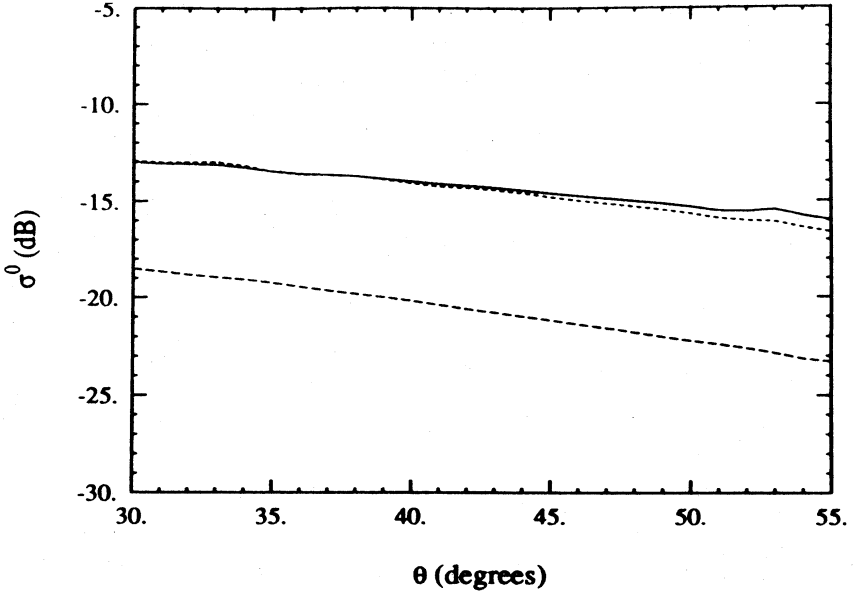

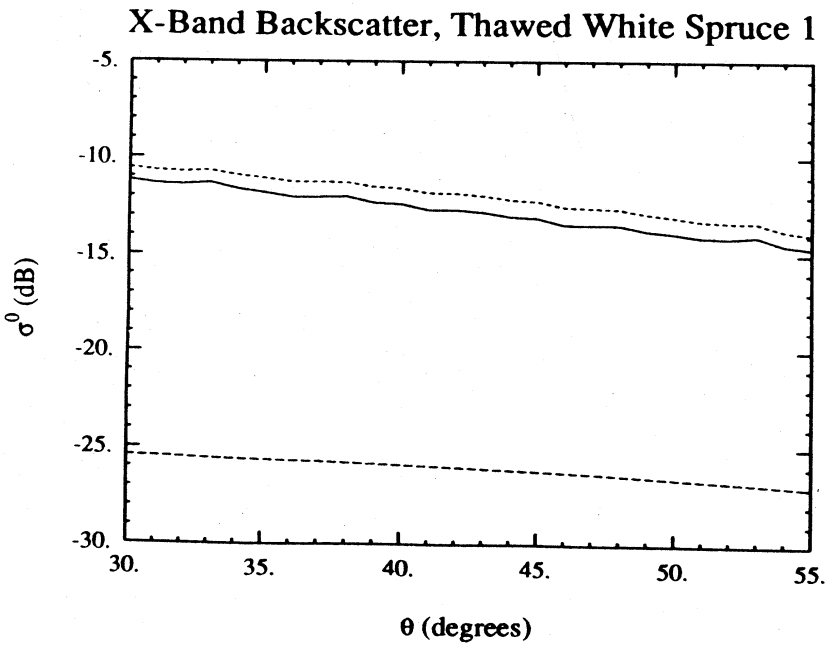

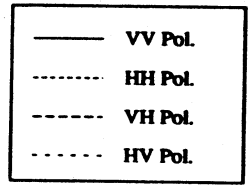

Figure 57. Modelled backscatter for white spruce 1 with thawed condtions.

Black Spruce

Black spruce stands at the Bonanza Creek Experimental Forest do not form closed canopies, and hence the simple two-layer canopy model used by MIMICS in the radiative transfer solutions does not strictly apply. However, the model is used to estimate the backscatter from stand BS-1 using the stand architecture and dielectric properties specified in Section 3 and with the surface layer treated as a half-space of snow.

MIMICS predictions of σ^o are shown in Figures 58 and 59 for frozen and thawed conditions respectively at L-, C- and X-bands. For the frozen condition, the backscatter from black spruce is estimated to be considerably less than that predicted for white spruce stands at all frequencies and polarizations. For the thawed condition, the backscatter from black spruce is less than that predicted for white spruce at all three polarizations at L-band and for VV and HV polarizations at C- and X-bands. The σ^o_{HH} at C- and X-bands is predicted to be higher for the black spruce than the white spruce. The biomass of the black spruce stand is 3.7 kg/m^2 which is about 20% that of the taller and denser white spruce stands. In addition, Figures 58 and 59 show $\sigma^o_{HH} >> \sigma^o_{VV}$ at all frequencies which contrasts with the results obtained for white spruce in Figures 45 and 49.

The relative contributions of the most significant source terms are shown for the frozen condition in Figures 60 and 61 for L- and C-bands, respecitvely, and for the thawed condition in Figures 62 and 63 for L- and C-bands, respectively. For L-band, σ^o_{HH} is dominated by the trunk-ground interaction term; the direct crown contribution to total backscatter is of secondary importance for frozen conditions (Figure 60) but is a major source term for thawed conditions (Figure 62) and especially at low angles of incidence. σ^o_{VV} and σ^o_{HV} at L-band are shown to be dominated by backscatter from the crown layer for both frozen and thawed conditions. For C-band and X-band (not shown), σ^o_{HH} is dominated by the ground-trunk interaction term

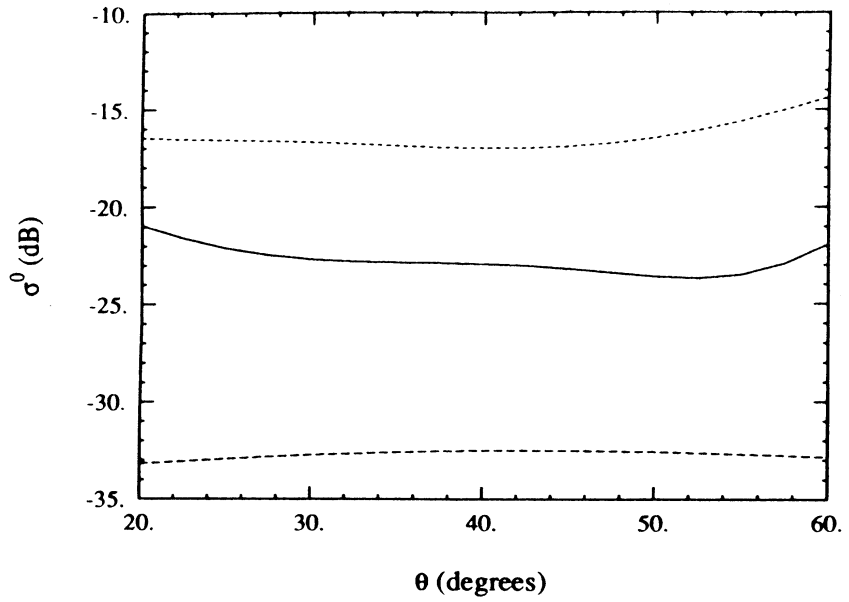

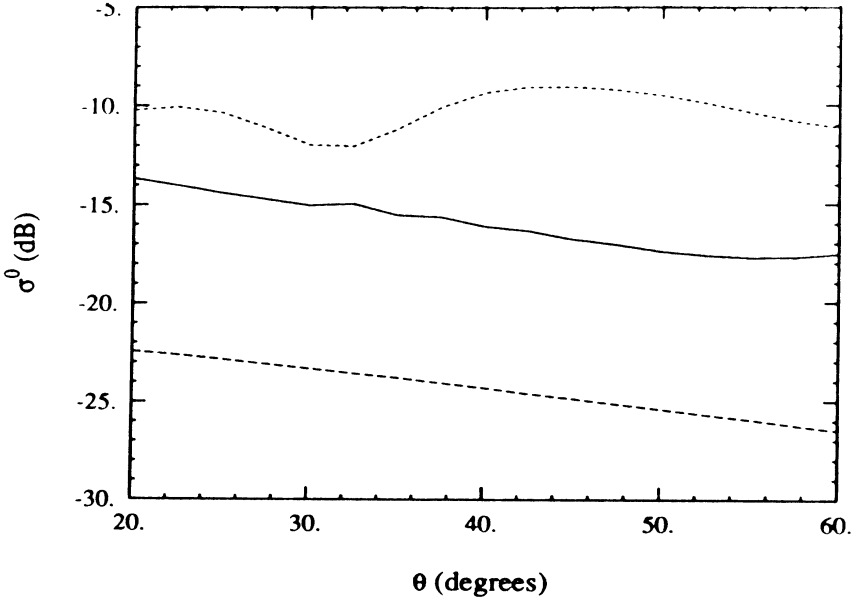

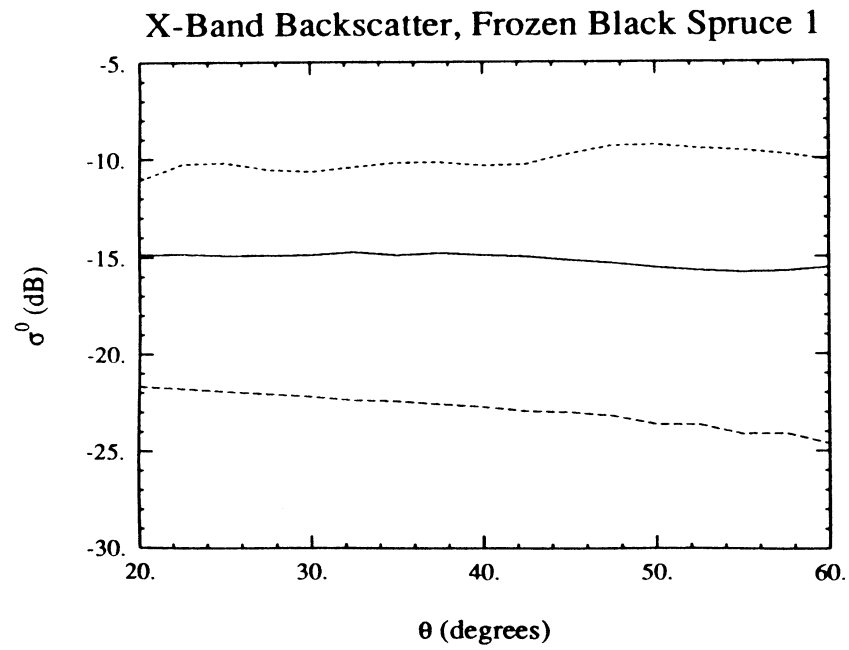

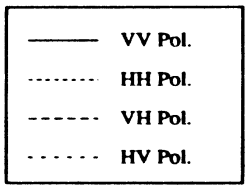

Figure 58. Modelled backscatter for black spruce 1 with frozen conditions.

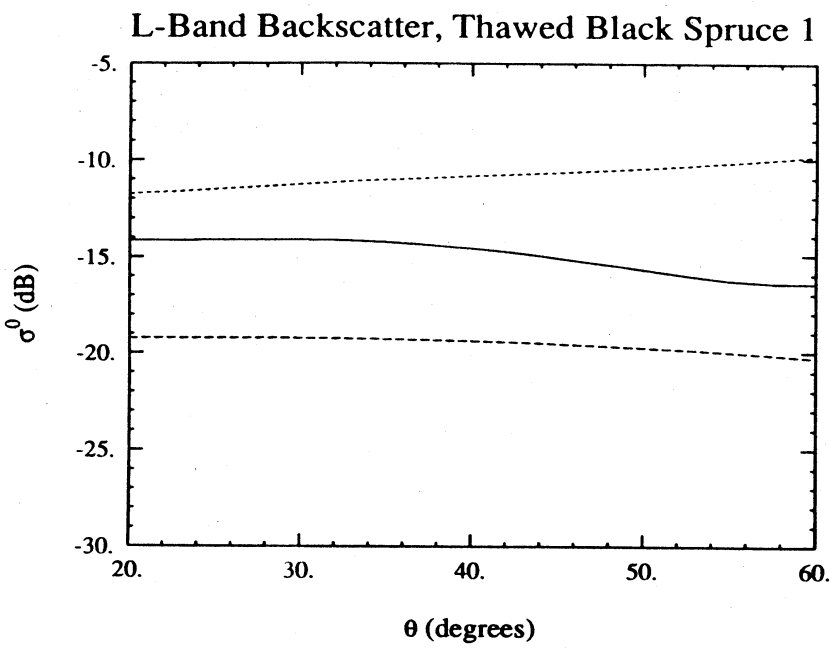

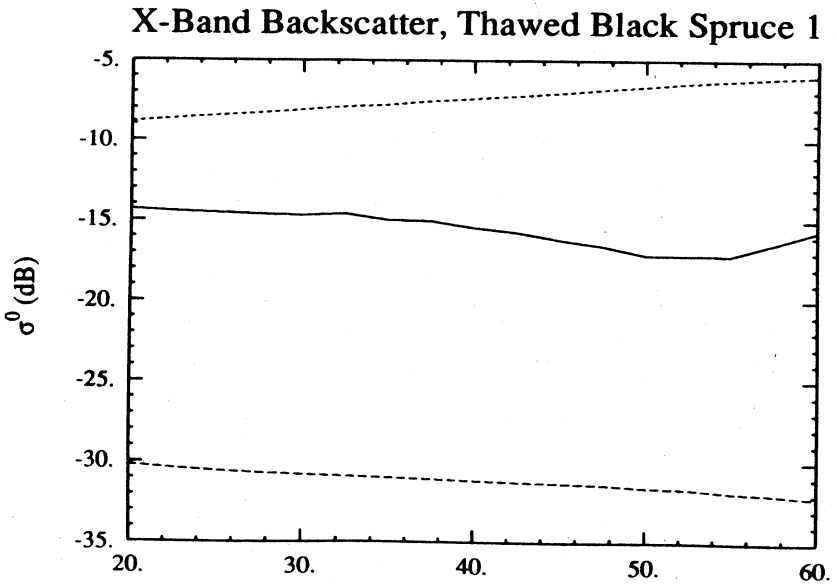

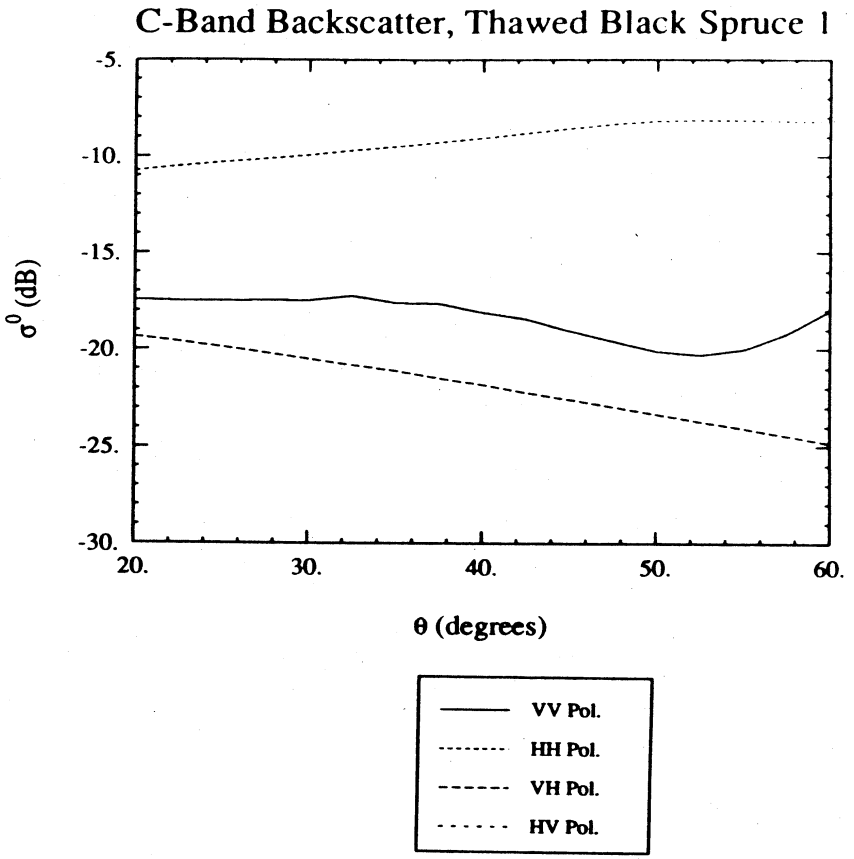

Figure 59. Modelled backscatter for black spruce 1 with thawed conditions.

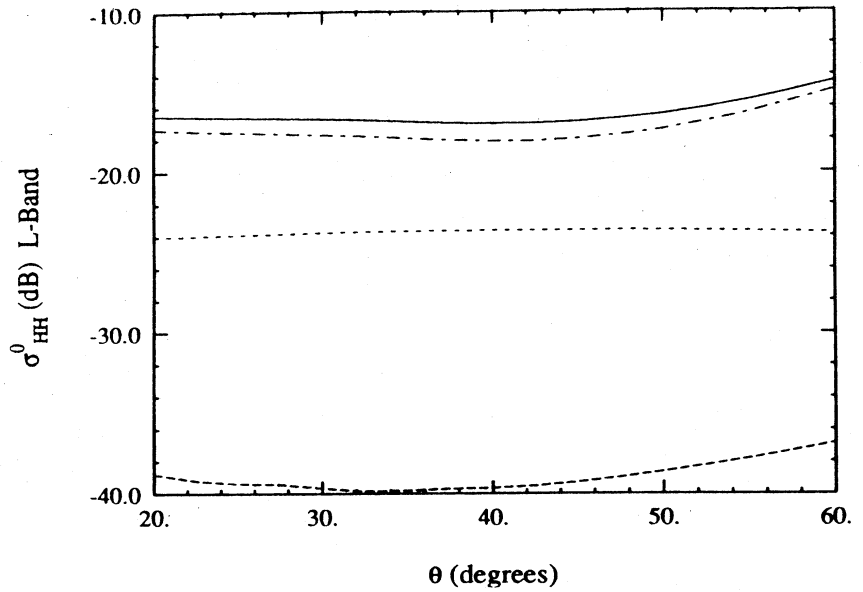

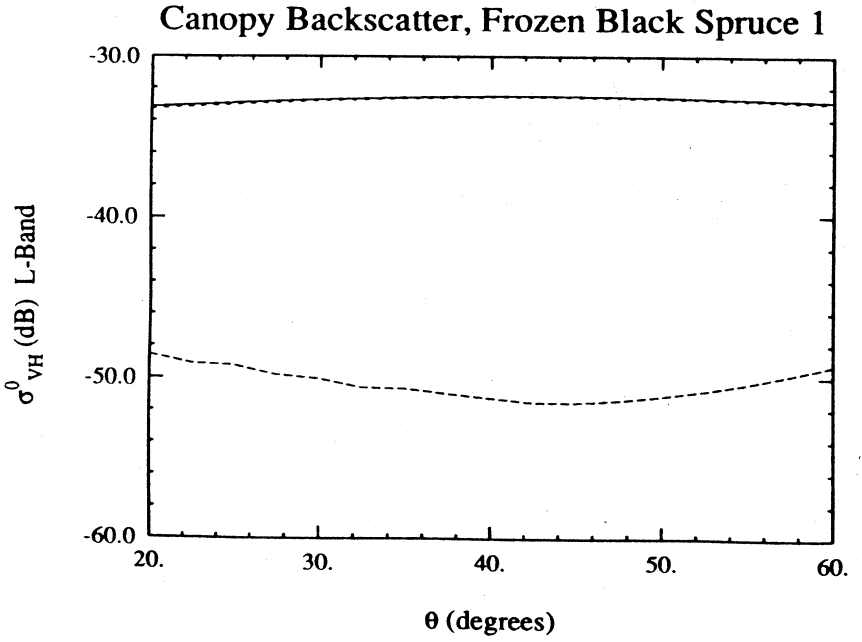

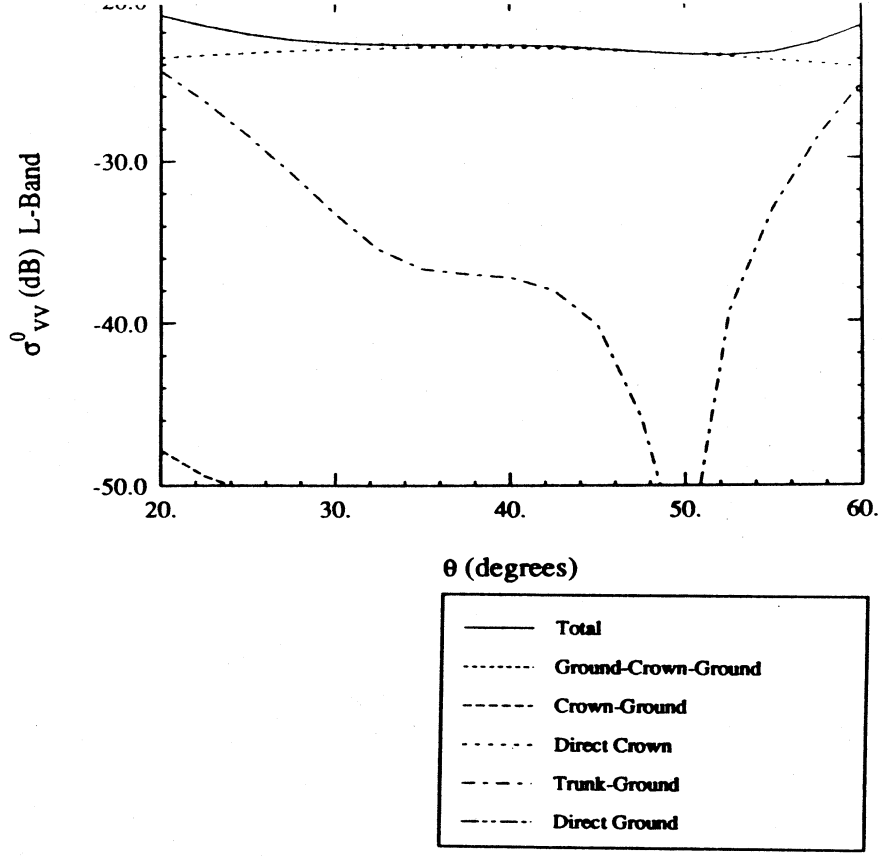

Figure 60. Components of modelled backscatter at L-band for black spruce 1 with frozen conditions.

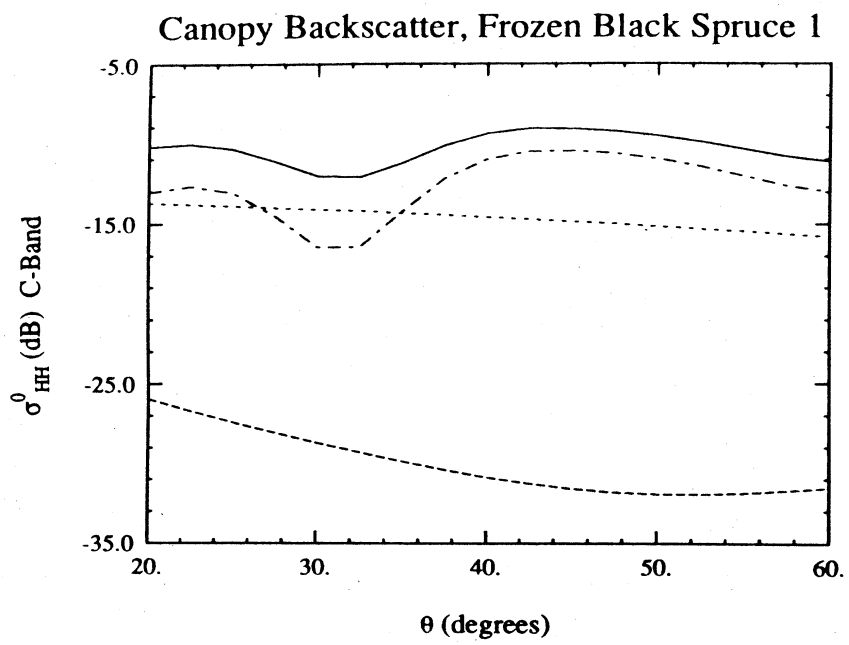

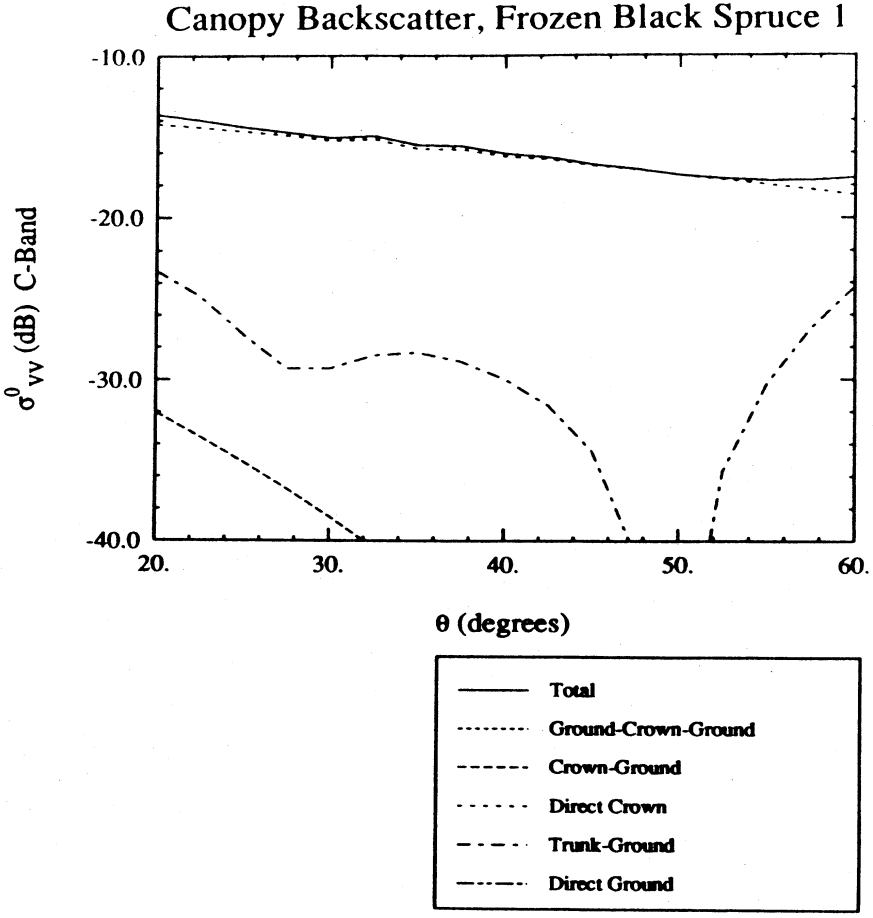

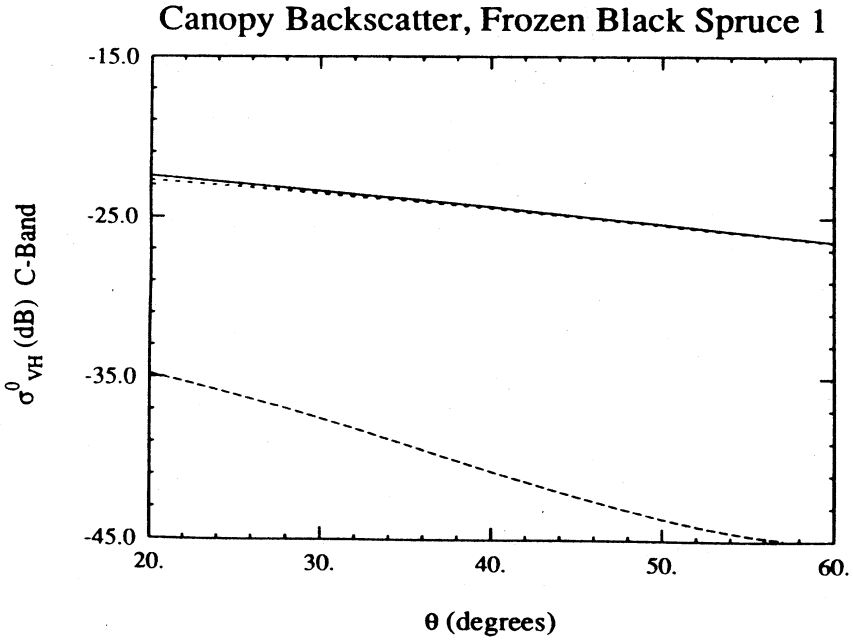

Figure 61. Components of modelled backscatter at C-band for black spruce 1 with frozen conditions.

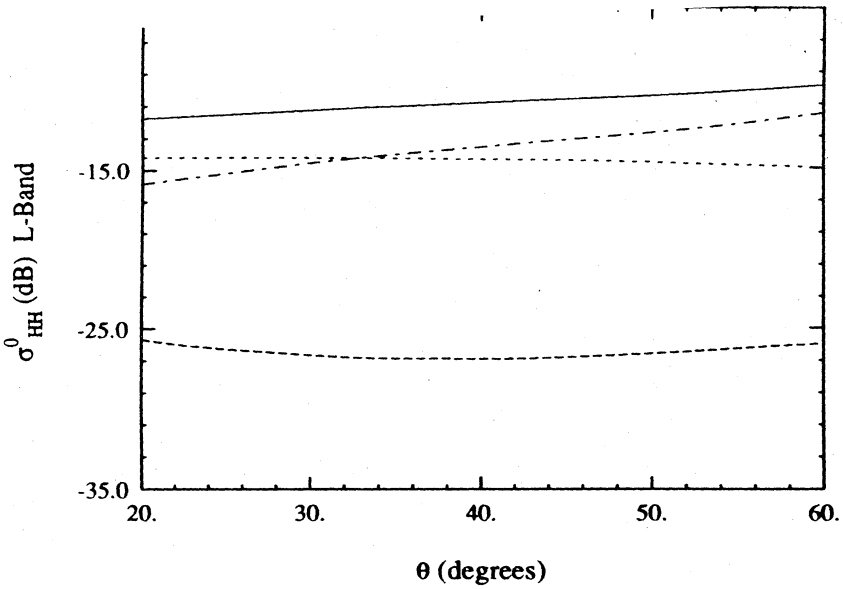

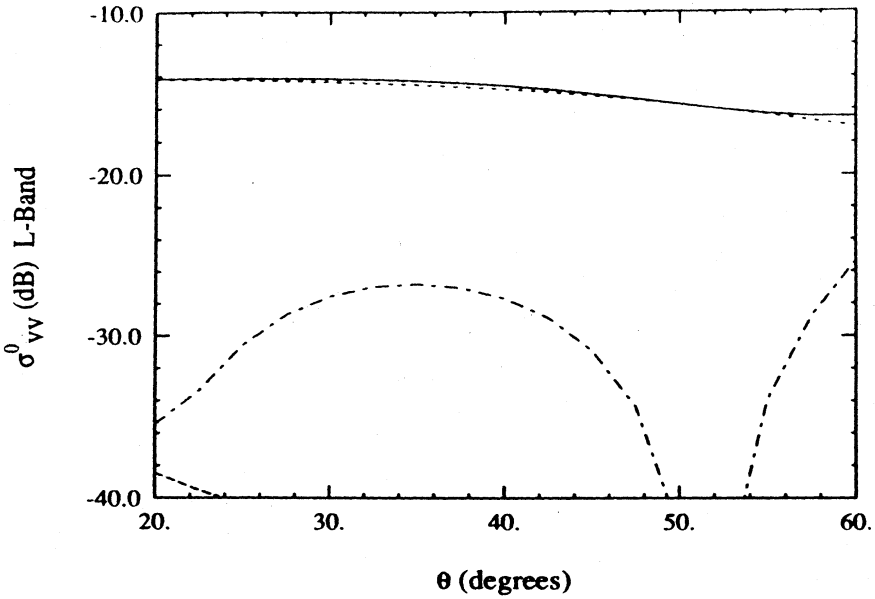

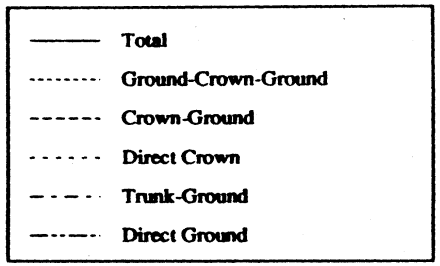

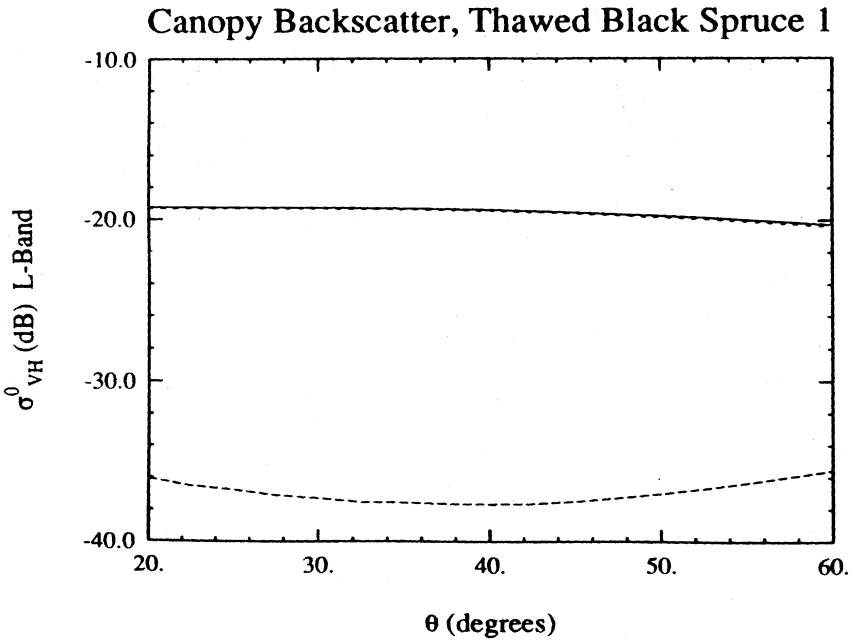

Figure 62. Components of modelled backscatter at L-band for black spruce 1 with thawed conditions.

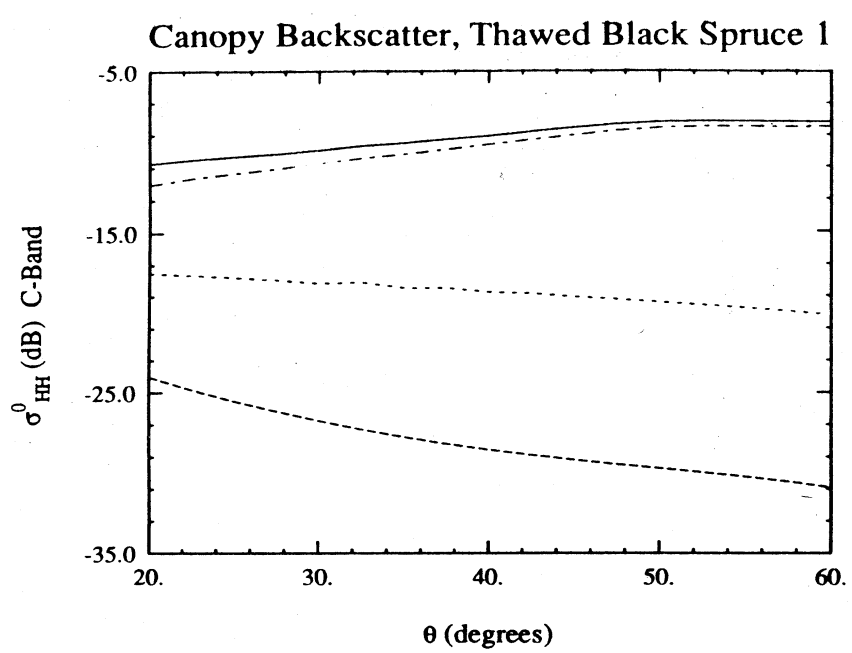

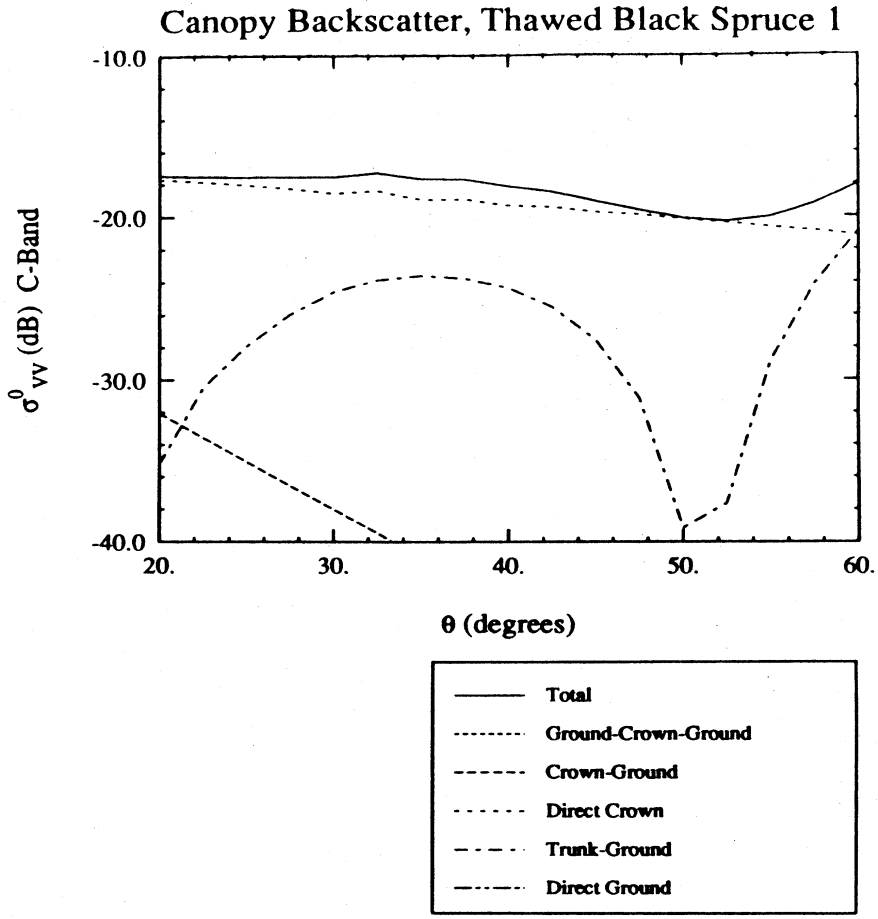

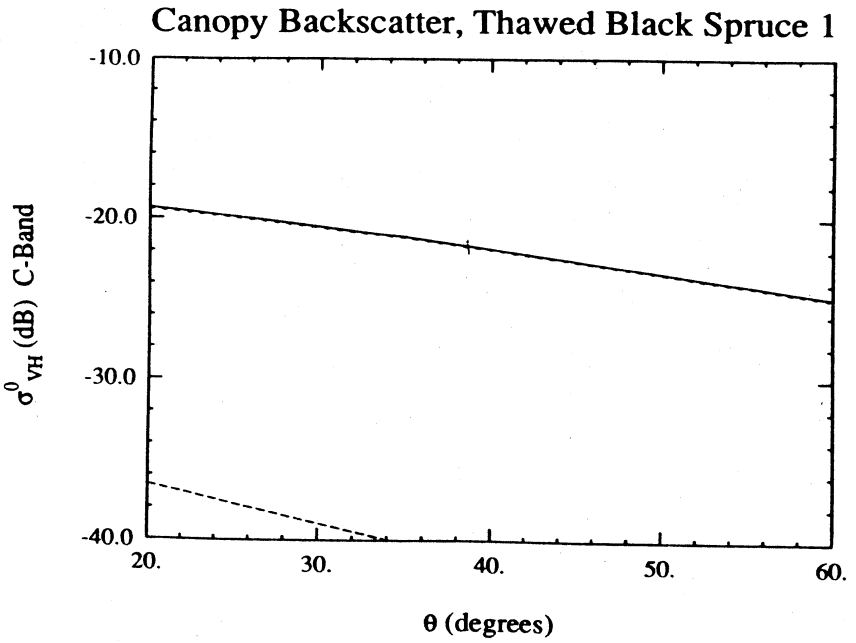

Figure 63. Components of modelled backscatter at C-band for black spruce 1 with thawed conditions.

while the backscatter at the other polarizations is controlled by the crown layer contribution.

For a sparse canopy such as black spruce, it is expected that direct backscatter from the snow-covered ground would be a significant scattering source at all three frequencies and at all polarizations. However, Figures 60 to 63 exhibit no backscatter contribution from the snow. Hence, the treatment of the snow as a half-space is clearly inadequate for such a sparse canopy. This situation can be rectified by treating the surface as a snow layer (of variable wetness) over a frozen soil substrate, but requires a matching of the boundary roughness conditions to provide appropriate estimates of backscatter. In addtion, inclusion of a two-layer radiative transfer solution for snow over soil will also enhance the specular scattering from the surface (particularly at L- and C-bands) since the dielectric constant of the frozen soil is known to be much greater than that of the snow. As a consequence, the MIMICS simulations illustrated by Figures 58 to 63 should underestimate σ^o especially for VV and HV polarizations under frozen conditions.

Balsam Poplar

Balsam poplar stand BP-2 is a mature closed-canopy stand, and therefor is relatively well-suited to simulation of backscatter using MIMICS. The tree density, height, diameter and biomass of this stand are similar to those of white spruce stand WS-5 whose MIMICS simulations are depicted in Figures 45 to 52. However, the modeled branch architecture of the balsam poplar is very dissimilar to that of white spruce, and the balsam poplars have no foliage. The input parameters used by MIMICS for balsam poplar stand BP-2 are specified in Section 3. The surface layer is modeled as a half-space of snow with dielectric properties as given in Section 3.

The net backscatter predicted by MIMICS for balsam poplar is plotted in Figures 64 and 65 for frozen and thawed conditions respectively. For the frozen condition, $\sigma^o_{HH}/\sigma^o_{VV}$ is

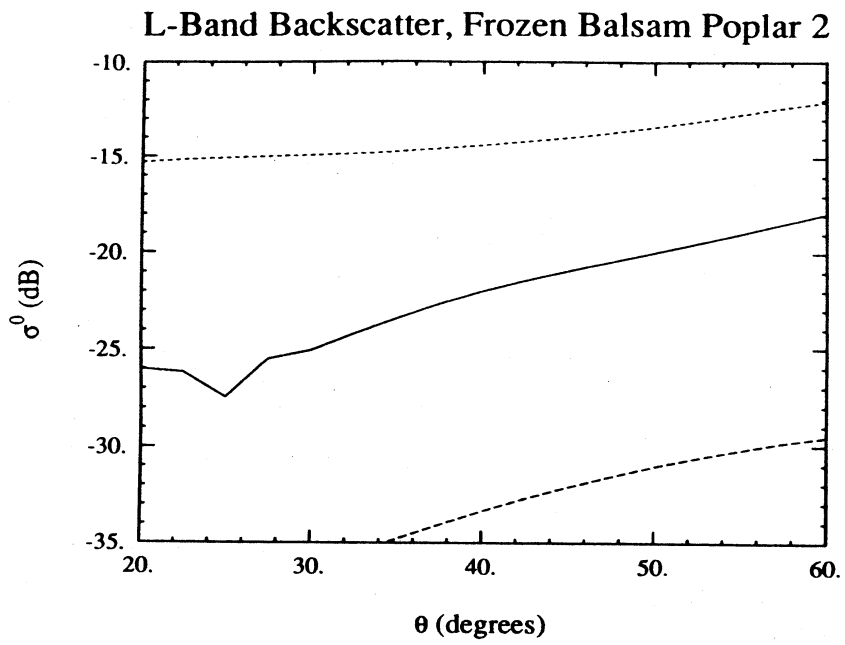

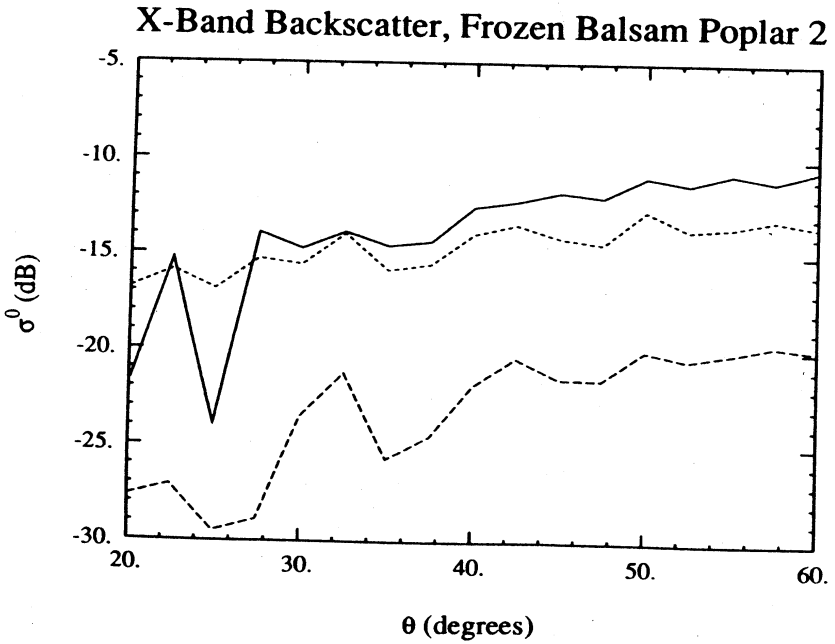

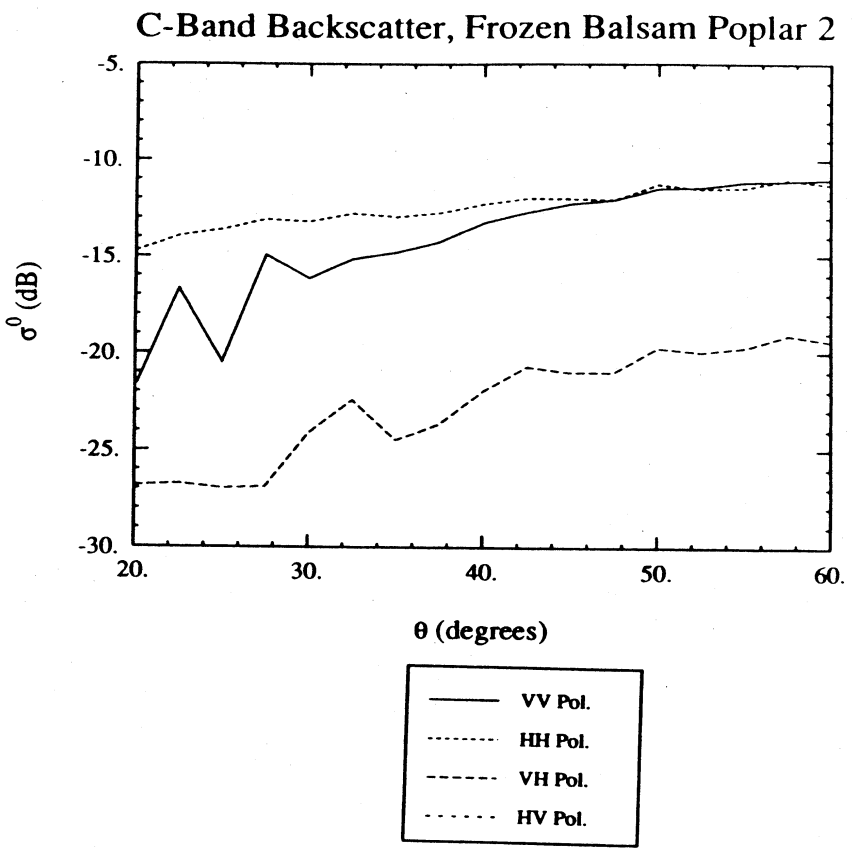

Figure 64. Modelled backscatter for balsam poplar 2 with frozen conditions.

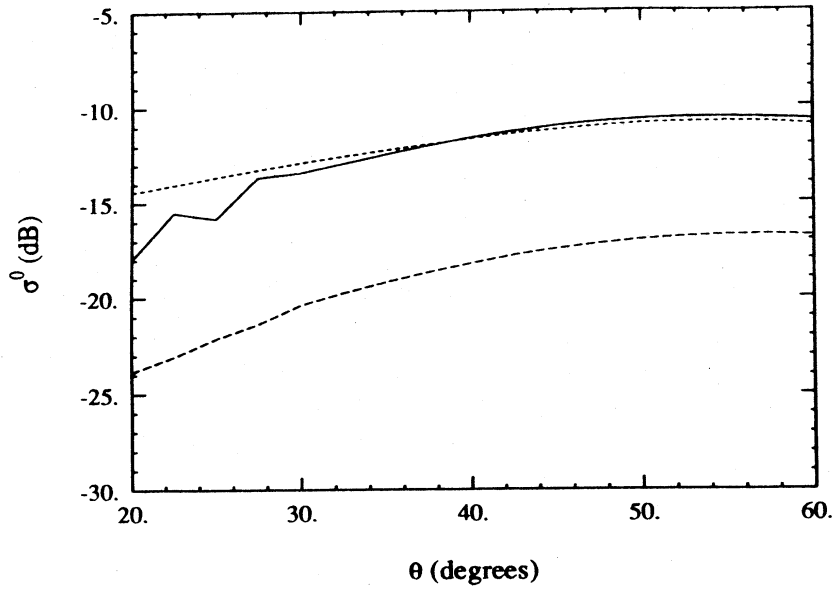

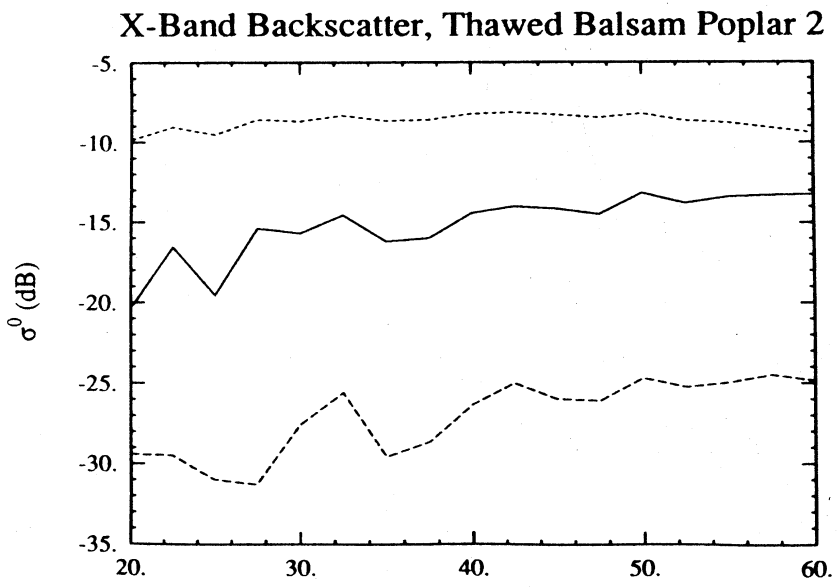

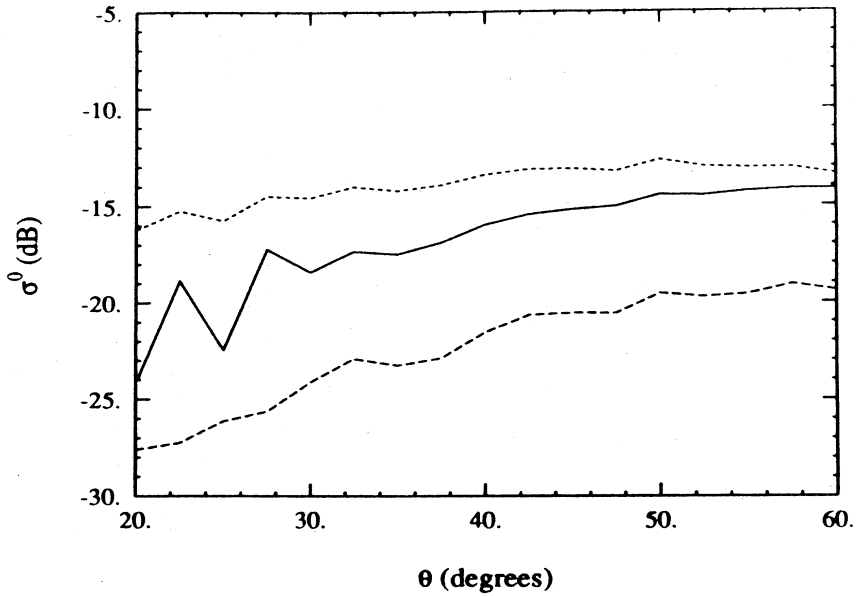

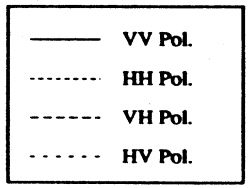

Figure 65. Modelled backscatter for balsam poplar 2 with thawed conditions.

shown to decrease with frequency in Figure 64, while the opposite is predicted for the thawed condition in Figure 65. In general, σ^o is shown to increase with frequency for a given polarization. σ^o is also shown to increase with angle of incidence; the non-monotonic behavior is due to the branch angle and size distributions of the crown layer. In a fashion similar to the L-band responses to white spruce and black spruce, the backscatter for the thawed conditions is always shown to exceed that for the frozen conditions at L-band. The effects of freezing and thawing at C- and X-bands are shown to be much more complicated.

The contributions of various source terms to the total backscatter are shown for frozen conditions by Figures 66 and 67 for L-band and C-band, respectively and for thawed conditions by Figures 68 and 69 for L- and C-bands, respectively. Again, the HH polarized backscatter is found to be dominated by the trunk-ground interaction term as supported by lesser contributions from scattering by the crown layer and from crown-ground interaction mechanisms. The VV and HV polarized backscatter is predicted by MIMICS to be almost entirely determined by backscatter from the crown-layer.

As mentioned previously with regards to the MIMICS simulations for black spruce, Figures 66-69 show that backscatter from the snow layer is predicted to also be negligible for balsam poplar. Since for frozen conditions, the canopy extinction for balsam poplar is modeled to be less than that for white spruce (as shown in Figures 70 and 71), it is expected that the treatment of the surface layer as a half-space of snow leads to an under prediction of σ^o by MIMICS particularly for σ^o_{VV} and σ^o_{HV}. The comparatively large propagation loss through the canopy modeled for balsam poplar with thawed conditions suggests that the failure to treat the surface layer in a more detailed fashion may not result in as large an under prediction for thawed conditions.

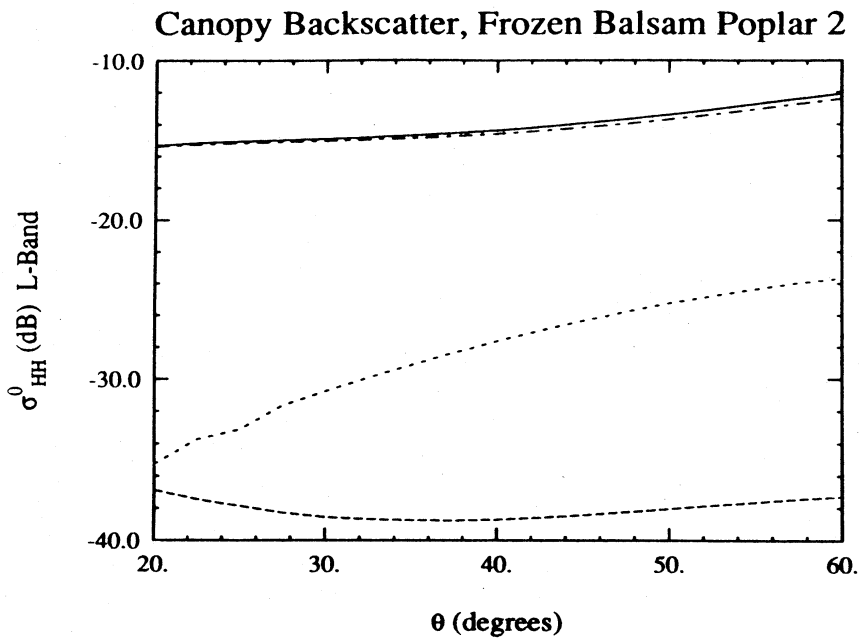

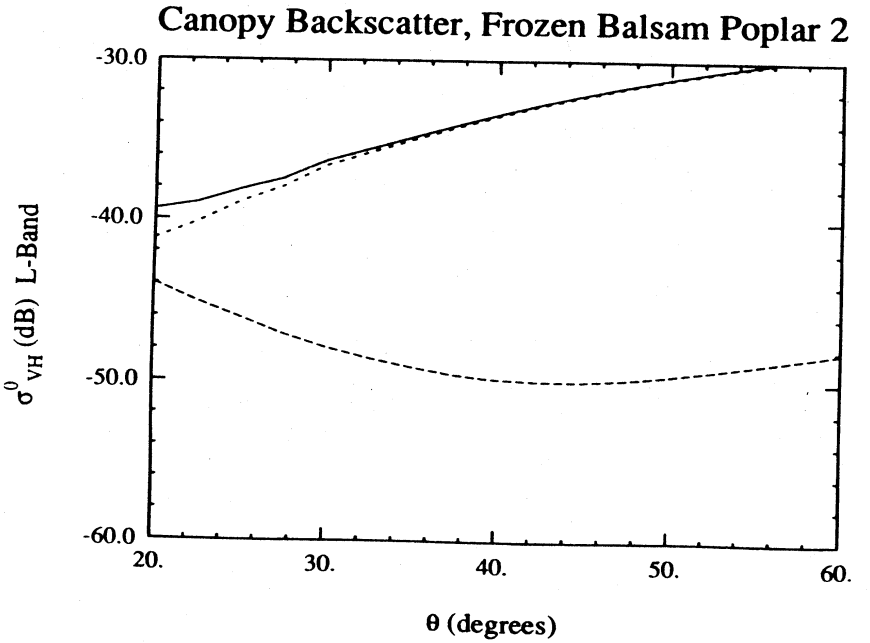

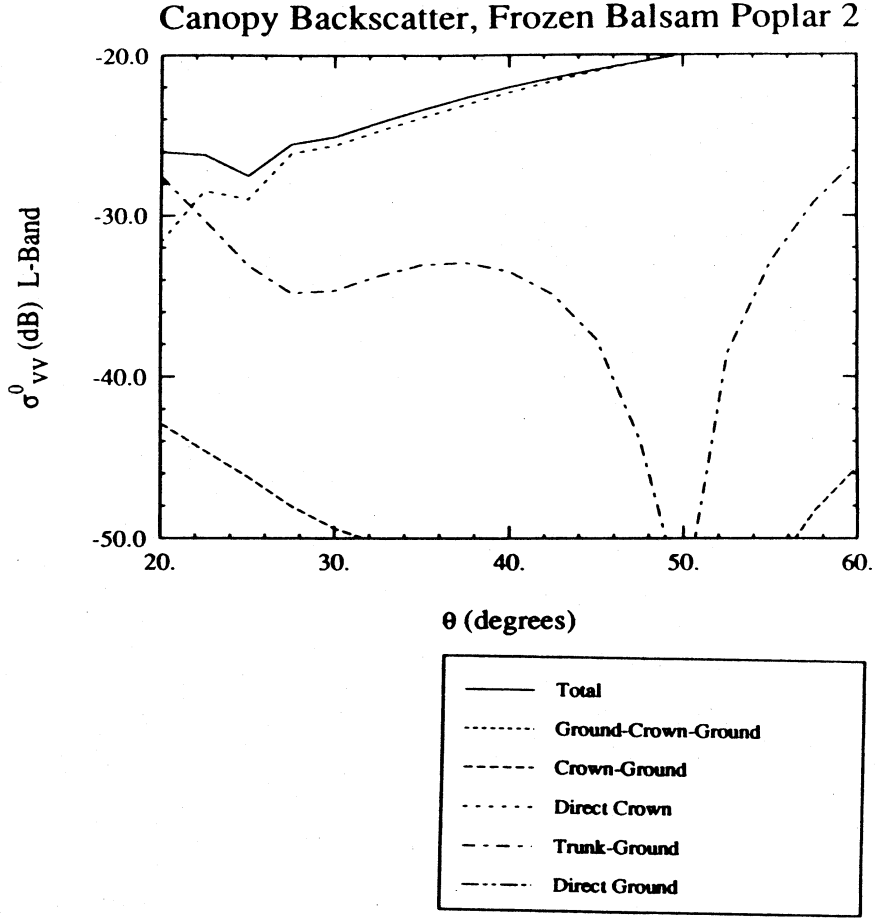

Figure 66. Components of modelled backscatter at L-band for balsam poplar 2 with frozen conditions.

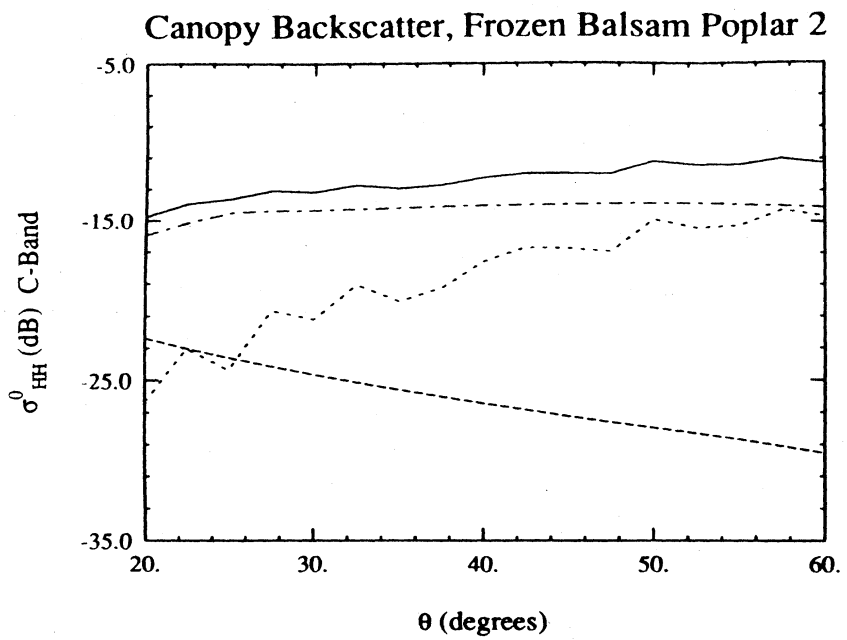

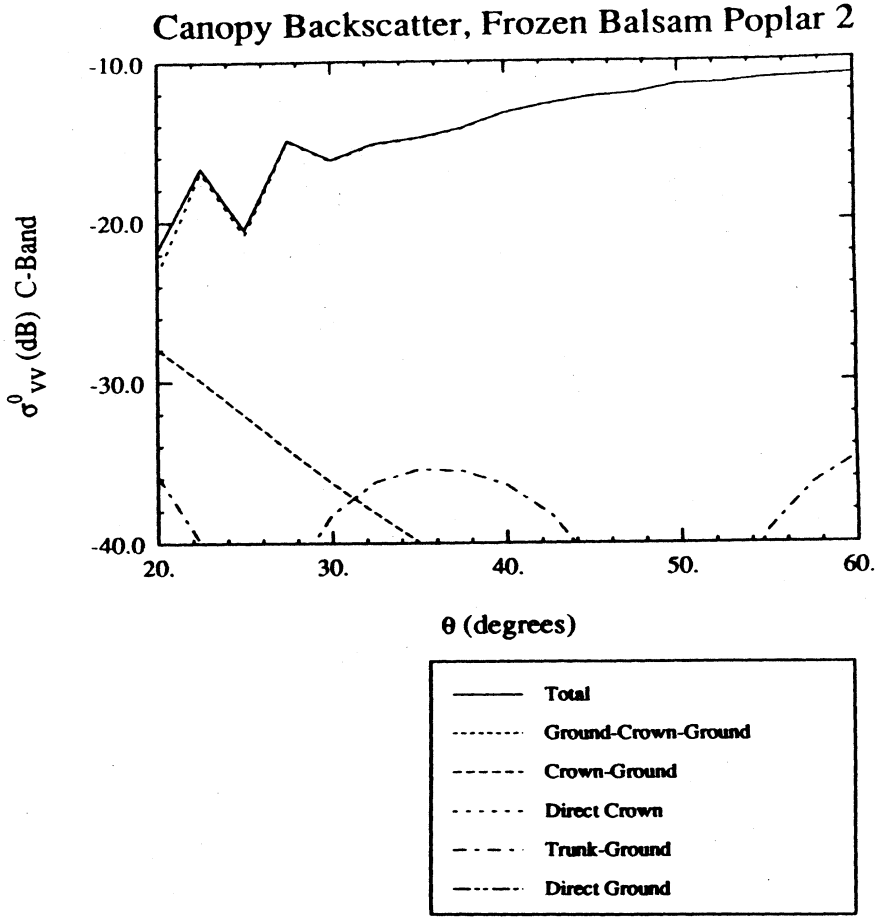

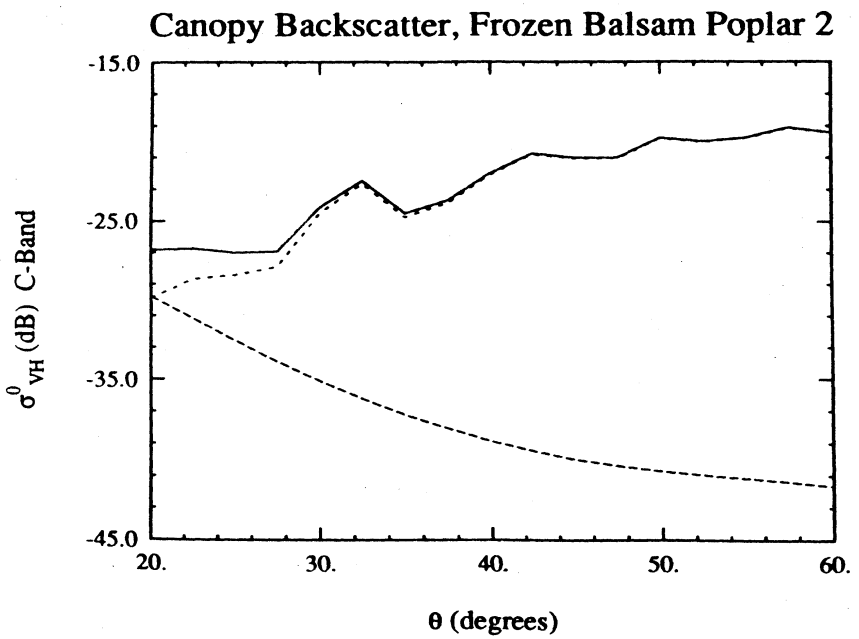

Figure 67. Components of modelled backscatter at C-band for balsam poplar 2 with frozen conditions.

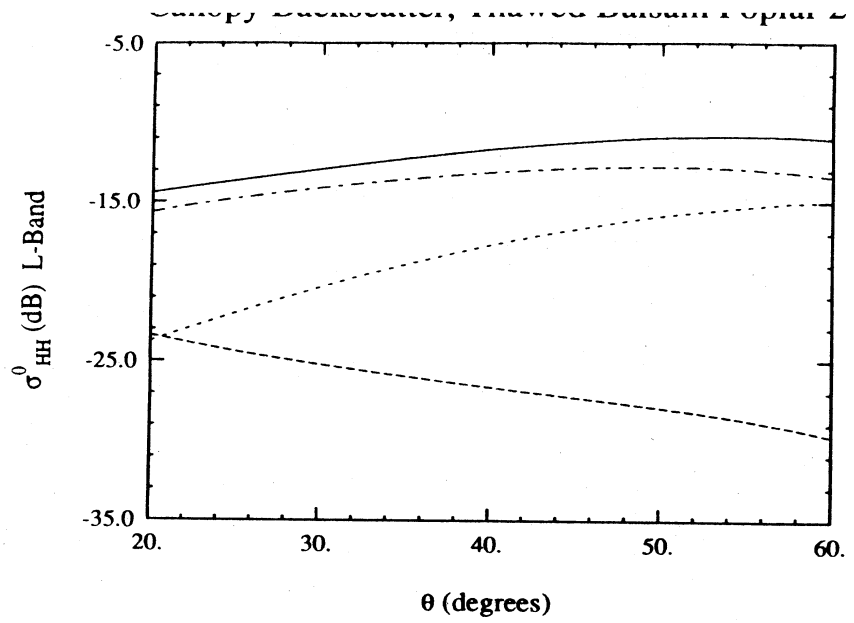

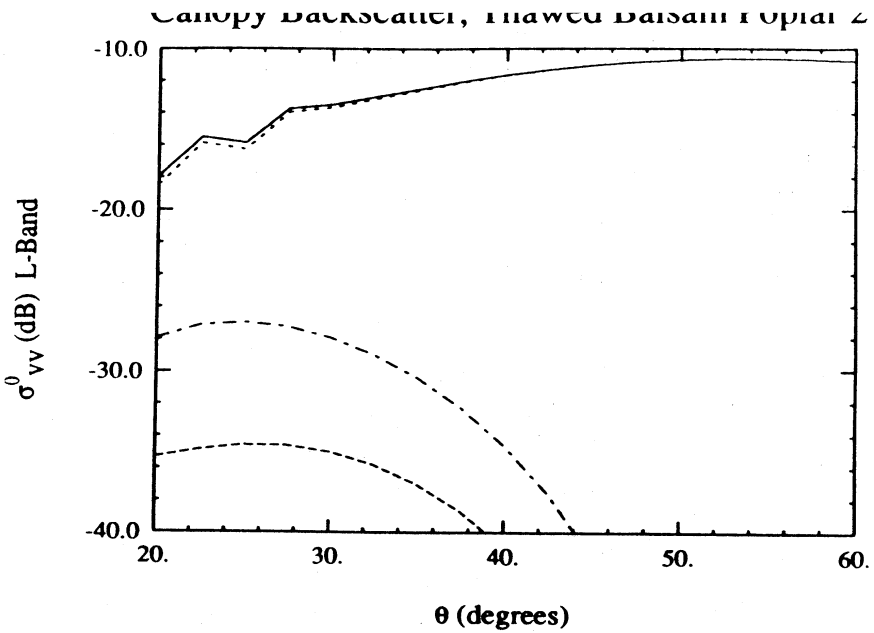

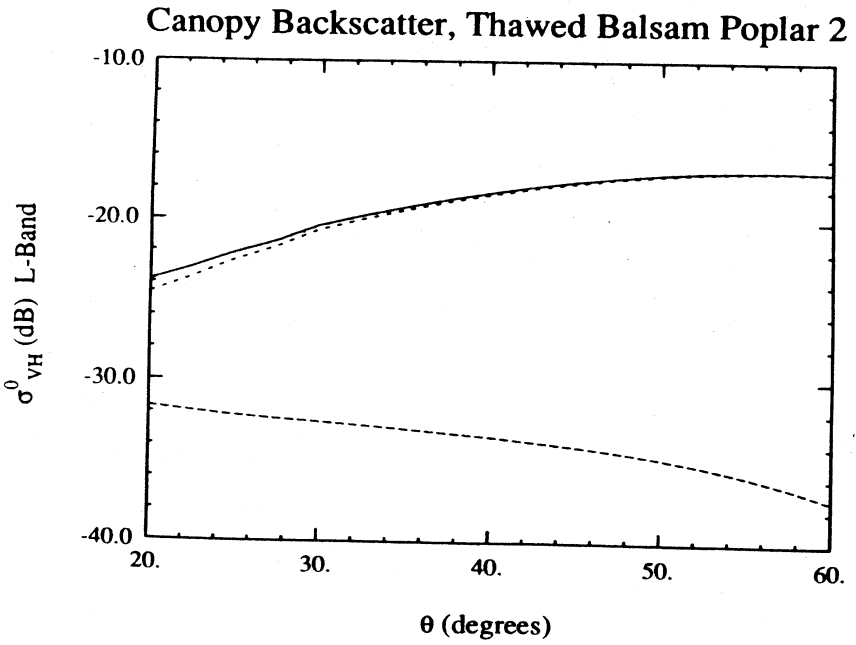

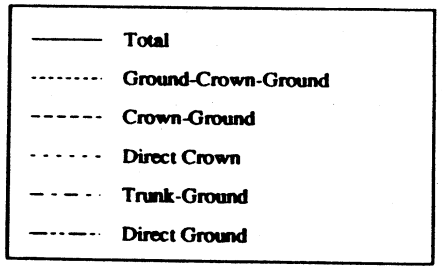

Figure 68. Components of modelled backscatter at L-band for balsam poplar 2 with thawed conditions.

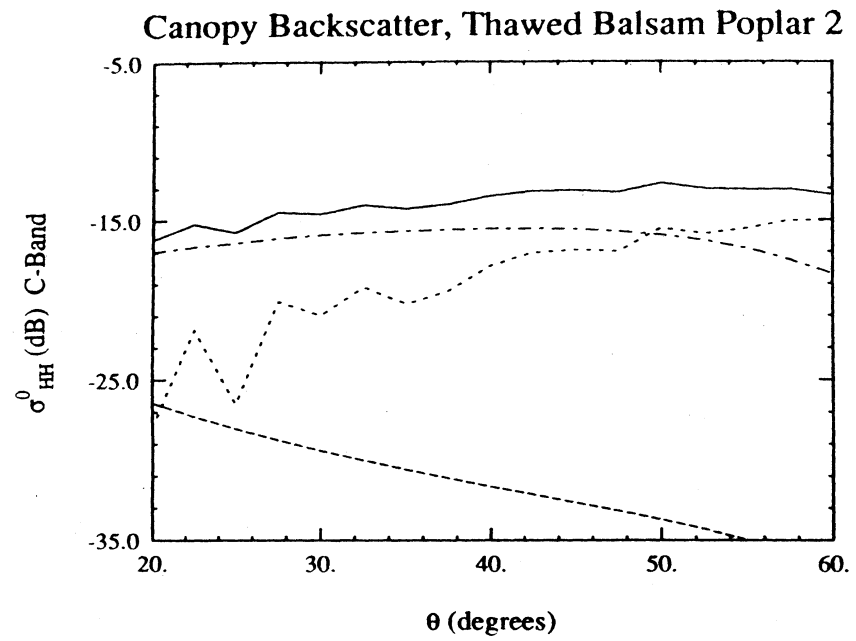

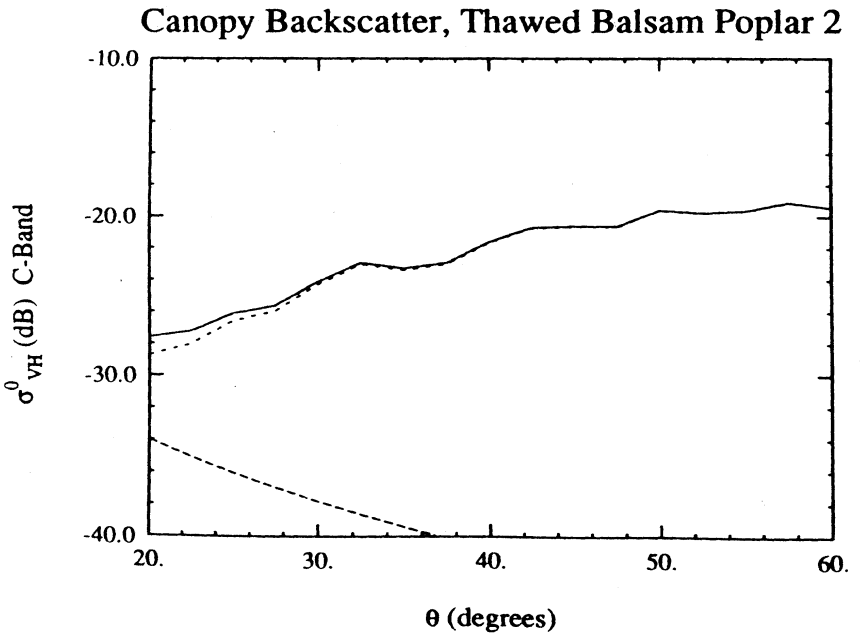

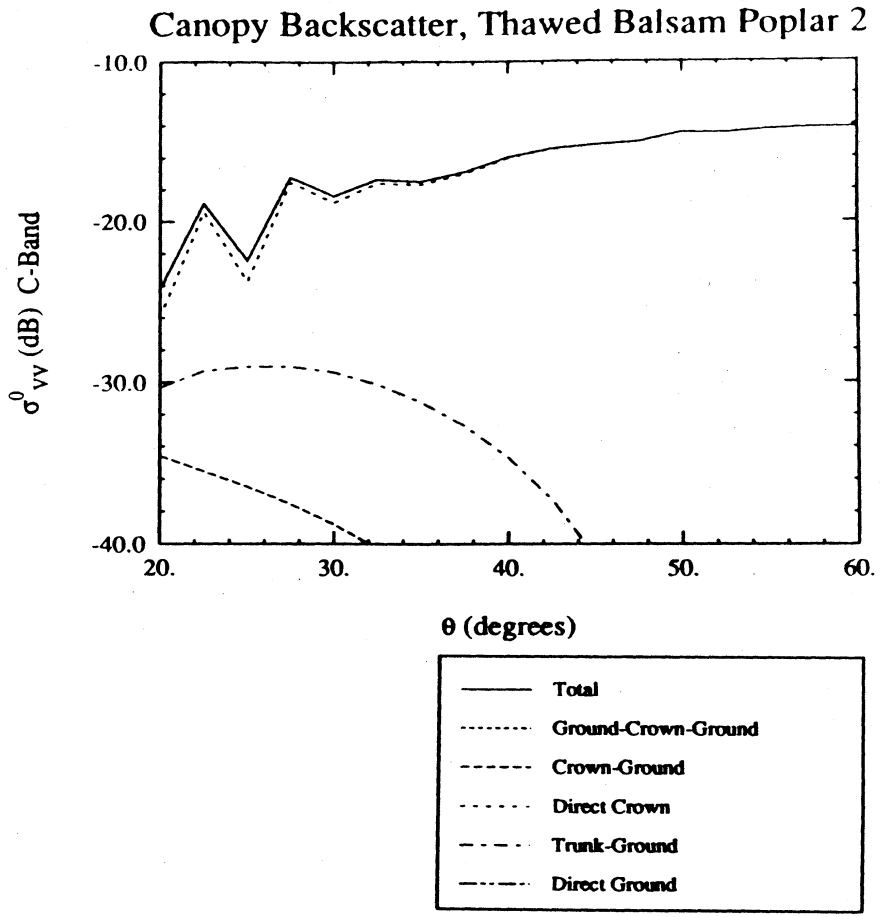

Figure 69. Components of modelled backscatter at C-band for balsam poplar 2 with thawed conditions.

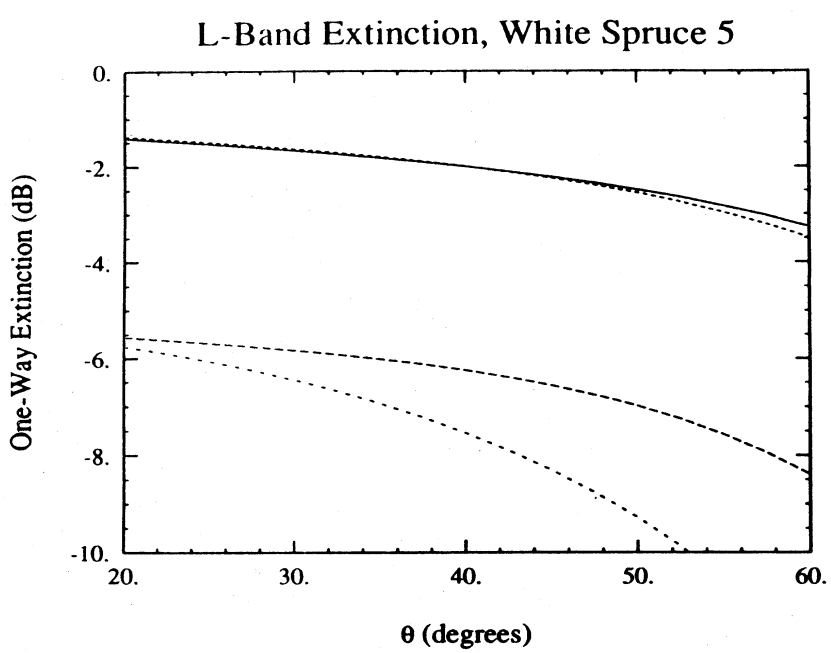

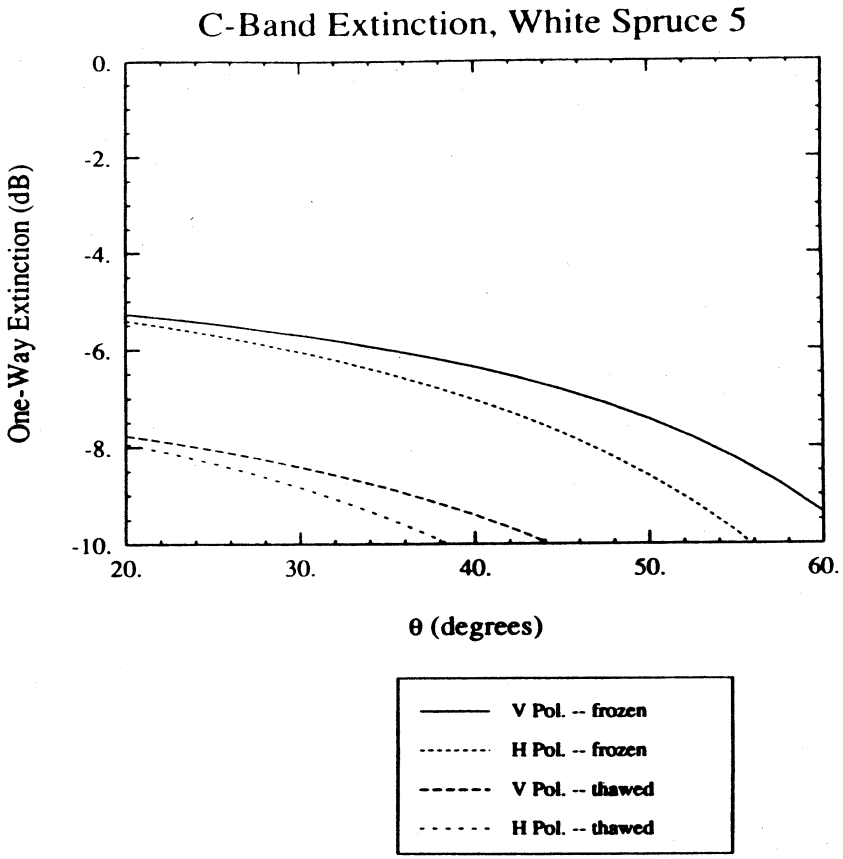

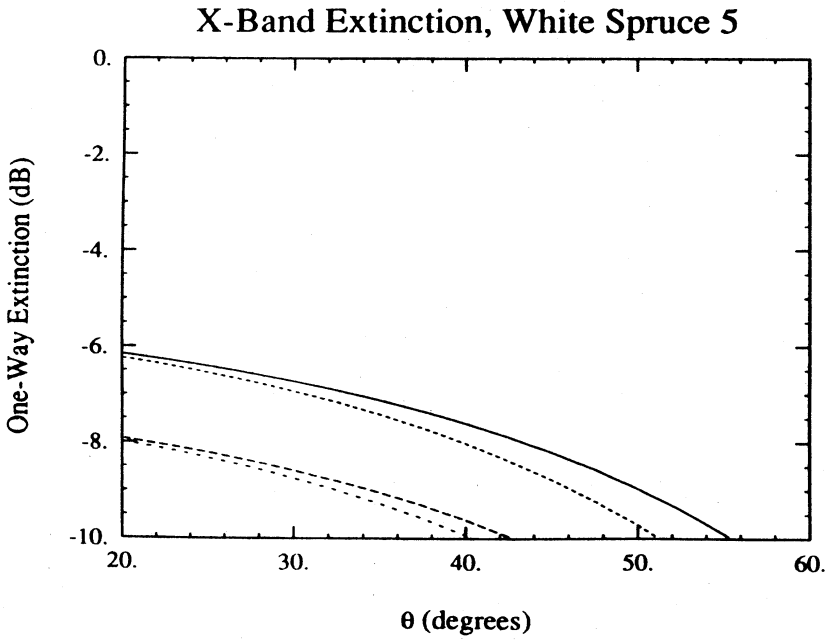

Figure 70. Modelled propagation loss through the tree canopy for white spruce 5.

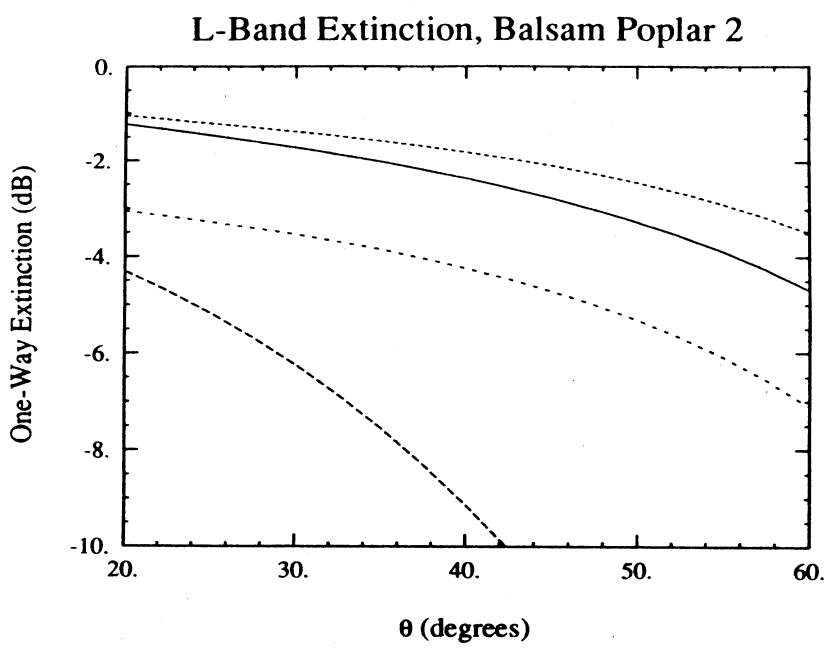

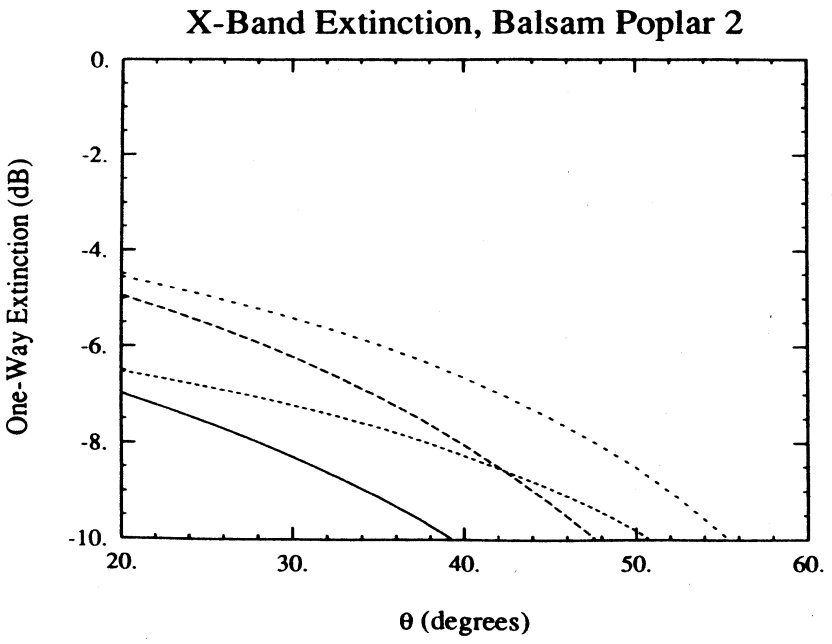

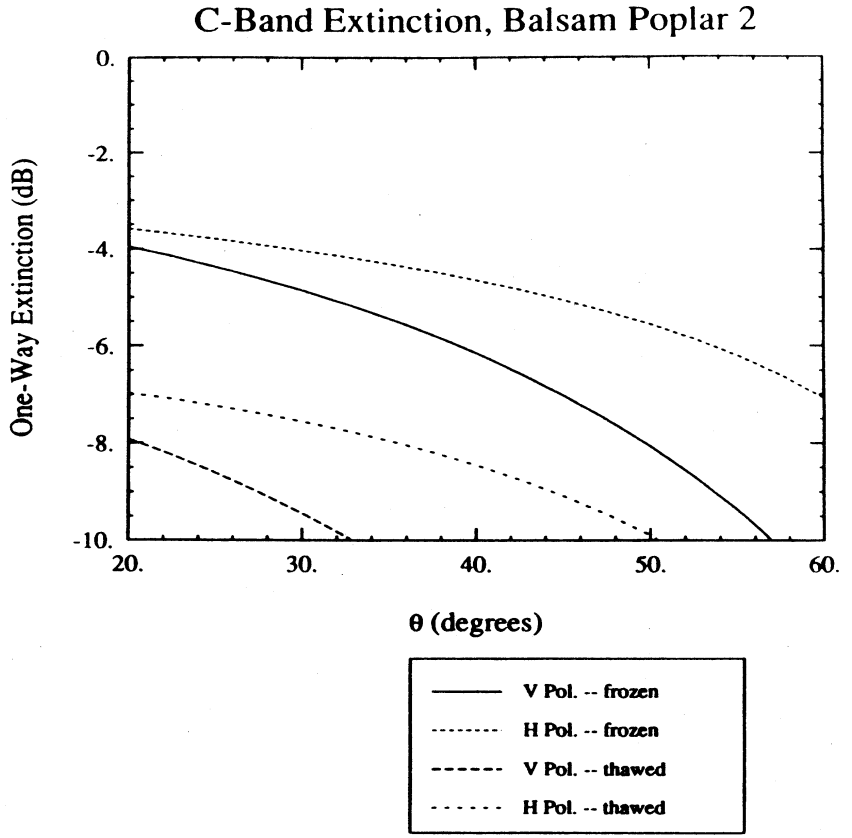

Figure 71. Modelled propagation loss through the tree canopy for balsam poplar 2.

MIMICS Validation

The MIMICS simulations for the boreal forest stands can be compared directly to the L-band backscatter derived from the JPL SAR imagery obtained on March 13 and March 19 for thawed and frozen conditions (Table 20). Due to the effects of ripples in the antenna patterns of the ERIM/NADC SAR at C- and X-bands, lack of absolute calibration necessitates comparison of the data for a given set of wave parameters (frequency and polarization) in a different fashion. The backscattered power extracted from the SAR imagery can be compared only between those stands at a common range location in the imagery and hence with the same ripple effects in the antenna pattern. Hence, the average backscatter is calculated for each stand, and those stands at a common range location (or angle of incidence) can be compared to the MIMICS simulations on the basis of stand-to-stand differences. This is accomplished by comparing backscatter differences relative to a benchmark stand. White spruce stand WS-1 is chosen for this purpose.

The direct comparison between MIMICS and the L-band SAR data is listed in Table 22. The correspondence between the observed and predicted values of σ^o is shown to be quite good for a blind comparison of the model to the SAR data particularly for the white spruce stands. However, it is also apparent that there is a consistent tendency for MIMICS to underpredict σ^o with the exception of σ^o_{HH} and σ^o_{HV} from black spruce with thawed conditions.

Non-random offsets between σ^o_{SAR} and σ^o_{MIMICS} may be related to either residual calibration errors in the SAR data or to errors inherent in the MIMICS model assumptions. The SAR calibration is considered to be quite good since the offsets are not uniform for a given SAR pass and as evidenced by the backscatter values derived from the snow-covered sandbars at $\theta = 50^o$. Table 20 shows the average backscatter from snow-covered frozen soil to be σ^o_{HH} = -19.5 dB, σ^o_{VV} = -19.3 dB and σ^o_{HV} = -30.6 dB; and these values are very close to the mean values observed by other investigators for similar

Table 22. Comparison of MIMICS estimates of σ^o to those values derived from the JPL SAR at L-band.

Polarization	Stand	σ^o (dB) Thawed condition March 13, 1988		Frozen Condition March 19, 1988	
		SAR Observation	MIMICS	SAR Observation	MIMICS
HH	white spruce-1	-10.0	-9.2	-13.1	-12.2
	white spruce-2	-8.4	-9.1	-11.4	-12.8
	white spruce-5	-8.1	-9.1	-11.1	-12.2
	black spruce-1	-12.9	-10.7	-14.9	-16.9
	balsam poplar-2	-9.2	-11.7	-12.7	-14.4
	alder	-8.7	-9.9	-11.3	-14.6
VV	white spruce-1	-10.4	-12.1	-14.9	-15.6
	white spruce-2	-9.9	-12.3	-14.5	-16.4
	white spruce-5	-9.1	-12.0	-14.8	-15.5
	black spruce-1	-14.4	-15.1	-16.4	-23.2
	balsam poplar-2	-10.4	-11.6	-14.8	-22.0
	alder	-9.7	-11.4	-14.0	-23.2
HV	white spruce-1	-15.2	-14.9	-21.0	-22.8
	white spruce-2	-14.2	-15.0	-20.4	-23.6
	black spruce-1	-20.0	-19.5	-23.7	-32.5

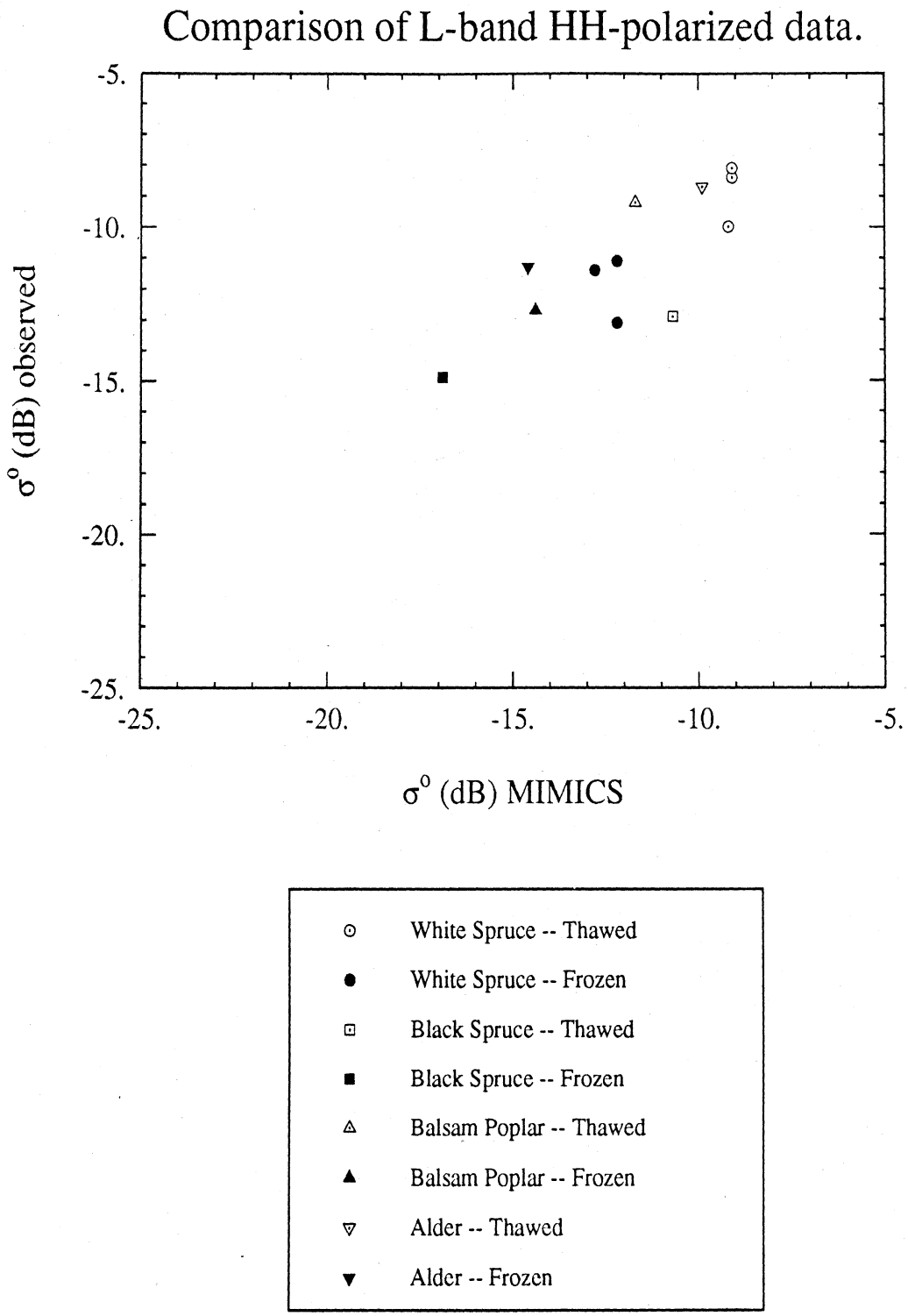

Figure 72. Comparison of MIMICS to HH-Polarized L-band SAR data for various forest stands.

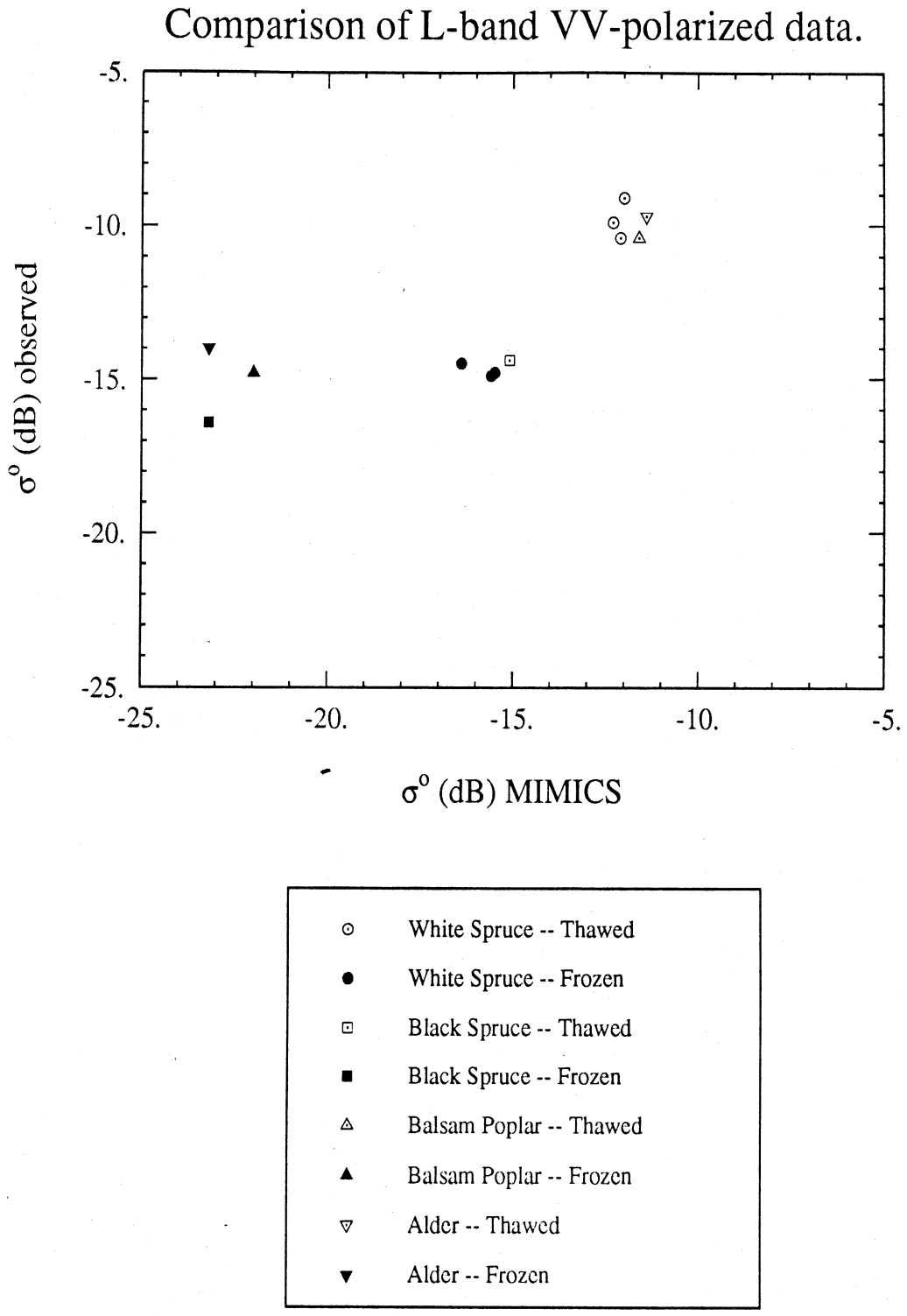

Figure 73. Comparison of MIMICS to VV-polarized L-band SAR data for various forest stands.

conditions (Ulaby and Dobson, 1989). Since the prediction offsets in Table 22 are tree specie, condition and polarization dependent, it is more likely that they are related to biases inherent in the scattering model.

The relationships between the SAR observations and the MIMICS predictions are shown graphically for HH and VV polarizations in Figures 72 and 73, respectively. The general tendency of MIMICS to underpredict σ^o_{HH} by 1 to 2 dB for stands other than white spruce is evident in Figure 72. It is clear in Figure 73 that the underestimates of σ^o_{VV} by MIMICS are greatest for frozen conditions and from those stands containing little (black spruce) or no (balsam poplar and alder) foliage in the crown layer. This is also true for σ^o_{HV}. These findings are consistent with expectations from the model results as regards the treatment of the surface scatter by MIMICS. Modification to the MIMICS treatment of the surface to account for scatter at the snow/soil interface would tend to increase σ^o in general; and the greatest impacts on net σ^o would be observed for the frozen condition wherein propagation loss through the crown layer is least and for σ^o_{VV} and σ^o_{HV} from stands of alder, balsam poplar and black spruce in particular since the contributions to net backscatter from other scattering source terms (such as that from the crown layer) are small.

An evaluation of the ability of MIMICS to predict the observed polarization ratios $\sigma^o_{HH}/\sigma^o_{VV}$ and $\sigma^o_{HH}/\sigma^o_{HV}$ is given in Table 23 for L-band. Close agreement between the model and the measurements is found for most stands and conditions with the exceptions of the frozen condition stands with relatively small propagation loss where the effects of underestimating σ^o_{VV} and σ^o_{HV} due to the snow/soil model are apparent. The model successfully predicts the polarization ratios to be smaller for the thawed conditions for both $\sigma^o_{HH}/\sigma^o_{VV}$ and $\sigma^o_{HH}/\sigma^o_{HV}$. These results are extremely encouraging for a blind comparison of the data to model predictions, wherein the model has not been revised or fitted for any free parameters.

The effects of changing environmental conditions in these boreal forest stands from frozen to thawed at L-band are given

Table 23. Comparison of Measured to Modelled Polarization Ratios at L-band for Boreal Forest Stands.

$\sigma^{o}_{HH}/\sigma^{o}_{VV}$ (dB)

Stand	Thawed Condtion March 13		Frozen Condition March 19	
	Observed	Model	Observed	Model
WS-1	0.4	2.9	1.8	3.4
WS-2	1.5	3.1	3.1	3.6
WS-5	1.0	2.9	3.7	3.3
BS-1	1.5	4.4	1.5	6.3
BP-2	1.2	-0.1	2.1	7.6
Alder	1.0	1.5	2.7	8.6

$\sigma^{o}_{HH}/\sigma^{o}_{HV}$ (dB)

WS-1	5.2	5.7	7.9	10.5
WS-2	5.8	5.9	9.0	10.8
BS-1	7.1	8.8	8.8	15.6

Table 24. Comparison of the Effects of Freezing on L-band Backscatter from Boreal Forest Stands $41^{o}<\theta<46^{o}$.

$\sigma^{o}_{thawed}/\sigma^{o}_{frozen}$

Stand	HH		VV		HV	
	observed	model	observed	model	observed	model
WS-1	3.1	3.1	4.5	3.6	5.8	7.9
WS-2	3.0	3.7	4.6	4.2	6.2	8.5
WS-5	3.0	3.1	5.7	3.6		7.9
BS-1	2.0	6.2	2.0	8.1	3.7	13.0
BP-2	3.5	2.7	4.4	10.4		15.1
alder	2.6	4.7	4.3	11.8		16.2

in Table 24. The model successfully predicts σ^o to increase for the thawed conditions and predicts the correct impact on polarization. The biggest effect of changing from frozen to thawed conditions is correctly modeled to be for σ^o_{HV} and the least effect for σ^o_{HH}. In addition, the relative magnitudes of the predicted changes are in very close agreement with those observed, particularly for the white spruce stands. The noteable exceptions to this general agreement are, of course, σ^o_{VV} and σ^o_{HV} for the discontinuous black spruce stand and the non-foliated balsam poplar and alder stands where the surface layer model incorporated into MIMICS is expected to be deficient.

For validation of MIMICS at C- and X-bands, the backscatter from each stand is ratioed to that from stand White Spruce-1 and compared at a common angle of incidence. These values are given in Tables 25 and 26 for C- and X-bands, respectively, and plotted in Figures 74 and 75, respectively. For the C-band comparisons plotted in Figure 74, most of the model predictions agree with the observations to within 1 dB with certain exceptions. As noted earlier for L-band, the C-band and X-band MIMICS estimates of σ^o_{VV} are too low for black spruce and may be due to the treatment of the snow layer. For balsam poplar stand BP-2, the like polarized backscatter estimated by MIMICS at low angles of incidence (i.e., $\theta = 27^o$) is too low by about 5 dB, and is also probably related to underestimates of forward scatter from the surface layer. In a similar manner, the like polarized backscatter from the alder stand is underestimated by 2-4 dB at $\theta = 31^o$, and is probably also related to the treatment of the snow layer.

The model validation results for L-, C-, and X-bands in comparison to the Alaskan SAR data are felt to be very encouraging. The results are generally in very close agreement with the observations. The differences found between the MIMICS predictions and the observed values of σ^o_{VV} and σ^o_{HV} for frozen conditions in black spruce, balsam poplar and alder are consistent with frequency and support the expectation that the surface layer model needs to be improved to adequately

Table 25. Comparison of C-band backscatter predicted by MIMICS to that derived from the ERIM/NADC SAR for frozen conditions on March 22, 1988. Backscatter is normalized to that of white spruce stand WS-1 at each angle of incidence.

σ^o/σ^o_{WS-1} (dB)

Stand	Angle of incidence	HH		VV	
		observed	MIMICS	observed	MIMICS
WS-2	27	1.07	-0.19	0.62	-0.32
	31	-1.1	-0.09	-0.57	-0.17
	53	-0.86	0.08	-0.4	-0.21
	55	0.05	0.09	0.3	-0.19
WS-5	53	-0.75	0.03	-0.28	0.0
	55	1.19	-0.01	0.62	0.0
BS-1	31	-2.92	-3.74	-0.62	-5.61
	55	-0.46	0.76	0.52	-4.56
BP-2	27	1.79	-5.12	0.96	-5.99
	53	-1.59	-0.82	-0.8	1.01
Alder	31	-6.27	-5.29	-3.7	-7.5
	55	-1.72	-1.71	1.77	1.49

Table 26. Comparison of X-band backscatter predicted by MIMICS to that derived from the ERIM/NADC SAR for frozen conditions on March 22, 1988. Backscatter is normalized to that of white spruce stand WS-1 at each angle of incidence.

σ^o/σ^o_{WS-1} (dB)

Stand	Angle of incidence	HH		VV	
		observed	MIMICS	observed	MIMICS
WS-2	27	-0.82	-0.09	-1.43	-0.2
	31	0.35	-0.02	-2.45	-0.14
	53	-0.87	0.19	0.09	-0.12
	55	0.19	0.29	0.08	-0.10
WS-5	53	-1.11	0.01	0.46	0.0
	55	0.9	0.0	0.55	0.0
BS-1	31	-0.43	-2.05	-3.53	-5.71
	55	-0.88	2.08	-0.33	-3.5
BP-2	27	-1.32	-6.68	0.26	-4.8
	53	-1.33	-2.66	0.40	0.26
Alder	31	-3.83	-2.75	-3.45	-6.07
	55	-2.51	-0.96	0.62	1.38

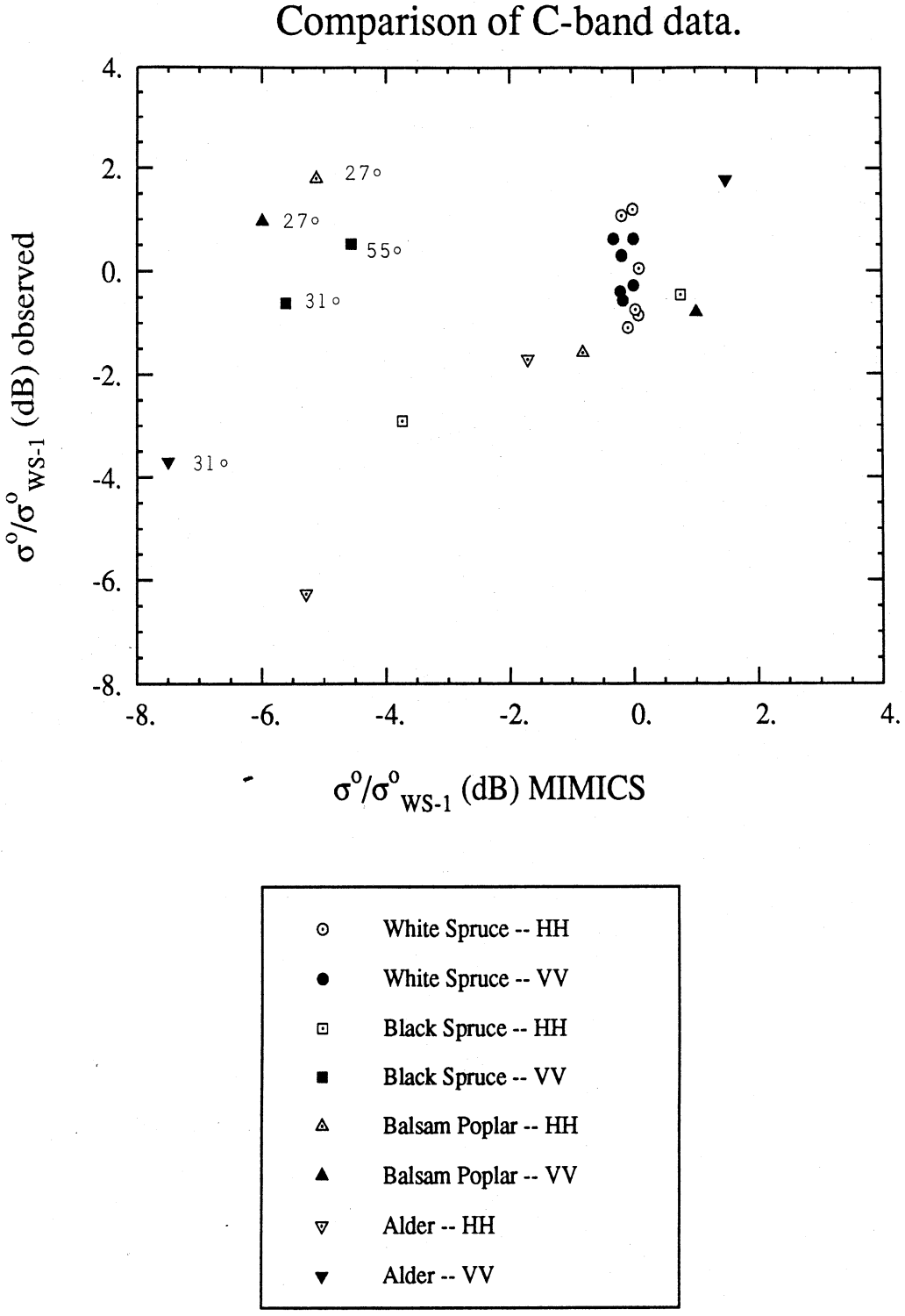

Figure 74. Comparison of relative backscatter from MIMICS to like-polarized C-band SAR data for various forest stands.

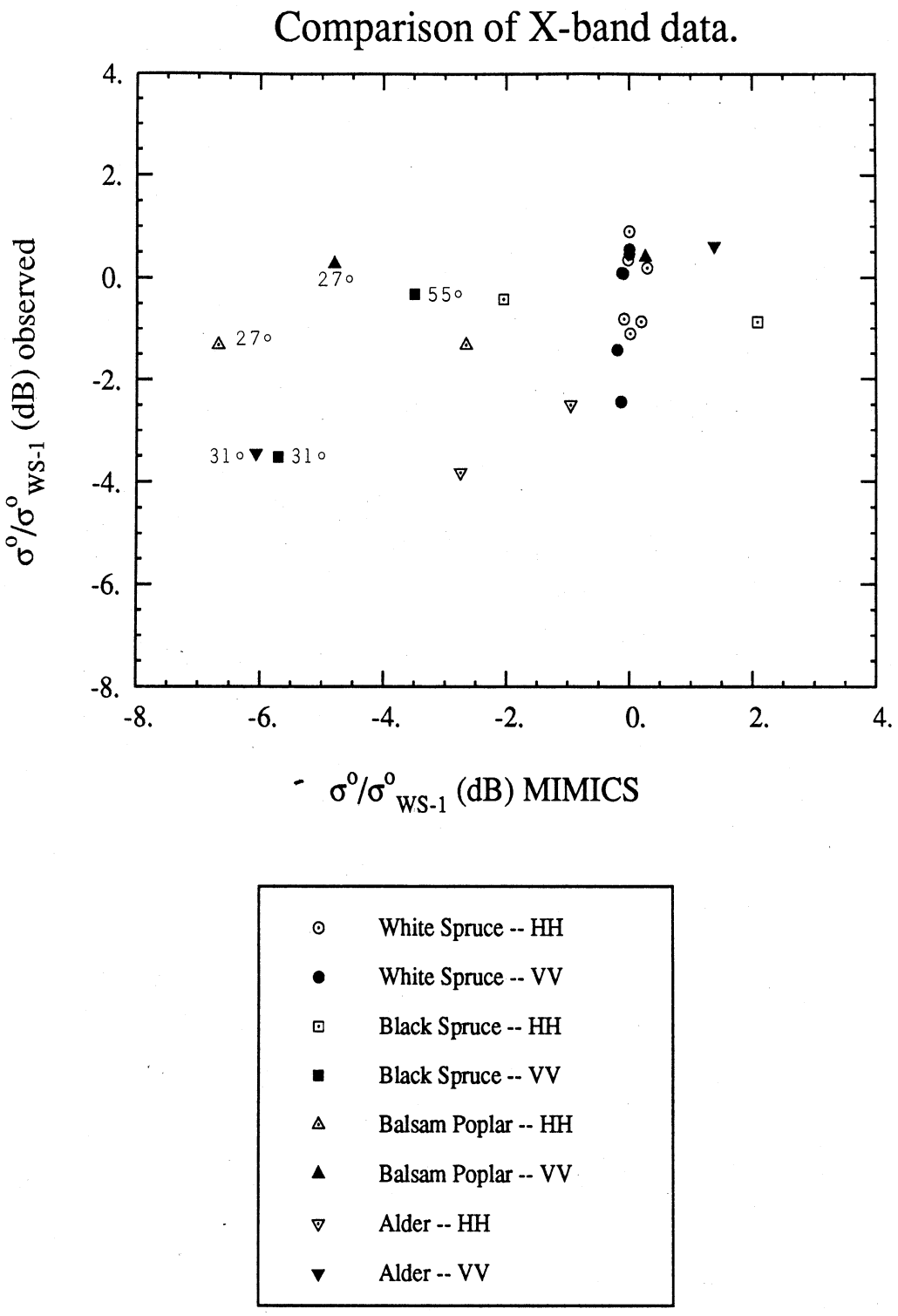

Figure 75. Comparison of relative backscatter from MIMICS to like-polarized X-band SAR data for various forest stands.

predict both backscatter and forward scattering at the snow-soil interface.

6.0 Conclusions

The Michigan Microwave Canopy Scattering (MIMICS) model has been used to simulate the backscatter and canopy extinction for a walnut orchard and for various boreal forest stands under both frozen and thawed winter conditions. In the case of the walnut orchard, MIMICS inputs for stand and crown layer architecture and dielectric properties of the canopy and soil substrate are derived from extensive and detailed in situ observations. In contrast, only some of the required model inputs for the boreal forest stands are derived from in situ data while other parameters, particularly those related to crown architecture, are supported by allometric relationships transported from other locations or other species. Consequently, errors inherent in these relationships will result in systematic biases in the MIMICS predictions for these stands. Additionally, for the boreal forest stands, the surface layer is modelled as a half-space of snow; this is known, a priori, to be an over simplification which ignores both backscatter and forward scatter at the snow-soil interface.

Comparisons of MIMICS estimates of canopy propagation loss at C- and X-bands to SAR derived observations for various boreal forest stands validate the accuracy of the model. The model successfully predicts the observed polarization behavior, angular dependence, and frequency dependence for frozen conditions. The model is used to simulate canopy propagation losses for both the crown and trunk layers of each specie and the modeled results appear to be congruent with the observations for white spruce. In addition, MIMICS is used to simulate the effects of thawed, winter conditions on the various stands and shows canopy extinction to be very sensitive to the resulting changes in canopy dielectric properties.

As expected, both model and measurements concur that canopy propagation losses increase with frequency and is greater for V than H polarization. The relative contributions of the crown and trunk layers to net canopy extinction are shown to vary as functions of frequency, stand conditions, and environmental conditions (i.e., frozen vs. thawed conditions).

Finally, this study illustrates the difficulty in conducting experiments to evaluate canopy propagation loss. Experimental observations are made for discrete realizations of an inherently statistical process while the model results predict the average behavior on a stand basis. Consequently, many empirical observations are required in order to adequately sample the process and evaluate higher order statistics. In practise this is difficult to achieve since many targets are required for determination of two-way propagation loss through the canopy; and is further complicated by the large physical size of the targets. The large size of the targets leads to logistical problems as well as leading to an experimental bias wherein minimum loss conditions tend to be over sampled since the targets must be placed in gaps between the trunks.

Validations of the L-band backscatter predicted by MIMICS for the walnut orchard show the model to be highly effective when the canopy is well characterized. The behavior of like and cross polarized backscatter is accurately simulated by MIMICS for both the multi-angle and the diurnal experiments. The absolute levels of each polarization configuration are predicted with outstanding accuracy. Furthermore, MIMICS proved capable of predicting the short term and diurnal variations observed in the measured data over a three-day period. L-band backscatter is shown to be sensitive to fluctuations in crown and trunk layer dielectric properties even for short orchard trees.

MIMICS validations with respect to the airborne SAR data obtained for boreal forest stands in Alaska during March of 1988 are also very convincing. However, the validation process

is complicated by the issues of SAR calibration. For the L-band validation, the the SAR calibration appears to be very good. As a consequence, the MIMICS model generally agrees with the observed L-band SAR observations to within 1 dB for those stands and conditions wherein net σ^o is not dominated by direct backscatter from the surface or surface/canopy interaction terms. For the C- and X-band validations, the backscatter values obtained by the ERIM/NADC SAR can only be evaluated on a relative basis due to uncorrected antenna ripple effects. Consequently, the absolute magnitude of the frequency response predicted by MIMICS cannot be evaluated using this data set at the current time.

The validation results presented in Section 5 for the boreal forest stands show that MIMICS accurately predicts the observed polarization behavior at a given frequency and also the effects of environmental change from thawed to frozen conditions at L-band. For the boreal forest stands, the MIMICS simulations show net backscatter to generally be dominated by scattering occurring in the crown layer with terms related to interactions with the surface layer (i.e., ground-trunk and crown-ground) being of secondary importance. The relative weighting of the various terms is shown by MIMICS to be highly dependent upon the wave parameters of frequency, polarization and angle of incidence and also upon the scene parameters of stand type, canopy architecture, and dielectric properties. As expected, the model shows scatter within the crown layer to become increasingly significant as frequency increases. The effects upon L-band backscatter induced by freezing the canopy are shown by both the model and the measurements to decrease σ^o at all polarizations (most for σ^o_{HV} and least for σ^o_{HH}). The effects of changing environmental conditions of the boreal forest stands upon C- and X-band backscatter are shown by the model to vary in a complicated fashion as functions of wave parameters and stand conditions.

These predictions cannot currently be tested with the available SAR data set.

It is apparent that MIMICS needs to be improved to account for discontinuous canopies such as black spruce where large gaps in the canopy present unobstructed return from the surface layer. In addition, systematic prediction errors in the model for σ^0_{VV} and σ^0_{HV} for black spruce and the non-foliated stands of alder and balsam poplar are congruent with expectations that the MIMICS treatment of the surface layer should be improved. Such an improvement would treat the surface layer as a 20-30 cm thick layer of snow with variable wetness over a frozen soil layer. The difficulty in applying this approach resides in defining the appropriate roughness of the snow-soil interface such that both forward scatter and backscattering process are accurately modeled.

REFERENCES

Cimino, J., M.C. Dobson, D.Gates, E. Kasischke, R. Lang, J. Norman, J. Paris, F.T. Ulaby, S. Ustin, V. Vanderbuilt, and J. Weber, 1988, "Eos Synergism Study 1987 Field Experiment Data Report," *JPL Technical Report,* May 1988.

Cimino, J.B., D. Casey, N. Christensen, M.C. Dobson, F. Ulaby, E. Kasischke, J. Richards, C. Slaughter, and L. Viereck, "The Effect of Changing Environmental Conditions on Microwave Signatures of Forest Ecosystems," accepted for publication in *Int. J. Rem. Sens.*, Feb. 1990.

Davis, R.J., J. Dozier, E. LaChapelle, and R. Pula, "Field and Laboratory Measurements of Liquid Water by Dilution," *Water Research,* Vol. 21, pp. 1415-1420, 1985.

Dobson, M.C., "Diurnal and Seasonal Variation in the Microwave Dielectric Constant of Selected Trees," *Proc. of Int. Geosci. Ren. Sens. Symp.*, 12-16 Sept. 1988, Edinburgh UK, Vol. 3, pp. 1754.

Dobson, M.C., K. McDonald, F.T. Ulaby, and J.F. Paris, "Diurnal Patterns in Multifrequency, Multipolarization Backscattering by a Walnut Orchard," *Proc. of Int. Geosci. Sens.* Symp., 12-16 Sept., 1988, Edinburgh, UK, Vol. 3, pp. 1755.

El-Rayes, M., "The Measurement and Modelling of the Dielectric Behavior of Vegetation Materials in the Microwave Region (0.5-20.4 GH_Z),"Ph.D. Thesis, Dept. of Electrical Engineering and Computer Engineering, University of Kansas, Lawrence, Kansas, Nov. 1986.

Eom, H.J. and A.K. Fung, "A Scatter Model for Leafy Vegetation up to Ku-Band," *Remote Sensing of Environment,* Vol. 15, pp. 185-200, 1984.

Fung, A.K. and F.T. Ulaby,"A Scatter Model for Leafy Vegetation," *IEEE Trans. Geoscience and Remote Sensing,* Vol. GE-16, pp. 281-286, 1978.

Hallikainen, M.T., F.T. Ulaby, and M. Abdelrazike, "Dielectric Properties of Snow in the 3 to 37 GH_Z Range," *IEEE Trans. Antennas and Propagation,* Vol. AP 34, No. 11, pp. 1329-1340, Nov. 1986.

Hallikainen, M.T., F.T. Ulaby, M.C. Dobson, M.A. El-Rayes, and L.K. Wu,"Microwave Dielectric Behavior of Wet Soil - Part I: Empirical Models and Experimental Observations," *IEEE Trans. Geoscience and Remote Sensing*, Vol. GE-23, No. 1, pp. 25-34, 1986.

Jaeger, B., "Report on Stand Characteristics Measured in Bonanza Creek Experimental Forest for the SAR-IFIT Project (Synthetic Aperture Radar-International Forestry Investigation Team), Summer 1988", Forest Soils Laboratory Technical Report, University of Alaska, Fairbanks, AK, December 1988.

Kasischke, E.S., *personal communication.*, Dec., 1988.

Kasischke, E.S., D. Beverstock, C.A. Russel, M.C. Dobson, and K.C. McDonald, "X- and C-band Forest Extinction Study," ERIM Tech Report, Environmental Research Institute of Michigan, Ann Arbor, MI, April 1989.

Kirby, C.L., "A Taper and Volume Table and Volume Formulae for Black Spruce in Saskatchewan," *Forestry Chronicle*, pp. 242-253, Sept. 1960.

Klein, J.D., "Calibration of Quadpolarization SAR Data Using Backscatter Statistics," *Proc. of International Geoscience Remote Sensing Symposium*, July 10-14 1989, Vancouver, B.C., Vol. 5, pp. 2893-2896.

Kwok, R., *personal communication*, Dec. 1989.

Lee, J.K. and J.A. Kong, "Active Microwave Remote Sensing of an Anisotropic Random Medium Layer," *IEEE Trans. Geos. Rem. Senc.*, Vol. GE-23, 910-928, 1985.

Lundgren, A.L. and W.A. Dolid, "Biological Growth Functions Describe Published Site Index Curves for Lakes Sates Timber Species," *Research Paper NC-36*, USDA Forest Services, North Central Forest Exp. Station, 1970.

Manning, G.H., M.R.C. Massie, and J. Rudd, "Metric Single-Tree Weight Tables for the Yukon Territory," Information Report BC-X-250, Pacific Forest Res. Centre, 1984.

Martens, S.N., S.L. Ustin, and J.M. Norman, "Measurement of Tree Canopy Architecture," accepted for publication in *Internat. Journal of Remote Sensing,* February 1990.

Nelson, N.D., T. Burk, and J.G. Isebrands, "Crown Architecture of Short-Rotation, Intensively Cultured Populus. I. Effects of Clone and Spacing on First-Order Branche Characterstics," *Canadian J. of Forest Research,* Vol. No. II, pp. 73-81, 1981.

Ruck, G.T., D.E. Barrick, W.D. Stuart, and C.K. Krichbaum, *Radar Cross Section Handbook*, Vol. 1, New York, NY: Plenum Press, 1970.

Sarabandi, K., "Electromagnetic Scattering from Vegetation Canopies," Ph.D. Thesis, Electrical Engineering, University of Michigan, Ann Arbor, MI, September 1989.

Singh, T., "Weight Tables for Important Tree Species in the Northwest Territories," *Forest Management Note, Note No. 27,* Northern Forest Res. Center, Edmonton, Alberta, December 1983.

Tsang, L. and J. Kong,"Application of Strong Fluctuation Random Medium Theory to Scattering from Vegetation-Like Half Space," IEEE Trans.on Geoscience and Remote Sensing, Vol. GE-19-19,No. 1, pp. 62-69, January 1981.

Tsang, L., J.A. Kong, and R.T. Shin, *Theory of Microwave Remote Sensing*, New York, NY: John Wiley and Sons, pp.160-162, 1985.

Ulaby, F.T. and M.A. El-Rayes, 1987, "Microwave Dielectric Spectrum of Vegetation, Part II: Dual-Dispersion Model," *IEEE Trans. Geos. Ren. Sens.*, Vol. GE-25, No. 5, pp. 550-557, September 1987.

Ulaby, F.T. and M.C. Dobson, *Handbook of Radar Scattering Statistics for Terrain*, Norwood, MA: Artech House, 1989.

Ulaby, F.T., K. Sarabandi, K. McDonald, M. Whitt and M.C. Dobson, "Michigan Microwave Canopy Scattering Model (MIMICS)" , accepted for publication in the *International Journal of Remote Sensing*, February 1990.

Ulaby, F.T., K. Sarabandi, K. McDonald, M. Whitt and M.C. Dobson, "Michigan Microwave Canopy Scattering Model (MIMICS)," The University of Michigan Radiation Laboratory, Report No. 022486-T-1, July 1988.

Ulaby, F.T., R.K. Moore, and A.K. Fung, *Microwave Remote Sensing: Active and Passive, Vol. III-From Theory to Applications*, Dedham, MA.: Artech House, 1986.

Ustin, S.L., S. Martens, J. Norman, and D. Goldhammer, "Measurement and Characterization of Tree Canapy Architecture," *Proc. of Int. Geosc. Ren. Sens. Symp.*, 12-16 Sept. 1988, Edinburgh, UK, Vol. 3, p. 1753.

VanCleve, K., and L.A. Viereck, "Distribution of Selected Chemical Element in Even-Aged Alders (Alnus) Ecosystems Near Fairbanks, Alaska,"*Artic and Alpine Research, V*ol. 4, No. 3, pp. 239-255, 1972.

VanCleve, K., L.A. Viereck, and R.L. Schlentner, "Accumulation of Nitrogen in Alder (Alnus) Ecosystems Near Fairbanks, Alaska," *Artic and Alpine Research,* Vol.3, No. 2, pp. 101-114, 1971.

Weber, J.A. and S.L. Ustin, "Water Relations of a Walnut Orchard: Simultaneous Measurement with Remote Sensing," *Proc. Int. Geos. Rem. Sens. Symposium,* 12-16 Sept. 1988, Edinburgh, U.K., Vol. 3, pp. 1749-1751.

Yarie, J. and K. VanCleve, "Biomass and Productivity of White Spruce Stands in Interior Alaska," *Canadian Journal of Forest Research*, Vol. 13, No. 5, pp. 767-772, 1983.

Zimmerman, M.H. and C.L. Brown, *Trees: Structure and Function*, New York, NY: Springer-Verlag, 1971.